

AD-A110 663

MOTOROLA INC SCOTTSDALE AZ GOVERNMENT ELECTRONICS DIV
DOUBLY ROTATED CUT SAW DEVICES.(U)
JAN 82 D F WILLIAMS, F Y CHO

F/8 9/1

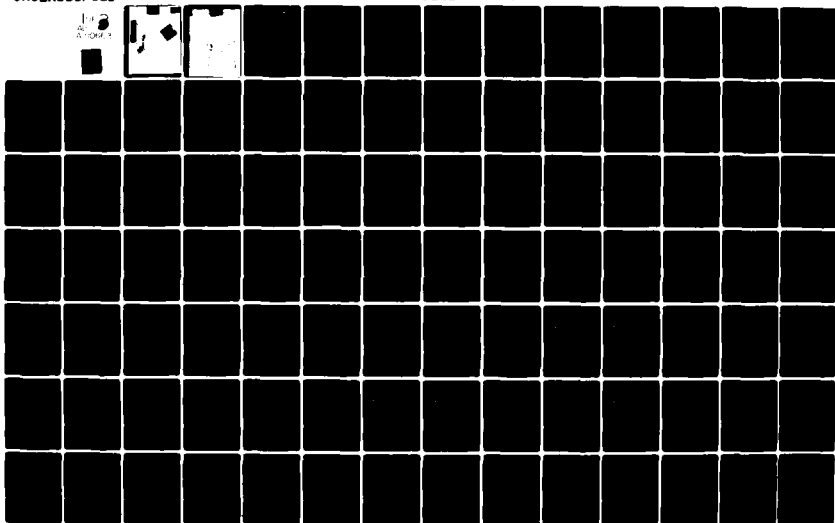
DAAK20-79-C-0275

UNCLASSIFIED

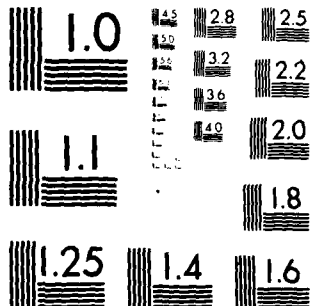
DELET-TR-79-0275-F

NL

10
A-110 663



11066

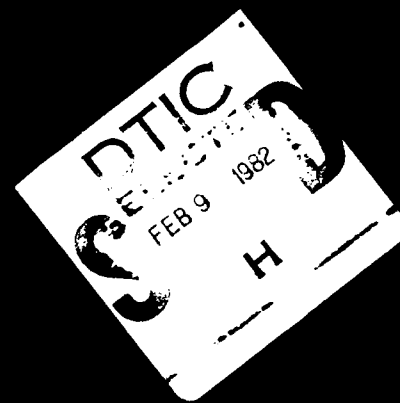


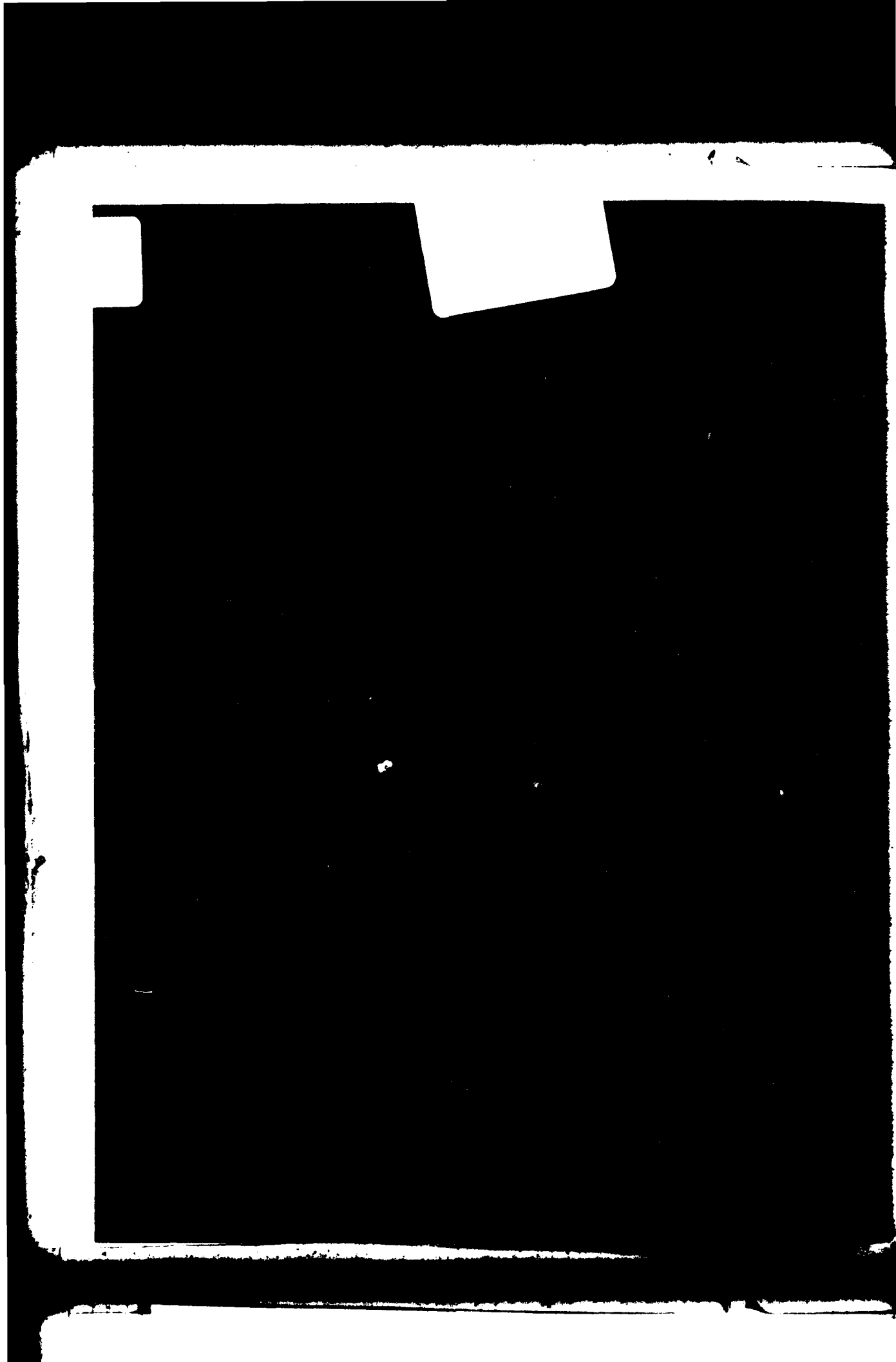
MICROCOPY RESOLUTION TEST CHART
NATIONAL BUREAU OF STANDARDS-1963-A

LEVEL III

122

AD A110663





UNCLASSIFIED

SECURITY CLASSIFICATION OF THIS PAGE (When Data Entered)

REPORT DOCUMENTATION PAGE		READ INSTRUCTIONS BEFORE COMPLETING FORM
1. REPORT NUMBER DELET-TR-79-0275-F	2. GOVT ACCESSION NO. AD-A110	3. REPORT TYPE & CATEGORY NUMBER 643
4. TITLE (and Subtitle) Doubly Rotated Cut SAW Devices		5. TYPE OF REPORT & PERIOD COVERED Final Report 15 August 1979 to 15 August 1981
6. AUTHOR(s) D.F. Williams, F.Y. Cho		7. PERFORMING ORG. REPORT NUMBER
8. PERFORMING ORGANIZATION NAME AND ADDRESS Motorola, GED 8201 E. McDowell Rd. Scottsdale, AZ 85252		9. CONTRACT OR GRANT NUMBER(s) DAAK20-79-C-0275
10. CONTROLLING OFFICE NAME AND ADDRESS Director, US Army Electronics Tech & Devices Lab, ERADCOM ATTN: DELET-MM Fort Monmouth, NJ 07703		11. PROGRAM ELEMENT, PROJECT, TASK AREA & WORK UNIT NUMBERS 612705.H94.09.11.01
12. MONITORING AGENCY NAME & ADDRESS (if different from Controlling Office)		13. REPORT DATE January 1982
		14. NUMBER OF PAGES 186
		15. SECURITY CLASS. (of this report) UNCLASSIFIED
		16. DECLASSIFICATION/DOWNGRADING SCHEDULE
17. DISTRIBUTION STATEMENT (of this Report) Approved for Public Release; Distribution Unlimited.		
18. DISTRIBUTION STATEMENT (of the abstract entered in Block 20, if different from Report)		
19. SUPPLEMENTARY NOTES		
20. KEY WORDS (Continue on reverse side if necessary and identify by block number) Surface Acoustic Waves, Quartz, Temperature, Power Flow Angle, Coefficient of Frequency, X-Ray Orientation.		
21. ABSTRACT (Continue on reverse side if necessary and identify by block number) The objective of this program is the exploratory development of doubly rotated cuts of quartz possessing superior Surface Acoustic Wave (SAW) properties for applications involving environmentally hardened devices. The key properties examined and optimized both theoretically and experimentally are: first, second and third order Temperature Coefficients of Delay (TCD), piezoelectric coupling factor, power flow angle, Bulk Acoustic Wave (BAW) inverse velocity surfaces, degeneracies and leaky waves, and sensitivities of the above quantities to misorientations and manufacturing tolerances.		

DD FORM 1 JAN 79 1473

EDITION OF 1 NOV 66 IS OBSOLETE

UNCLASSIFIED

SECURITY CLASSIFICATION OF THIS PAGE (When Data Entered)

67

UNCLASSIFIED

SECURITY CLASSIFICATION OF THIS PAGE(When Data Entered)

The program consists of two major task areas comprising an interactive numerical/experimental approach. Task I involves the numerical computation of the key SAW properties for doubly rotated quartz substrates for the purpose of locating promising angular ranges with properties superior to the singly rotated cuts now in existence. More detailed calculations follow to refine the angular coordinates in order to specify cuts for experimental verification in Task II. In Task II, sets of substrates with promising orientations identified in Task I will be prepared and SAW device patterns will be fabricated for evaluation of the key SAW properties. The experimental results of this task will be correlated with the theoretical predictions and an iterative process developed for refinement of both theoretical and experimental parameters. As the program proceeds, working SAW device models are delivered as a demonstration of progress and an indication of the future potential of the doubly rotated cuts. This report contains the results and summary of Task I, Task II and the results of an iteration. The discovery of variation of power flow angle as a function of temperature and methods for compensation of the temperature coefficient of frequency as the power flow angle changes is discussed.

Accession For	
NTIS	CRA&I
DTIC	DDP
Unannounced	
Justification	
By	
Distribution/	
Availability C	
Avail. Mode.	
Dist	Special



UNCLASSIFIED

SECURITY CLASSIFICATION OF THIS PAGE(When Data Entered)

TABLE OF CONTENTS

Section	Page
I INTRODUCTION	1
1 PROGRAM OBJECTIVE	1
2 PROGRAM SCOPE	1
3 TECHNICAL APPROACH SUMMARY OF TASK I	1
4 TECHNICAL APPROACH SUMMARY OF TASK II	2
II TECHNICAL DISCUSSION OF TASK I	4
1 INTRODUCTION	4
a. Calculation of Temperature Coefficients	5
b. Rayleigh Wave	6
c. Methods for Calculating the Temperature Dependence of the Rayleigh Velocity	7
d. Piezoelectric Coupling Factor	90
e. Power Flow Angle	92
f. Proximity and Excitation Strength of Bulk Acoustic Wave (BAW) Spectrum	93
g. Degeneracies	96
h. Sensitivities Due to Crystal Misorientation	98
2 WAFER FABRICATION	100
a. Face Definitions	101
b. Running the X-Ray Program	101
c. Analysis of X-Ray Program	103
d. Determination of the Actual ψ Angle	105
e. Determination of α and β	106
f. Procedure Used to Zero X-Ray Machine	107
g. Cutting Techniques for Doubly Rotated Orientations	109
h. Wafer Polishing	109
III TECHNICAL DISCUSSION OF TASK II	111
1 INTRODUCTION	111
2 THEORETICAL PROPAGATION CHARACTERISTICS	111
3 MASK DESIGN	112
4 EXPERIMENTAL MEASUREMENT OF TCF	114
5 EXPERIMENTAL PROPAGATION CHARACTERISTICS	114
6 EXPERIMENTAL MEASUREMENT OF FREQUENCY VERSUS TEMPERATURE	120

TABLE OF CONTENTS (Cont)

Section	Page
IV TECHNICAL DISCUSSION OF 2ND ITERATION	131
1 INTRODUCTION	131
2 EXPERIMENTAL RESULTS	131
3 THEORETICAL RESULTS	132
4 TEMPERATURE VARIATION OF THE SAW POWER FLOW ANGLE	147
5 REPRESENTATIVE EXPERIMENTAL DATA IN THE SELECTED AREAS	152
V CONCLUSION	158
APPENDIX A — VOLUME PERTURBATION OF AULD	161
APPENDIX B — VOLUME PERTURBATION FORMULA OF SINHA AND TIERSTEN	165
APPENDIX C — THE DIFFERENTIATION METHOD	167
APPENDIX D — SOLUTION METHOD	171
APPENDIX E — EQUIVALENCE OF TEMPERATURE COEFFICIENTS OF FREQUENCY AND DELAY	173
APPENDIX F — X-RAY RUN	175
APPENDIX G — X-RAY PROGRAM	179

LIST OF FIGURES

Figure		Page
1	Finite Difference Method Versus Experiment ST-Cut (Quartz)	10
2	Finite Difference Method Calculation for Hauden's Cut (YXwlt) $56^{\circ}/40^{\circ}/27^{\circ}$	11
3	Tiersten's Method Versus Finite Difference and Experiment	12
4	Calculated Values of TCF ⁽¹⁾ Versus Propagation Angles	14
5	TCF Map of SAW Device on Quartz	82
6	Temperature Coefficients of the Fundamental Constants of Quartz	84
7	Nonzero Power Flow Angle	90
8	Bragg Condition for Excitation of BAW	91
9	Polar Plots of Inverse Velocities for a (YXwlt) $0/27/137.8$	92
10	Polar Plots of Inverse Velocities for a (YXwlt) $7/27/135.59$	93
11	Flow Diagram of Calculation for Reflected Angles in Doubly Rotated Cut of Quartz	99
12	Two Possible Ways of Defining the Crystal Axes on a Lumbered Bar	100
13	X-Ray Position Chart	101
14	Direction of Mask Alignment Angle Rotation ψ	102
15	Crystal Rotation (YXwlt) $\phi/\theta/0$	102
16	Actual -Z Face, Crystalline Axes, α , β , and $\Delta\psi$	103
17	Mask Rotation to Obtain Desired ψ	104
18	Position of Step 3, 10.1 Alignment Wafer	105
19	Position of Step 5, 10.1 Alignment Wafer Rotated by 180 Degrees About -Y Axis	105
20	SAW Oscillator Device	113
21	Photograph of a Fabricated Wafer With Propagation Directions of $8^{\circ}27'/27^{\circ}54'/133^{\circ}54' \pm n(0.2^{\circ})$	115
22	Frequency Temperature Curve With Different ψ Angles	116
23	Measurement System	117
24	Test Circuits	118
25	Experimental Set-Up For Laser Probe	121
26	Angular Relation of Incidence and Reflected Beam	121
27	Test Set-up for Laser Probing of Acoustic Wave Beam-Steering Characteristics	123
28	Intensity Distribution at Near Field	124
29	Intensity Distribution at Far Field	125

LIST OF FIGURES (Cont)

Figure	Page
30 Experimental Frequency Response (Test No. 1)	126
31 Experimental Frequency Response (Test No. 2)	127
32 Experimental Frequency Response (Test No. 3)	128
33 Experimental Frequency Response (Test No. 4)	129
34 Experimental Frequency Response (Test No. 5)	130
35 Frequency-Temperature Dependence for (YX wlt) 0.633/26.15/137.0	133
36 Frequency-Temperature Dependence for (YX wlt) 1.05/28.0667/136.534	134
37 Frequency-Temperature Dependence for (YX wlt) 0.633/26.15/136.813 to (YX wlt) 0.633/25.15/ 137.016	135
38 Frequency-Temperature Dependence for (YX wlt) 5.583/27.833/134.994 to (YX wlt) 5.583/ 27.833/135.794	136
39 Frequency-Temperature Dependence for (YX wlt) 6/26.967/135.812 to (YX wlt) 6/26.967/ 136.012	137
40 Frequency-Temperature Dependence for (YX wlt) 7.417/27.833/134 to (YX wlt) 7.417/27.833/ 135.2	138
41 Frequency-Temperature Dependence for (YX wlt) 8.033/26.9667/134.618 to (YX wlt) 8.033/ 26.9667/136.818	139
42 TCF Contour Map ($\text{PHI} = 0^\circ$)	141
43 TCF Contour Map ($\text{PHI} = 10^\circ$)	142
44 TCF Contour Map ($\text{PHI} = 20^\circ$)	143
45 TCF Contour Map ($\text{PHI} = 30^\circ$)	144
46 Power Flow Angle Against Temperature for (YX wlt) 14.283/39.117/40.6	148
47 Pictorial Representation of Device Response	149
48 Device Response to Short Gated 270.4 MHz Input Pulse	150
49 Transducer Design	152
50 Power Flow Angle Compensated SAW Device	153
51 Temperature Stable Cut of Quartz for SAW	154
52 Temperature Stable Cut of Quartz for SAW	155
53 Temperature Stable Cut of Quartz for SAW	156
54 Temperature Stable Cut of Quartz for SAW	157

LIST OF TABLES

Table	Page
1 Crystal Elastic Constants' Temperature Derivatives	86
2 Propagation Characteristics of Selected Orientations	89
3 Propagation Characteristics of Selected Orientations	91
4 Power Flow Angles ST-Cut	93
5 $\partial \text{TCF}^{(1)} / \partial \psi$ For Selected Cuts	99
6 $\partial \text{TCF}^{(1)} / \partial \phi$ and $\partial \text{TCF}^{(1)} / \partial \theta$ For Selected Cuts	100
7 Experimental Velocities of Cuts	119
8 Comparison of Experimental and Calculated Results	122
9 Comparison of Experimental and Calculated Results	132
10 Propagation Characteristics of Crystal Orientations	140
11 Propagation Characteristics of Selected Orientations	145
12 $\partial \text{TCF}^{(1)} / \partial \psi$ For Selected Cuts	146
13 $\partial \text{TCF}^{(1)} / \partial \phi$ and $\partial \text{TCF}^{(1)} / \partial \theta$ For Selected Cuts	147
14 Temperature Dependence of the Power Flow Angle on Doubly Rotated Cuts at Orientations (YX wlt) PHI/THETA/PSI	150

SECTION 1

INTRODUCTION

1. PROGRAM OBJECTIVE

The objective of this program is the exploratory development of doubly rotated cuts of quartz possessing superior Surface Acoustic Wave (SAW) properties for applications involving environmentally hardened devices. The key properties examined and optimized both theoretically and experimentally are: first, second and third order Temperature Coefficients of Delay (TCD), piezoelectric coupling factor, power flow angle, Bulk Acoustic Wave (BAW) inverse velocity surfaces, leaky waves, and sensitivities of the above quantities to misorientations and manufacturing tolerances.

2. PROGRAM SCOPE

The program consists of two major task areas comprising an interactive numerical/experimental approach. Task I involves the numerical computation of the key SAW properties for doubly rotated quartz substrates for the purpose of locating promising angular ranges with properties superior to the singly rotated cuts now in existence. More detailed calculations follow to refine the angular coordinates in order to specify cuts for experimental verification in Task II. In Task II, sets of substrates with promising orientations identified in Task I are prepared and SAW device patterns fabricated for evaluation of the key SAW properties. The experimental results of this task are correlated with the theoretical predictions and an iterative process develops for refinement of both theoretical and experimental parameters. As the program proceeds, working SAW device models are delivered as a demonstration of progress and an indication of the future potential of the doubly rotated cuts.

3. TECHNICAL APPROACH SUMMARY OF TASK I

To accurately characterize the properties of doubly rotated quartz, three basic capabilities are essential:

- a. Theoretical approach and associated computer software which will accurately and quickly locate promising zero TCD cut angles and characterize the other key SAW parameters
- b. Source of rotated quartz substrates of superior quality which can be quickly fabricated and the angular orientation determined with a high degree of precision
- c. Required fabrication facilities and measurement tools to accurately determine the key SAW device parameters.

In the theoretical area, this program has characterized two basic theoretical approaches for the identification of zero TCDs on rotated cuts of quartz. For this study, two computer programs available at Motorola are used. The first program calculates the first, second and third order TCDs of rotated cuts using a finite difference method.¹ This technique is simple, well established, and has been used for analytically determining the temperature coefficient curves for singly and doubly rotated cuts of quartz. To more accurately define the temperature coefficient properties, a second program which encompasses lattice skewing effects is used. This more complete theoretical approach is based on the work of Sinha and Tiersten², and its utility has been verified.

The final theoretical work is the characterization of the other key parameters with standard SAW programs used routinely for material characterization and device development.

Accurately oriented quartz bars, supplied by Motorola, Carlisle, are cut at Motorola, lapped and finely polished at Motorola and Crystal Technology Inc. A mechanical polishing procedure is used. During this program, several substrates from a single bar with incremental angular deviation about a promising angular position are fabricated. By careful organization of the angle selection and cut procedures, a substantial savings in time and money is achieved.

The angular orientation of the doubly rotated substrates are defined to an accuracy of within ± 5 minutes using X-ray diffractometry. Equipment used includes Laue pattern X-ray equipment, X-ray diffractometers, and precision wafer cut and polishing equipment.

4. TECHNICAL APPROACH SUMMARY OF TASK II

During this period the first iteration theoretical calculations performed to characterize doubly rotated cuts of quartz were completed. Theoretically temperature-stable cuts with zero TCF⁽¹⁾ and TCF⁽²⁾ as small as -1.0×10^{-8} were located. This represents a better than three-fold improvement over the ST cut. Experimental measurements of the TCF's have been performed on some doubly rotated cuts. Zero TCF⁽¹⁾ SAW devices for which the second order temperature term is the dominant term have been fabricated. Measured values of TCF⁽²⁾ of these devices as low as -1.5×10^{-8} have been obtained. The agreement between the experimental and the calculated results was excellent. Measured first order TCF's and those calculated by Sinha and Tiersten's perturbation program were found to differ by less than 3 ppm/C°, and second order TCF's calculated by the finite difference method were found to differ by less than 0.005 ppm/C°². Both the measured and calculated third order TCF's were found to be too small to be a significant factor in device performance.

¹"Numerical Computation of Acoustic Surface Waves in Layered Piezoelectric Media-Computer Program Descriptions", William Jones, William Smith, Donald Perry, Final Report F19628-70-C-0027, prepared for Air Force Cambridge Research Laboratories by Hughes Aircraft Company.

²"On the Temperature Dependence of the Velocity of Surface Waves in Quartz", B.K. Sinha and H.F. Tiersten, Proceedings of the 32nd Annual Symposium of Frequency Control, 1978, pp. 150-153.

A complete SAW test area and optical laboratory form the basis for the experimental evaluation of the key SAW parameters of the doubly rotated quartz delay lines, oscillators and resonators. The equipment is set up for rapid display, measurement and recording of propagation directions, TCF's, velocities, beam steering angles and diffraction.

The excellent agreement between the experimental and theoretical results, and the success with which low TCF cuts have been located, confirmed the utility and accuracy of the techniques used in the program. The second theoretical and experimental iterations promise to yield orientations and devices with even greater temperature stability than those already obtained.

SECTION II

TECHNICAL DISCUSSION OF TASK I

1. INTRODUCTION

Quartz is the most commonly used substrate for fabricating Surface Acoustic Wave (SAW) devices. In SAW narrowband filter, oscillator, and resonator applications, the temperature stability of the device is an important design parameter. Currently, almost all SAW devices fabricated on quartz use the ST-Cut, which exhibits a parabolic frequency dependence in temperature. For many applications, the temperature dependence of devices fabricated on ST quartz is too large. Thus it is desirable to find crystal cuts with superior temperature performance. Of course, many other design parameters must be considered when choosing a crystal cut. Some of the more important ones are the piezoelectric coupling coefficient, acoustic losses, dependence of device performance on cut misorientation, excitation of bulk modes, and beam steering angle. These parameters can all be determined for a given cut.

The objectives of this program are to find crystal cuts which exhibit zero temperature coefficients of delay so that there will be no frequency-temperature dependence observed in temperature stable oscillators, resonators and filters. Computer models and experimental verification were used to investigate the temperature dependence of different cuts of crystal for SAW devices.

Defining τ as the delay time for an acoustic wave to propagate between two points on the surface of the crystal, we wish to find orientations for which τ is constant in temperature, or more formally $(1/\tau)(d\tau/dT)|_{T=25 \text{ degrees C}} = 0$.

If F is the frequency of a SAW resonator, then the 1st order derivative is: $(1/F)(dF/dT) = -(1/\tau)(d\tau/dT)$. It is desirable to have the higher order derivatives to be as close to zero as possible, or $(1/2\tau)(d^2\tau/dT^2)|_{T=25 \text{ degrees C}} = 0$, etc.

Letting l be the length between two points, (τ) is simply given by $\tau = (l/V_s)$, $(1/\tau)(d\tau/dT) = (1/l)(dl/dT) - (1/V_s)(dV_s/dT)$.

Two computer programs for calculating τ as a function of the stress, the dielectric and piezoelectric constants of a substrate material are available for this study. Furthermore, the temperature variation of those constants for quartz are available, allowing one to calculate $(1/V_s)(dV_s/dT)$ by a finite difference method (note that higher order terms can be calculated the same way). If the crystal expansion coefficients are known, it is then a simple matter to calculate $(1/\tau)(d\tau/dT)$ for any particular orientation. Perturbation

programs developed by Sinha and Tiersten to calculate $(1/\tau)(d\tau/dT)$ are also available. Combined with a search method, the cuts for which first order temperature coefficient of frequency vanishes can be found.

a. Calculation of Temperature Coefficients

It has been shown that determining the temperature dependence of τ (time delay) is equivalent to determining the temperature dependence of F (frequency) via the relation $F \propto 1/\tau$.

Since the experimental data is derived from frequency measurements, the frequency characteristics of the devices is first determined. The relation between the temperature coefficient of frequency (TCF) and temperature coefficient of delay (TCD) are related as follows (See Appendix E):

$$\alpha_F^{(1)} = -\alpha_\tau^{(1)} \quad (1)$$

$$\alpha_F^{(2)} = -\alpha_\tau^{(2)} + (\alpha_\tau^{(1)})^2 \quad (2)$$

$$\alpha_F^{(3)} = -\alpha_\tau^{(3)} + 2\alpha_\tau^{(1)} \alpha_\tau^{(2)} - (\alpha_\tau^{(1)})^3 \quad (3)$$

where $\alpha_F^{(i)}$ is the i th order TCF, $\alpha_\tau^{(i)}$ is the i th order TCD.

Using the relations above, one can always relate one set of the temperature coefficients to the other.

The various procedures outlined in the following sections will yield the quantities $\alpha_v^{(i)}$, $i = 1, 2, 3$, with $V_i(T) \cong V_i(T_0)(1 + \alpha_v^{(1)} dT + \alpha_v^{(2)} dT^2 + \alpha_v^{(3)} dT^3)$ and $dT = T - T_0$.

The problem of interest is not only, however, in finding the $\alpha_v^{(i)}$'s but in finding the delay time τ and the frequency dependence F of a device. The frequency dependence $F(T) = F(T_0)(1 + \alpha_F^{(1)} dT + \alpha_F^{(2)} dT^2 + \alpha_F^{(3)} dT^3)$ is a function of not only V , but of $\ell(T_0) = \ell(T_0)(1 + \alpha_\ell^{(1)} dT + \alpha_\ell^{(2)} dT^2 + \alpha_\ell^{(3)} dT^3)$, the spacing between reflectors in a resonator (or the length of the delay line in an oscillator)

From the above relations and $(1 + X)^{-1} \cong 1 - X + X^2 - X^3$ if $X \ll 1$, then:

$$F = V/\ell \cong \{ V, (1 + \alpha_v^{(1)} dT + \alpha_v^{(2)} dT^2 + \alpha_v^{(3)} dT^3) \} / \ell_0 (1 + \alpha_\ell^{(1)} dT + \alpha_\ell^{(2)} dT^2 + \alpha_\ell^{(3)} dT^3) \quad (4)$$

$$\cong F(T_0) \{ 1 + \alpha_v^{(1)} dT + \alpha_v^{(2)} dT^2 + \alpha_v^{(3)} dT^3 \quad (5)$$

$$- \alpha_\ell^{(1)} dT - \alpha_\ell^{(1)} \alpha_v^{(1)} dT^2 - \alpha_\ell^{(1)} \alpha_v^{(2)} dT^3$$

$$- \alpha_\ell^{(2)} dT^2 - \alpha_\ell^{(2)} \alpha_v^{(1)} dT^3 - \alpha_\ell^{(3)} dT^3$$

$$+ (\alpha_\ell^{(1)})^2 dT^2 + (\alpha_\ell^{(1)})^2 \alpha_v^{(1)} dT^3$$

$$+ 2\alpha_\ell^{(1)} \alpha_\ell^{(2)} dT^3 - (\alpha_\ell^{(1)} dT)^3 \} \quad (6)$$

or

$$\alpha_1^{(1)} = \alpha_v^{(1)} - \alpha_1^{(1)} \quad (7)$$

$$\alpha_1^{(2)} = \alpha_v^{(2)} - \alpha_v^{(1)} \alpha_1^{(1)} + (\alpha_1^{(1)})^2 - \alpha_1^{(2)} \quad (8)$$

$$\alpha_1^{(3)} = \alpha_v^{(3)} - \alpha_1^{(1)} \alpha_v^{(2)} + \alpha_v^{(1)} (\alpha_1^{(1)})^2 \quad (9)$$

$$-(\alpha_1^{(1)})^3 + 2\alpha_1^{(1)} \alpha_1^{(2)} - \alpha_v^{(1)} \alpha_1^{(2)} - \alpha_1^{(3)}$$

giving the frequency dependence directly. The calculation of the temperature coefficients of velocity, $\alpha_v^{(1)}$, is achieved by calculating the phase velocity with the Finite Difference Technique or other techniques discussed below for a variety of temperatures. As the velocity is a function of temperature, a linear regression program is used in the finite difference technique to curve fit the data to a third order polynomial. The constants $\alpha_v^{(1)}$, $\alpha_v^{(2)}$ and $\alpha_v^{(3)}$ are thus obtained by optimum curve fitting of the data points to the polynomial. The temperature coefficients of length, $\alpha_l^{(i)}$, are found in standard references. It should be noted that the α_l 's also depend on the direction of propagation, and must be calculated for each direction of propagation considered by a simple geometrical transformation analogous to that used to rotate all of the other physical constants.

b. Rayleigh Wave

We will briefly discuss the Rayleigh wave solutions in their general form in this section. The coordinate system is defined with the Z or 1 axis being the direction of propagation and the -Y or 3 axis normal to the crystal surface. V_R will denote the Rayleigh wave velocity, $\beta_R = \omega/V_R$, the wave number, u_i ($i = 1, 2, 3$), the particle displacements along the 1, 2, or 3 axis, $u_4 = \phi$, the electric potential. Also, T_{ij} denotes the stress tensor.

$S_{ij} = (1/2)(du_i/dx_j + du_j/dx_i)$, the strain tensor, c_{ijkl} , the elastic tensor, ρ the density of the substrate, D , the electric displacement, E , the electric field, ϵ_{ij} the dielectric constant, e_{ijk} the piezoelectric constant. We also use Δ for the difference, where, for example,

$$\Delta\rho = \rho(T) - \rho(T_0) = \rho(T_0)(\alpha_\rho^{(1)}dT + \alpha_\rho^{(2)}dT^2 + \alpha_\rho^{(3)}dT^3), \text{ and let } P = \text{power/unit width in the } x \text{ direction.}$$

We assume relations such as

$$T = -e \cdot E + c^E:S \text{ or } S = e \cdot E + S^E:T \quad (10)$$

$$D = \epsilon^S \cdot E + e:S \quad D = \epsilon^T \cdot E + d:T$$

$$\rho \partial^2 u_i / \partial t^2 - c_{ijkl} \partial^2 u_k / \partial x_j \partial x_l - e_{kij} \partial^2 \phi / \partial x_k \partial x_l = 0 \quad (11)$$

$$e_{ikl} \partial^2 u_k / \partial x_l \partial x_i - \epsilon_{ik} \partial^2 \phi / \partial x_i \partial x_k = 0$$

The general solution for a wave traveling on the surface can be written

$$u_j = \left[\sum_m C_m \alpha_j^{(m)} \exp(-i\omega/V_j) \sum_{i=1}^3 b_i^{(m)} x_i \right] \exp(i\omega t) \text{ for } j = 1 \text{ to } 4 \quad (12)$$

$$\text{For the Rayleigh wave, this reduces to } U_j = \sum_{m=1}^4 C_m \alpha_j^{(m)} \exp(-i\beta_R b^{(m)} y) \exp(i\beta_R z - i\omega t) \quad (13)$$

where the coefficient C_m , $\alpha_j^{(m)}$ (weighting factors), β_R (wave number), and $b^{(m)}$ (complex decay constants) are to be calculated by the standard iterative procedure on a computer.

The fields are calculated as $E = \nabla u_4$ with $E_x = 0$, $E_y = (-i\beta_R b^{(m)})u_4$ and $E_z = (i\beta_R)u_4$.

c. Methods for Calculating the Temperature Dependence of the Rayleigh Velocity

In the following sections, four methods for calculating the temperature characteristics of the Rayleigh wave are discussed.

(1) Finite Difference Technique of Calculating Temperature Dependence of the Rayleigh Velocity

Before $TCD^{(1)} = (1/\tau)(d\tau/dT)$ can be calculated, one must first calculate the dependence of the Rayleigh wave velocity on temperature. The most straightforward method for doing this is the finite difference method. The Rayleigh wave velocities are calculated for different temperatures, yielding the values $V_i(T_i)$, $i = 1, 2, \dots, n$. This is done by first calculating the fundamental constants at the temperature T_i of interest. The fundamental constants are then rotated into the coordinate system of interest. An iterative procedure is used to calculate a velocity V_i for which Christoffel's equation and the boundary conditions are satisfied simultaneously (see Appendix D). Simple finite difference techniques can be used to calculate $(1/V_i)(dV_i/dT)$, $(1/2V_i)(d^2V_i/dT^2)$, etc. For example, after calculating $V_i(T_i)$ for $T_1 = T_0$, $T_2 = T_0 + \Delta T$, $T_3 = T_0 - \Delta T$, we can use $(1/V_i)(dV_i/dT)$ at $T_0 \cong (1/V_0(T_0))(V_i(T_0 + \Delta T) - V_i(T_0 - \Delta T))/2\Delta T$. Alternately, standard linear regression of polynomials may be employed to yield those coefficients. Another approach consists of calculating directly the frequency-temperature characteristics of the orientation for several widely differing temperatures. A measure of the temperature stability is then used. Letting $F(T)$ be the frequency of the device, the measure of deviation is calculated as

$$\begin{aligned} \text{RMS frequency deviation} = \\ \left[\left(\sum_{i=1}^n (F(T_i) - F(T_0))^2 \right) / n \cdot F(T_0)^2 \right]^{1/2} \text{ with} \\ F(T) = V_i(T) / \lambda_0 (1 + \alpha_L^{(1)}(\Delta T) + \alpha_L^{(2)}(\Delta T)^2 + \alpha_L^{(3)}(\Delta T)^3), \end{aligned} \quad (14)$$

although $\alpha_L^{(1)}$, $\alpha_L^{(2)}$, and $\alpha_L^{(3)}$ are calculated for purposes of comparison.

In much of the earlier work, the SAW velocities were calculated at three temperature points, $T_1 = -50^\circ\text{C}$, $T_2 = 25^\circ\text{C}$, and $T_3 = 100^\circ\text{C}$, to save on computer time. The following formulas were used for the calculations of first and second order temperature coefficients of velocity.

$$\alpha_V^{(1)} = [V(T_1) - V(T_3)]/[V(T_2) (T_1 - T_3)] \quad (15)$$

$$= [V(100) - V(-50)]/[V(25) \cdot 150]$$

$$\alpha_V^{(2)} = [V(T_1) + V(T_3) - 2 \cdot V(T_2)]/[V(T_2) \cdot 2 (T_3 - T_2)(T_2 - T_1)] \quad (16)$$

$$= [V(100) + V(-50) - 2 \cdot V(25)]/[V(25) \cdot 2 (75)(75)]$$

In the more recent works, six temperature points were calculated for each orientation to provide data for the linear regression analysis. The six temperature points were 100°C , 85°C , 75°C , -25°C , -10°C , and -50°C . The results were used to calculate $\text{TCF}^{(1)}$, $\text{TCF}^{(2)}$ and $\text{TCF}^{(3)}$.

(2) Perturbation Technique of Calculating Temperature Dependence of the Rayleigh Velocity

Perturbation theory may be applied to the problem of calculating the first, second and third order dependence of the Rayleigh velocity V , of a piezoelectric substrate, once the solution to the Rayleigh wave propagation at a temperature reference T_0 is known.

Perturbation techniques allow calculations of small changes in the solutions to a problem caused by small changes in the physical parameters of the problem, once the solution to the unperturbed problem is known. One can apply perturbation techniques either to boundary perturbation such as mass loading on the surface or to volume perturbations such as adding a thin conducting layer to the interior of piezoelectric substrates. As the boundary conditions are unaffected by changes in temperature while material constants such as c_{ij} are temperature dependent, one can apply the volume perturbation theory to the problem.

The general approach to the problem of determining the temperature dependence of V , will be as follows. First, the Rayleigh wave propagation problem will be solved in the standard way in its entirety at room temperature, T_0 . Given the solution of the problem at T_0 and the dependence of the physical constants (such as c_{ij}) on temperature at T_0 , one will apply the volume perturbation formula, calculating the temperature dependence of V . The dependence of V , on T is then used to calculate the frequency characteristics of the actual device given the thermal expansion coefficients as a function of temperature. At this point, the frequency temperature dependence of the substrate as a function of the crystal cut and direction can be thoroughly explored. See Appendix A for a complete discussion of this method.

(3) Approach of Sinha and Tiersten

The primary difficulty with the perturbation technique is that it does not take into account the change of coordinate systems induced by the thermal expansion in the material. This comes about because the material distorts as temperature changes. Thus, the set of axes to which the fundamental elastic constants refer, which is fixed to the crystal, is no longer equivalent to the axes used to calculate V_s . This problem is elegantly solved by Sinha and Tiersten^{1,2}. The first simplification which occurs is that the density of the material remains constant with temperature. Furthermore, the $\alpha_F^{(0)}$ simply become $\alpha_F^{(0)} = \alpha_F^{(0)}$, as the length in this coordinate system does not change. The only difficulty is that the elastic constants previously used no longer refer to the proper coordinate system and must be rederived from the original experimental data. This procedure has already been carried out for the first order temperature derivation of quartz² but has not been done for the second and third order coefficients. Nonetheless, the procedure yields more accurate results for the first order dependence. See Appendix B for a mathematical description of the salient features of this technique.

(4) Differentiation Method

A method for determining the theoretical temperature dependence of Rayleigh Surface Waves consists of formally differentiating the wave equation and boundary conditions. The boundary conditions and wave equation must be true at all temperatures, placing constraints on how the parameters of the wave equation may vary. In this technique, the derivatives of these equations with respect to temperature are set to zero and solved for the velocity-temperature dependence. This method follows the methods used by Bechmann, Ballato, and Lukaszek to compute the temperature dependence of the fundamental elastic constants from frequency data, except that the simplifying assumptions of assuming bulk wave solutions cannot be made. This method was later used by Hauden³ to search for temperature stable cuts of quartz. See Appendix C for a discussion of this method.

(5) Summary of Approaches

Of all the techniques presented, the finite difference technique satisfies all of the basic requirements for calculating temperature coefficients of delay. Arbitrary crystal structures may be

¹"On the Temperature Dependence of the Velocity of Surface Waves in Quartz," Sinha and Tiersten, 1978 Ultrasonics Symposium Proceedings, pp. 662-665.

²"Temperature Dependence of the Fundamental Elastic Constants of Quartz," Sinha and Tiersten, Proceedings of the 32nd Annual Symposium on Frequency Control, 1978, pp. 150-153.

³"Higher Order Temperature Coefficients of Quartz SAW Oscillators," D. Hauden, M. Michael, J. J. Gagnepain, Frequency Control Symposium (1978), pp. 77-86.

investigated once the density, piezoelectric, elastic, and dielectric constants and their temperature variation are known. When double precision on the computer is used and when the velocity over a large temperature range is calculated, it becomes a very accurate numerical approach. The computational efficiency of the finite difference method is not as high as some of the other techniques, owing to the need for repeated calculation of the surface wave velocity.

A comparison between the experimental results of Schulz¹ and Motorola's finite difference program adapted from Jones et al.² as shown in Figure 1. The results for this cut and many other orientations studied have been found to be very good. The slight shift of the analytical curve versus experimental curve can be explained by a crystal misorientation.

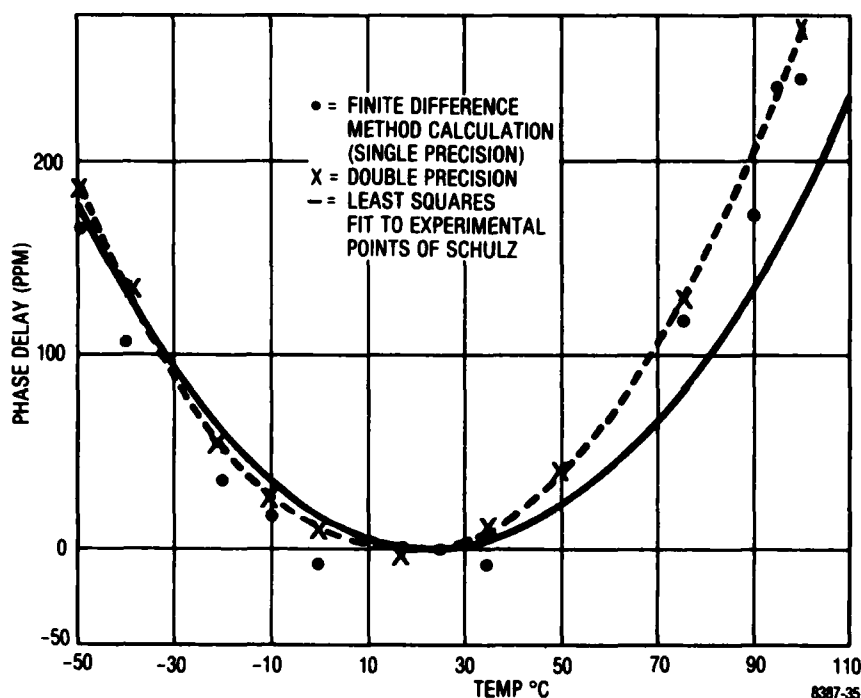


Figure 1. Finite Difference Method Versus Experiment ST-Cut (Quartz)

¹"Surface Acoustic Wave Delay Lines with Small Temperature Coefficient," Schulz, Manfred B., Proc. IEEE, Sept. 1970, pp. 1361-1362.

²"Numerical Computation of Acoustic Surface Waves in Layered Piezoelectric Media - Computer Program Descriptions", Jones, Smith, and Perry, Hughes Aircraft Company, Final Report, Air Force Cambridge Research Laboratories, Contract No. F19628-70-C-0027.

Figure 2 displays a phase delay versus temperature plot for the orientation (YXwlt) 56/40/27 in quartz obtained from Hauden's graphs². Using the differentiation approach, he calculated $\alpha_T^{(1)} = 0$, $\alpha_T^{(2)} = -0.04 \times 10^{-3} \text{ ppm}/^\circ\text{C}^2$, $\alpha_T^{(3)} = -22.7 \times 10^{-6} \text{ ppm}/^\circ\text{C}^3$ for a cut close to (YXwlt) 56/40/27. The Finite Difference approach was used to verify his first order calculation but is in disagreement on the second and third order calculations. This can be resolved by experiment.

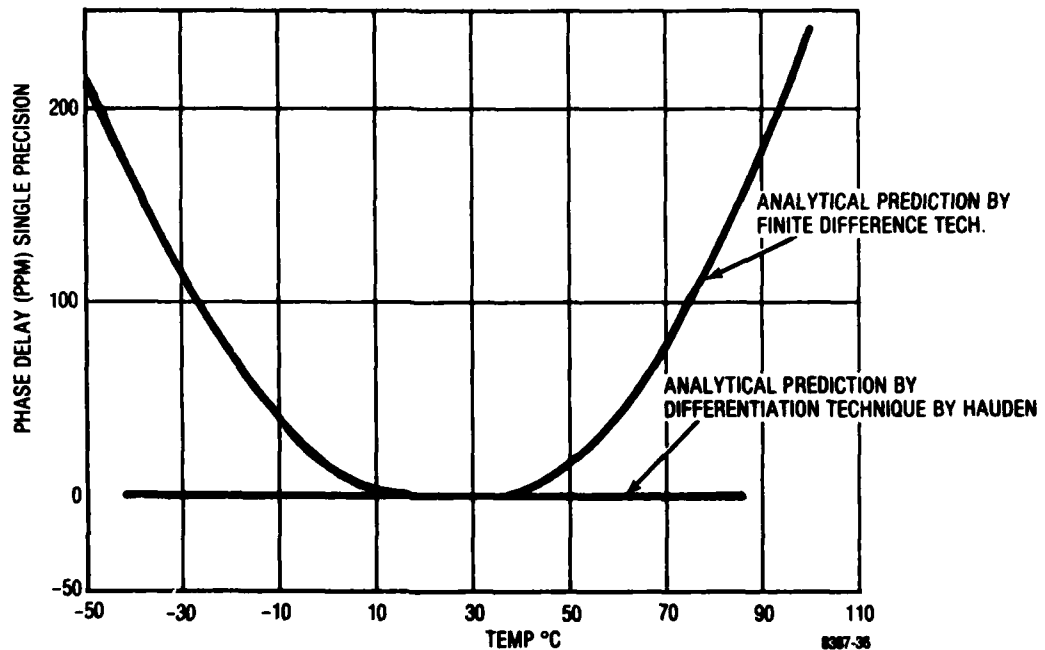


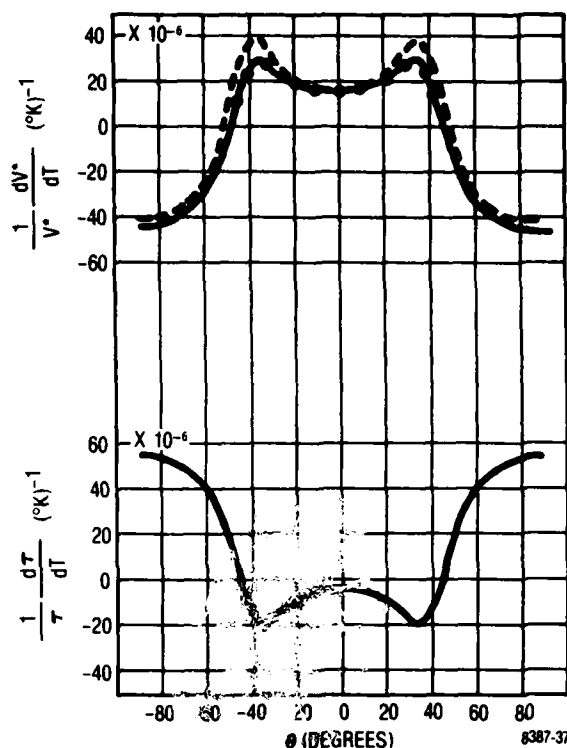
Figure 2. Finite Difference Method Calculation for Hauden's Cut (YXwlt) 56°/40°/27°

Tiersten's Perturbation program, while very difficult to extend to higher orders, is available for calculating the first order TCD.

Figure 3 shows the results of Tiersten's calculation¹ and compares those results with the Finite Difference method as well as experiment. The cut used for comparison is the AT-Cut. The improvement in accuracy is substantial. It offers the significant advantages of being quite cost efficient, as well as being more accurate in the first order on off-axis cuts, our primary area of interest. In the task of making quartz cuts along the surface of zero TCD, accurate values for the first order TCD prove more useful than the less exact values for the first, second, and third order TCD's provided by other methods, because it is a necessary (but not sufficient) condition for zero TCD cut to get a zero first order. Since it is the dominating term, it is important to first get an accurate first order zero TCD locus. Then one may search for the intersection of this locus with the zero second and third order terms with the finite difference technique.

¹"Temperature Dependence of the Fundamental Elastic Constants of Quartz," B. K. Sinha and H. F. Tiersten, Proceedings of the 32nd Annual Symposium on Frequency Control, 1978, pp. 150-153.

²"Higher Order Temperature Coefficients of Quartz SAW Oscillators," D. Hauden, M. Michael, J. J. Gagnepain, Frequency Control Symposium (1978), pp. 77-86.



TEMPERATURE COEFFICIENTS OF ACTUAL VELOCITY AND DELAY FOR SURFACE WAVES ON AT-CUT QUARTZ AS A FUNCTION OF PROPAGATION DIRECTION RELATIVE TO THE DIAGONAL AXIS AT 25°C. THE DOTTED CURVE SHOWS THE AVERAGE OF THE CALCULATED VALUES AT 0°C AND 50°C FROM REF. 1. THE CIRCLES ARE THE AVERAGE OF THE EXPERIMENTAL VALUES AT 0°C AND 50°C
GRAPH OBTAINED FROM REF 1

Figure 3. Tiersten's Method Versus Finite Difference and Experiment

(6) Investigative Approach

A necessary but not sufficient condition to find a temperature stable cut of quartz is that $\alpha_F^{(1)} = 0$. In practice, a sufficient condition for finding a zero temperature cut is that $\alpha_F^{(1)} = \alpha_F^{(2)} = \alpha_F^{(3)} = 0$. Thus every zero temperature cut must be on the locus of angles which satisfy the condition $\alpha_F^{(1)} = 0$. Thus the first problem is to locate accurately such cuts. Both the finite difference approach and Tiersten's method were used to calculate the TCF.

The approach used in this program is to identify the areas (angles) where $TCF^{(1)}$, $TCF^{(2)}$ and $TCF^{(3)}$ are relatively low by using the Finite Difference Approach and then define the exact orientation that has zero $TCF^{(1)}$ in those areas by the Sinha and Tiersten approach.

In case the condition $TCF^{(1)} = TCF^{(2)} = TCF^{(3)} = 0$ cannot be met, a compromise approach would be to find an orientation where the first and third order effects tend to cancel out in the temperature range of interest and to find the minimum second order effect orientation amount for those cuts. This approach would provide an effective low TCF cut of quartz for SAW application.

(7) Analytical Results on Zero TCF on Quartz

IRE standard angle definitions (YX wlt) PHI/THETA/PSI for quartz were used throughout the investigation¹. Consider the TCFs to be functions of these angles, which define an angular volume $0 \leq \text{PHI} \leq 30^\circ$, $-90^\circ \leq \text{THETA} \leq 90^\circ$, $0 \leq \text{PSI} \leq 180^\circ$, which spans the space of possible cuts and propagation directions. The set of points at which $\text{TCF}^{(1)}(\text{PHI}, \text{THETA}, \text{PSI}) = 0$ forms a surface in this angular volume. Likewise, the set of points at which $\text{TCF}^{(2)}(\text{PHI}, \text{THETA}, \text{PSI}) = 0$ also form surfaces in this angular volume.

Our object is to find a point where $\text{TCF}^{(1)} = \text{TCF}^{(2)} = \text{TCF}^{(3)} = 0$. If the surface of zero $\text{TCF}^{(1)}$ intersected with the surface of zero $\text{TCF}^{(2)}$, the result would be a line (or a point if the two surfaces are tangent to each other) of angular points on which $\text{TCF}^{(1)} = \text{TCF}^{(2)} = 0$. The intersection of this line with the surface on which $\text{TCF}^{(3)} = 0$ would yield a single point at which $\text{TCF}^{(1)} = \text{TCF}^{(2)} = \text{TCF}^{(3)} = 0$. Neglecting higher order terms, we would have found a temperature stable cut.

The calculated values of $\text{TCF}^{(1)}$ versus propagation angles are shown in Figure 4. The zero $\text{TCF}^{(1)}$ is identified by the areas where $\text{TCF}^{(1)}$ changes sign.

Using the Finite Difference approach with the available crystal constants, the calculated results show that the zero $\text{TCF}^{(1)}$ surfaces do not intersect with the zero $\text{TCF}^{(2)}$ surfaces, based on the interpolated results of the $10^\circ \times 10^\circ \times 10^\circ$ resolution. It is not likely that a finer resolution will provide contrary information because $\text{TCF}^{(1)}$ and $\text{TCF}^{(2)}$ are relatively slow varying functions as shown in Figure 4.

¹"Standards on Piezoelectric Crystals 1949," Proc. IRE 14, Dec. 1949, pp. 1378-1395.

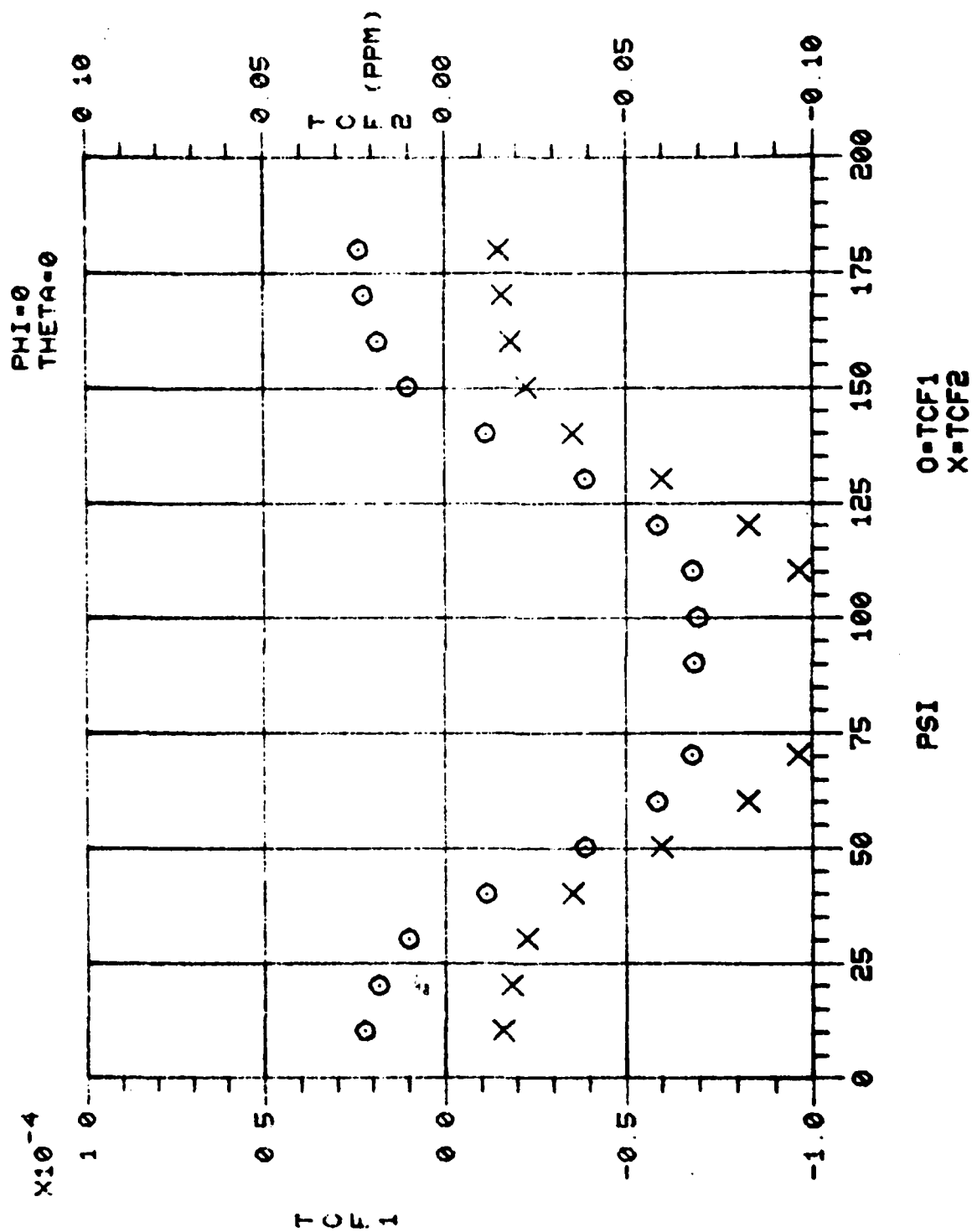
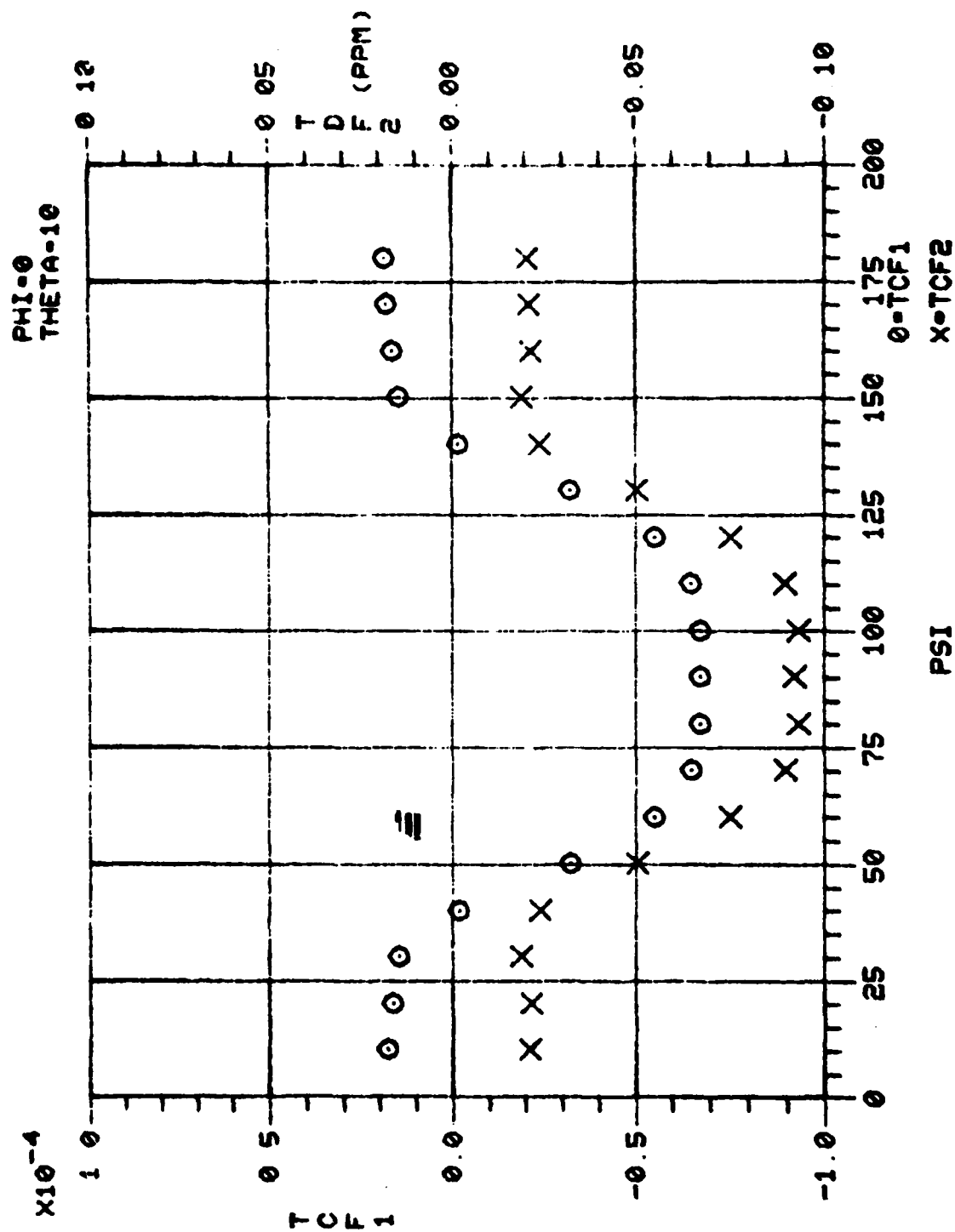


Figure 4. Calculated Values of TCF⁽¹⁾ Versus Propagation Angles (Sheet 1 of 71)



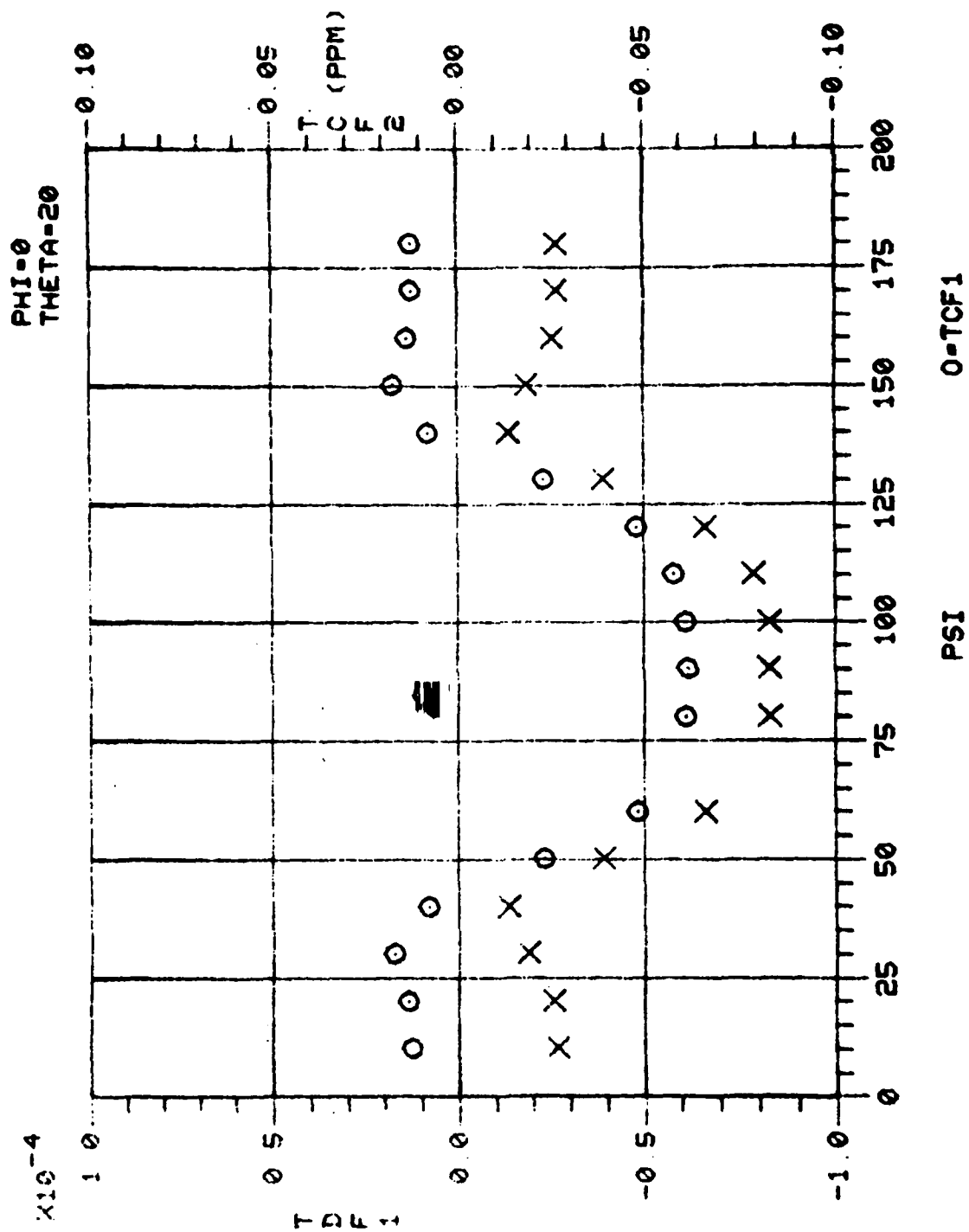


Figure 4. Calculated Values of TCF⁽¹⁾ Versus Propagation Angles (Sheet 3 of 71)

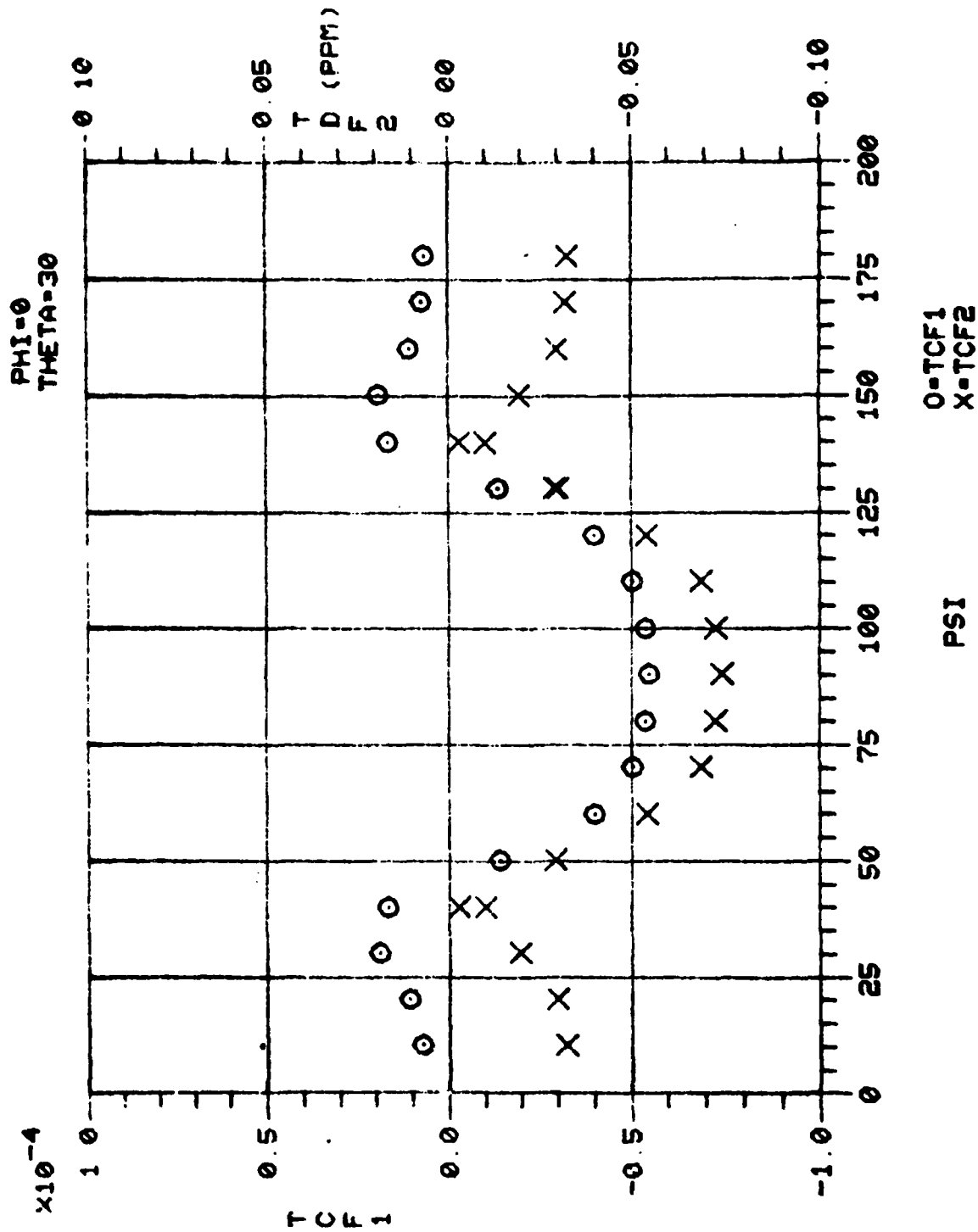


Figure 4. Calculated Values of TCF⁽¹⁾ Versus Propagation Angles (Sheet 4 of 71)

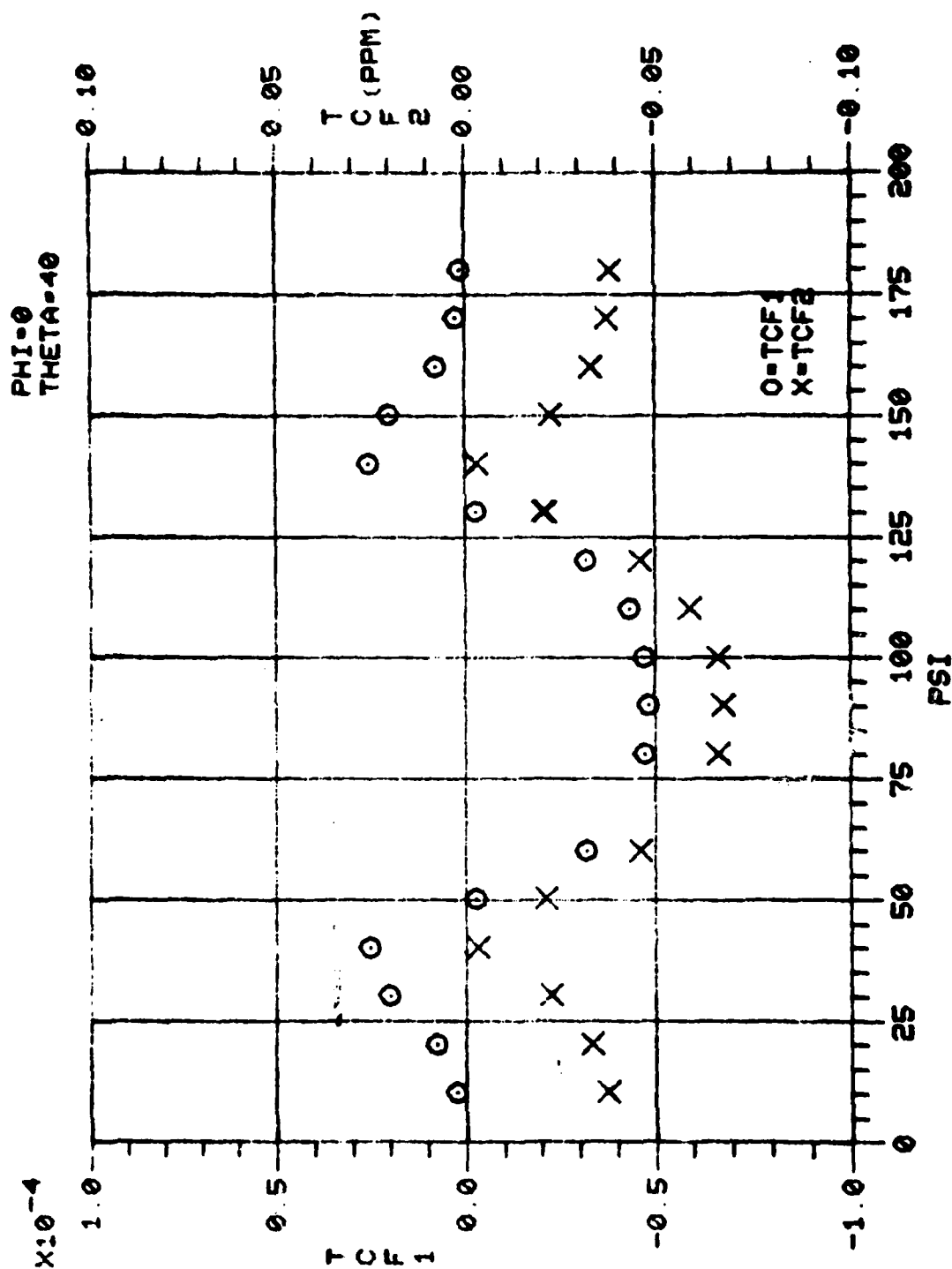


Figure 4. Calculated Values of TCF⁽¹⁾ Versus Propagation Angles (Sheet 5 of 71)

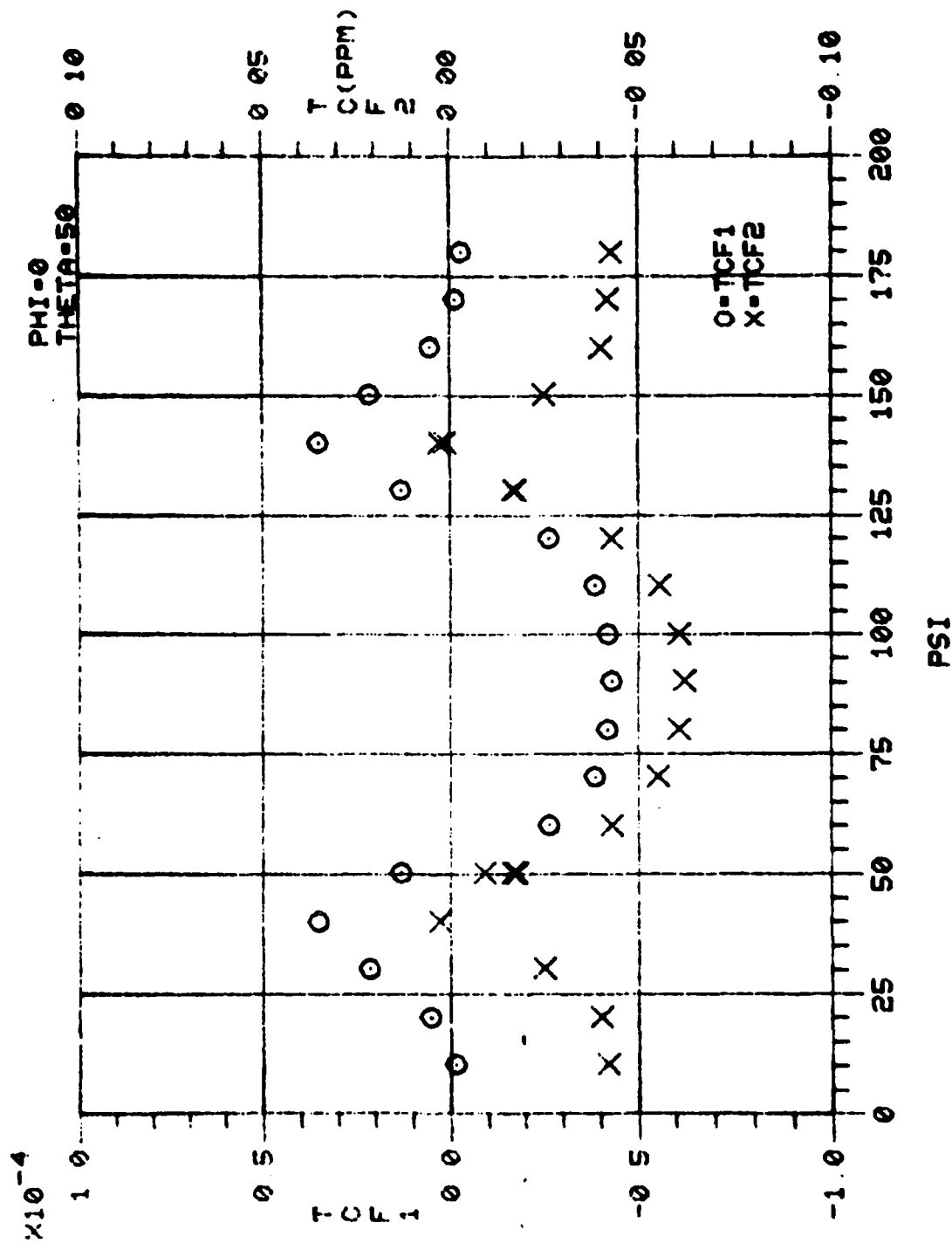


Figure 4. Calculated Values of TCF⁽¹⁾ Versus Propagation Angles (Sheet 6 of 71)

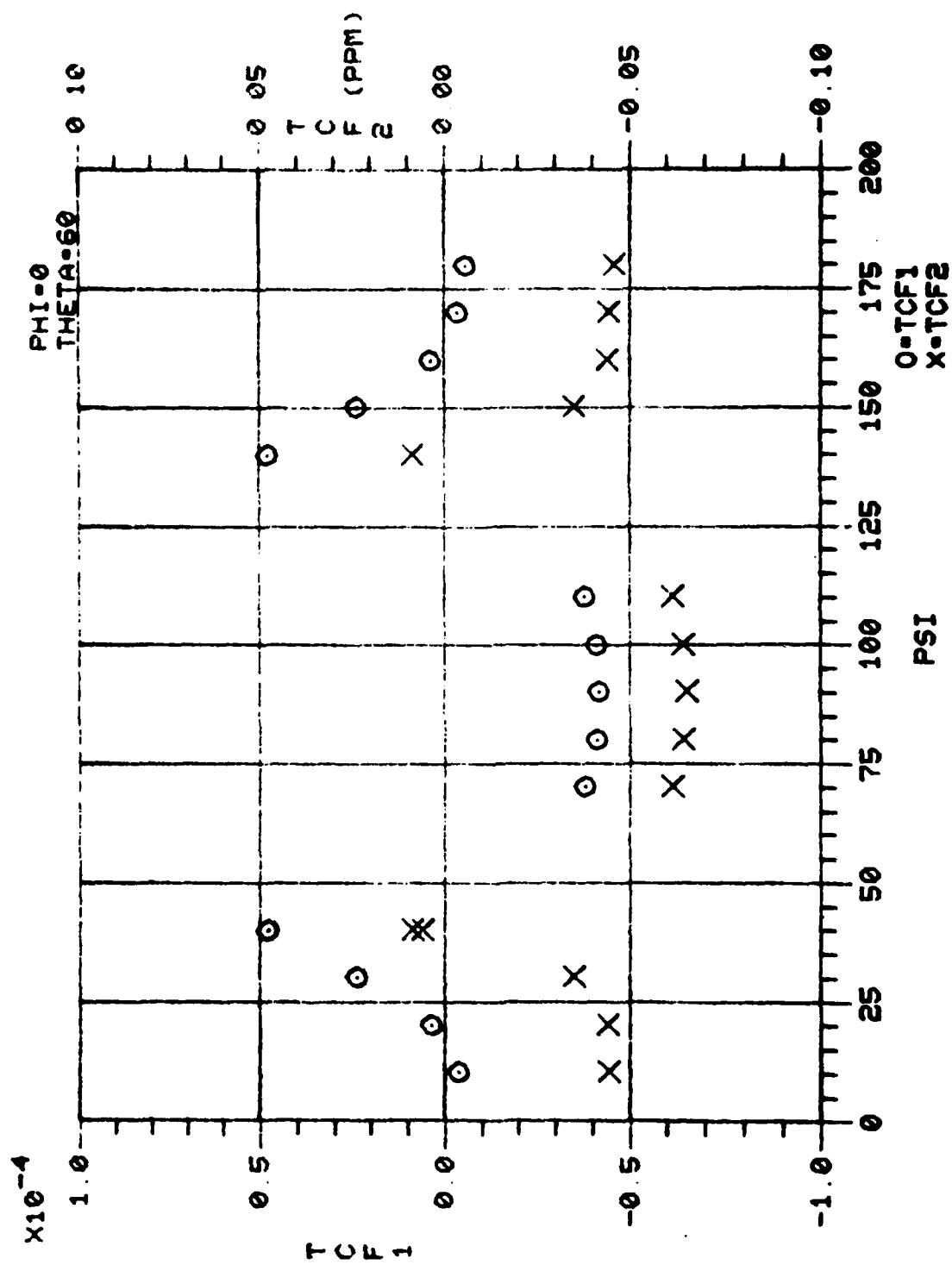


Figure 4. Calculated Values of TCF⁽¹⁾ Versus Propagation Angles (Sheet 7 of 71)

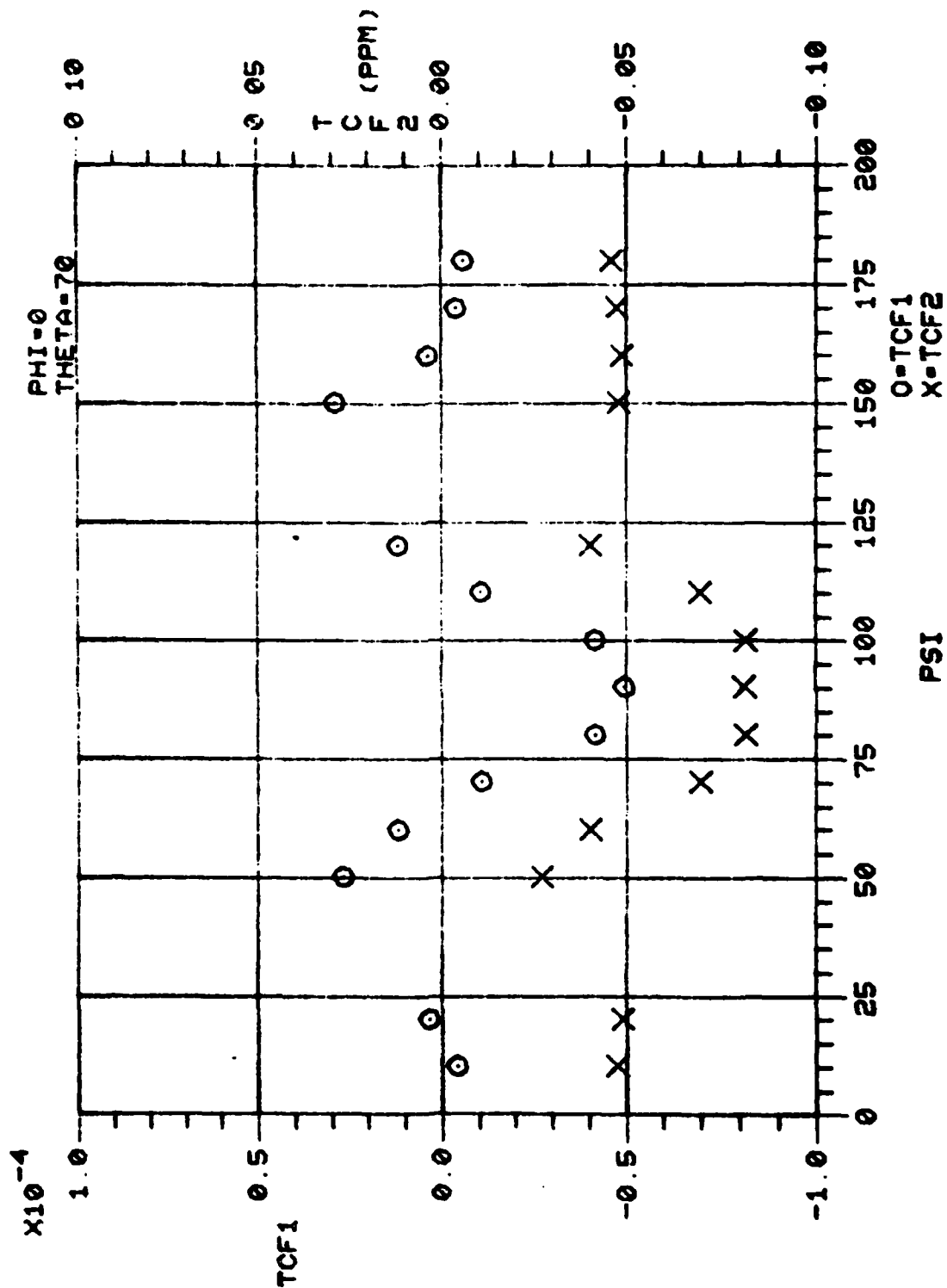


Figure 4. Calculated Values of TCF⁽¹⁾ Versus Propagation Angles (Sheet 8 of 71)

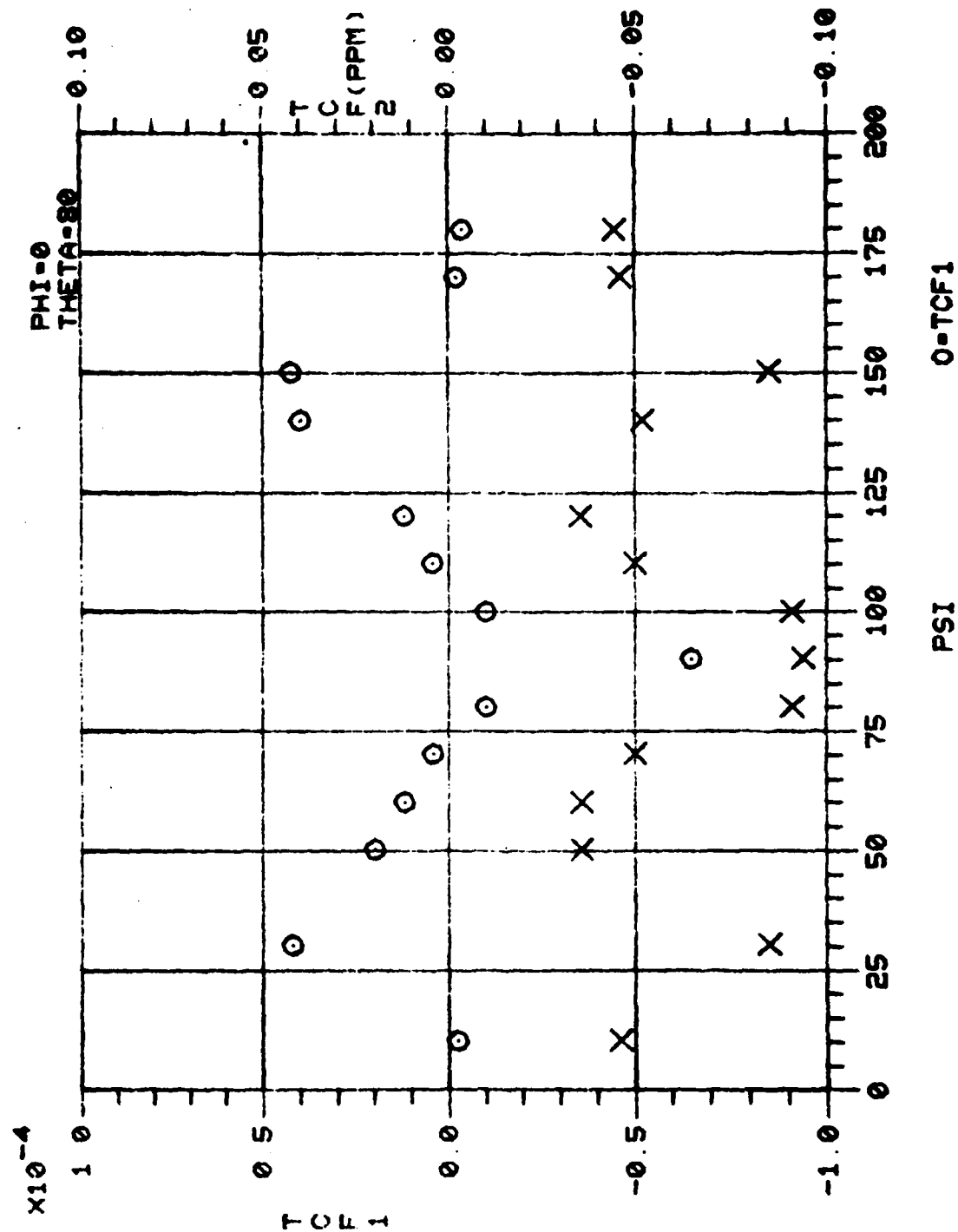
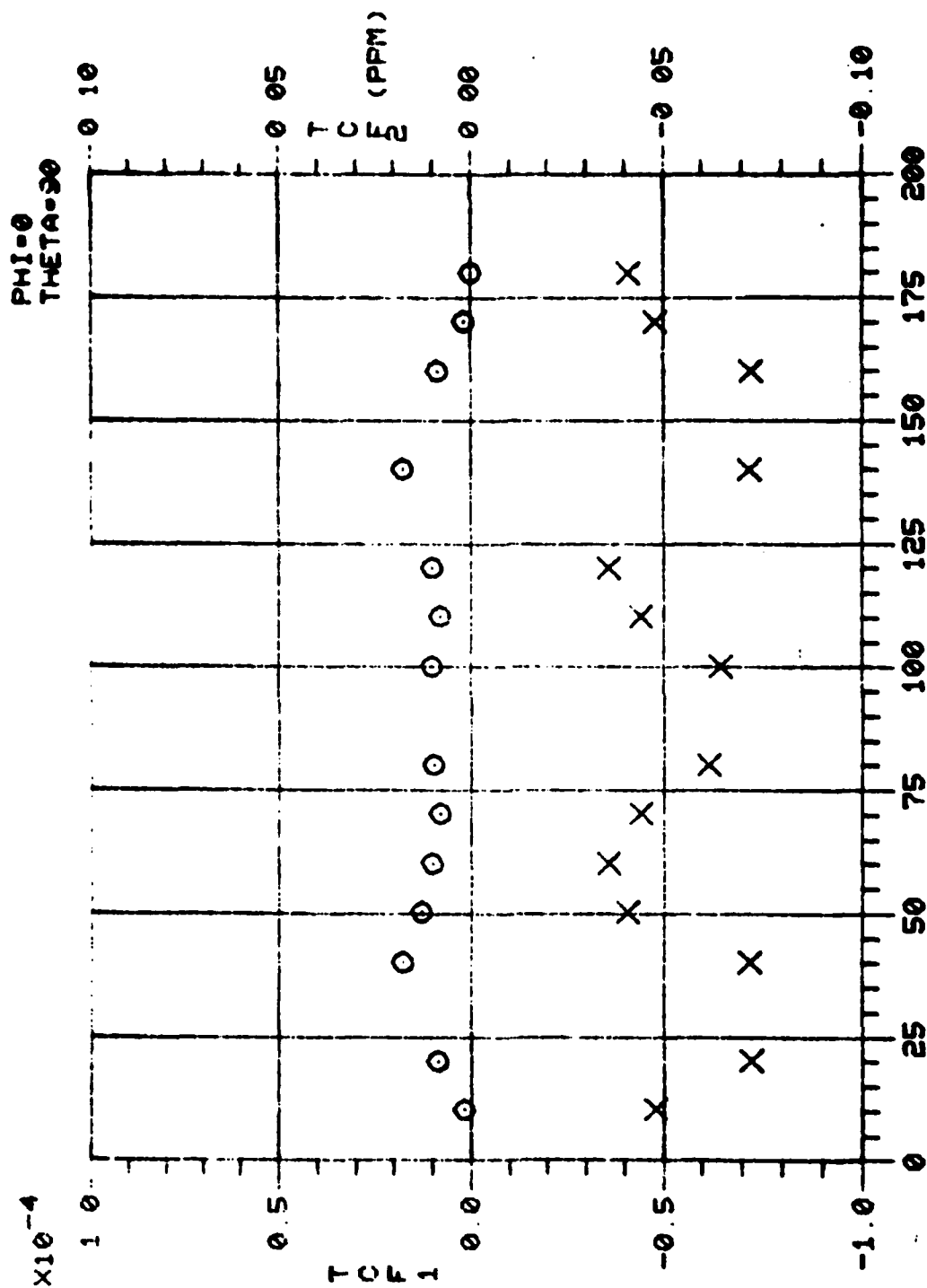
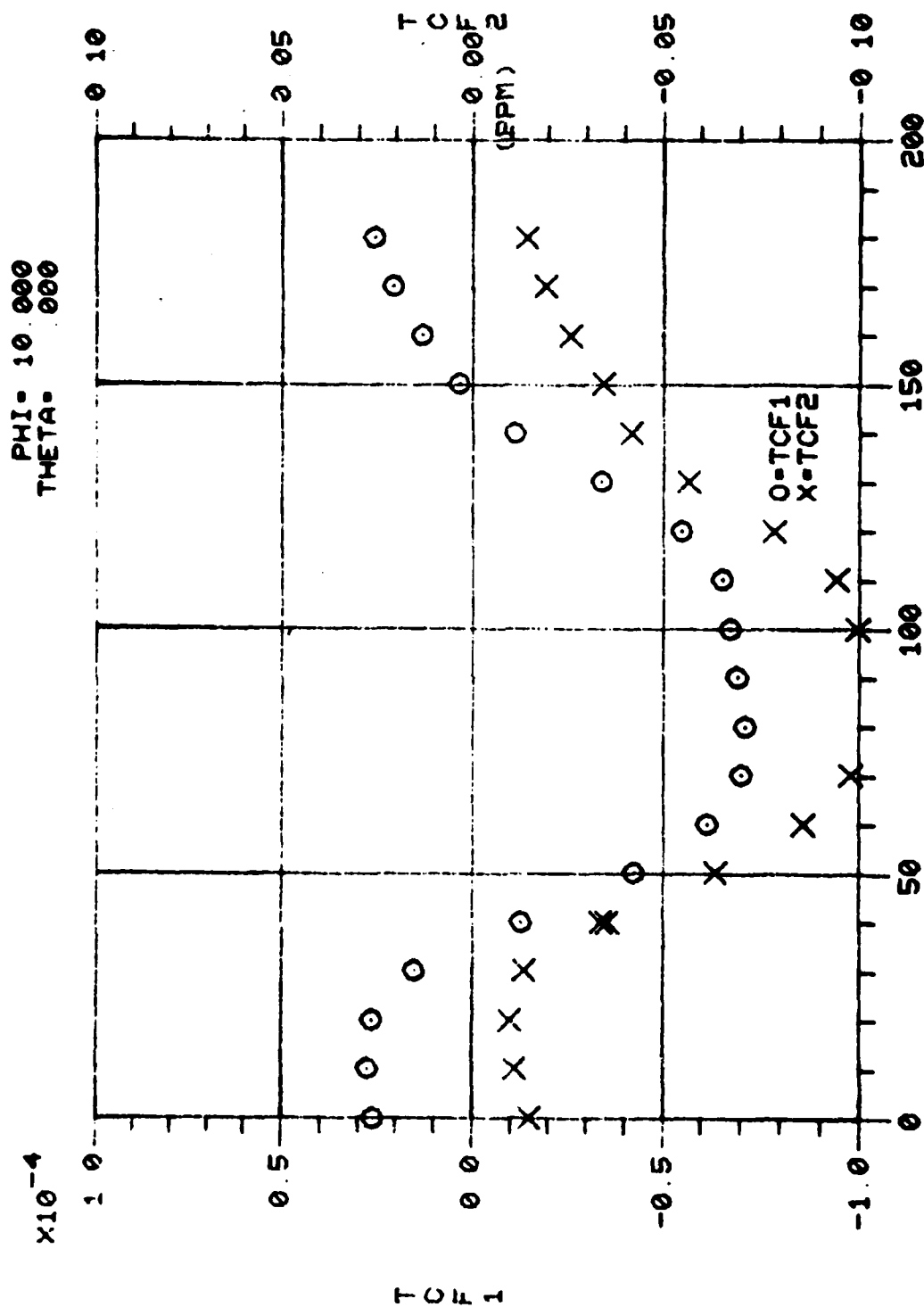


Figure 4. Calculated Values of TCF⁽¹⁾ Versus Propagation Angles (Sheet 9 of 71)



O=TCF1
X=TCF2

Figure 4. Calculated Values of TCF⁽¹⁾ Versus Propagation Angles (Sheet 10 of 71)



PSI
Figure 4. Calculated Values of TCF⁽¹⁾ Versus Propagation Angles (Sheet 11 of 71)

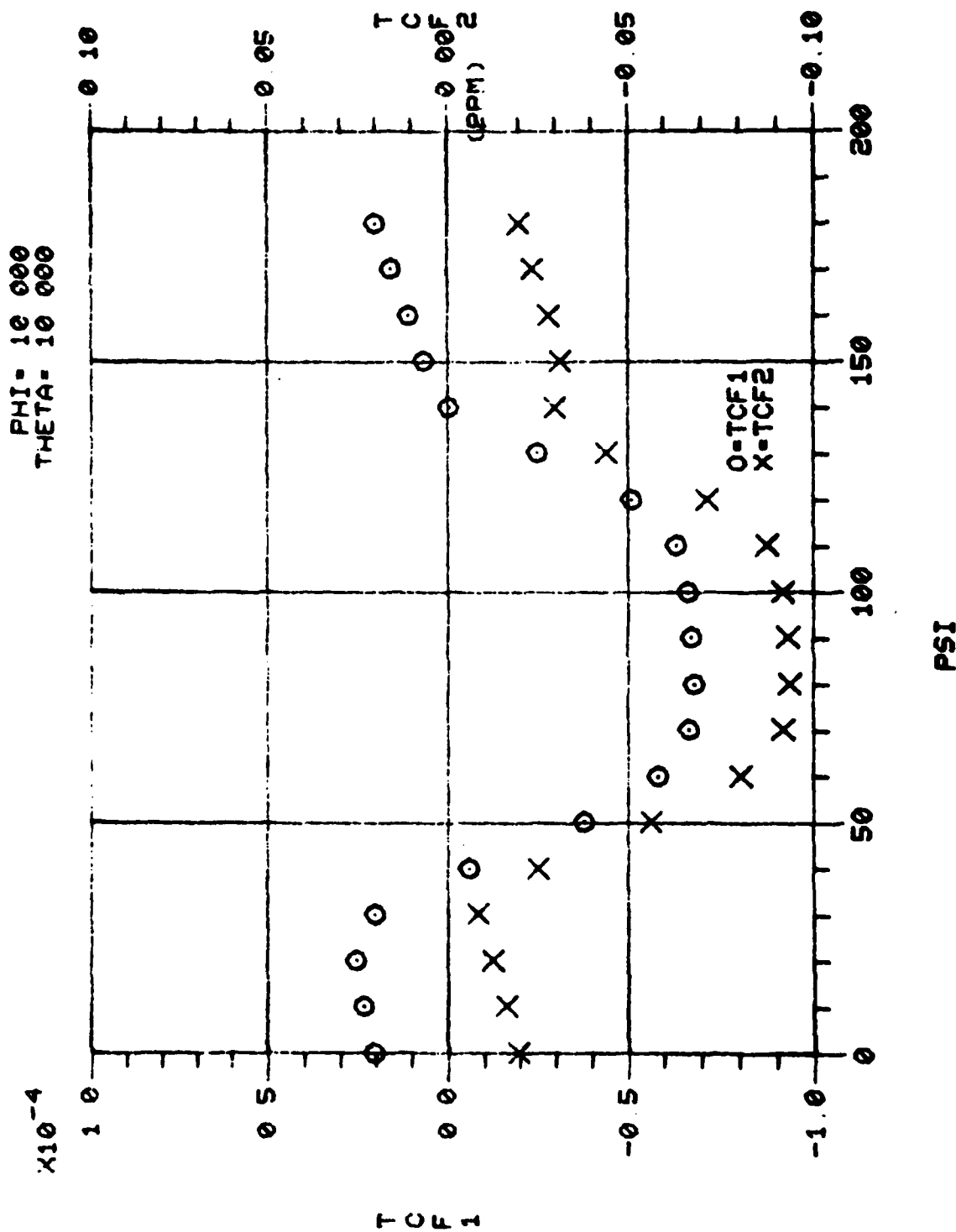


Figure 4. Calculated Values of TCF⁽¹⁾ Versus Propagation Angles (Sheet 12 of 71)

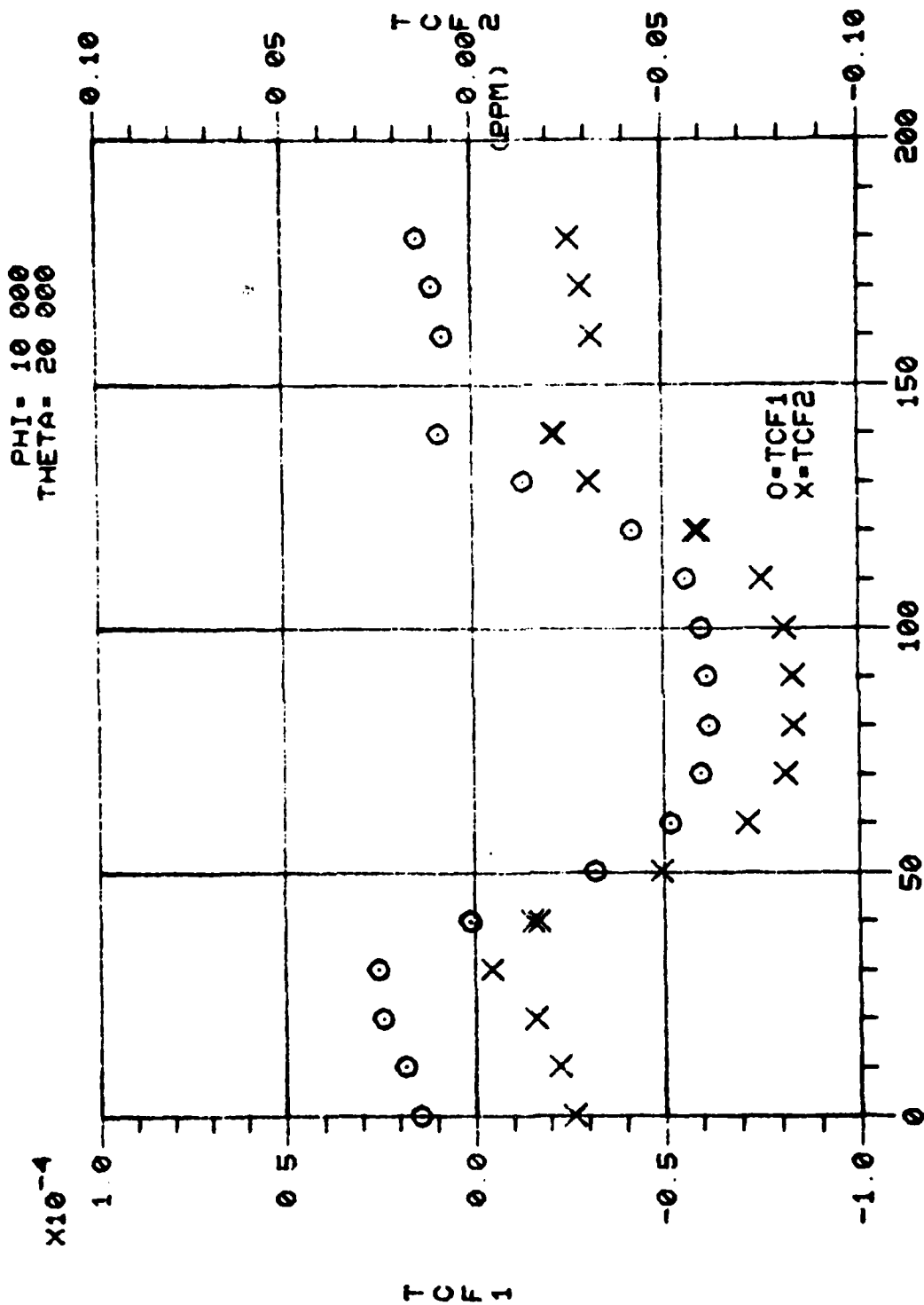
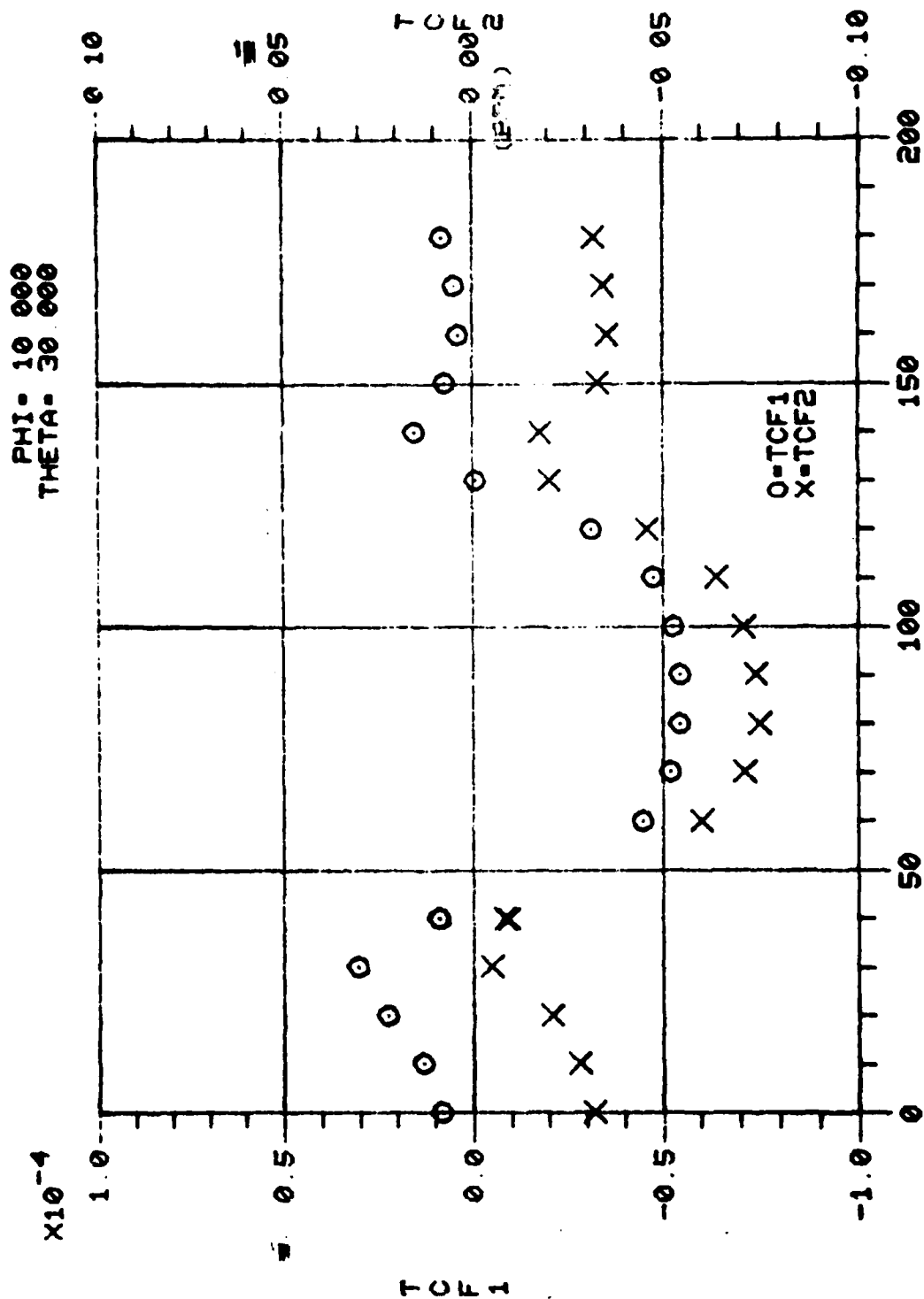


Figure 4. Calculated Values of TCF⁽¹⁾ Versus Propagation Angles (Sheet 13 of 71)



PSI

Figure 4. Calculated Values of TCF⁽¹⁾ Versus Propagation Angles (Sheet 14 of 71)

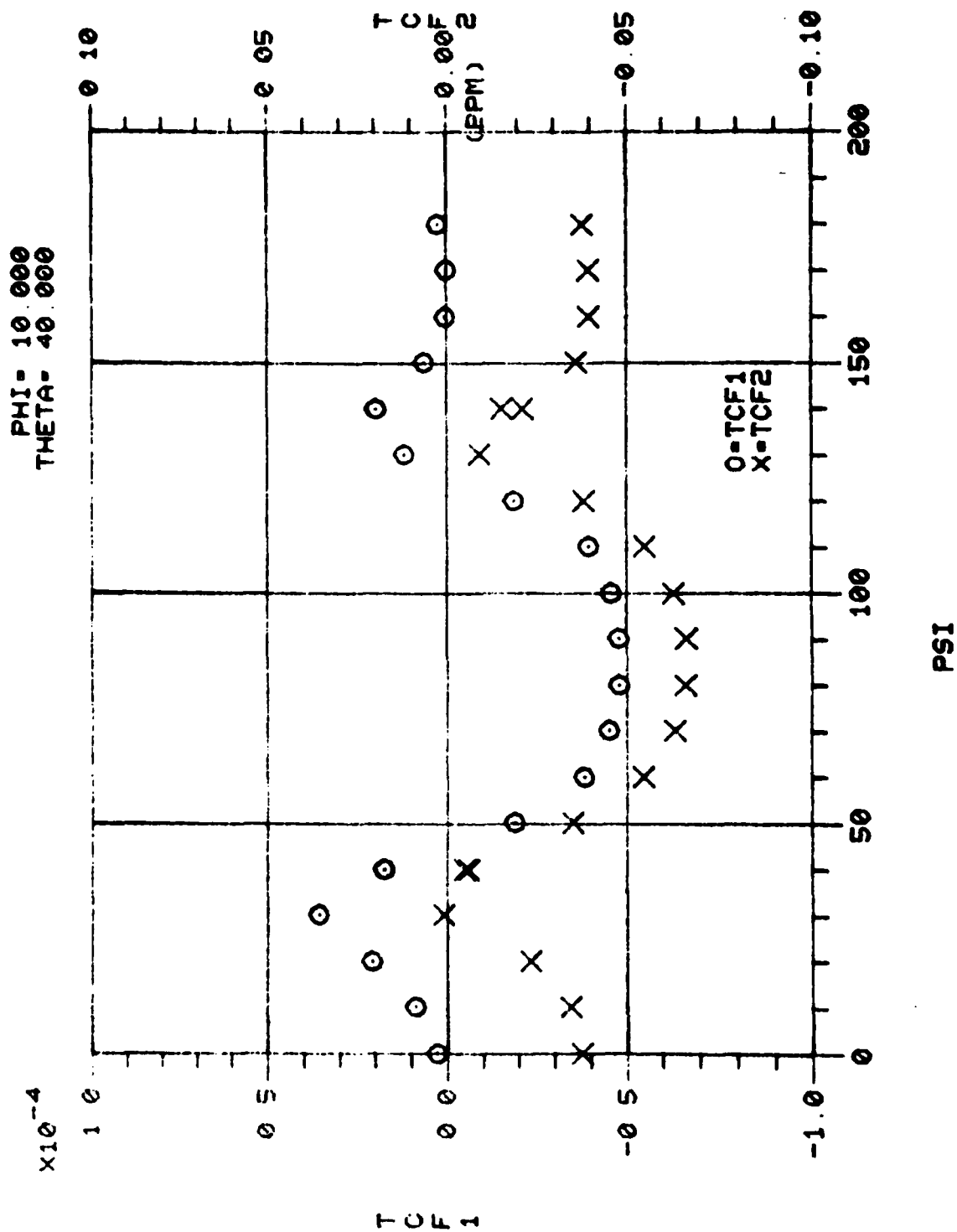


Figure 4. Calculated Values of TCF⁽¹⁾ Versus Propagation Angles (Sheet 15 of 71)

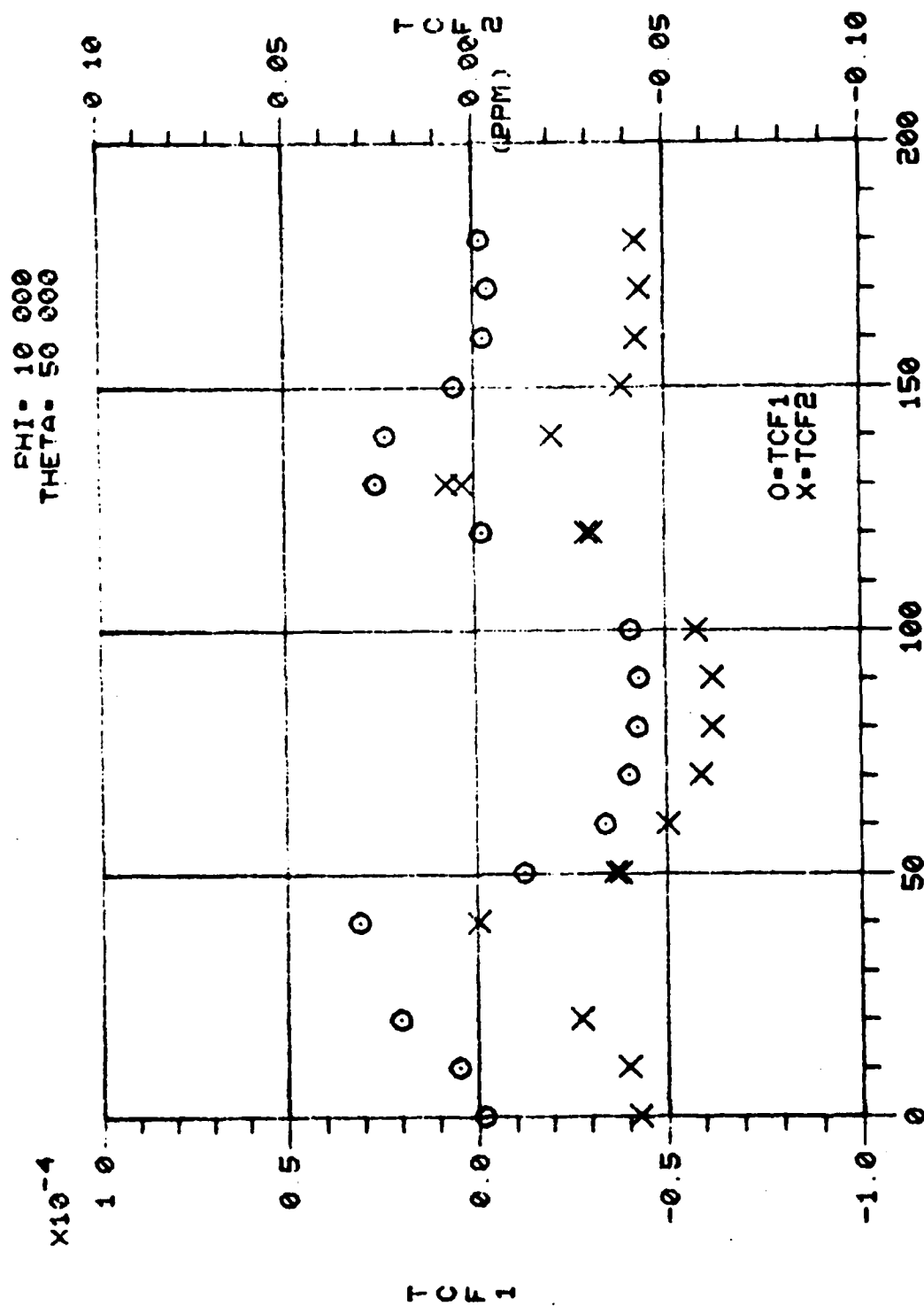


Figure 4. Calculated Values of TCF⁽¹⁾ Versus Propagation Angles (Sheet 16 of 71)

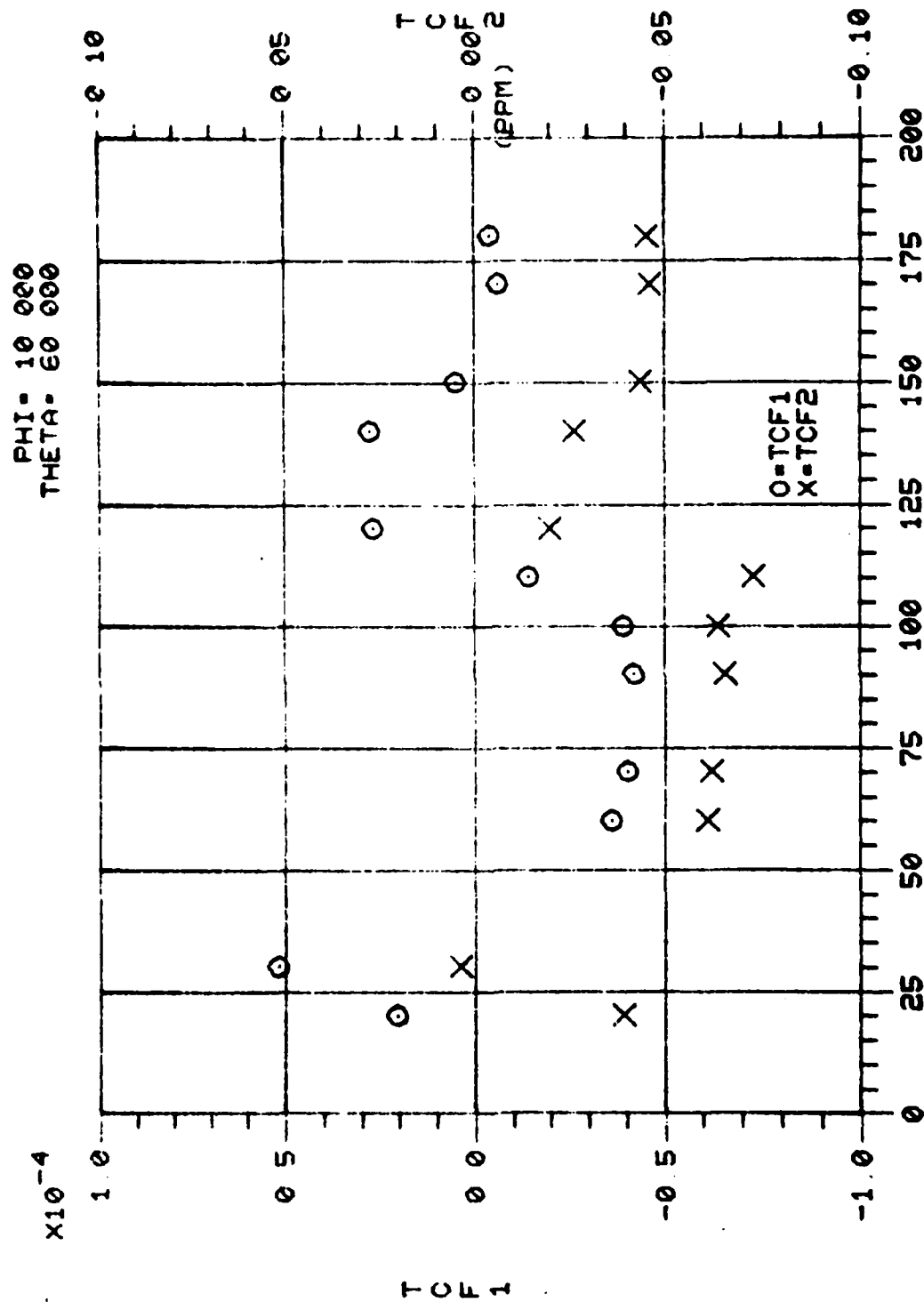


Figure 4. Calculated Values of TCF⁽¹⁾ Versus Propagation Angles (Sheet 17 of 71)

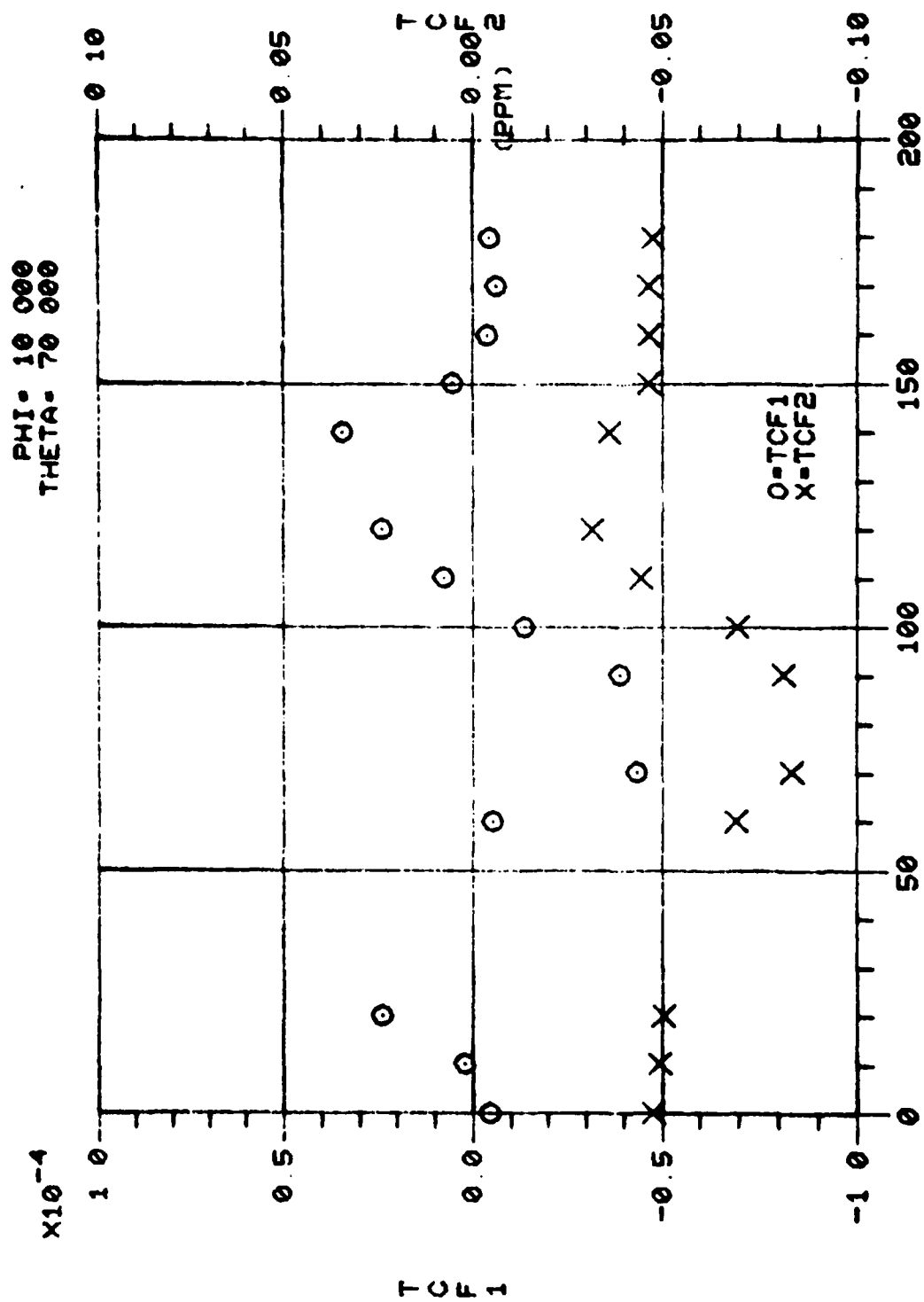


Figure 4. Calculated Values of TCF⁽¹⁾ Versus Propagation Angles (Sheet 18 of 71)

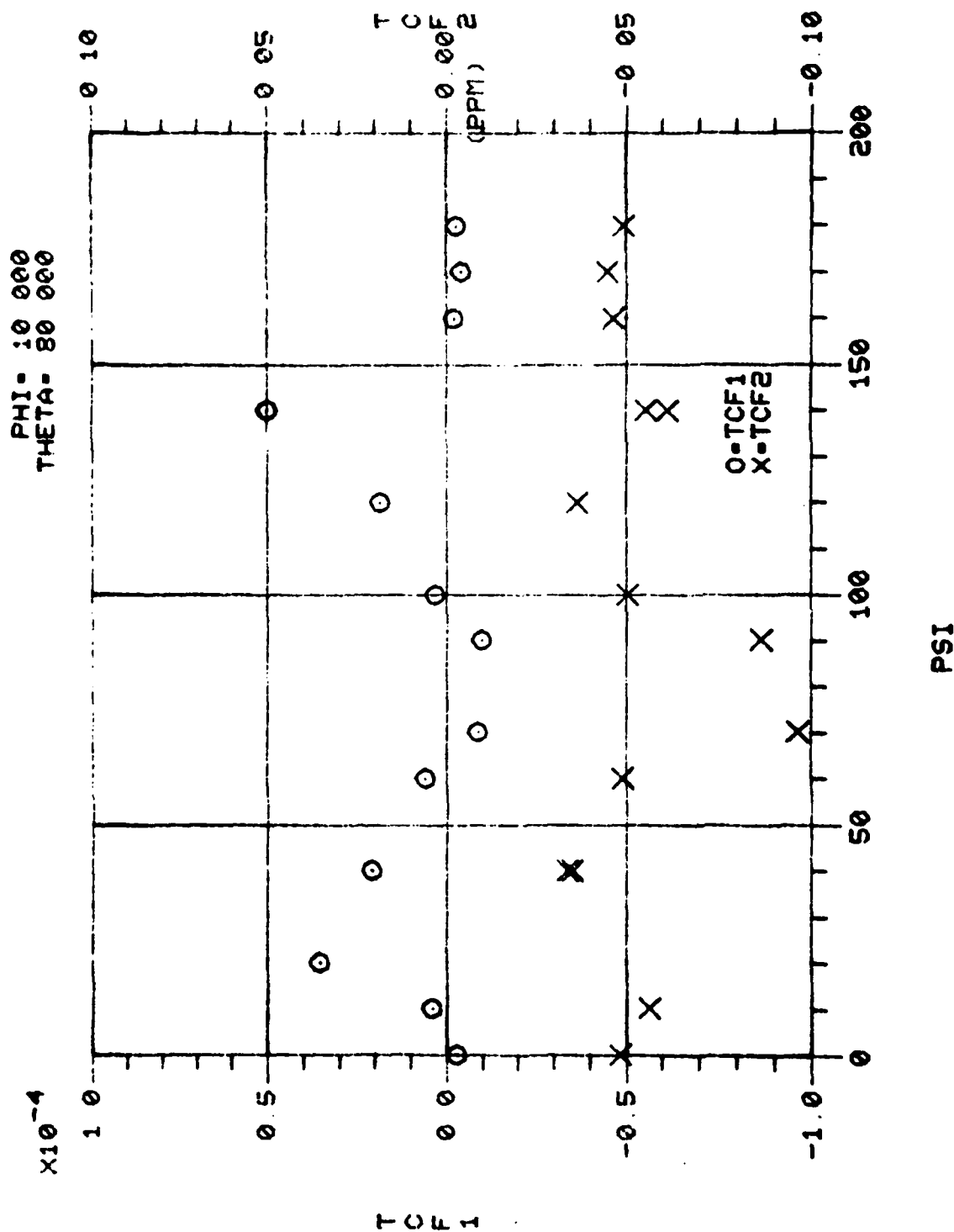


Figure 4. Calculated Values of TCF⁽¹⁾ Versus Propagation Angles (Sheet 19 of 71)

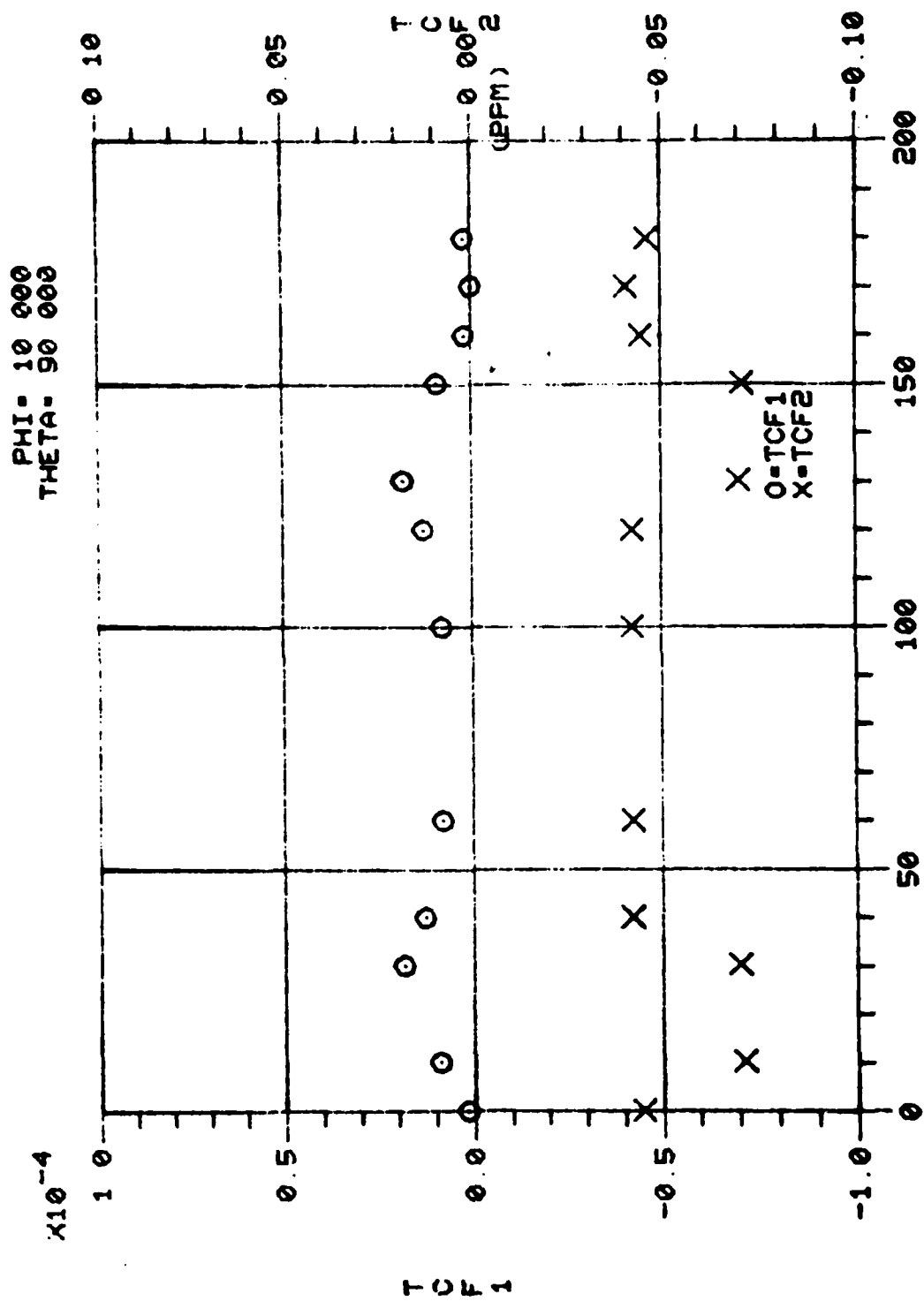


Figure 4. Calculated Values of TCF⁽¹⁾ Versus Propagation Angles (Sheet 20 of 71)

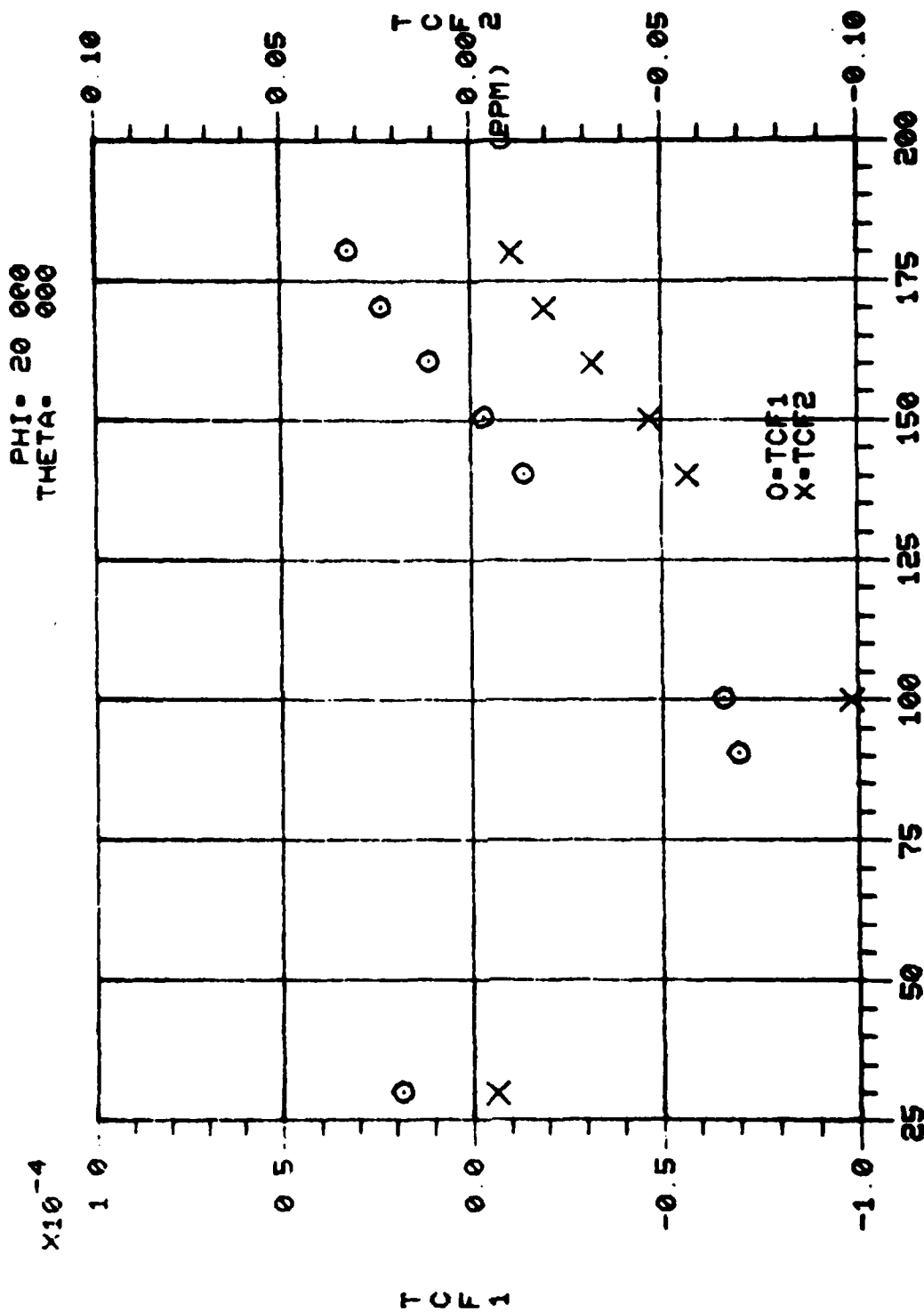


Figure 4. Calculated Values of TCF⁽¹⁾ Versus Propagation Angles (Sheet 21 of 71)

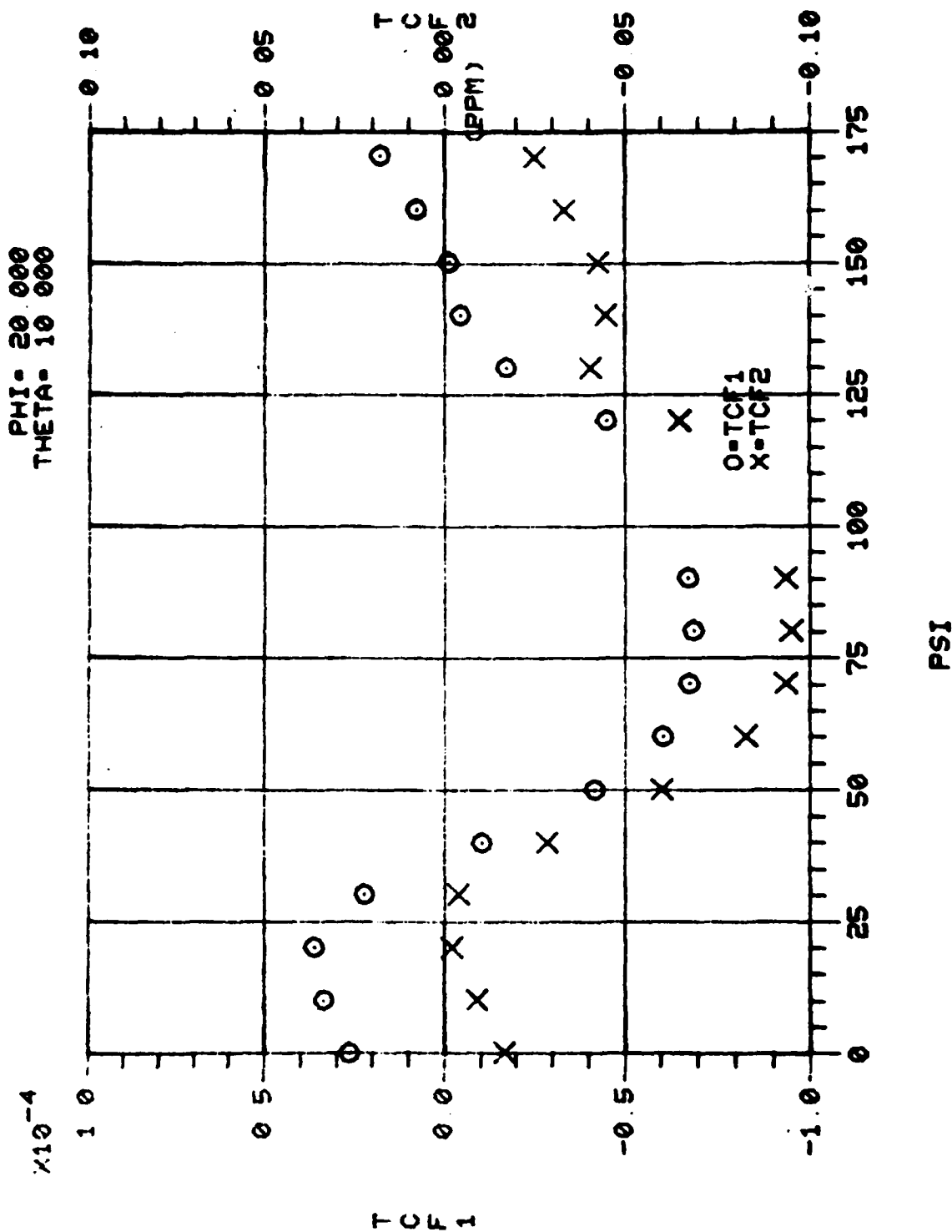


Figure 4. Calculated Values of TCF⁽¹⁾ Versus Propagation Angles (Sheet 22 of 71)

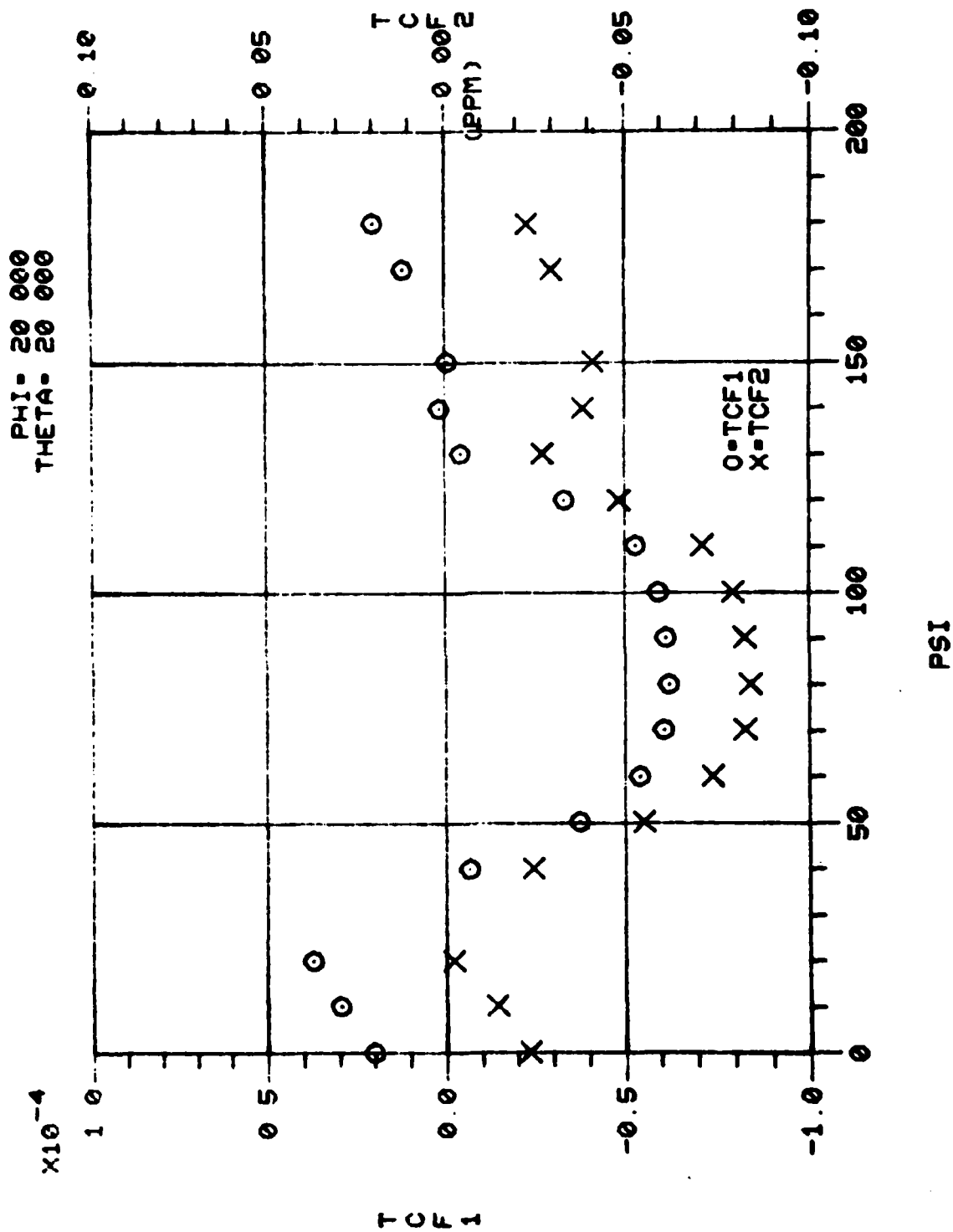
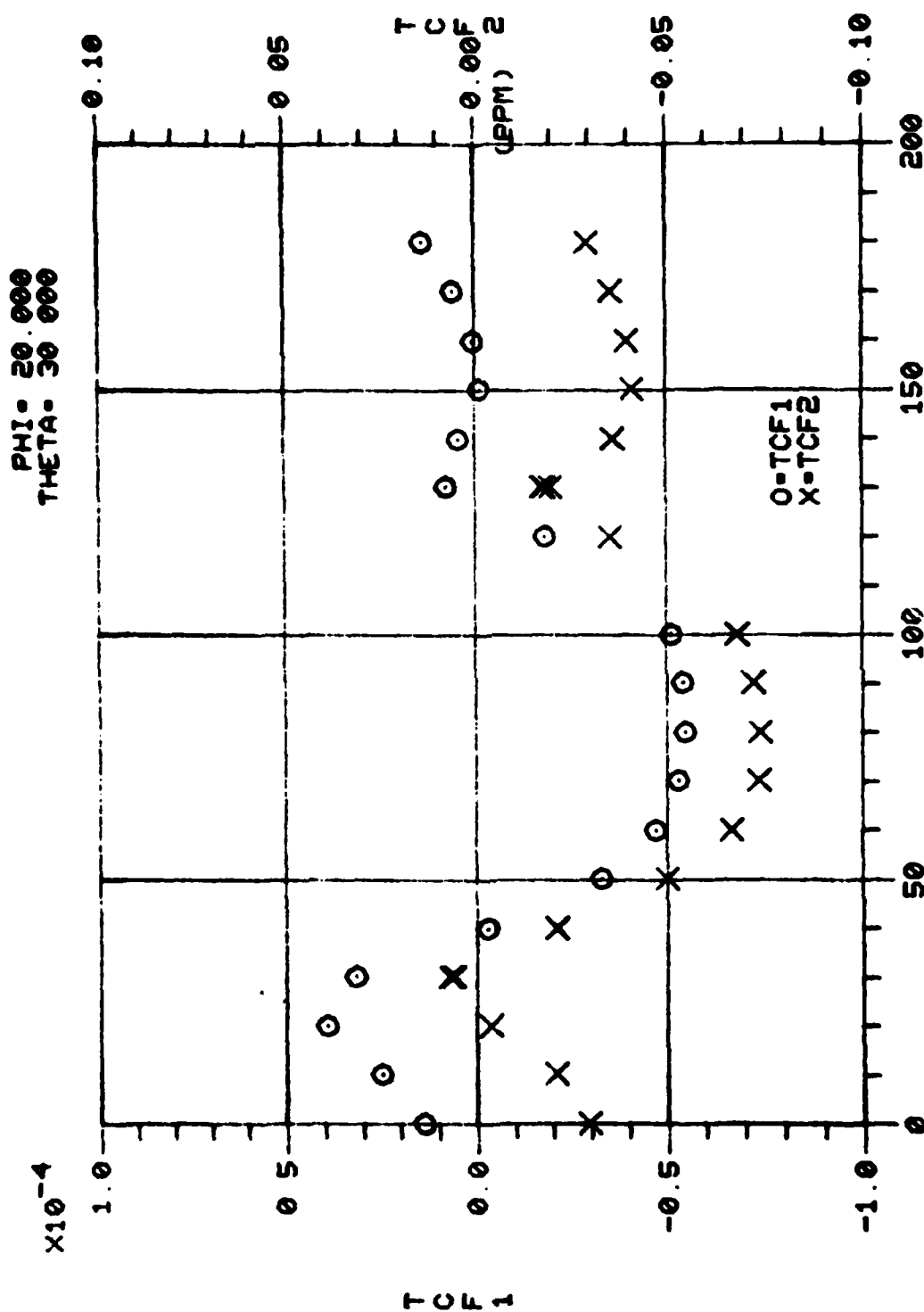


Figure 4. Calculated Values of TCF⁽¹⁾ Versus Propagation Angles (Sheet 23 of 71)



PSI

Figure 4. Calculated Values of TCF⁽¹⁾ Versus Propagation Angles (Sheet 24 of 71)

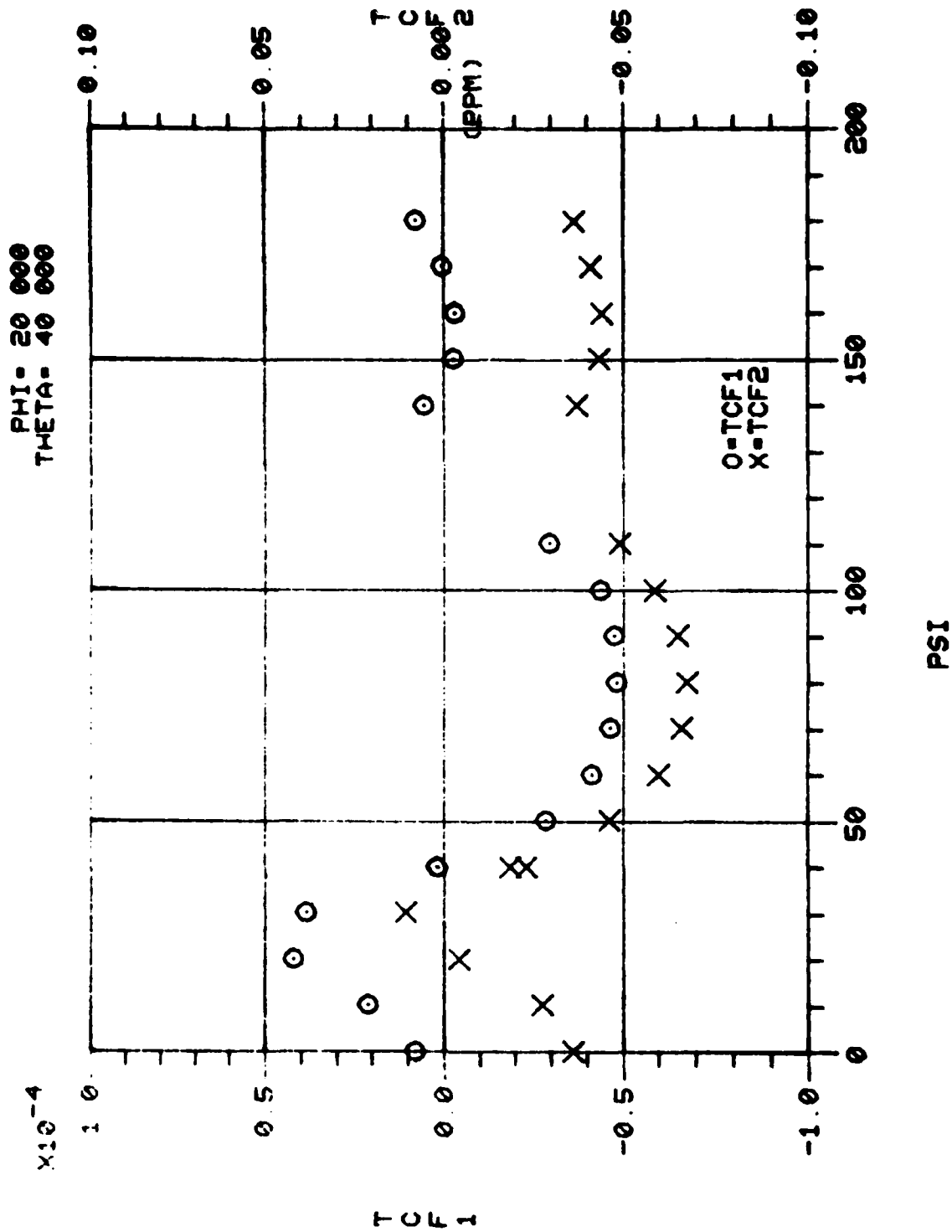


Figure 4. Calculated Values of TCF⁽¹⁾ Versus Propagation Angles (Sheet 25 of 71)

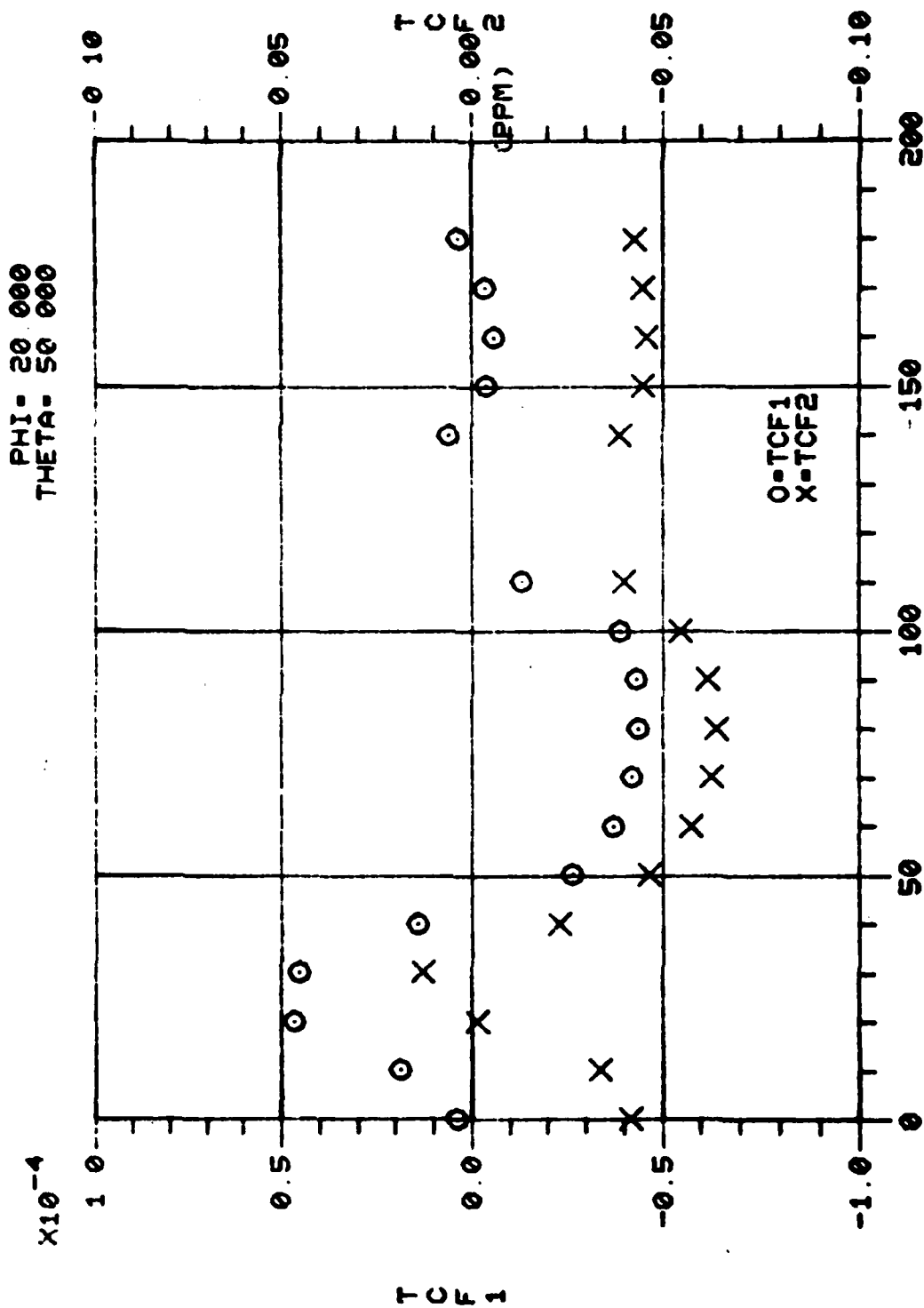


Figure 4. Calculated Values of TCF⁽¹⁾ Versus Propagation Angles (Sheet 26 of 71)

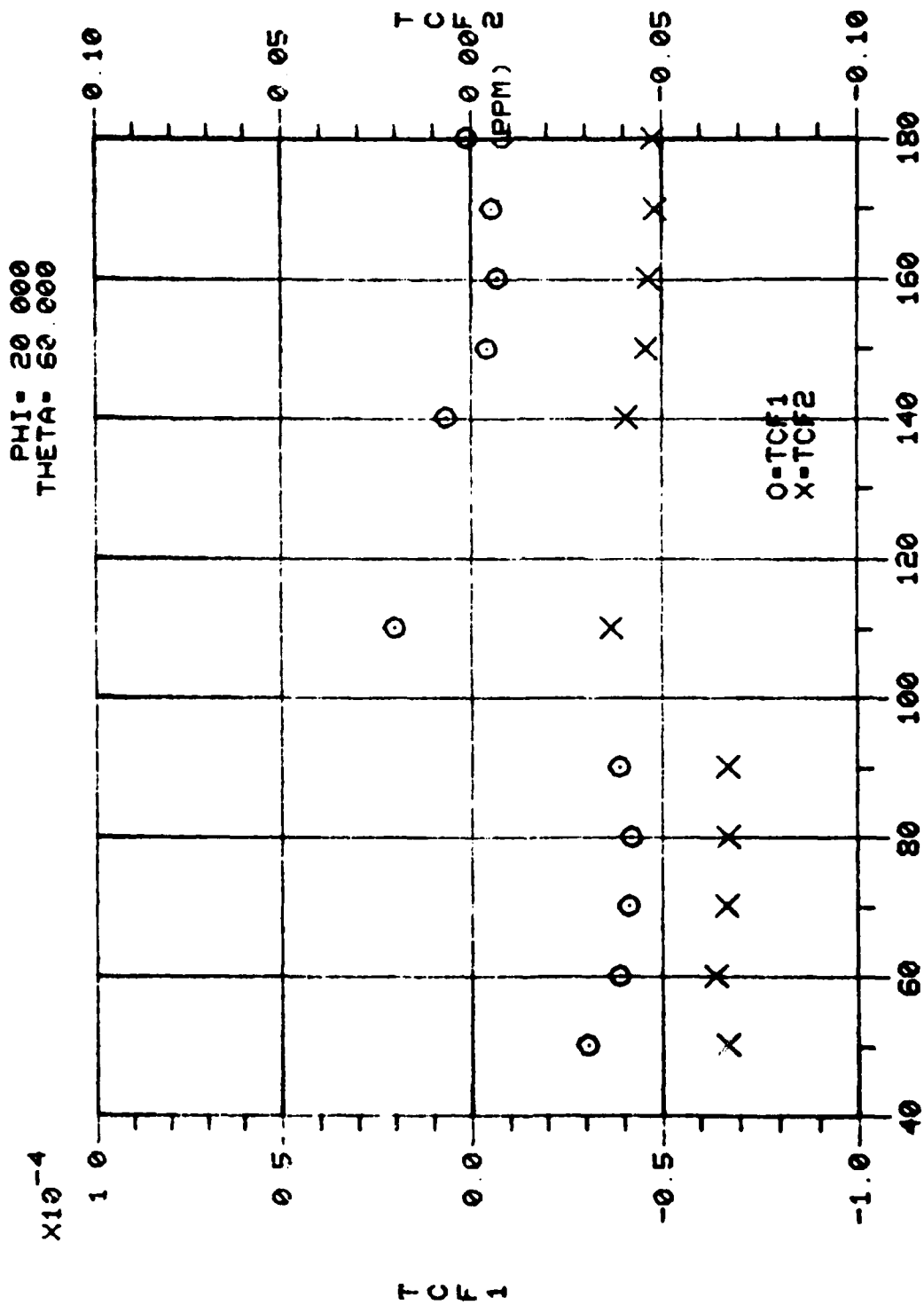


Figure 4. Calculated Values of TCF⁽¹⁾ Versus Propagation Angles (Sheet 27 of 71)

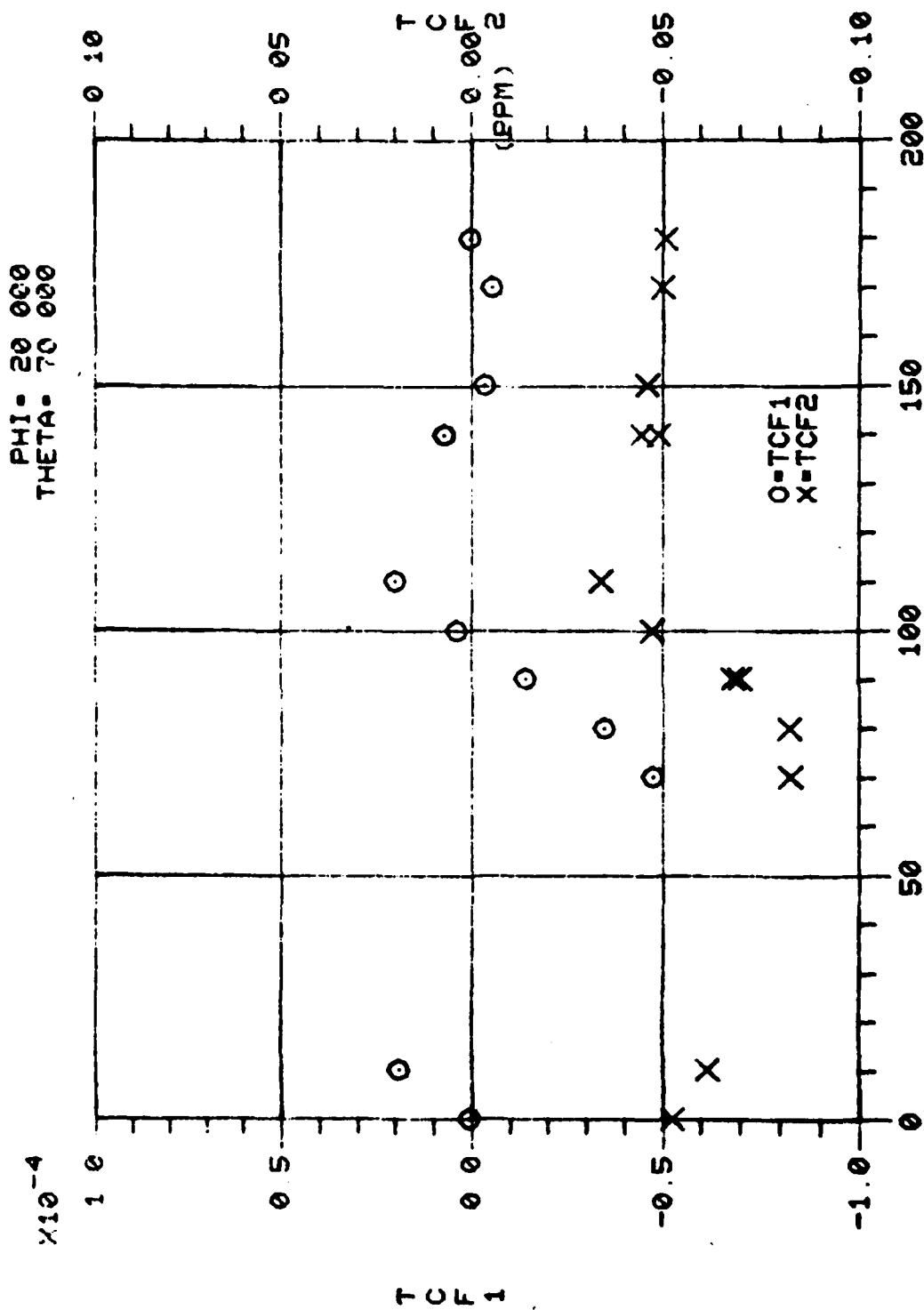
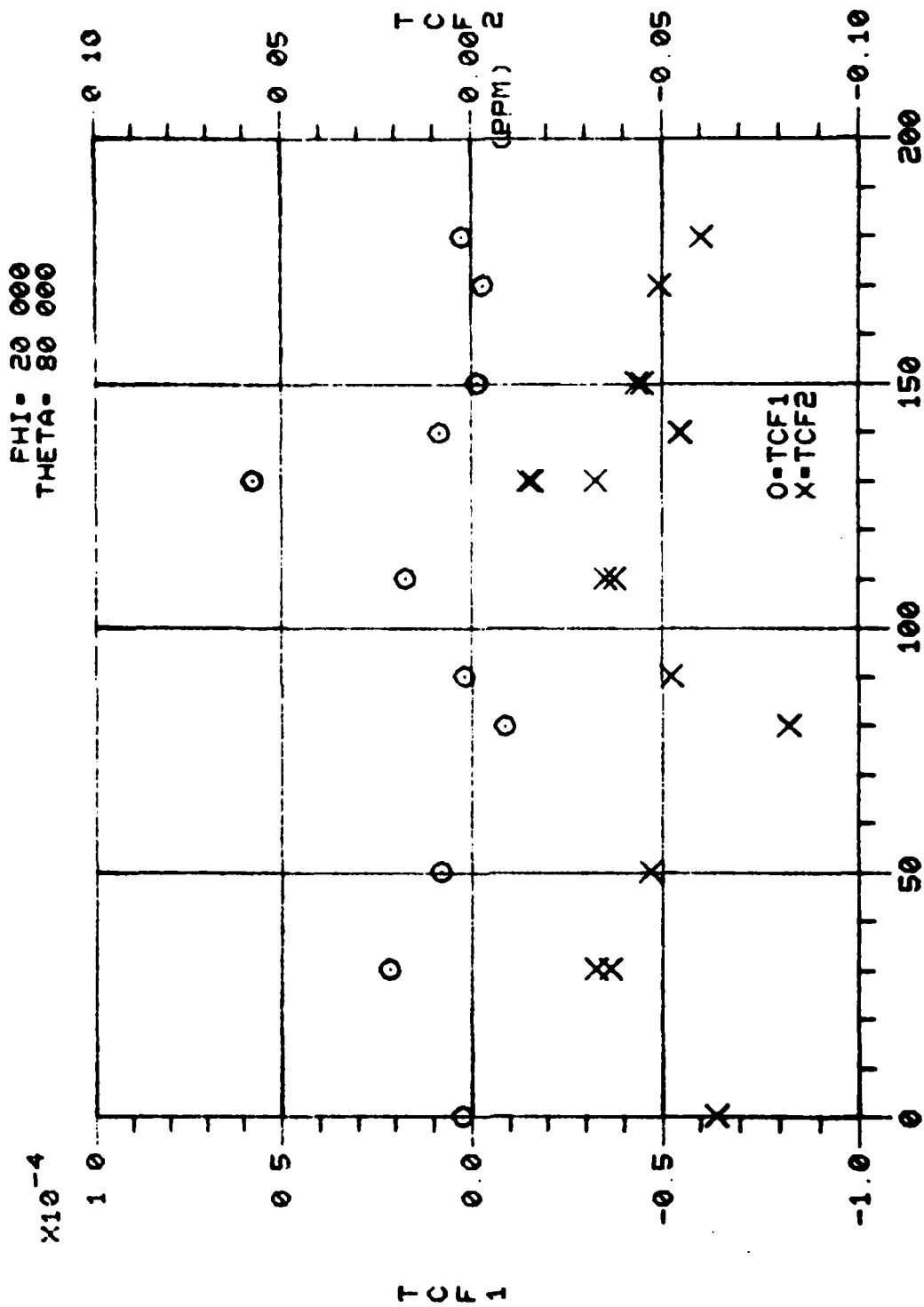
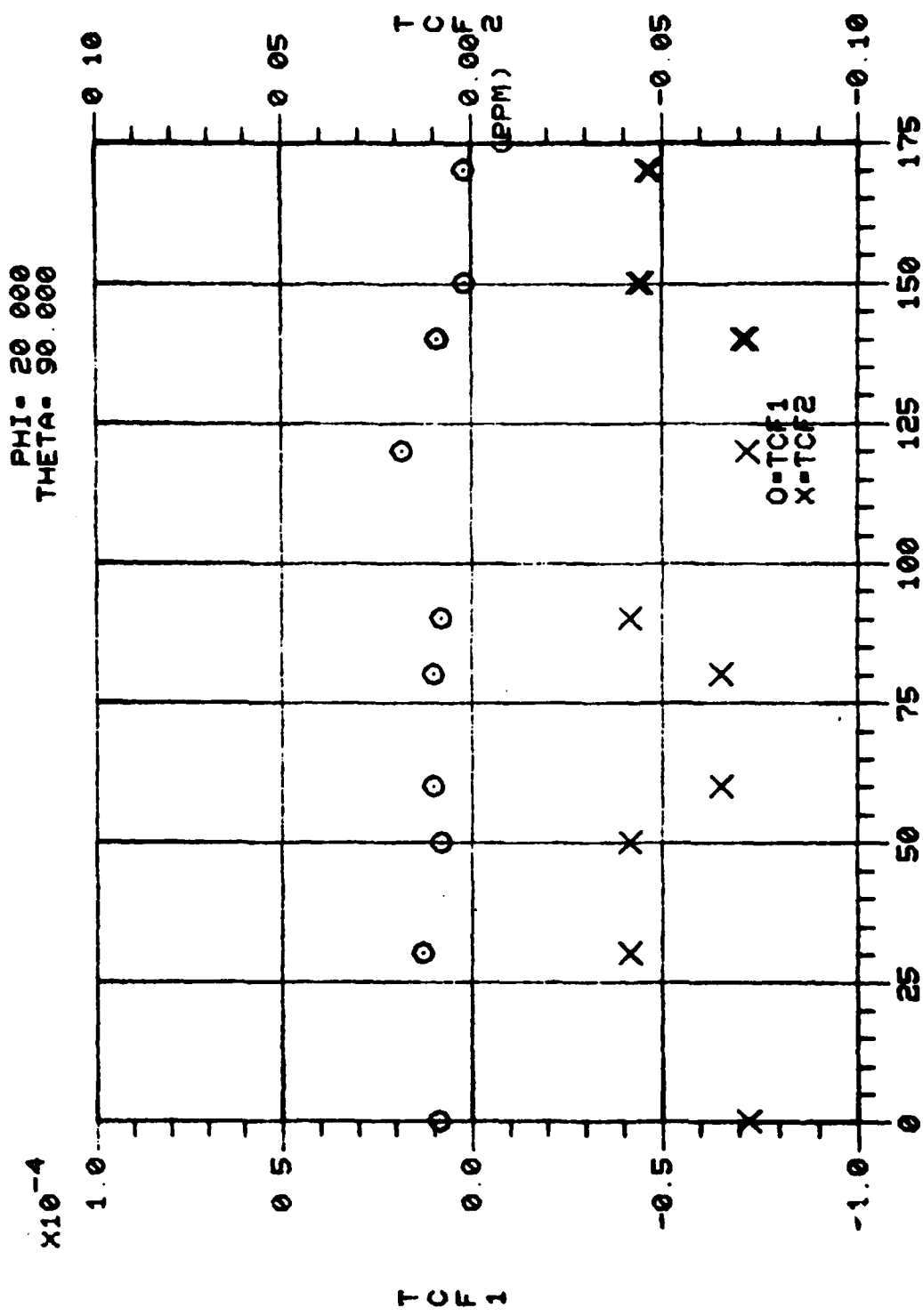


Figure 4. Calculated Values of TCF⁽¹⁾ Versus Propagation Angles (Sheet 28 of 71)



PSI
 Figure 4. Calculated Values of $TCF^{(1)}$ Versus Propagation Angles (Sheet 29 of 71)



PSI

Figure 4. Calculated Values of TCF⁽¹⁾ Versus Propagation Angles (Sheet 30 of 71)

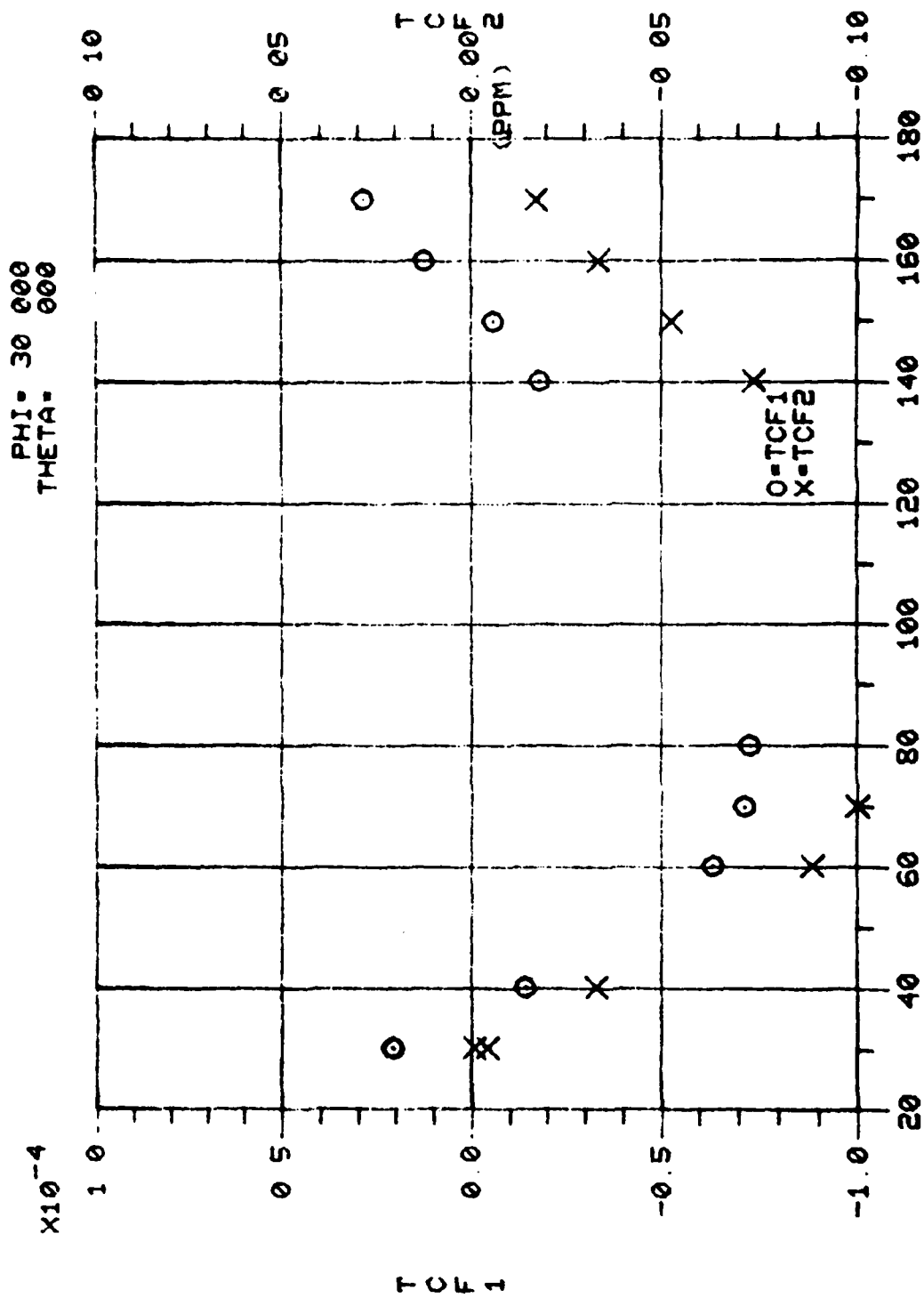


Figure 4. Calculated Values of TCF⁽¹⁾ Versus Propagation Angles (Sheet 31 of 71)

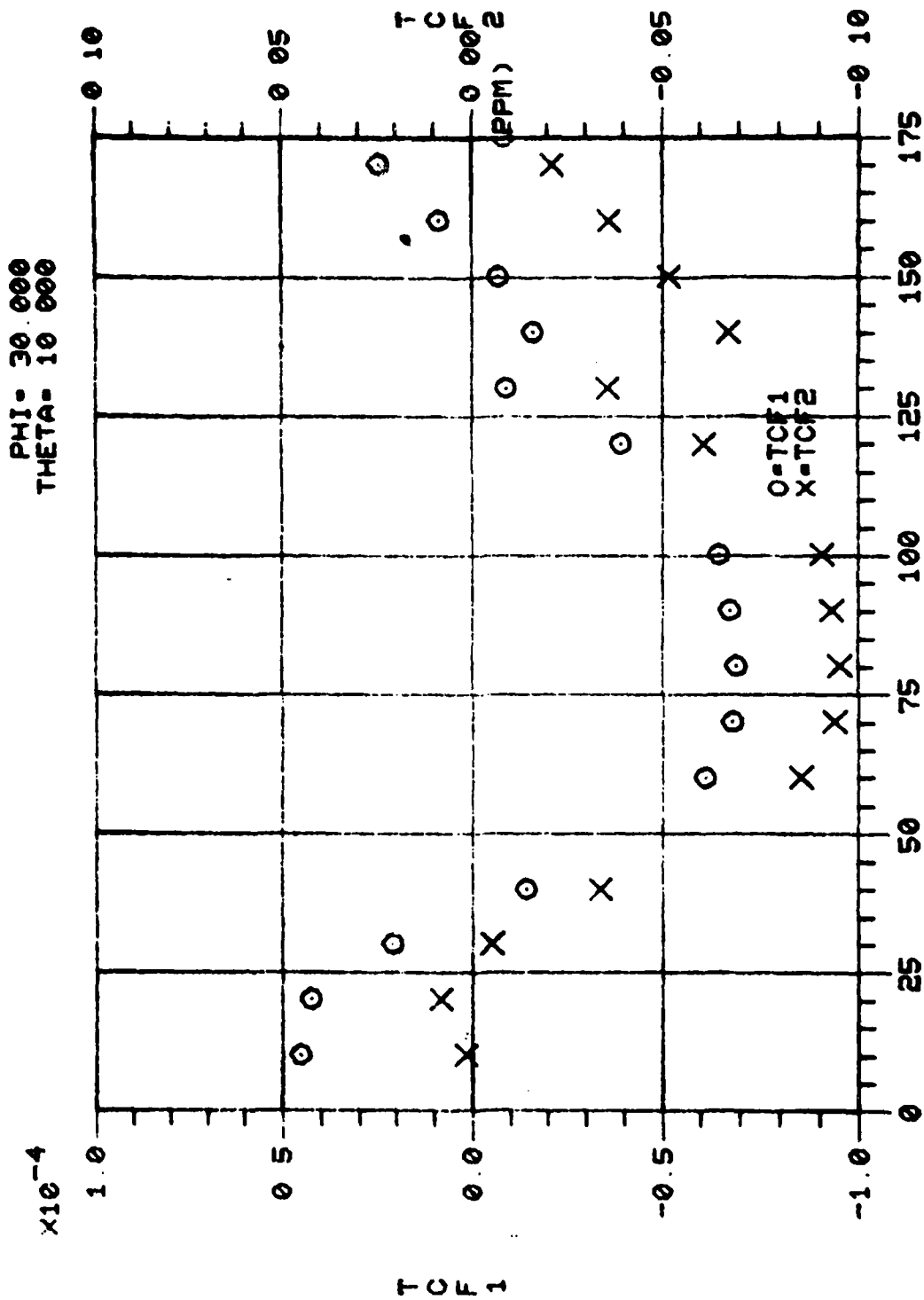
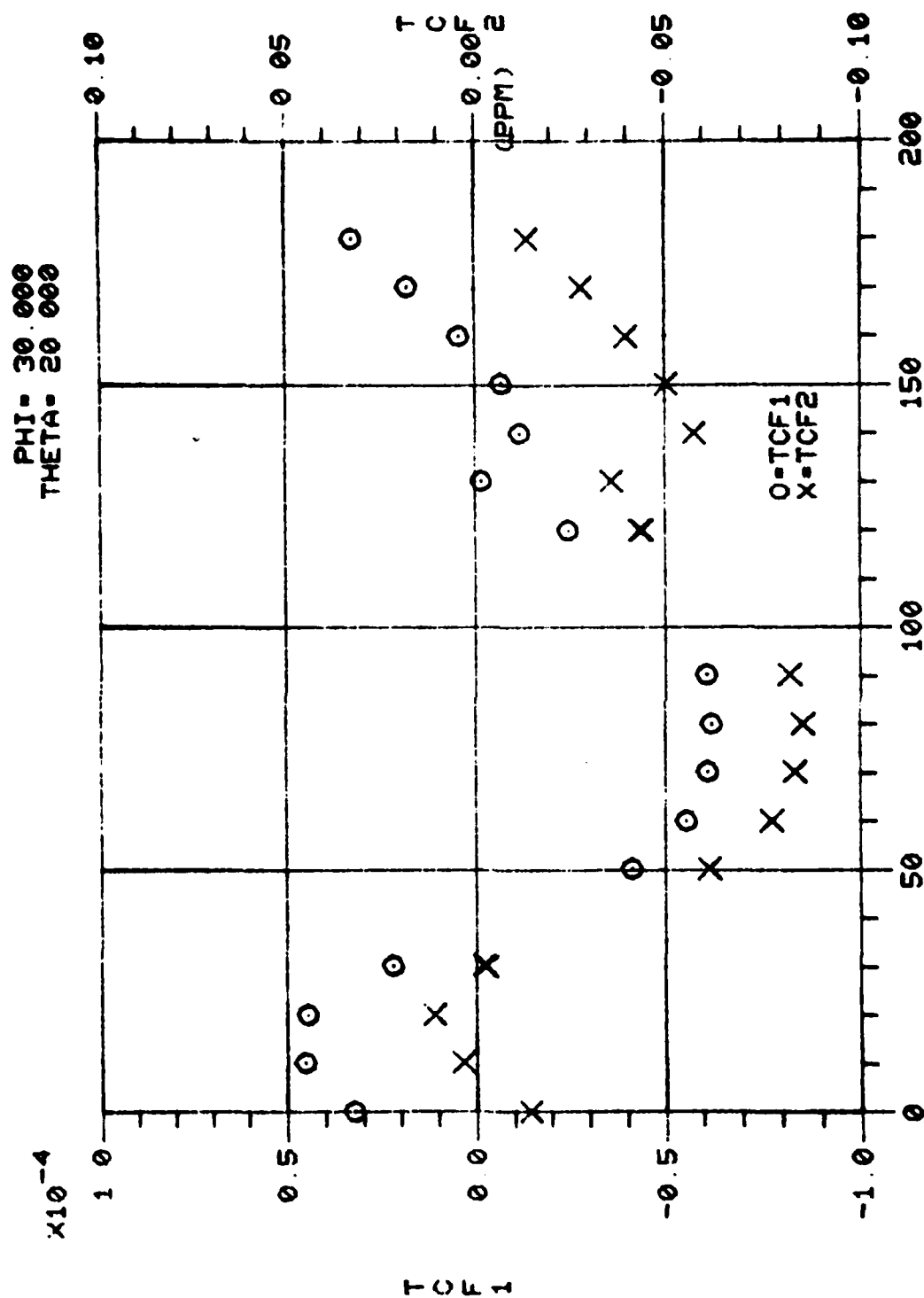


Figure 4. Calculated Values of TCF⁽¹⁾ Versus Propagation Angles (Sheet 32 of 71)



PSI

Figure 4. Calculated Values of TCF⁽¹⁾ Versus Propagation Angles (Sheet 33 of 71)

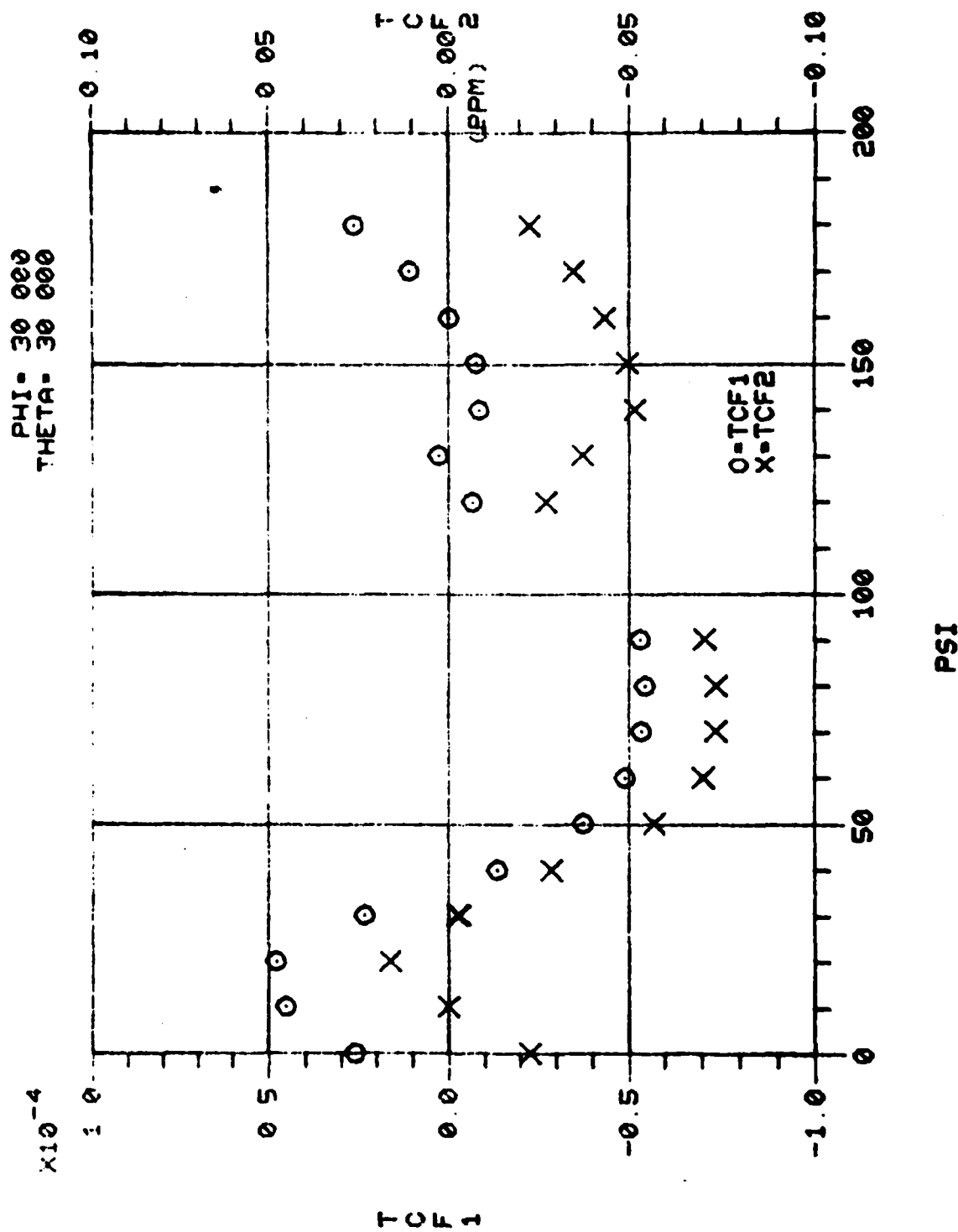


Figure 4. Calculated Values of TCF⁽¹⁾ Versus Propagation Angles (Sheet 34 of 71)

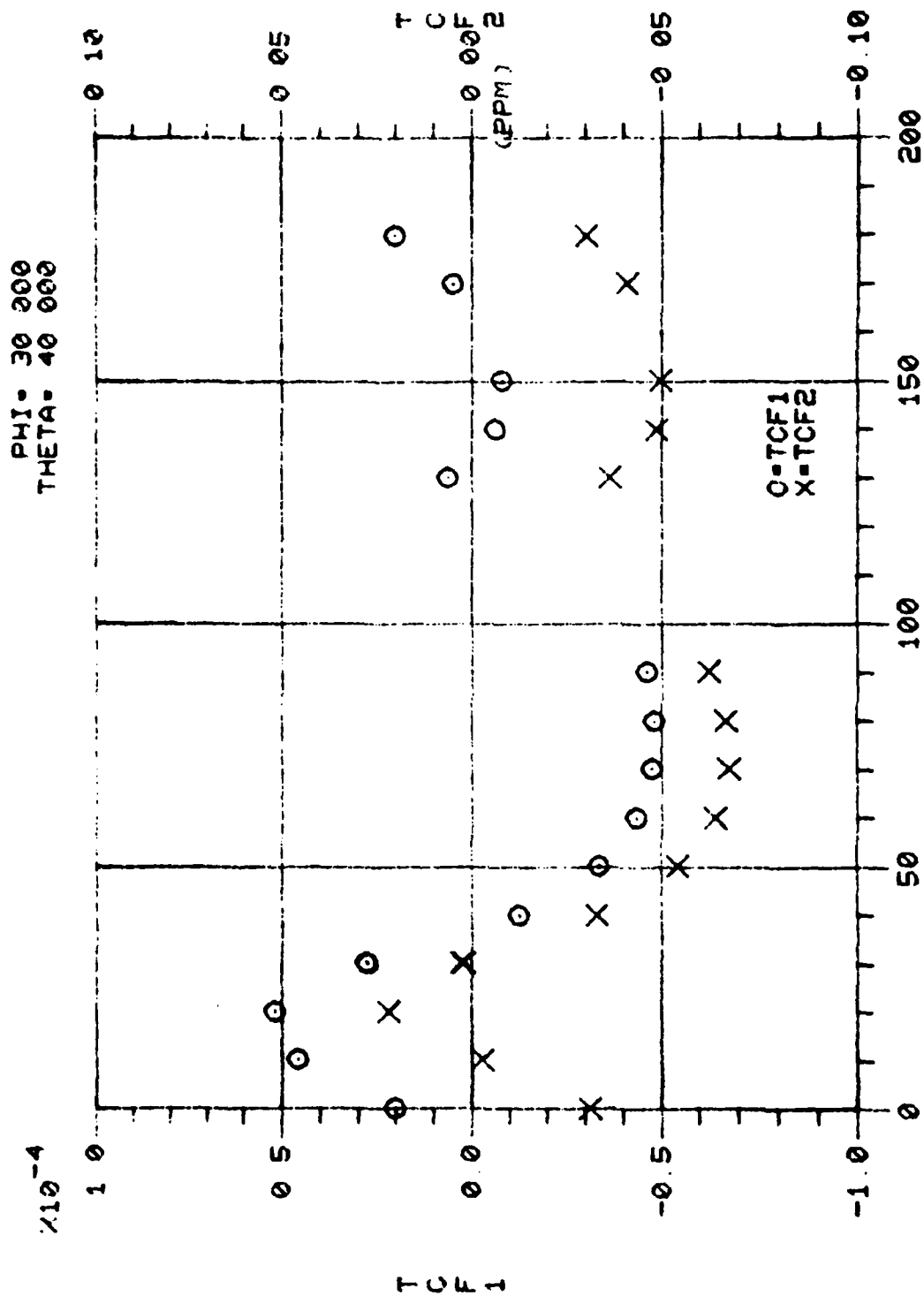
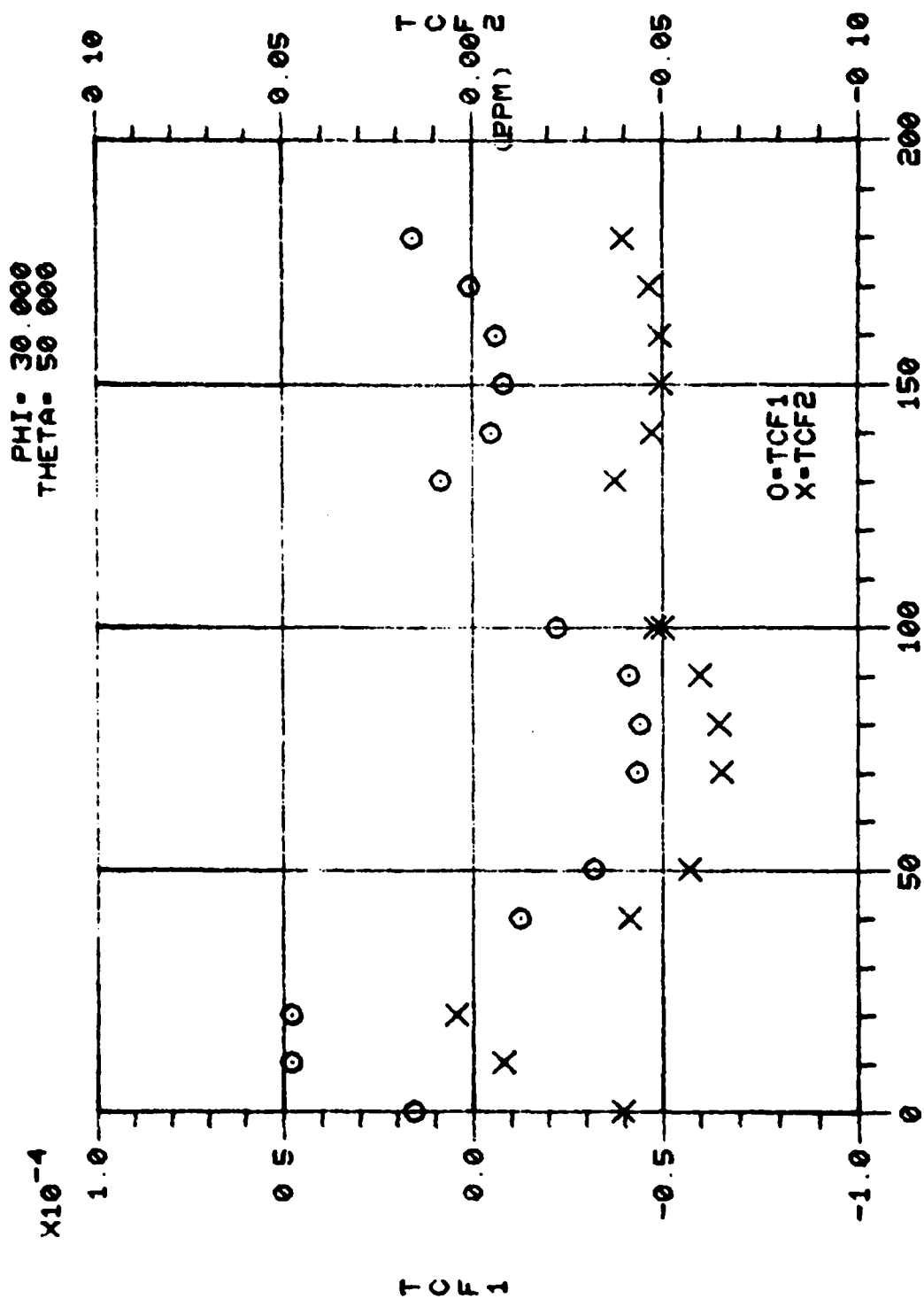


Figure 4. Calculated Values of TCF^{1,2} Versus Propagation Angles (Sheet 35 of 71)



PSI

Figure 4. Calculated Values of TCF⁽¹⁾ Versus Propagation Angles (Sheet 36 of 71)

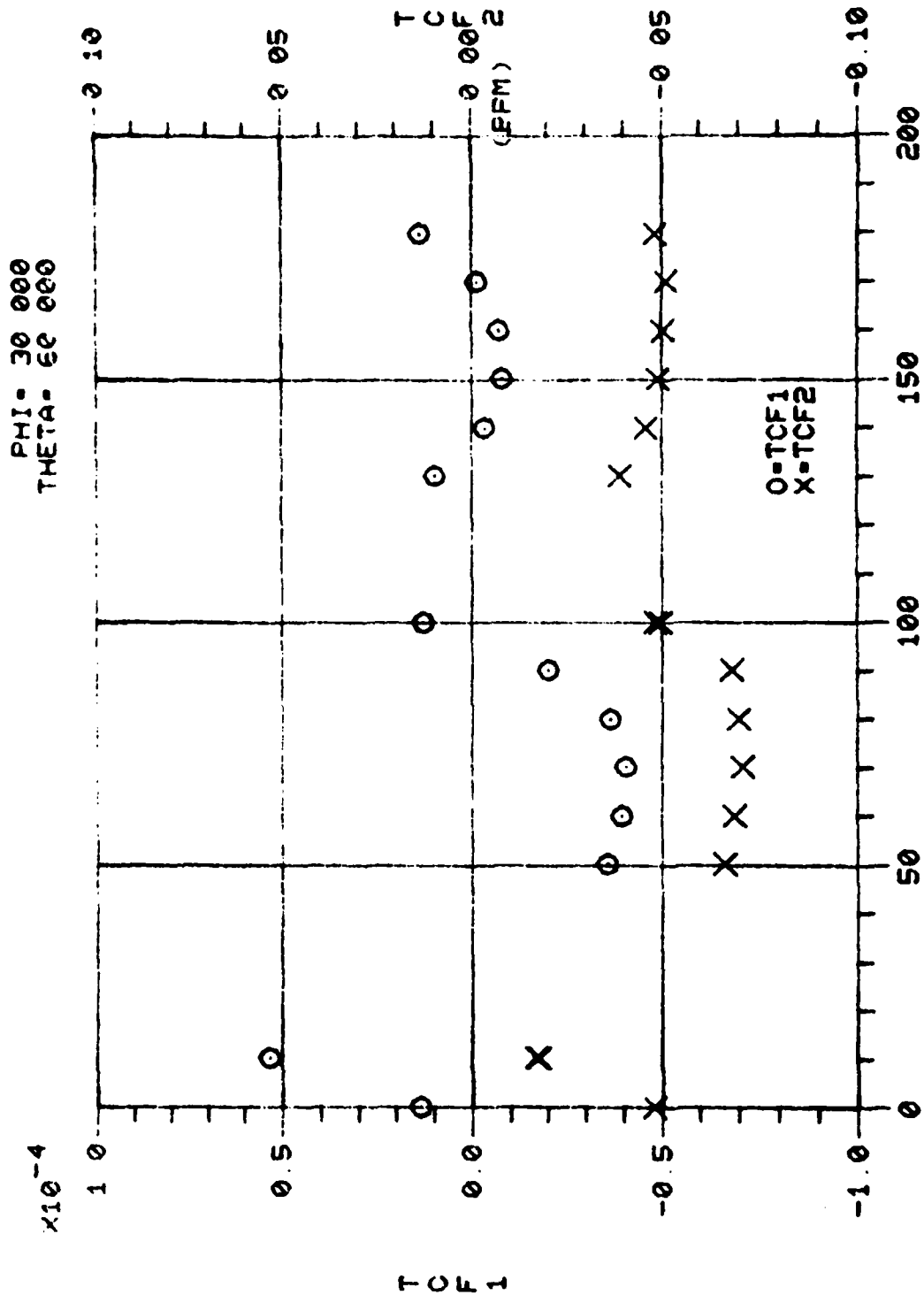


Figure 4. Calculated Values of TCF⁽¹⁾ Versus Propagation Angles (Sheet 37 of 71)

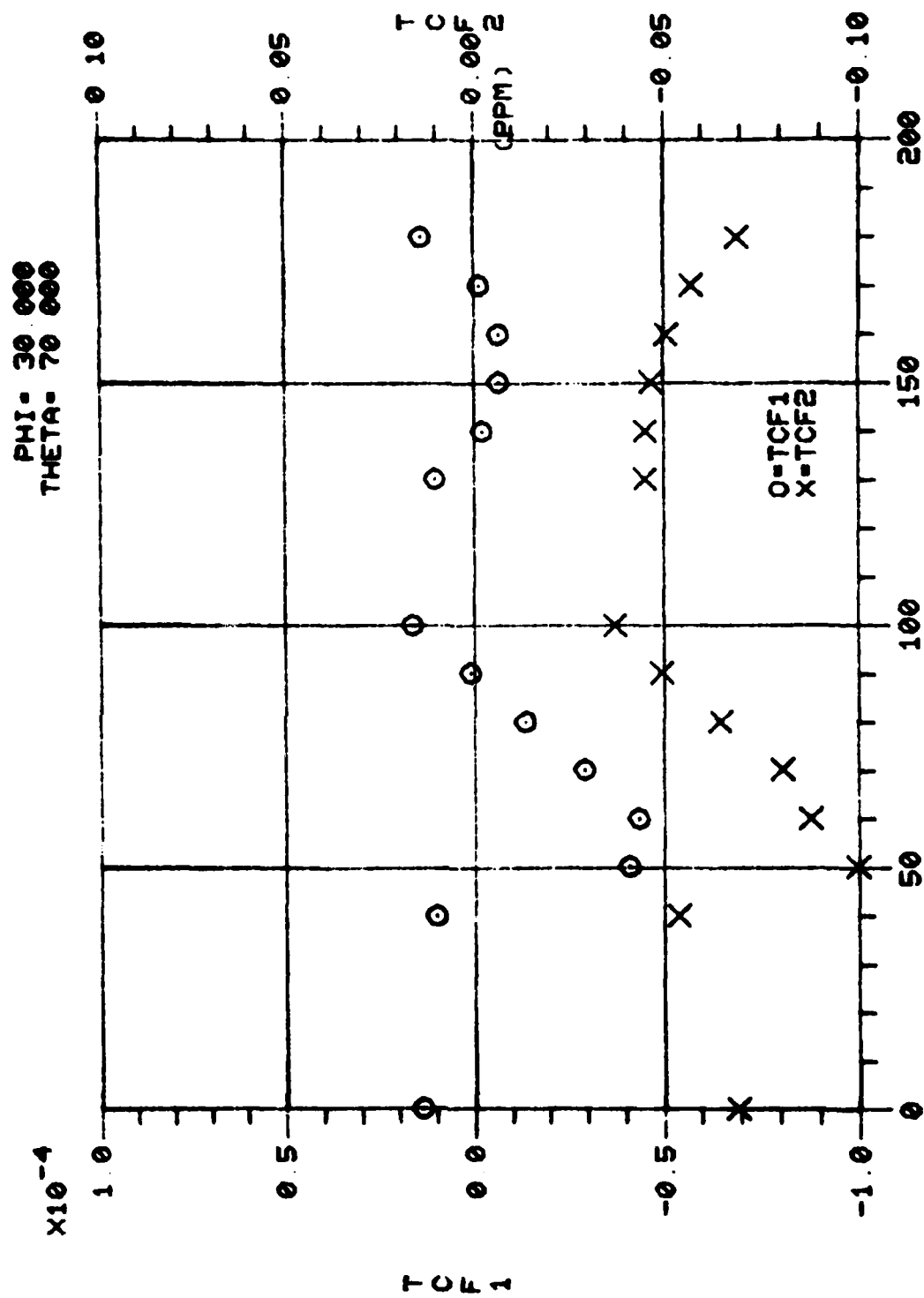


Figure 4. Calculated Values of TCF⁽¹⁾ Versus Propagation Angles (Sheet 38 of 71)

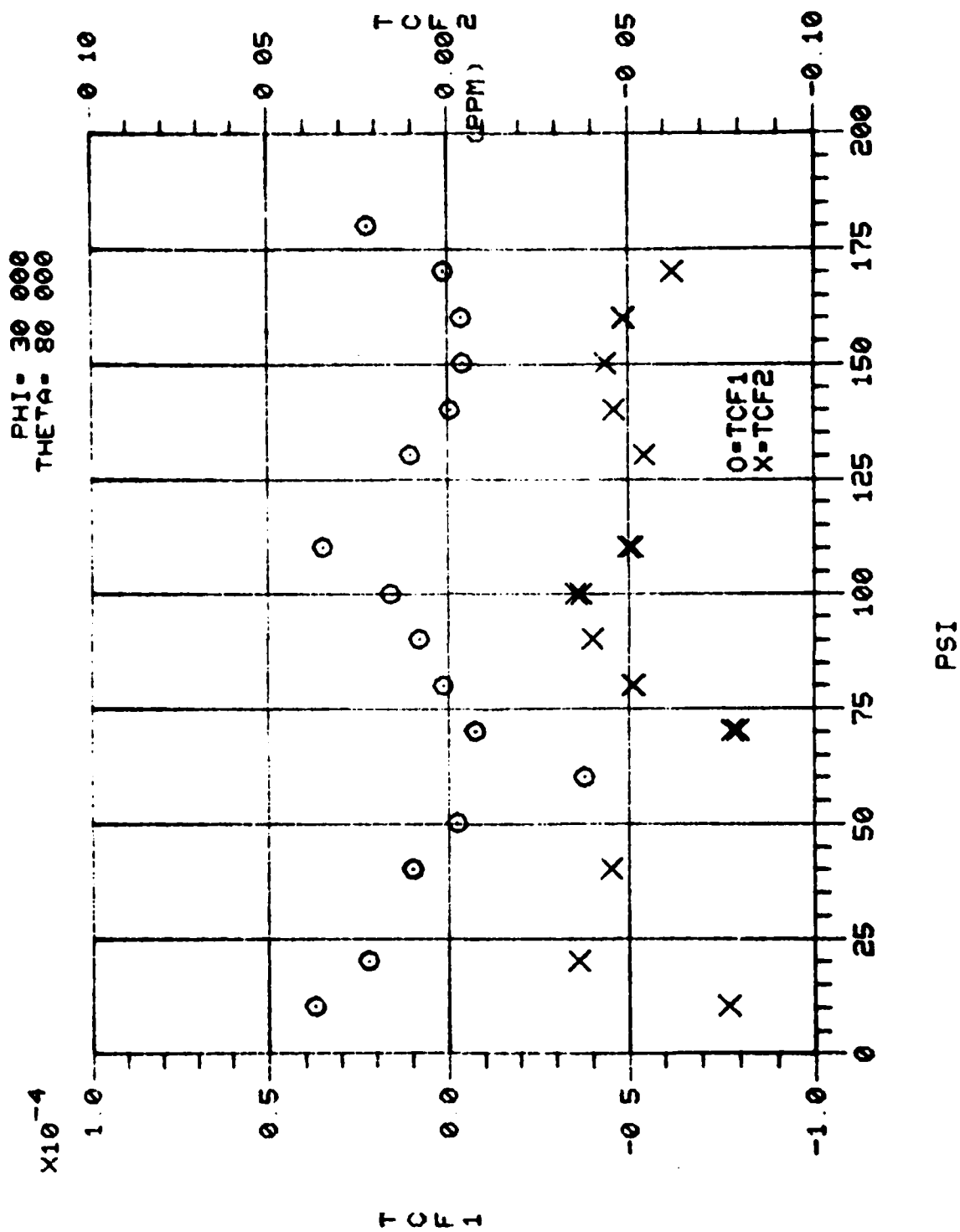
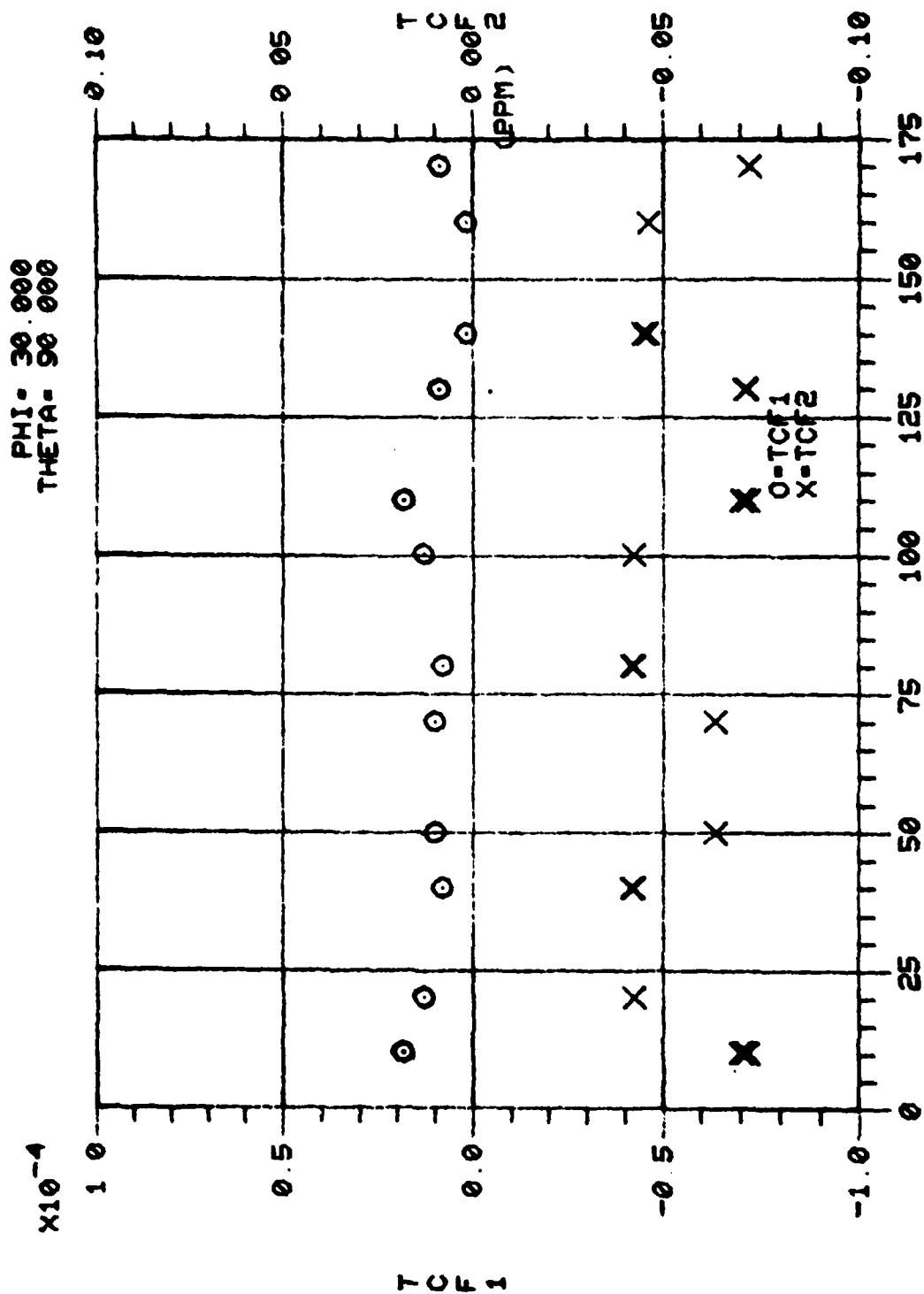
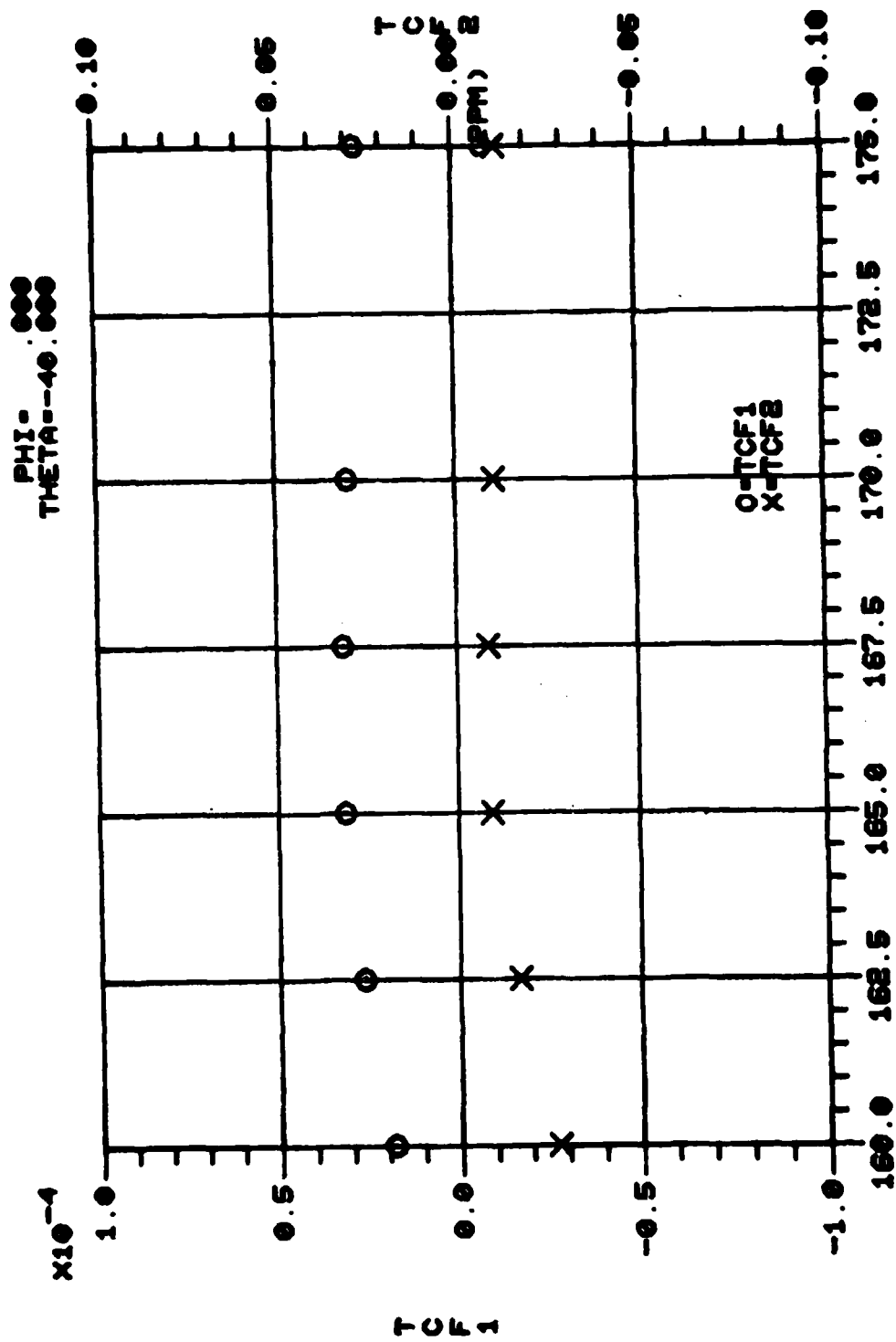


Figure 4. Calculated Values of TCF⁽¹⁾ Versus Propagation Angles (Sheet 39 of 71)



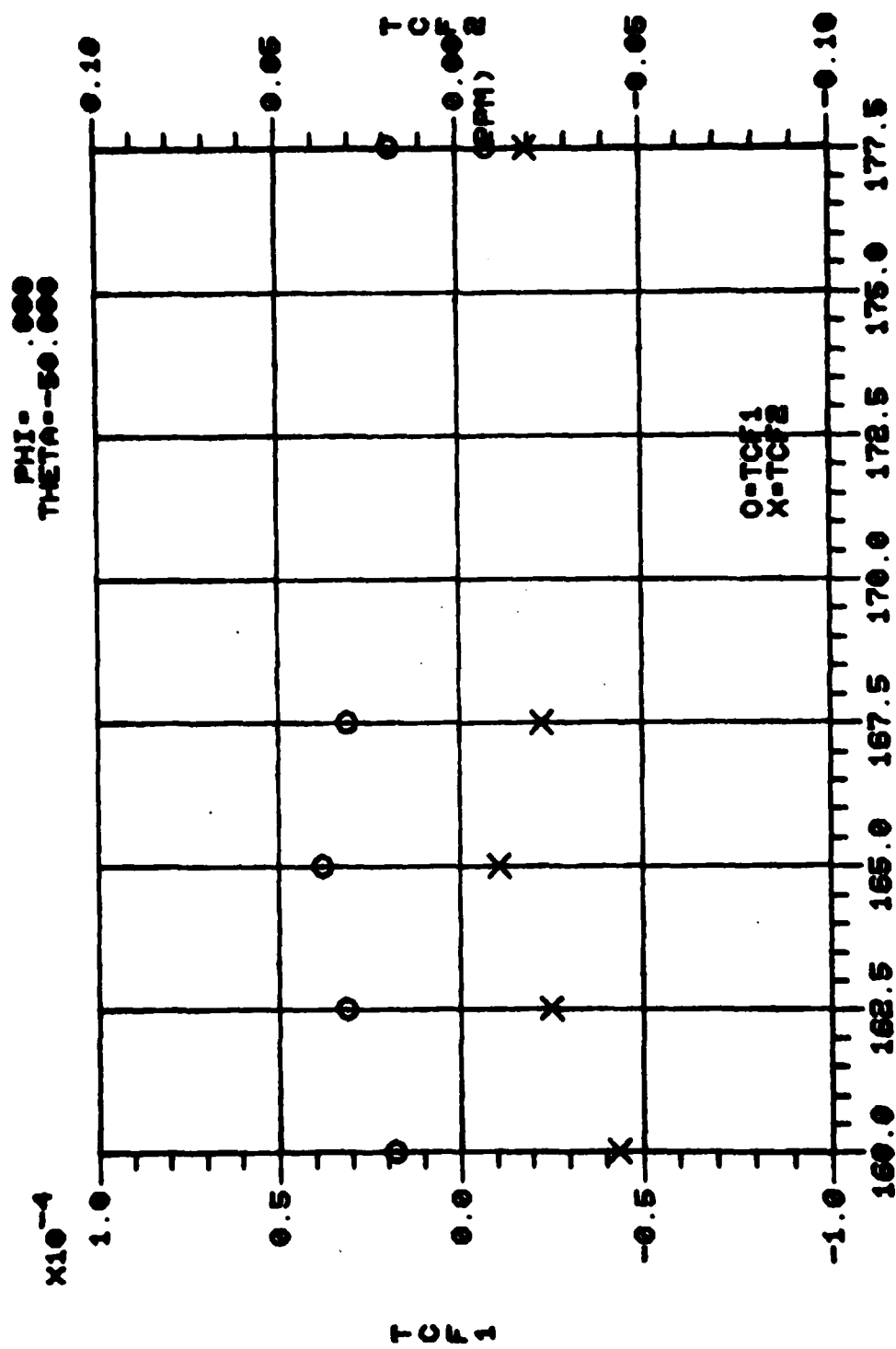
PSI

Figure 4. Calculated Values of TCF⁽¹⁾ Versus Propagation Angles (Sheet 40 of 71)

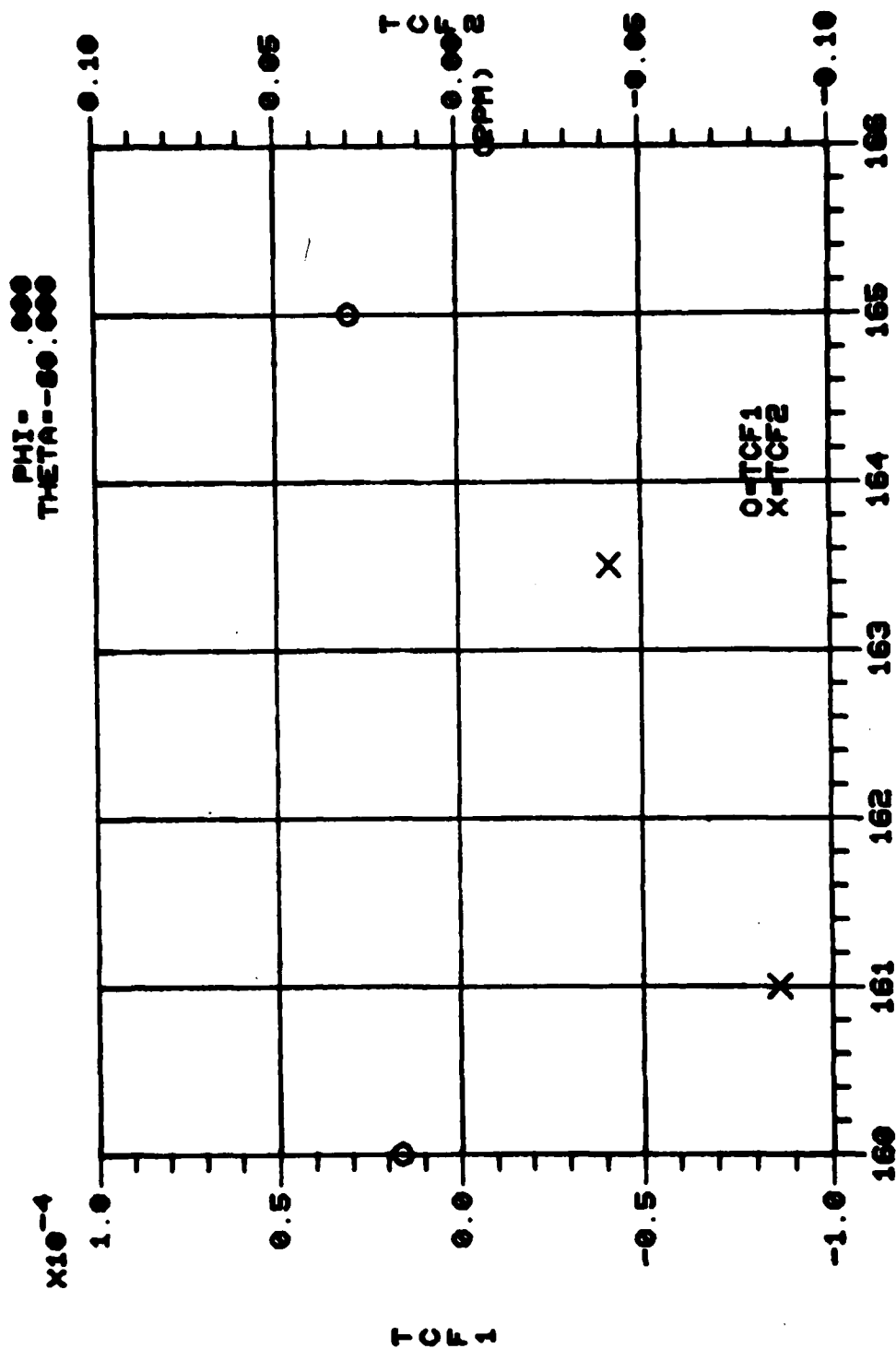


PSI

Figure 4. Calculated Values of TCF⁽¹⁾ Versus Propagation Angles (Sheet 41 of 71)



PSI
 Figure 4. Calculated Values of TCF⁽¹⁾ Versus Propagation Angles (Sheet 42 of 71)



PSI

Figure 4. Calculated Values of $TCF^{(1)}$ Versus Propagation Angles (Sheet 43 of 71)

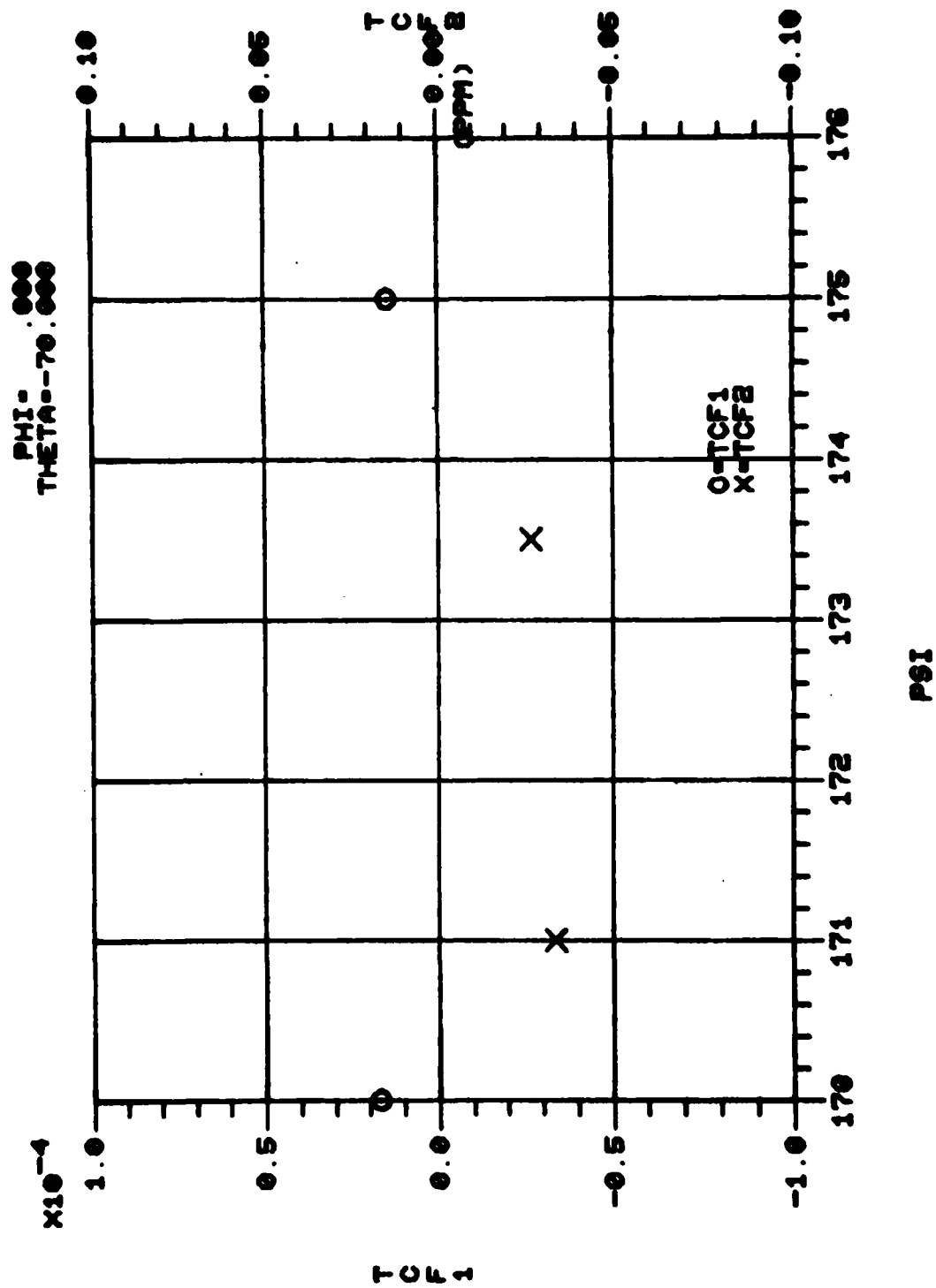


Figure 4. Calculated Values of $\text{TCF}^{(1)}$ Versus Propagation Angles (Sheet 44 of 71)

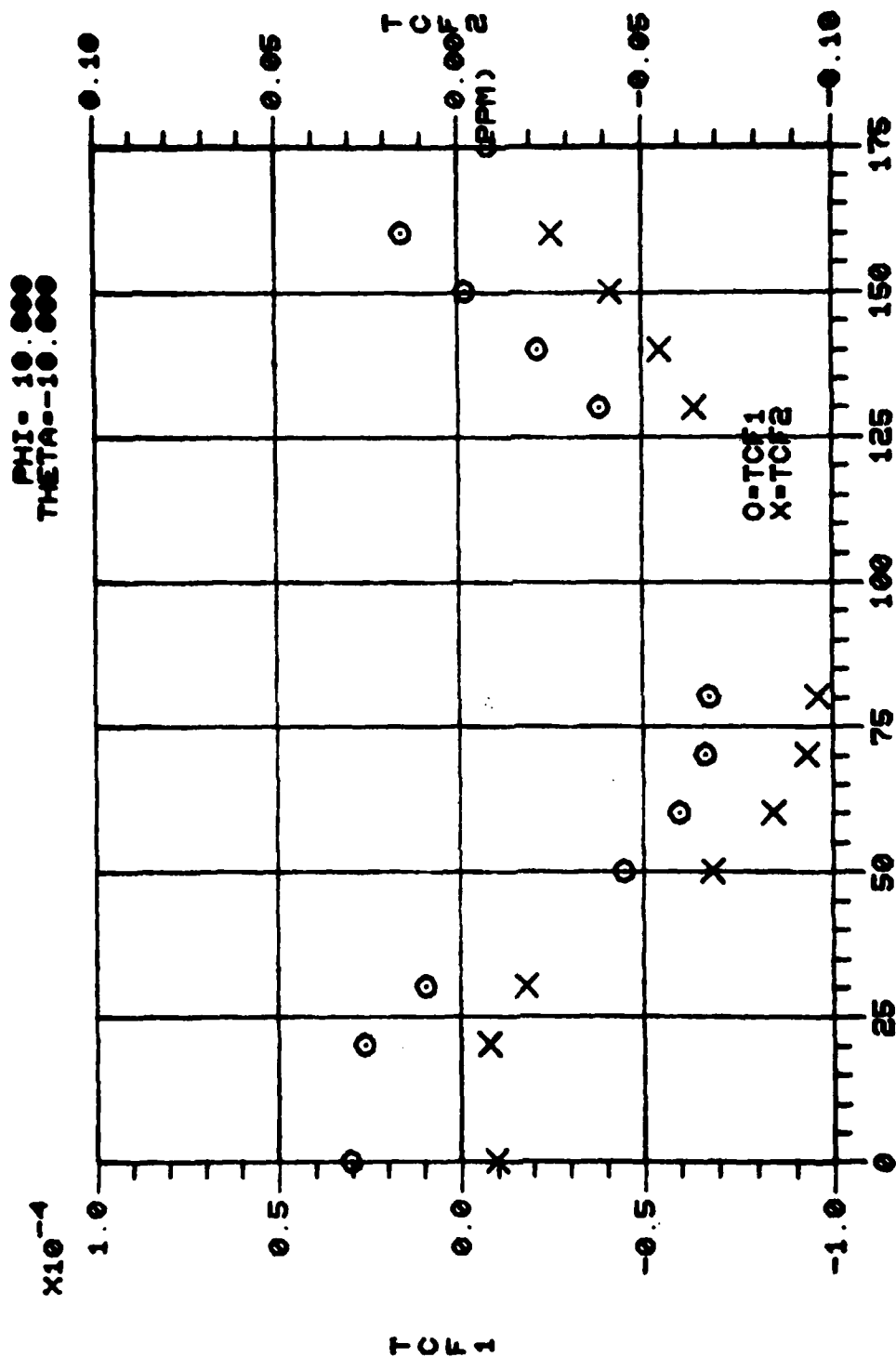


Figure 4. Calculated Values of TCF⁽¹⁾ Versus Propagation Angles (Sheet 45 of 71)

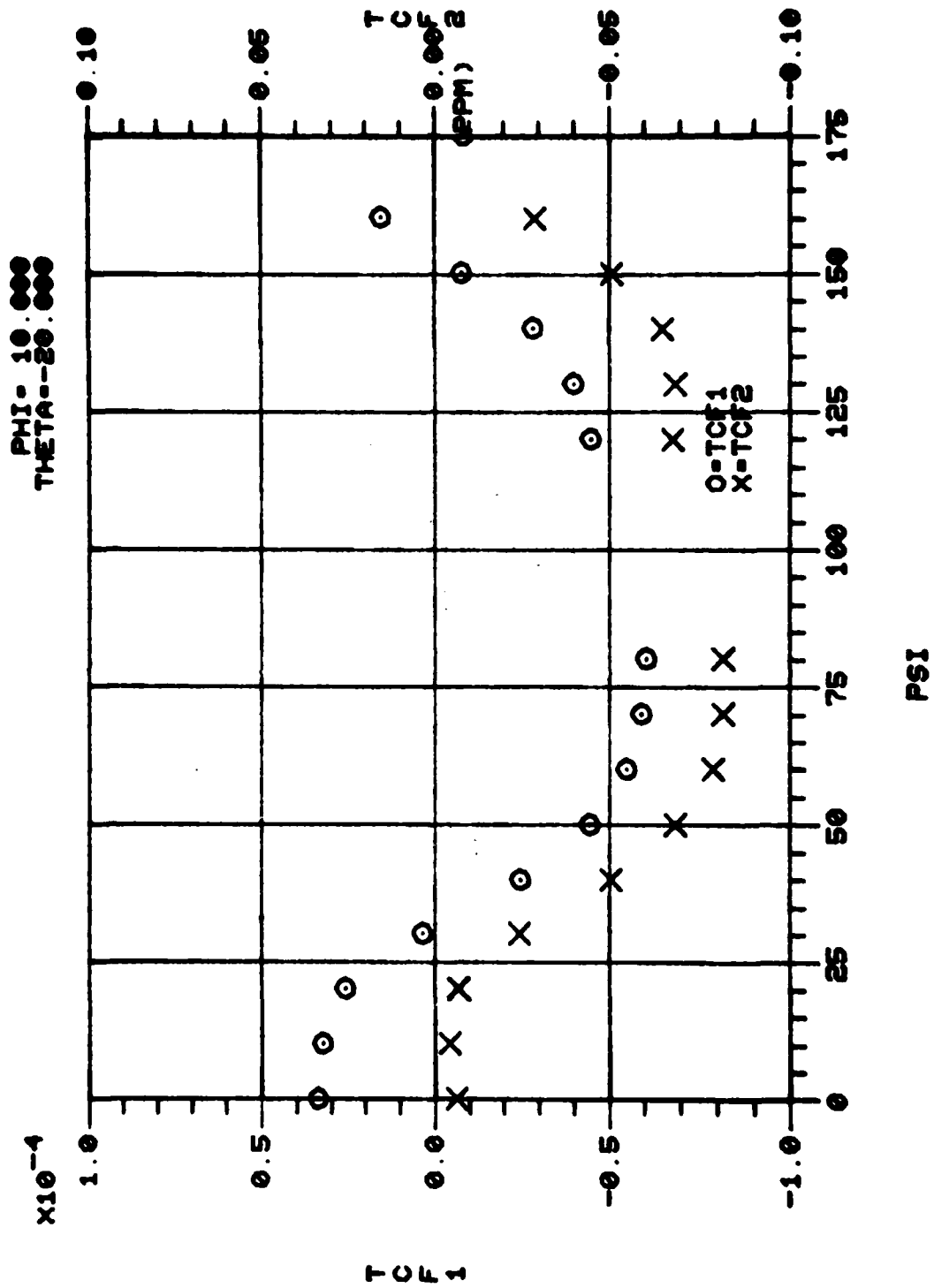


Figure 4. Calculated Values of TCF⁽¹⁾ Versus Propagation Angles (Sheet 46 of 71)

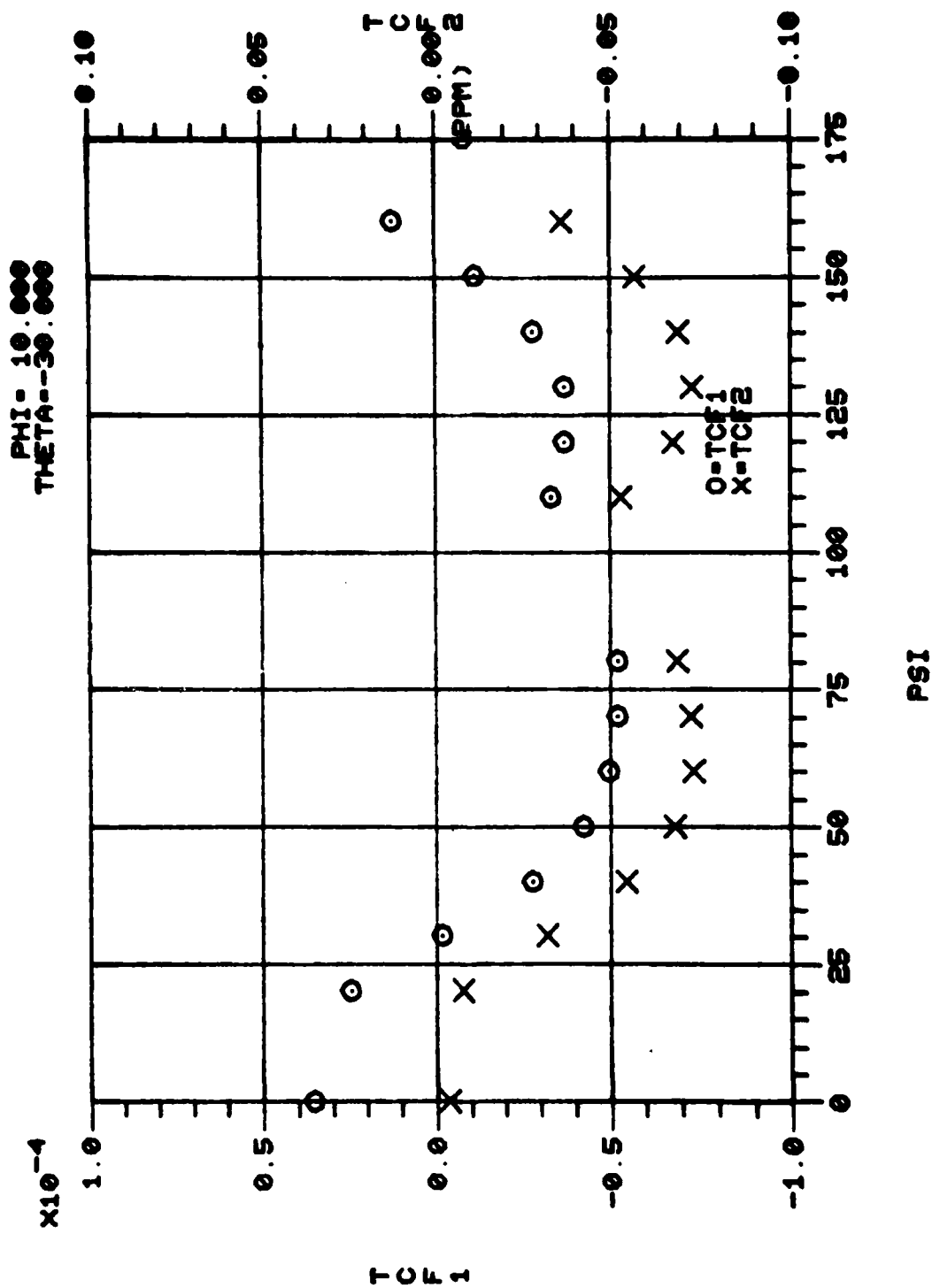
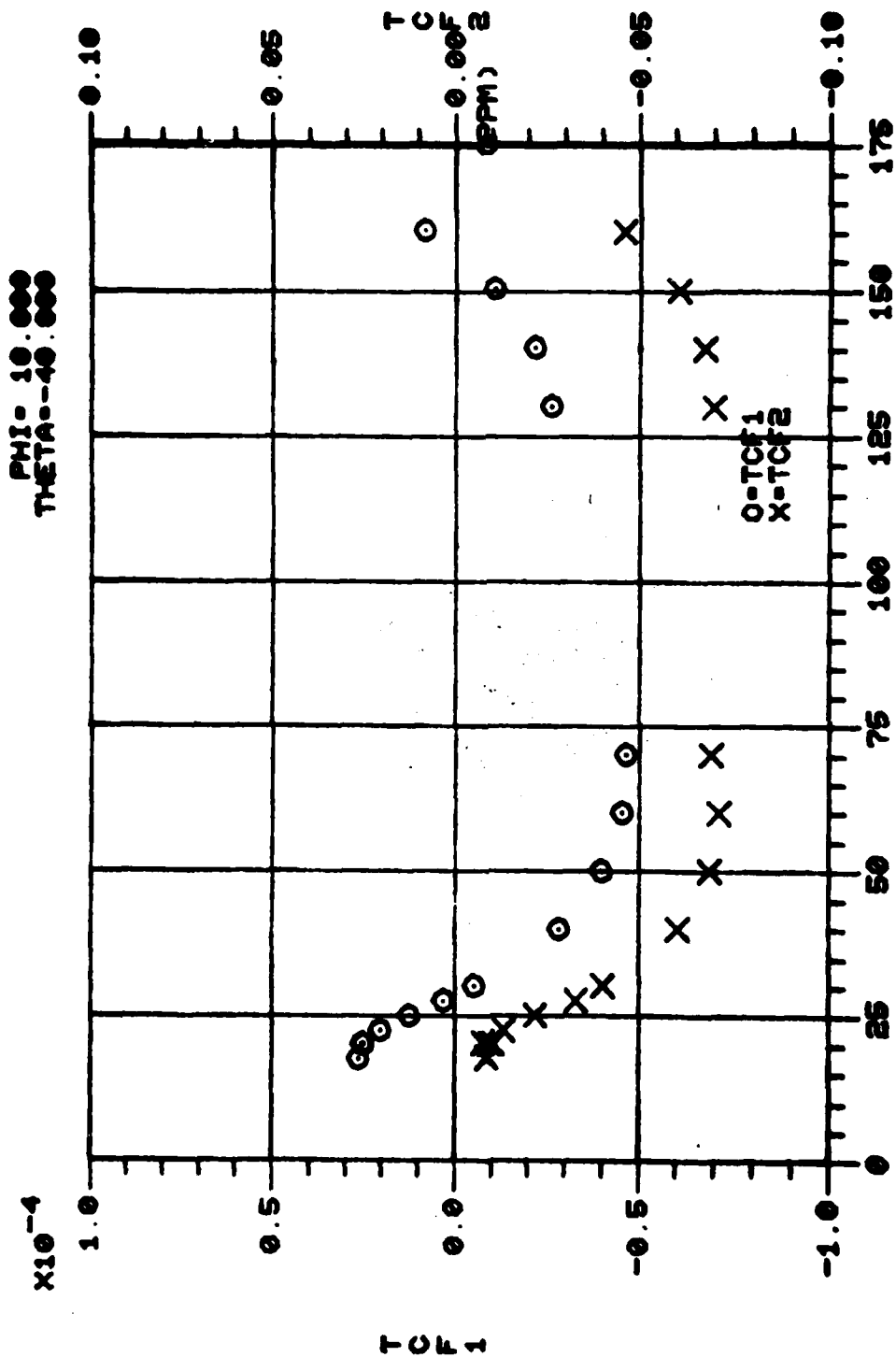


Figure 4. Calculated Values of TCF⁽¹⁾ Versus Propagation Angles (Sheet 47 of 71)



PSI

Figure 4. Calculated Values of TCF⁽¹⁾ Versus Propagation Angles (Sheet 48 of 71)

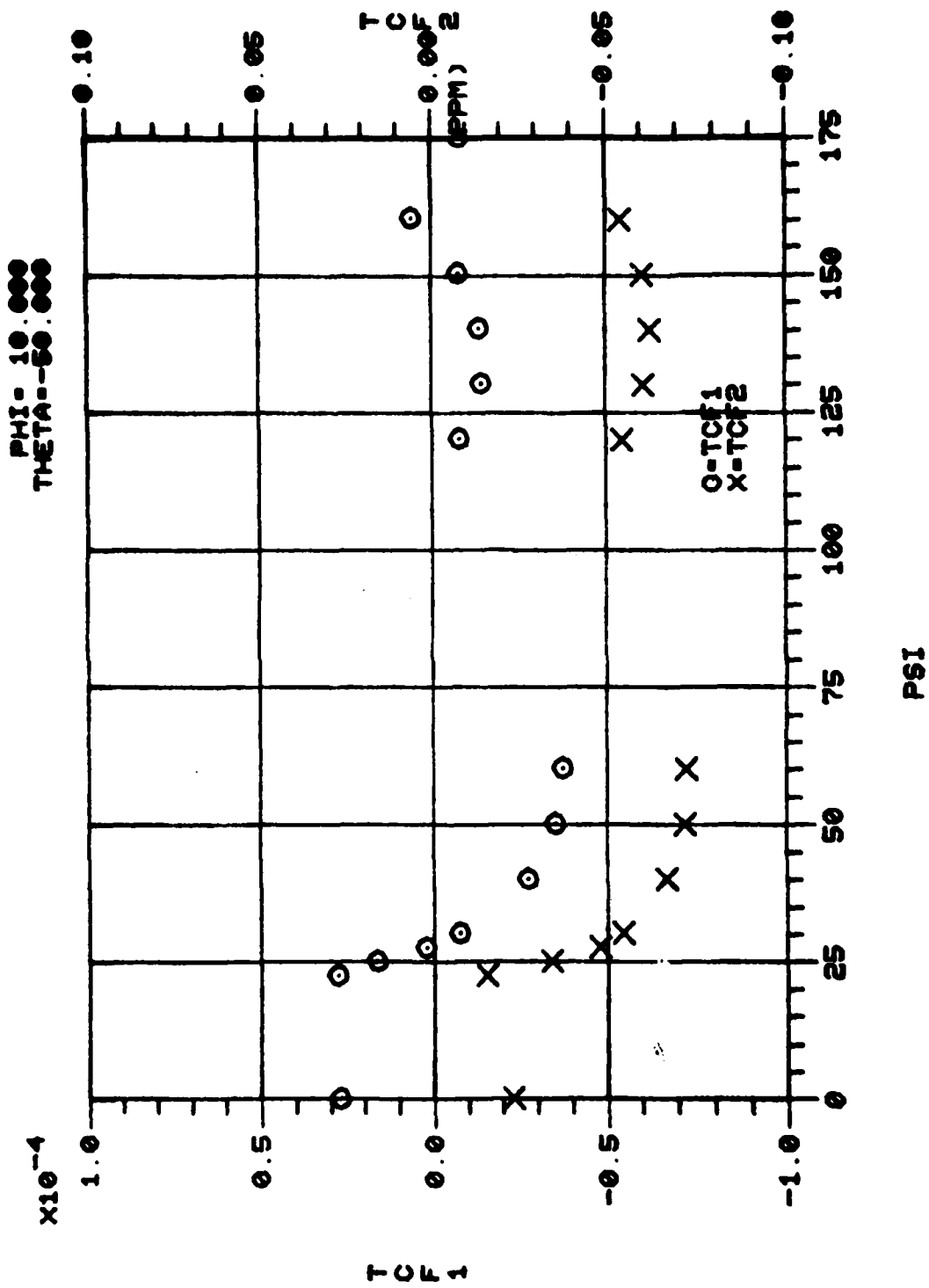


Figure 4. Calculated Values of TCF⁽¹⁾ Versus Propagation Angles (Sheet 49 of 71)

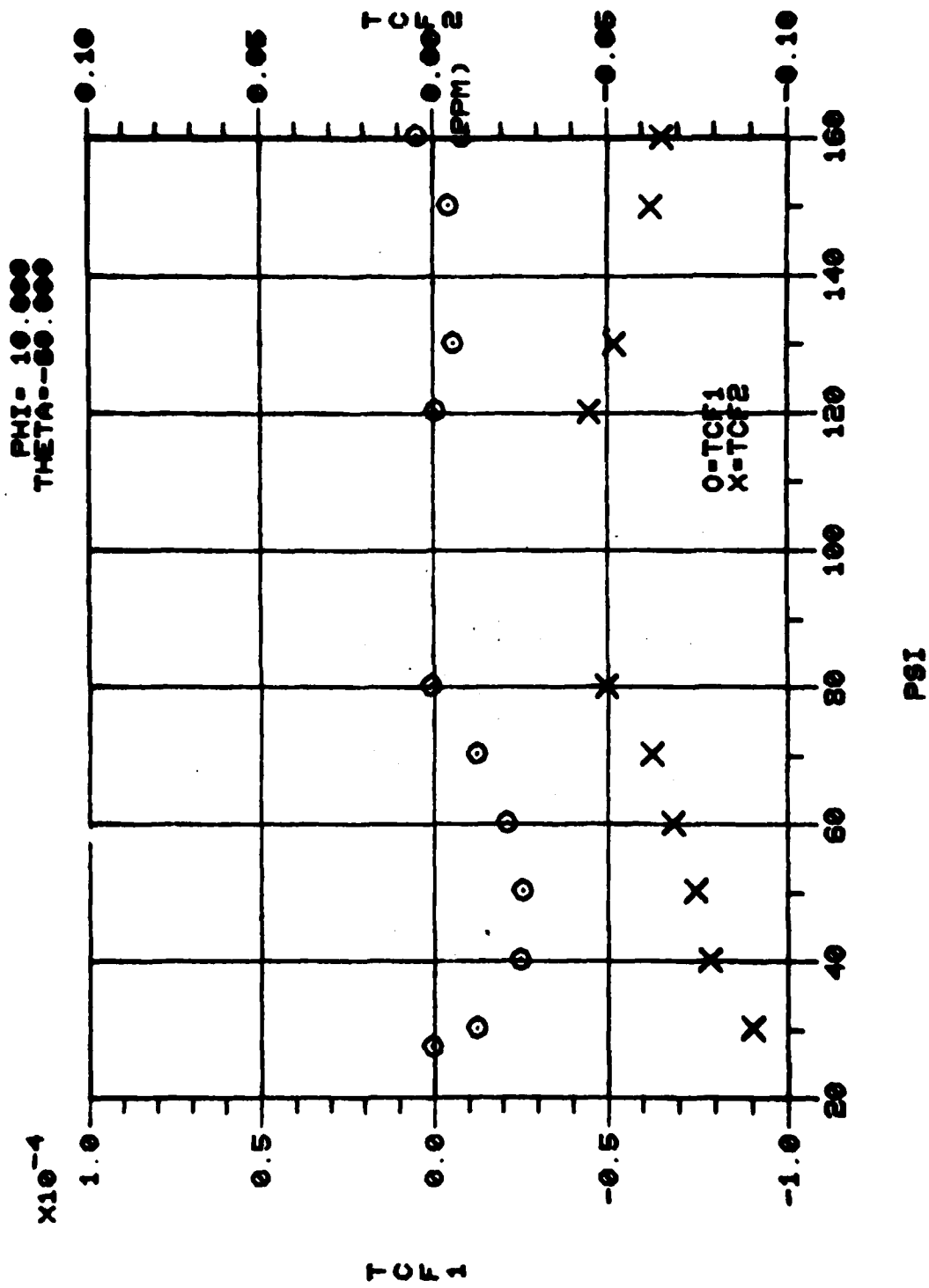


Figure 4. Calculated Values of TCF⁽¹⁾ Versus Propagation Angles (Sheet 50 of 71)

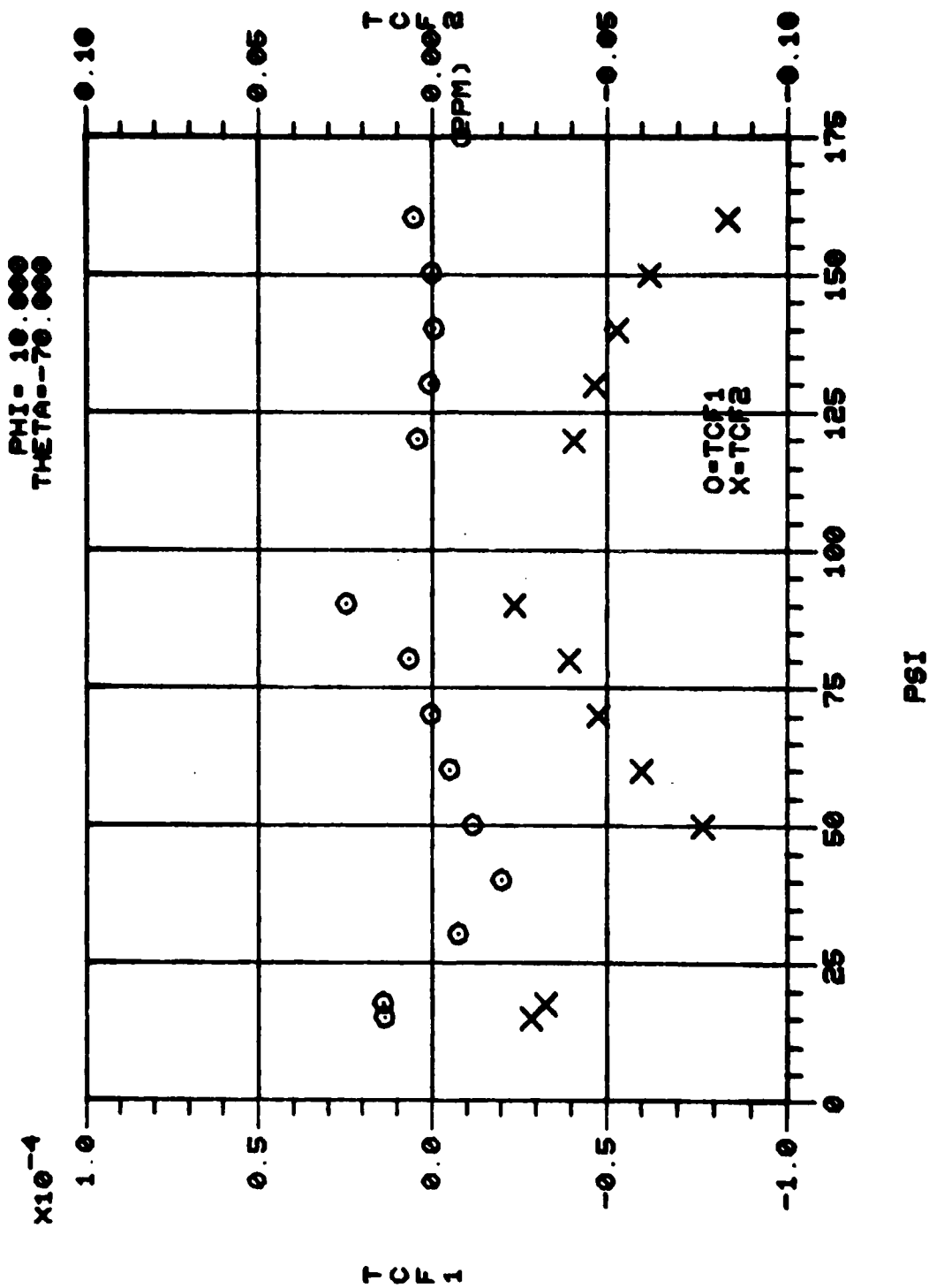
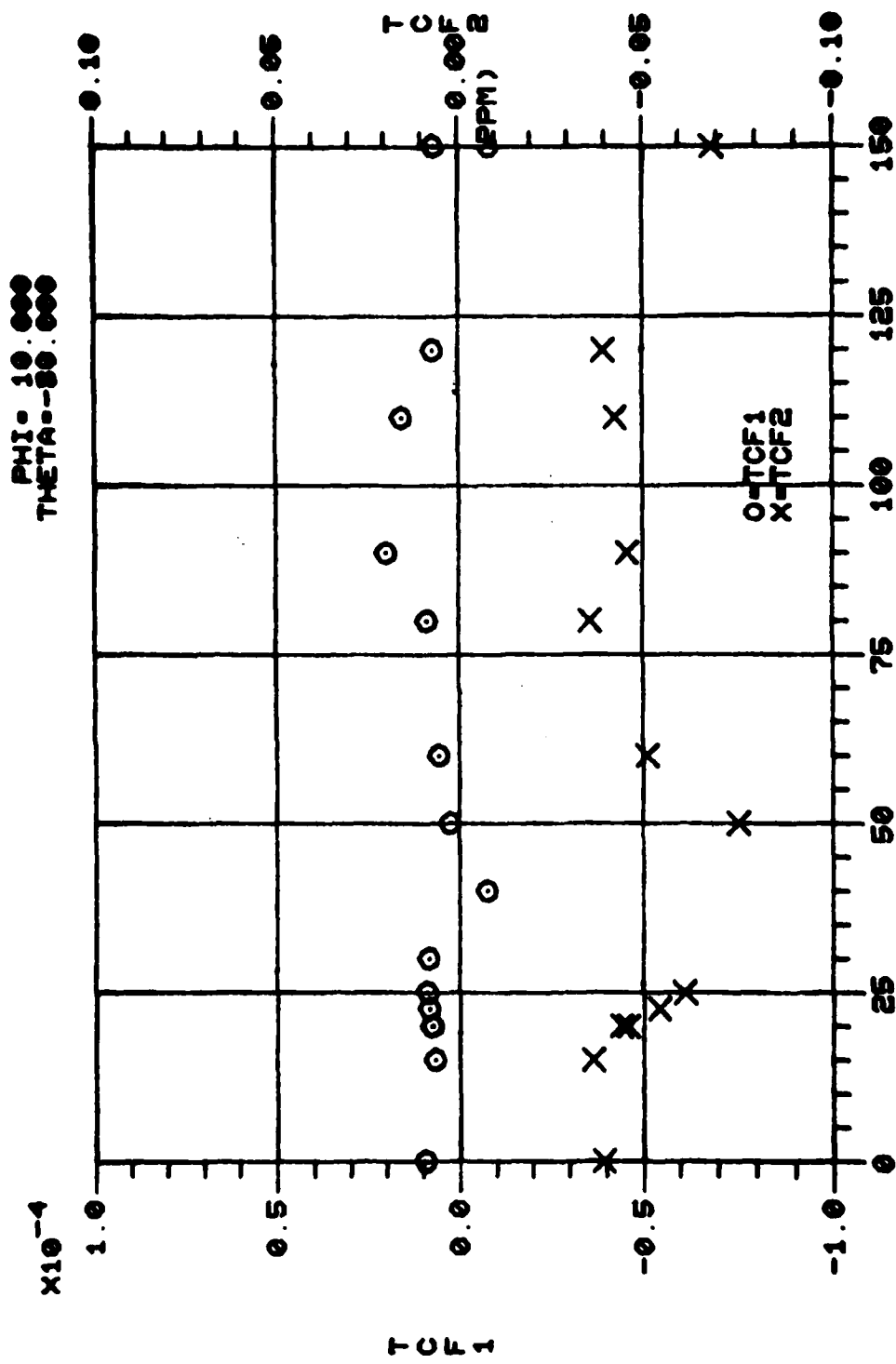


Figure 4. Calculated Values of $TCF^{(1)}$ Versus Propagation Angles (Sheet 51 of 71)



PSI
 Figure 4. Calculated Values of TCF⁽¹⁾ Versus Propagation Angles (Sheet 52 of 71)

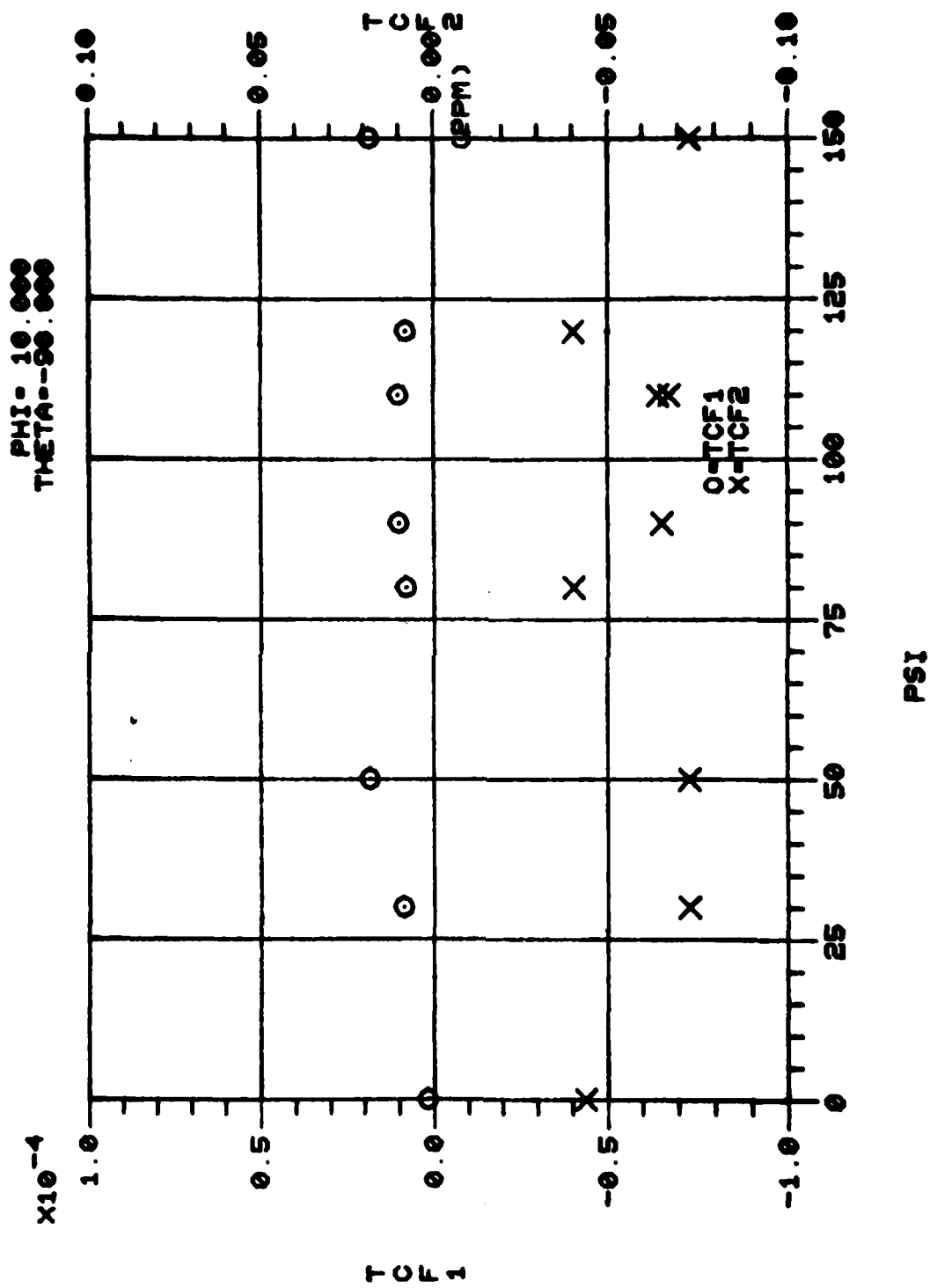


Figure 4. Calculated Values of TCF⁽¹⁾ Versus Propagation Angles (Sheet 53 of 71)

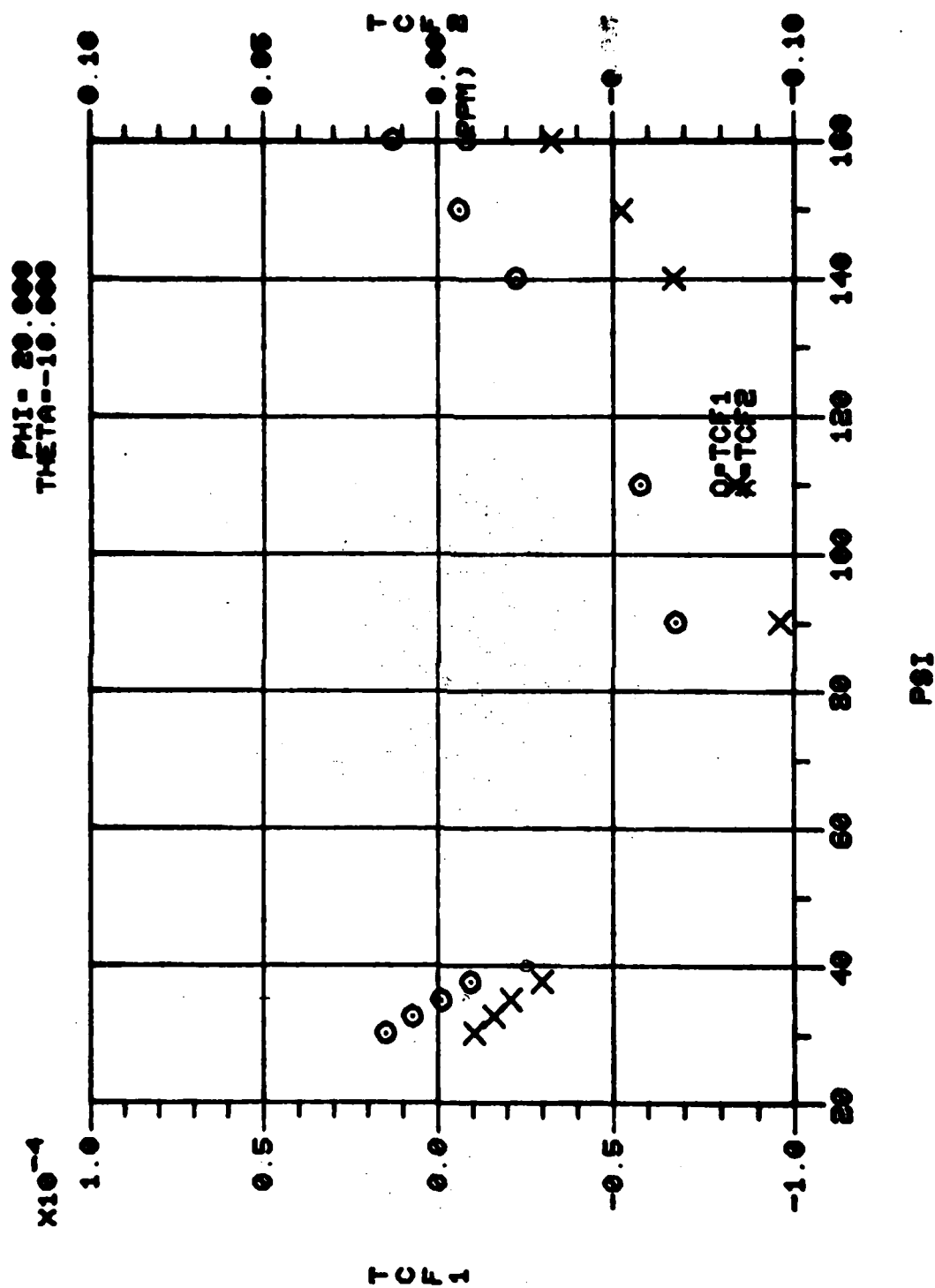


Figure 4. Calculated Values of TCF⁽¹⁾ Versus Propagation Angles (Sheet 54 of 71)

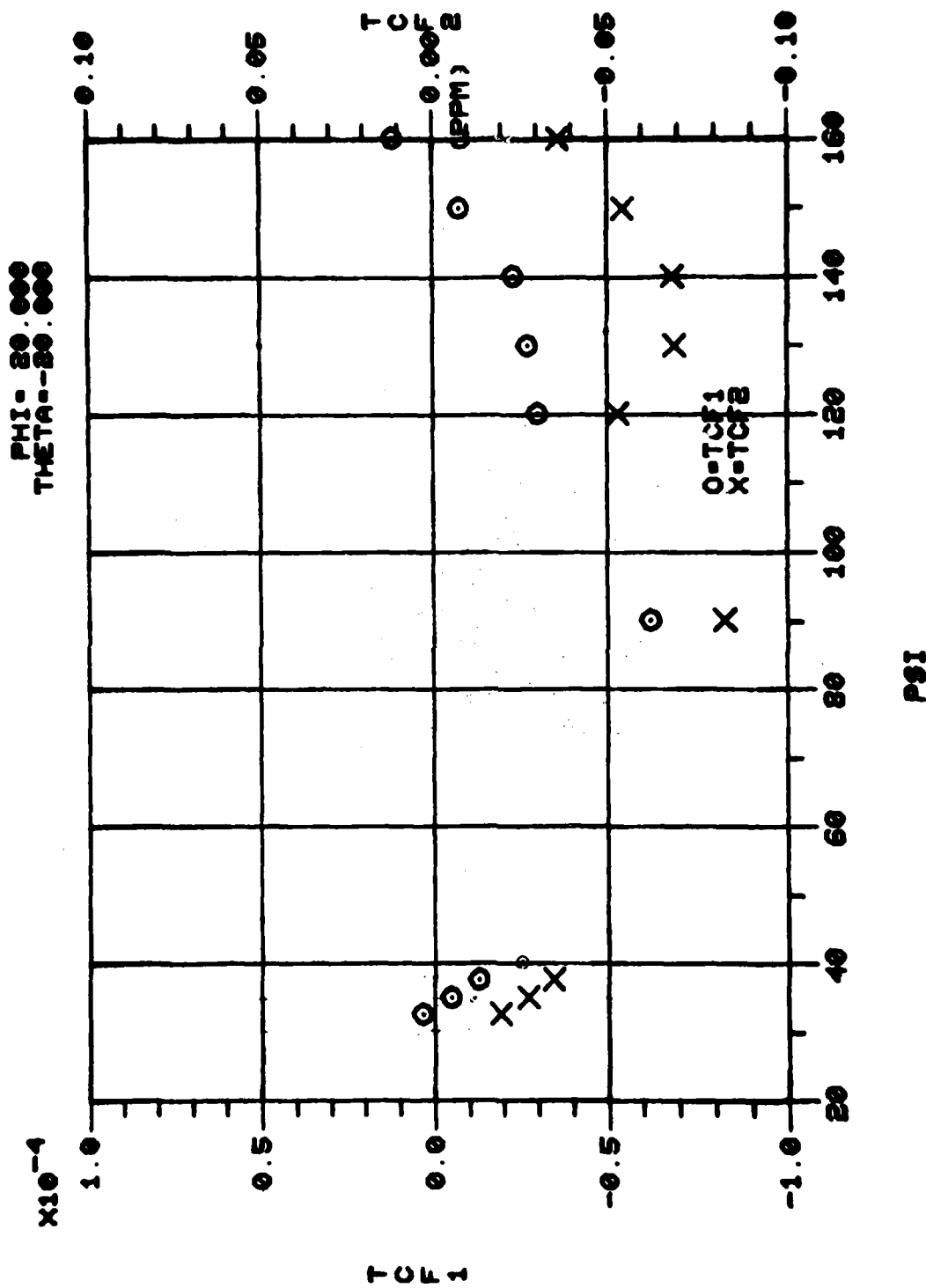


Figure 4. Calculated Values of TCF⁽¹⁾ Versus Propagation Angles (Sheet 55 of 71)

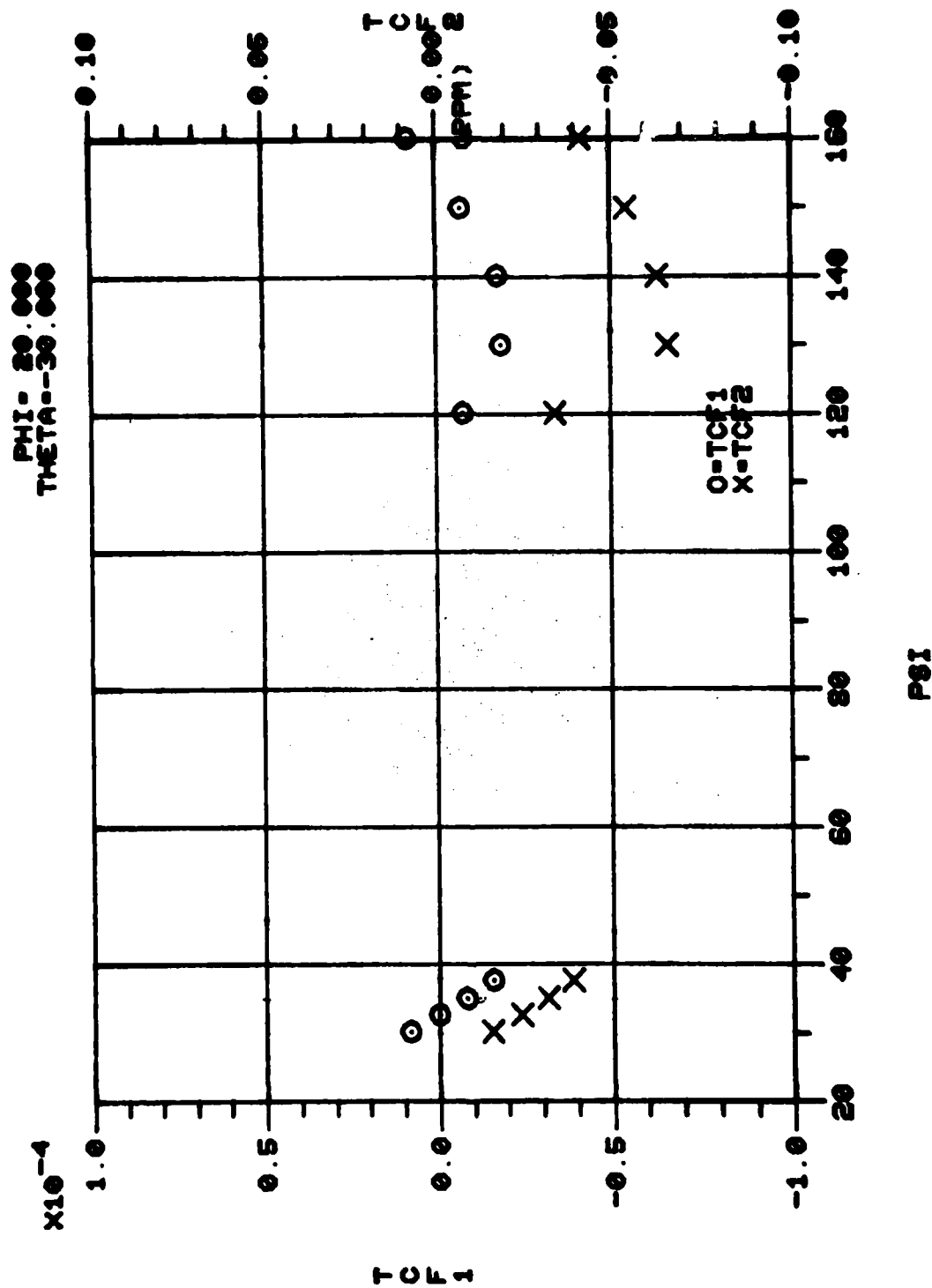


Figure 4. Calculated Values of TCF⁽¹⁾ Versus Propagation Angles (Sheet 56 of 71)

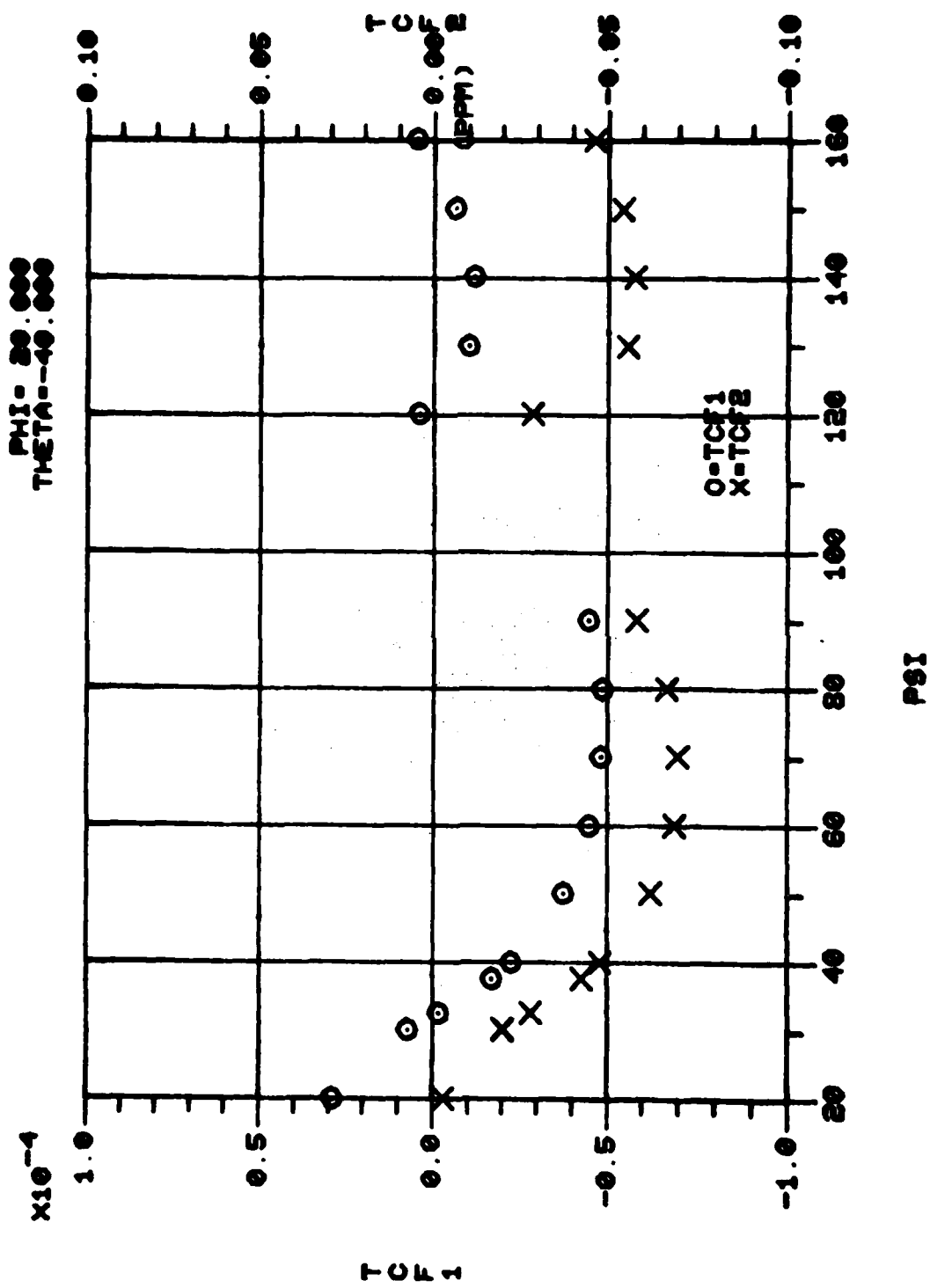
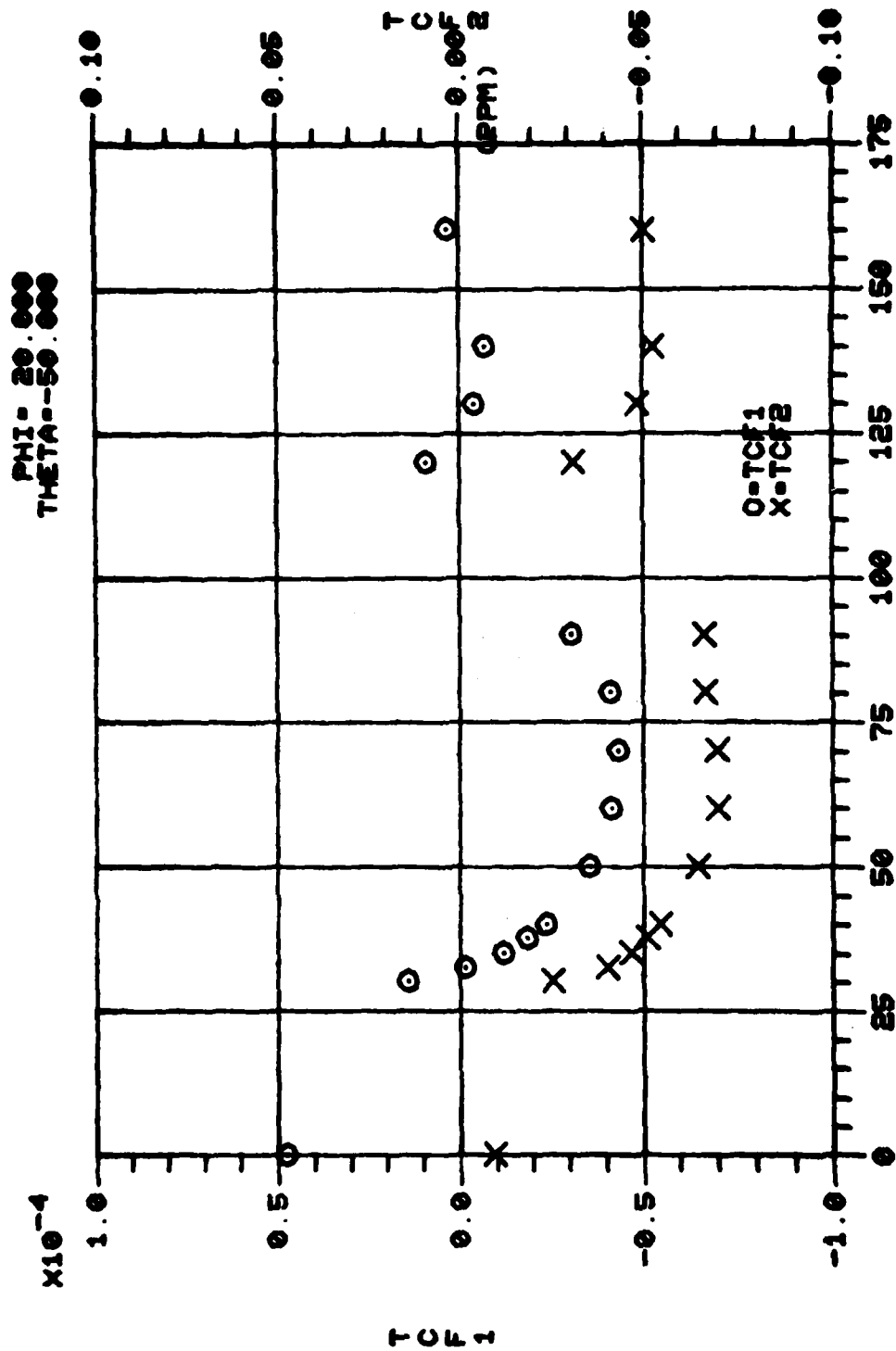


Figure 4. Calculated Values of $TCF^{(1)}$ Versus Propagation Angles (Sheet 57 of 71)



PSI

Figure 4. Calculated Values of TCF⁽¹⁾ Versus Propagation Angles (Sheet 58 of 71)

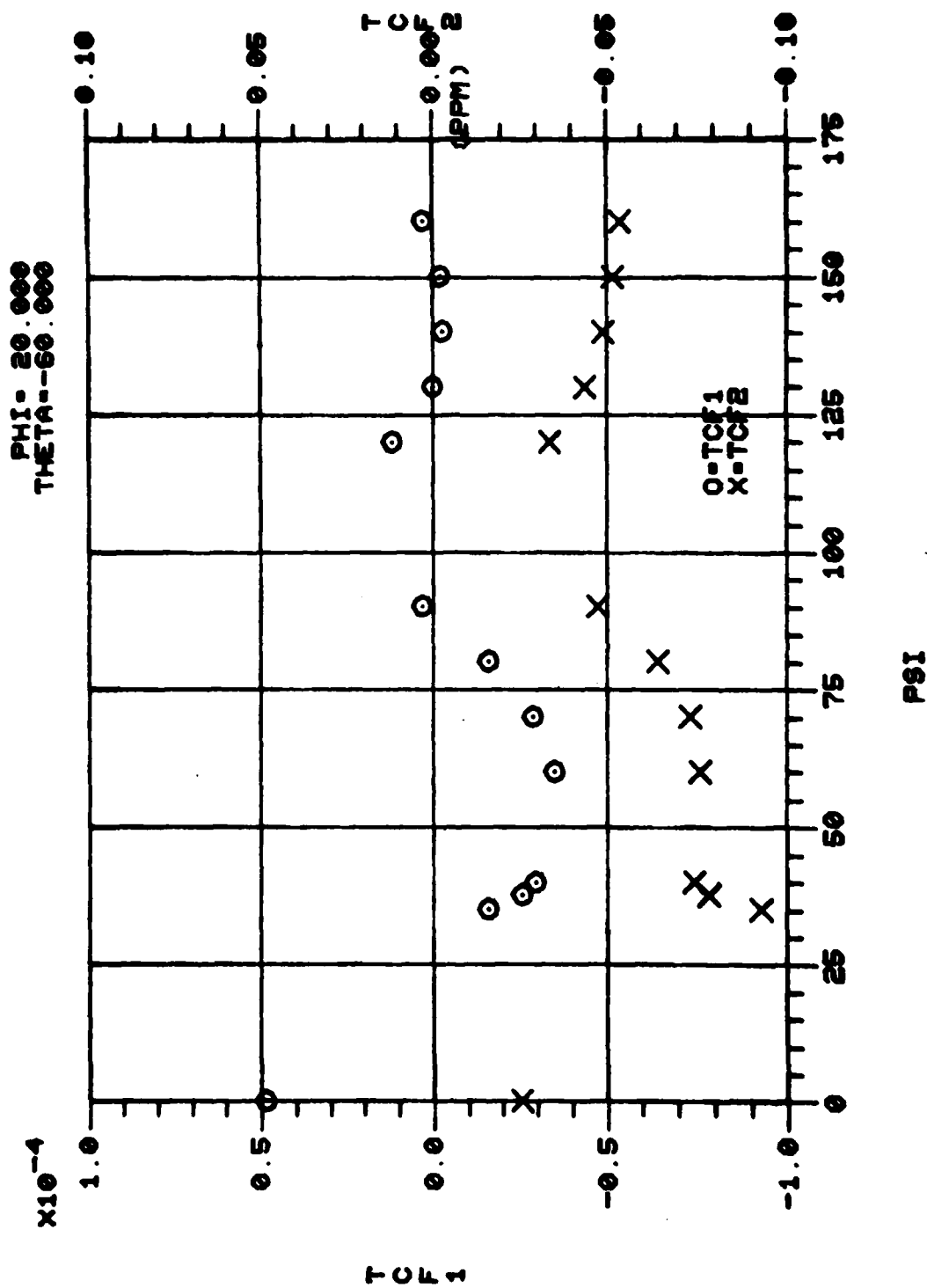


Figure 4. Calculated Values of TCF⁽¹⁾ Versus Propagation Angles (Sheet 59 of 71)

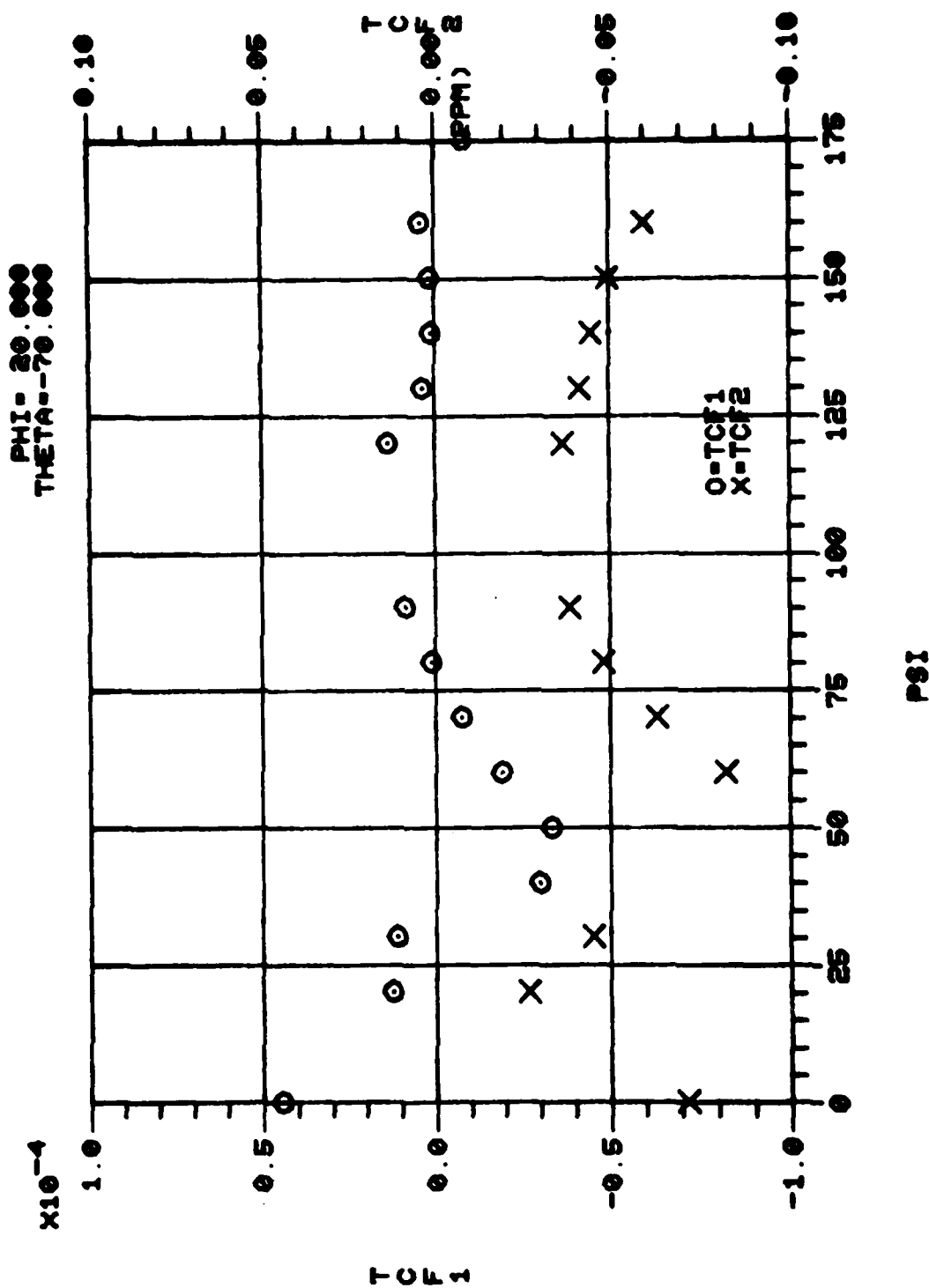
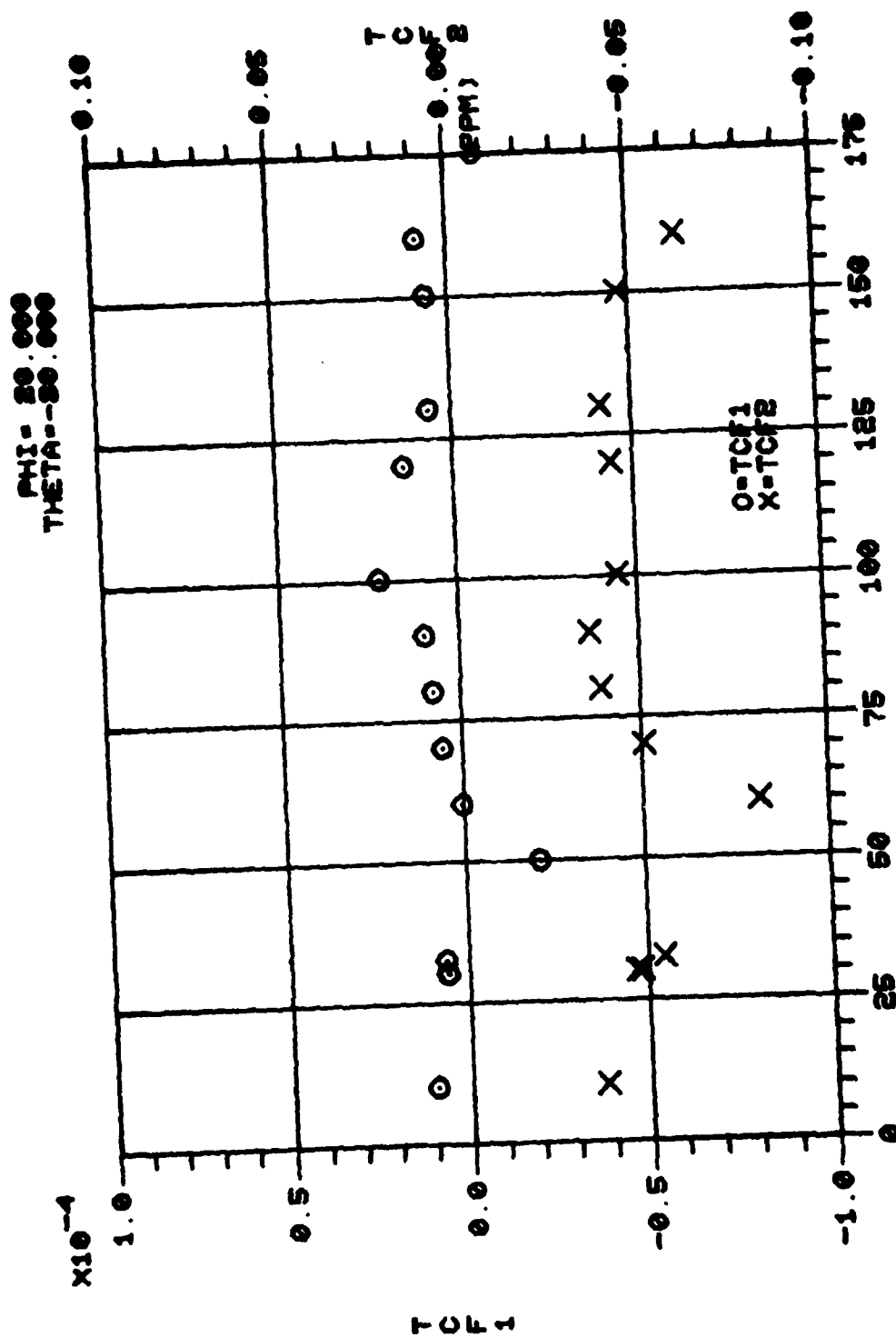


Figure 4. Calculated Values of TCF⁽¹⁾ Versus Propagation Angles (Sheet 60 of 71)



PSI
 Figure 4. Calculated Values of TCF⁽¹⁾ Versus Propagation Angles (Sheet 61 of 71)

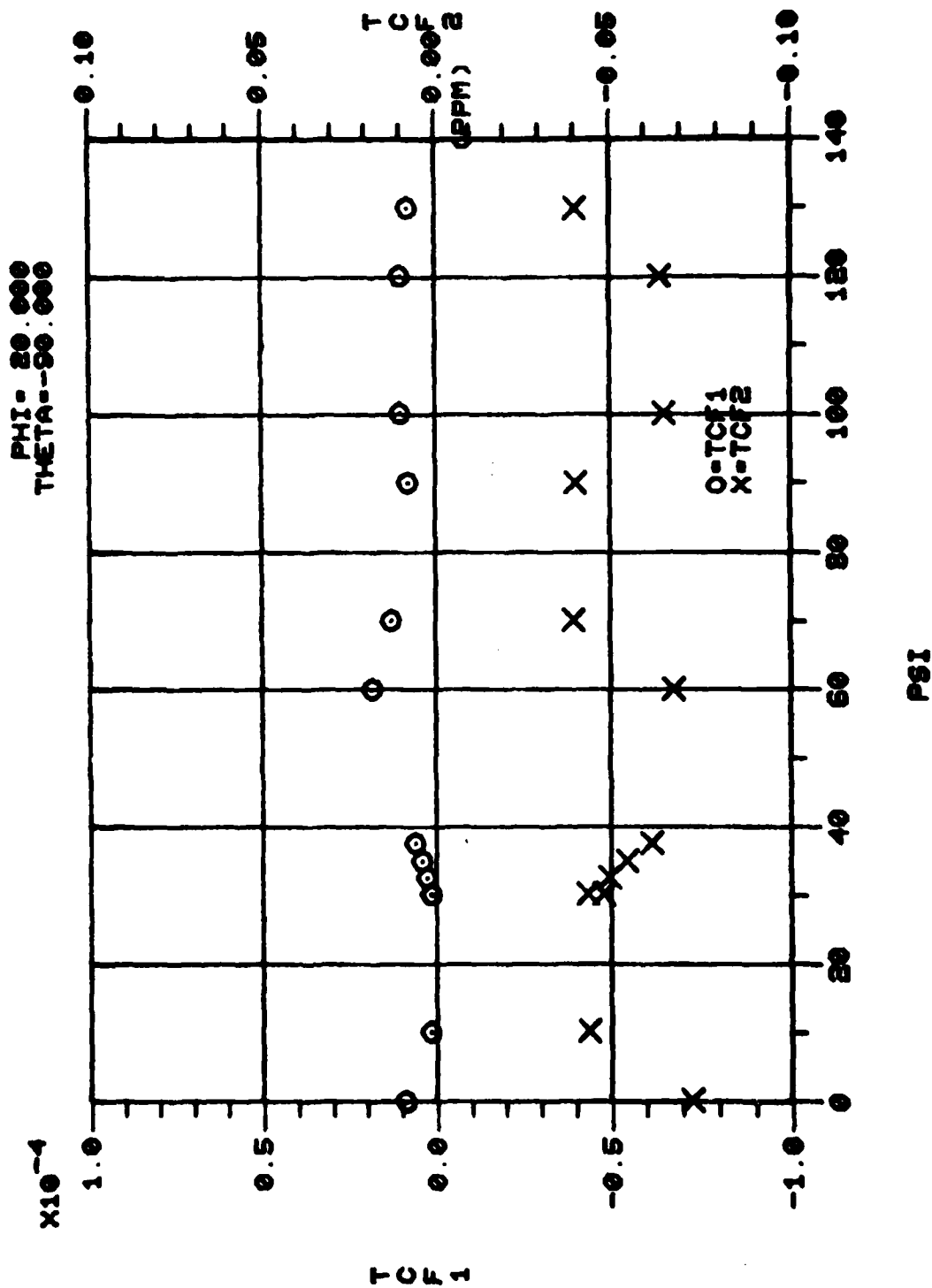


Figure 4. Calculated Values of TCF⁽¹⁾ Versus Propagation Angles (Sheet 62 of 71)

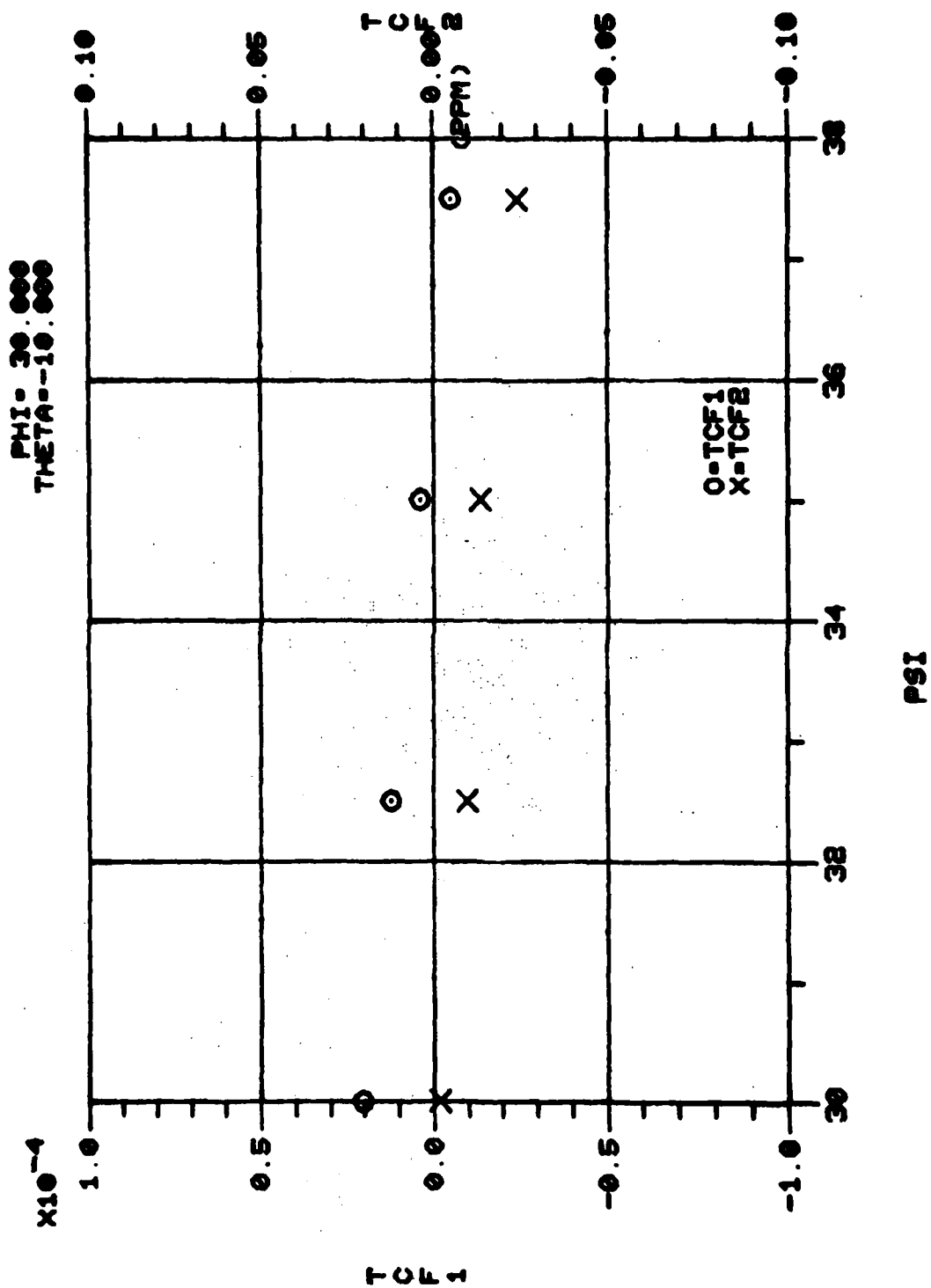


Figure 4. Calculated Values of TCF⁽¹⁾ Versus Propagation Angles (Sheet 63 of 71)

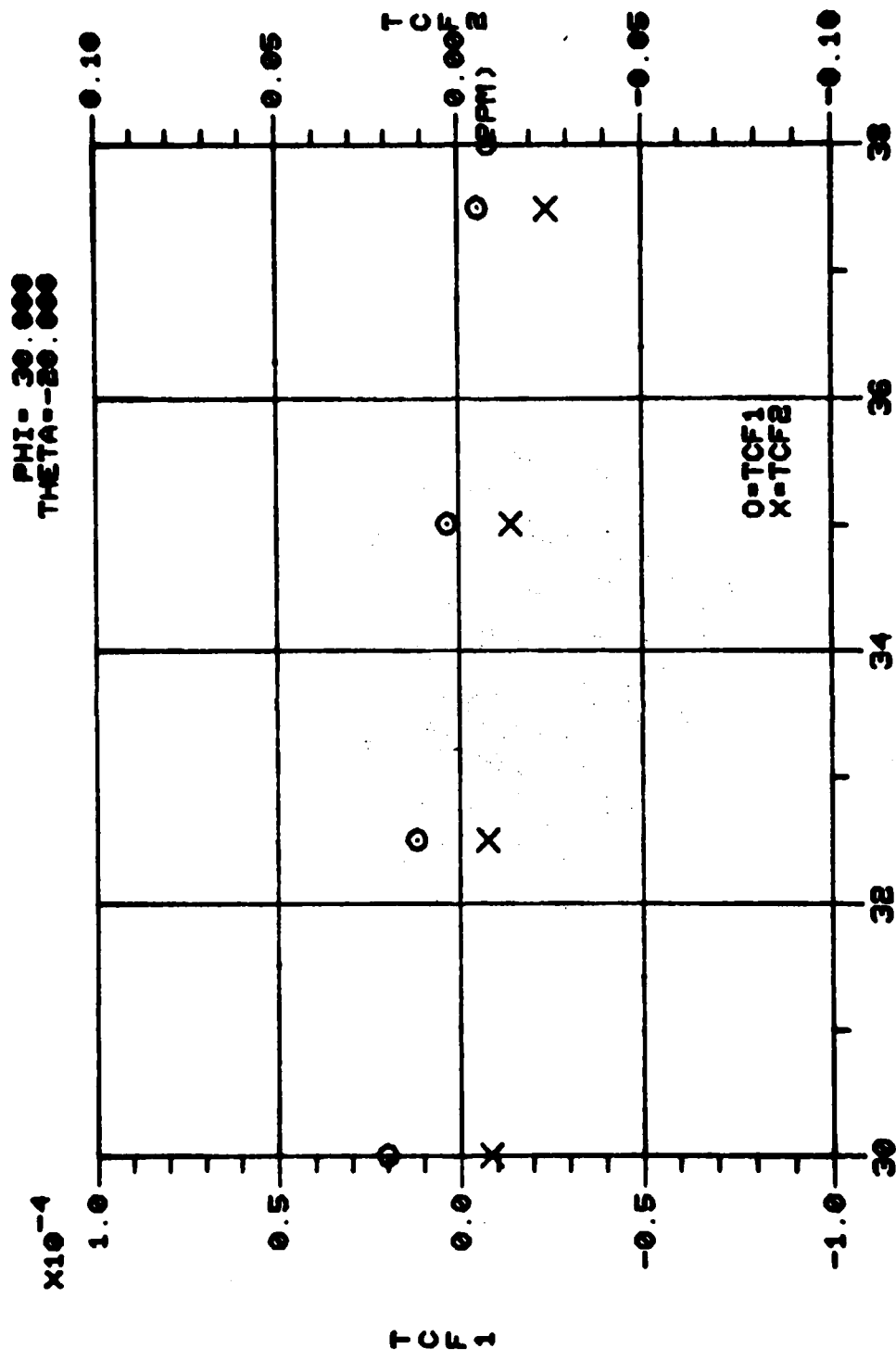


Figure 4. Calculated Values of TCF⁽¹⁾ Versus Propagation Angles (Sheet 64 of 71)

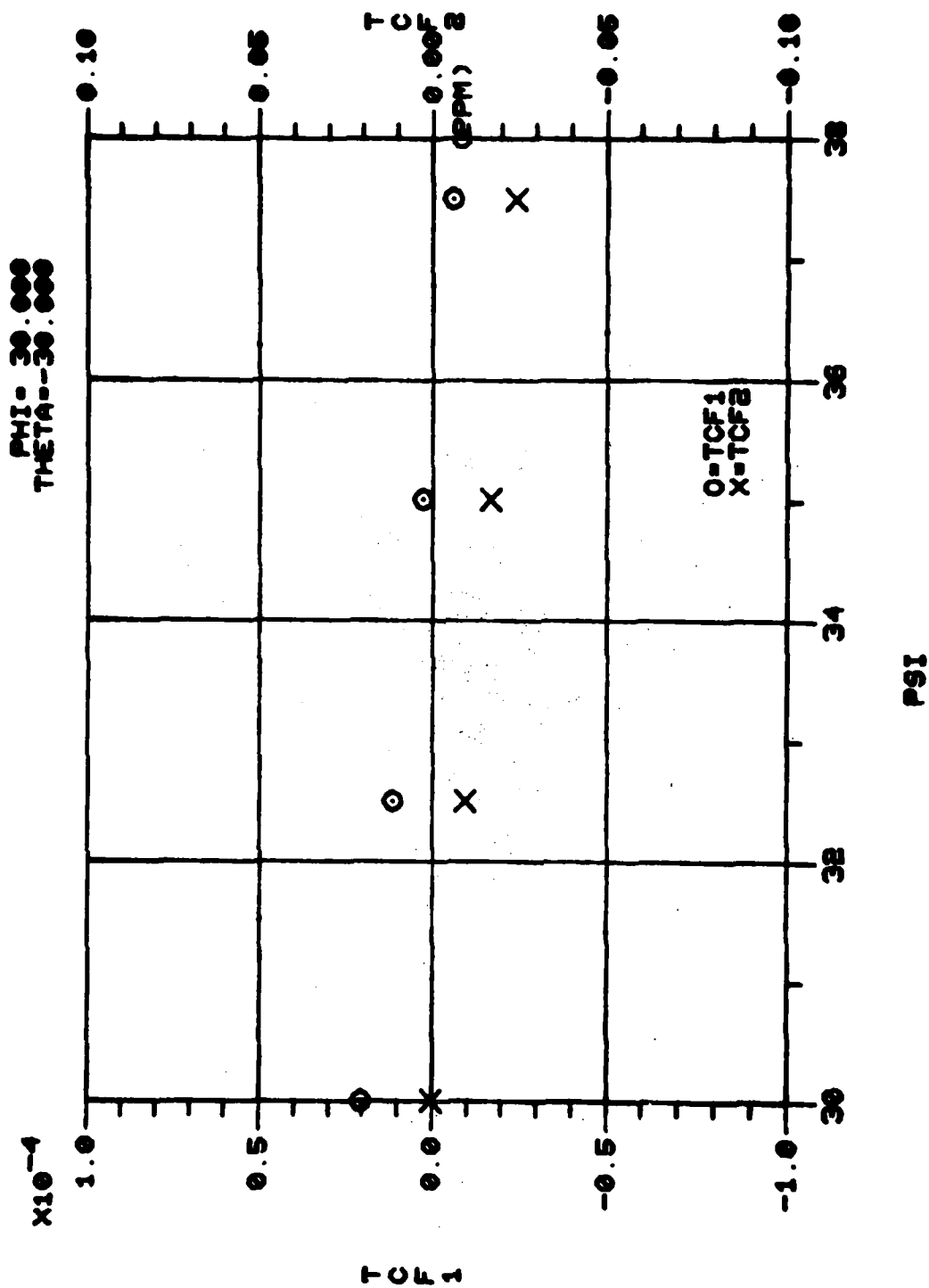


Figure 4. Calculated Values of TCF⁽¹⁾ Versus Propagation Angles (Sheet 65 of 71)

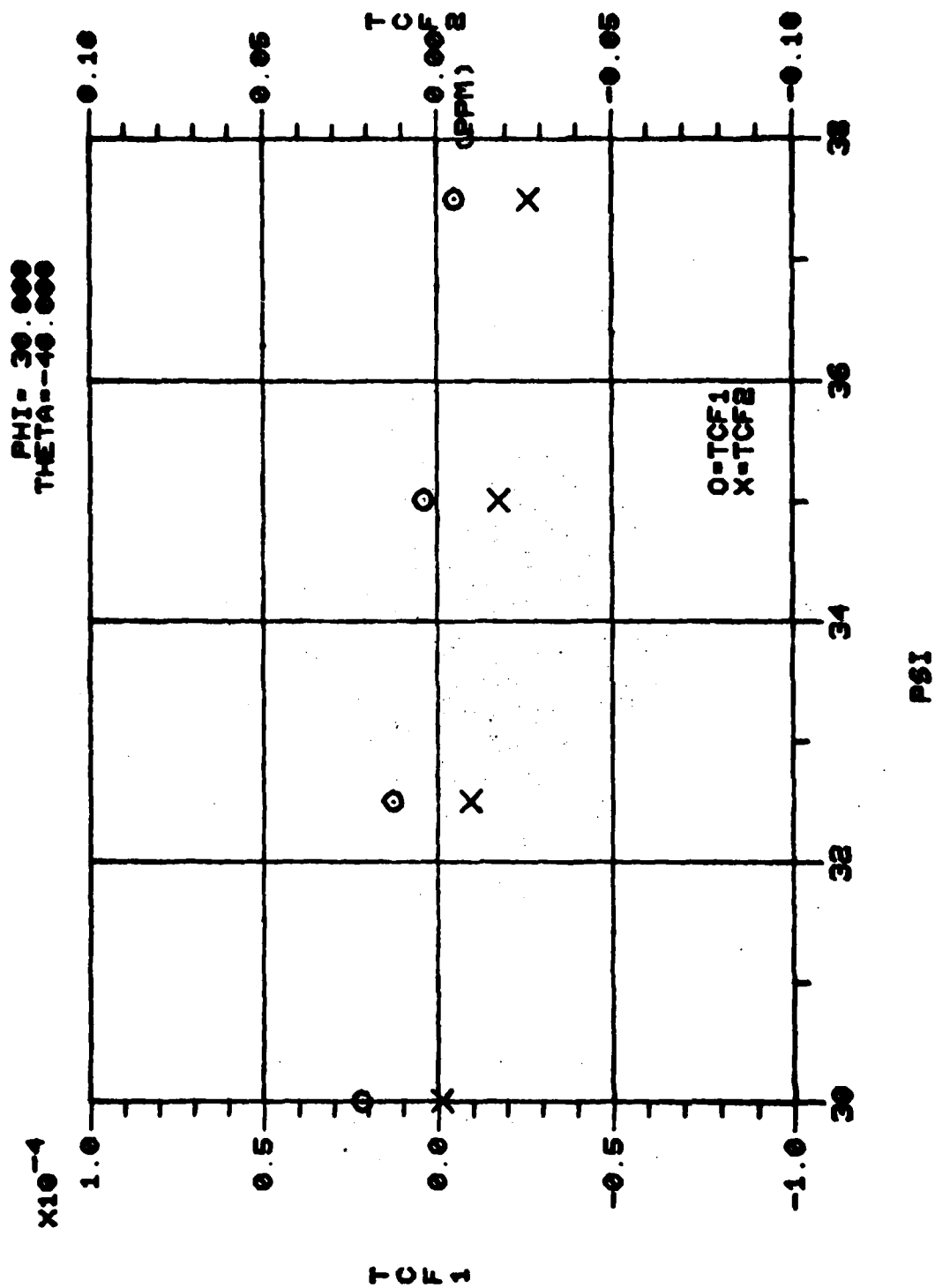


Figure 4. Calculated Values of TCF⁽¹⁾ Versus Propagation Angles (Sheet 66 of 71)

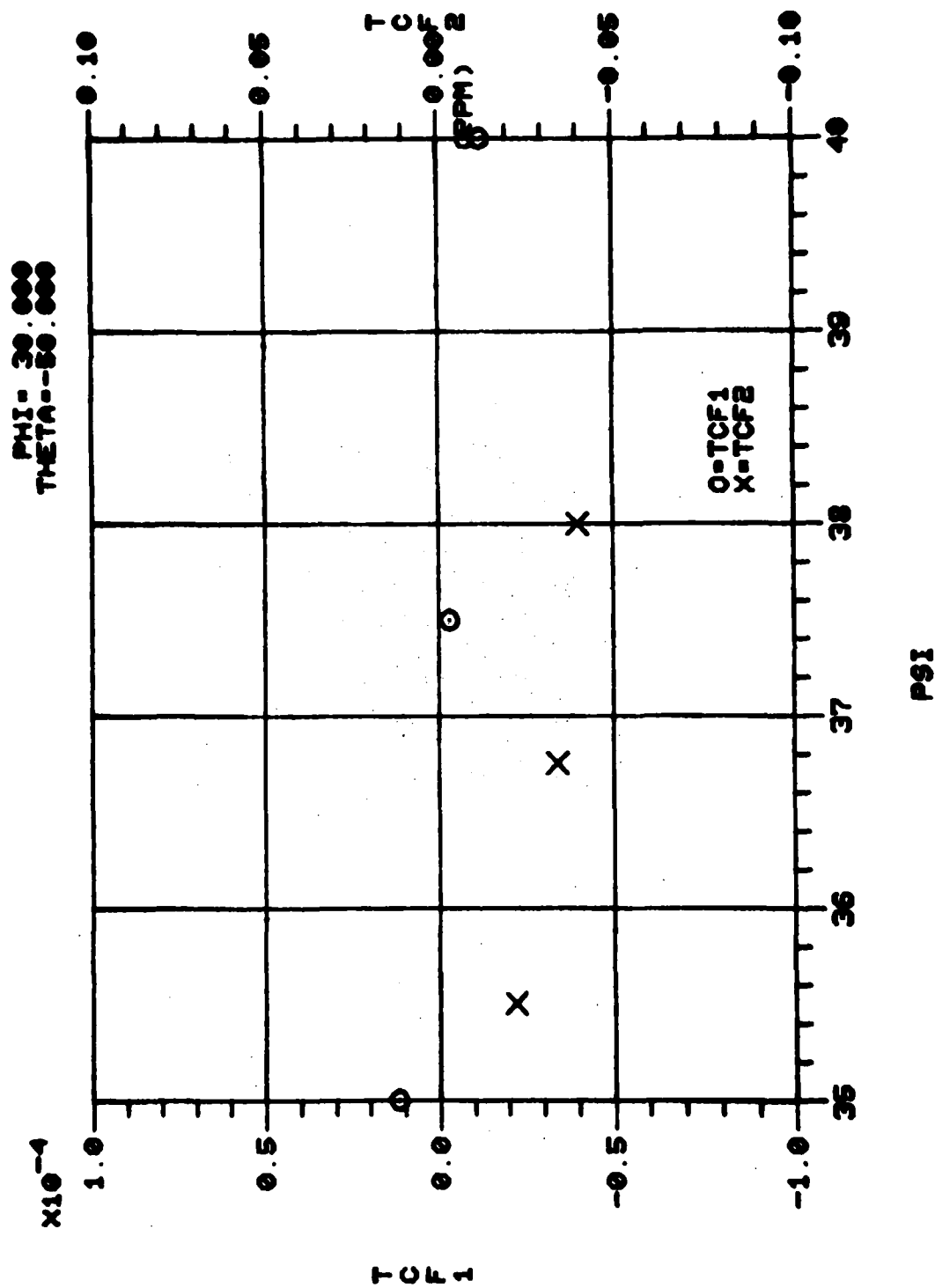


Figure 4. Calculated Values of $TCF^{(1)}$ Versus Propagation Angles (Sheet 67 of 71)

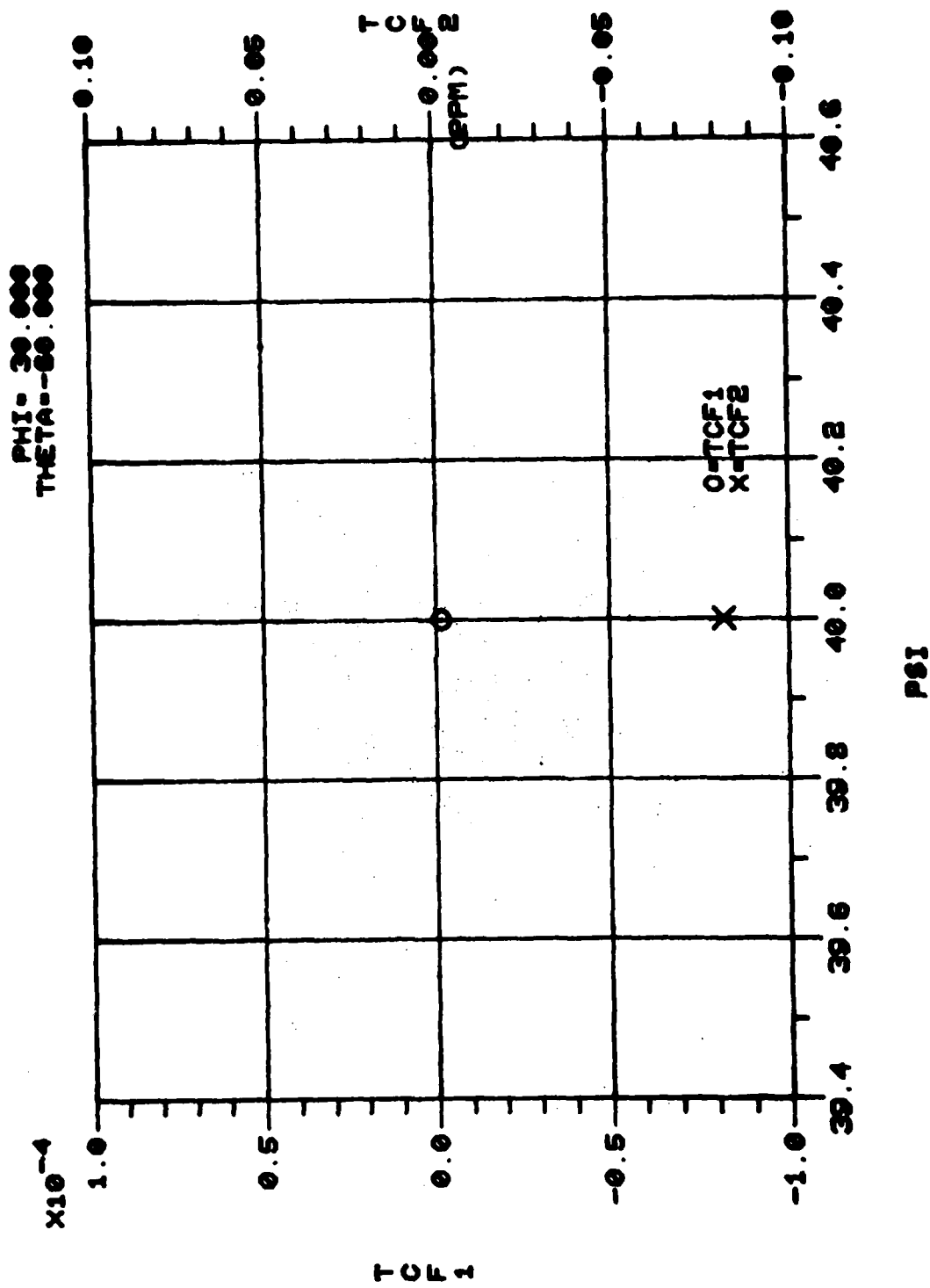


Figure 4. Calculated Values of TCF⁽¹⁾ Versus Propagation Angles (Sheet 68 of 71)

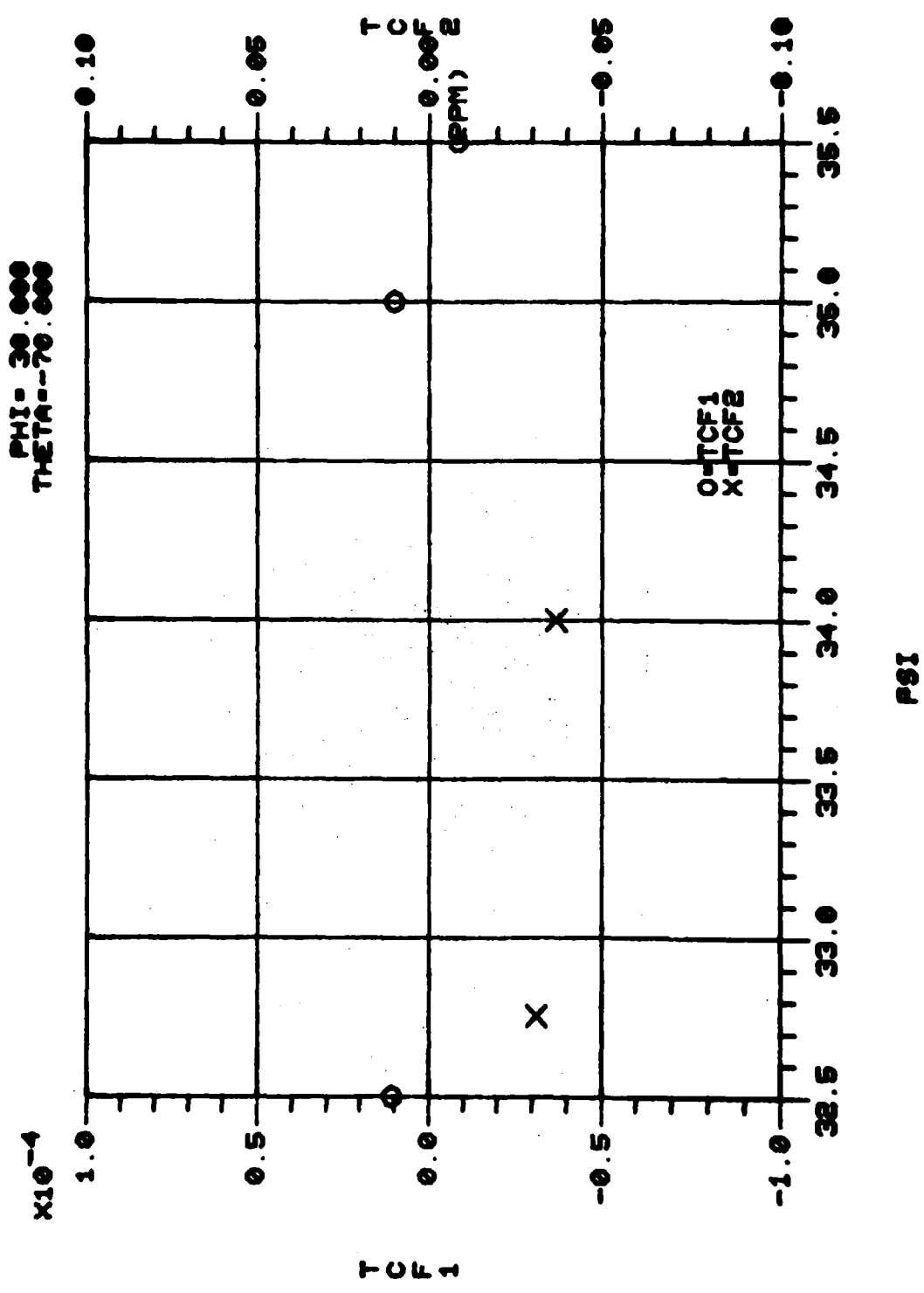


Figure 4. Calculated Values of TCF⁽¹⁾ Versus Propagation Angles (Sheet 69 of 71)

PHI = 30.000
 THETA = -20.000

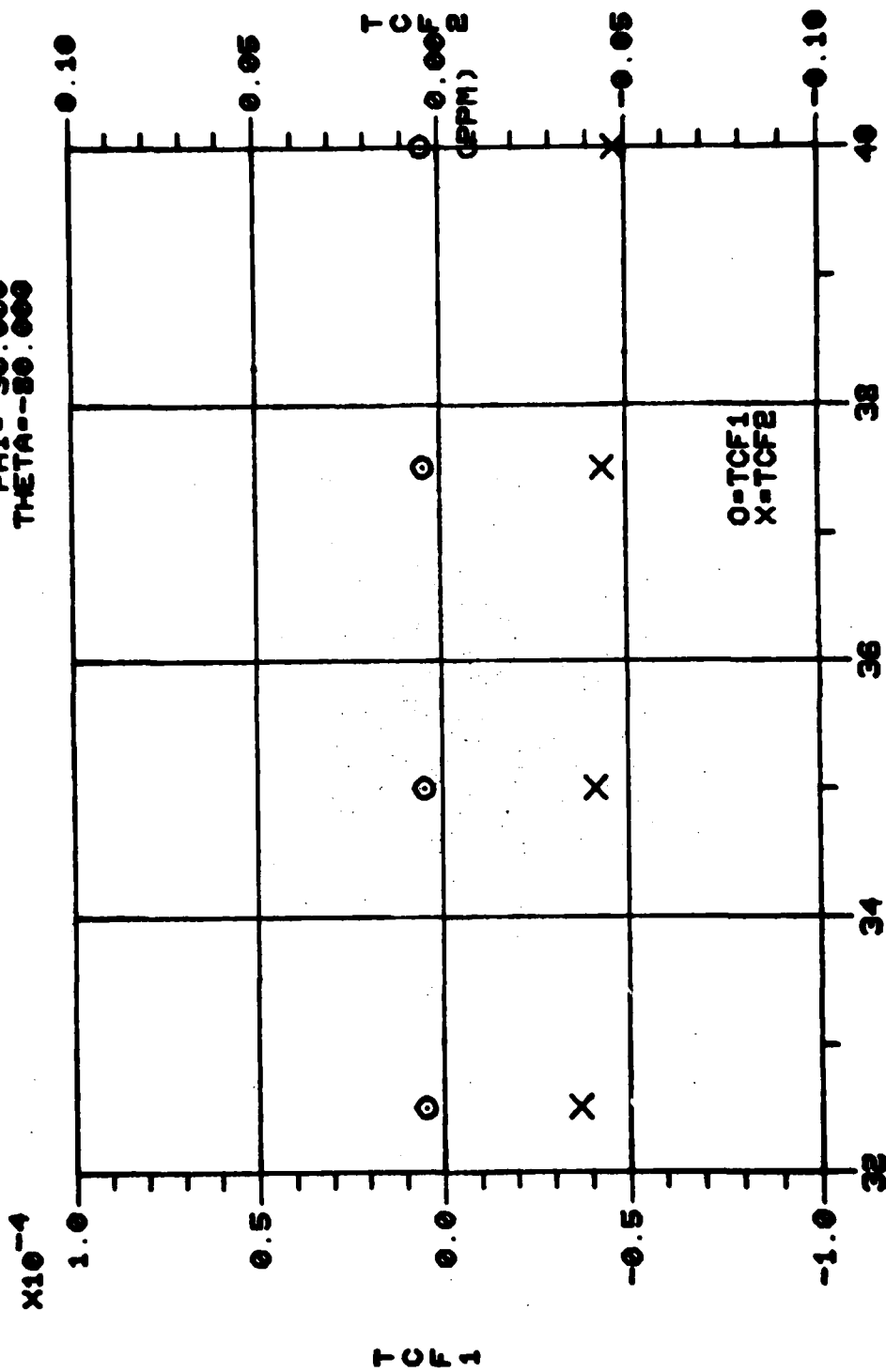
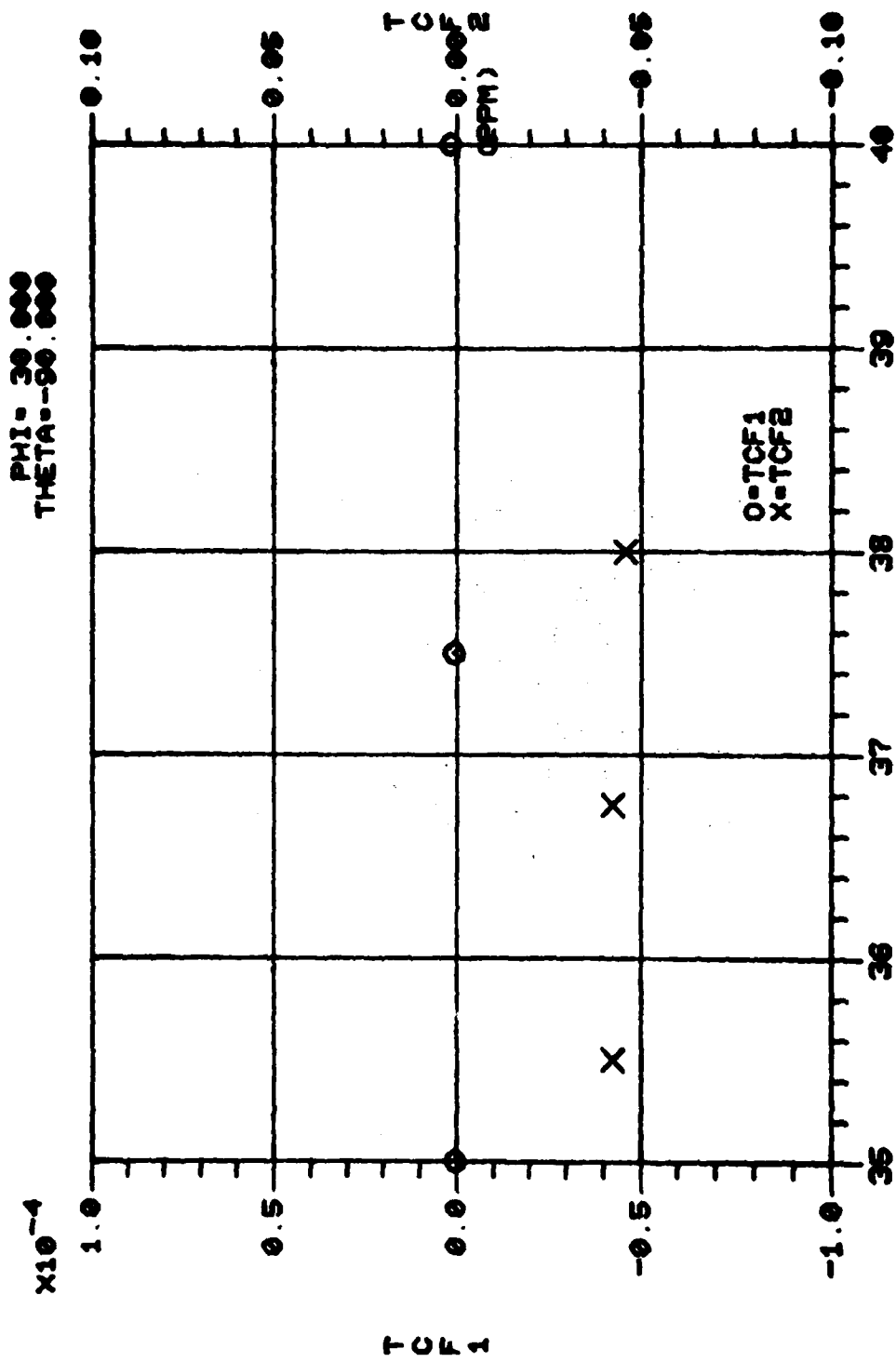


Figure 4. Calculated Values of TCF⁽¹⁾ Versus Propagation Angles (Sheet 70 of 71)



PSI
Figure 4. Calculated Values of TCF⁽¹⁾ Versus Propagation Angles (Sheet 71 of 71)

Calculations were performed on a $10^\circ \times 10^\circ \times 10^\circ$ grid over the angular ranges $0 \leq \text{PHI} \leq 30^\circ$, $0 \leq \text{PSI} \leq 180^\circ$, and $-90^\circ \leq \text{THETA} \leq 90^\circ$. These angular ranges, due to the symmetry of quartz, include all possible angular orientations. These initial calculations defined the "angular volumes" of low TCF orientations. Calculations were then performed on a $2.5^\circ \times 2.5^\circ \times 2.5^\circ$ grid near promising orientations. In this way, the entire angular range was explored and a large computer-based data file built. Maps of first and second order TCF's are shown in Figure 5. Zero first order TCF contours are drawn. In addition, contours of the second order TCF are drawn and shaded in areas where the second order TCF is less than $0.01 \text{ PPM}/^\circ\text{C}^2$. This represents a substantial improvement over ST quartz, for which the second order for TCF is approximately $0.03 \text{ PPM}/^\circ\text{C}^2$. Where data points were missing, lines were connected by interpolation.

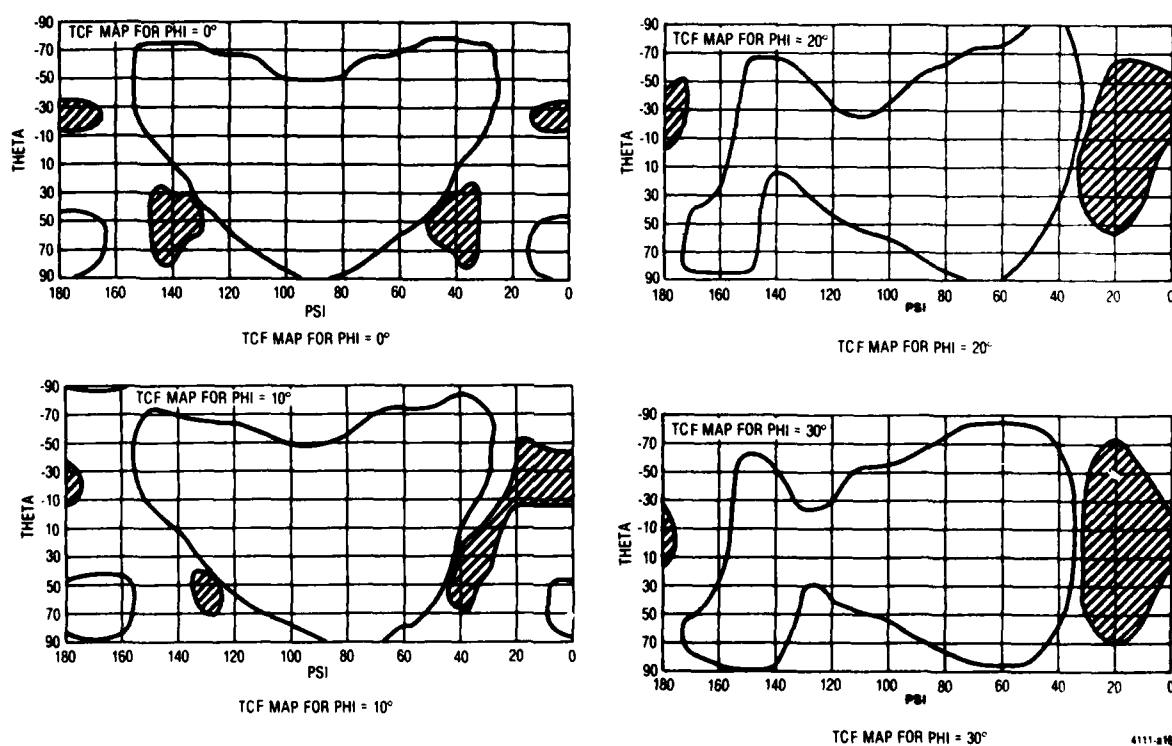


Figure 5. TCF Map of SAW Device on Quartz

Despite the number and density of points at which the first and second order TCFs were calculated, wherever $\text{TCF}^{(1)}$ was found to be less than or equal to zero, we found $\text{TCF}^{(2)}$ to be less than 0. The reason for this probably lies in the lack of independence of the crystal constants themselves. Using the volume perturbation approach of Auld¹, one obtains equation A-8 of Appendix A.

¹"Acoustic Fields and Waves in Solids," Auld, B. A., Vol. II, John Wiley & Sons, 1973, N. Y., p. 297.

For small changes in ρ and $c^{(i)}$, one might expect that the TCFs are well correlated with the temperature derivatives of the fundamental constants for Rayleigh waves in quartz. A list of some of the crystal elastic constants¹¹ temperature derivatives is in Table 1.

TABLE 1. CRYSTAL ELASTIC CONSTANTS' TEMPERATURE DERIVATIVES

	TC ⁽¹⁾	TC ⁽²⁾	TC ⁽³⁾
C_{11}	-48.5×10^{-6}	-107×10^{-9}	-70×10^{-12}
C_{12}	-3000	-3050	-1260
C_{13}	-550	-1150	-750
C_{14}	101	-48	-590
C_{33}	-160	-275	-250
C_{44}	-177	-216	-216
C_{66}	178	118	21
ρ	-34.92	-15.9	5.3
α_{11}	13.7	6.5	-1.9
α_{33}	7.5	2.9	-1.5

Figure 6 shows a plot of these values. The correlation is quite high, except for the case of C_{14} and suggests that the TCFs should be correlated also. Plots of $TCF^{(1)}$ and $TCF^{(2)}$ versus angles shown in Figure 4 reflect this correlation.

Of course, if the two TCF surfaces do not intersect to form a line of zero $TCF^{(1)}$ and $TCF^{(2)}$, we must use a slightly different approach to finding temperature stable cuts. The largest variation in constants occurs for C_{12} . As we are interested in the temperature range from -50°C to 100°C , the maximum deviation of T from $T_0 = 25^\circ\text{C}$ is $|T - T_0| = 75^\circ\text{C}$. Calculating the changes in the constant C_{12} for this maximum temperature change gives:

$$\begin{aligned} \frac{1}{C_{12}} | \Delta C_{12}^{(1)} | &= 2.25 \times 10^{-1} \\ \frac{1}{C_{12}} | \Delta C_{12}^{(2)} | &= 1.72 \times 10^{-2} \\ \frac{1}{C_{12}} | \Delta C_{12}^{(3)} | &= 5.32 \times 10^{-4} \end{aligned} \tag{17}$$

¹¹"Higher Order Temperature Coefficients of the Elastic Stiffnesses and Compliances of Alpha-Quartz", Bechmann, Ballato, Lukaszek, Proc. IRE, Aug 1962, pp. 1812-1922.



Figure 6. Temperature Coefficients of the Fundamental Constants of Quartz

AD-A110 663

MOTOROLA INC SCOTTSDALE AZ GOVERNMENT ELECTRONICS DIV

F/6 9/1

DOUBLY ROTATED CUT SAW DEVICES.(U)

JAN 82 D F WILLIAMS, F Y CHO

DAAK20-79-C-0275

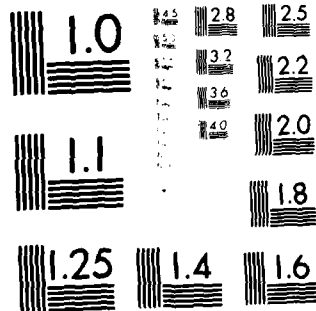
UNCLASSIFIED

DELET-TR-79-0275-F

NL



1106



MICROCOPY RESOLUTION TEST CHART
NATIONAL BUREAU OF STANDARDS-1963-A

Thus the most significant term is the first order term. The second order term is still quite significant but one order of magnitude below the first, while the third order term is almost three orders of magnitude below the first. Since the delay time τ is dependent on the crystal constants, the most significant term should be $TCF^{(1)}$. The least significant term should be $TCF^{(3)}$. After numerous calculations of the TCFs for many orientations, this appears to be the case.

The investigative approach used has been to first locate the surfaces of zero $TCF^{(1)}$ (the most significant term) with the finite difference program. Near these surfaces of zero $TCF^{(1)}$, low values of $TCF^{(2)}$ are sought, using already calculated results of the finite difference programs. Where low values of $TCF^{(2)}$ have been found, the perturbation approach was used to more accurately locate the zero $TCF^{(1)}$ surface, this being the most significant term in the total temperature dependence. $TCF^{(3)}$'s are then calculated to assure that their effect on the total temperature dependence is small. To date, this has always been found to be the case.

(8) Results of the Investigative Approach

Table 2 consists of a summary of the results of using the investigative approach described in paragraph (7) above. There are three areas where low TCF cuts have been located. These areas are centered near (YX wlt) 0/27/138, (YX wlt) 7/27/135.5, and (YX wlt) 15/40/40. These orientations have zero $TCF^{(1)}$, calculated by the Sinha and Tiersten approach, with $TCF^{(2)}$ and $TCF^{(3)}$ calculated with Finite Difference approach. These areas were chosen because of zero $TCF^{(1)}$, low $TCF^{(2)}$, and a low $TCF^{(3)}$ which can be mostly cancelled out by the first order TCF if the propagation direction is slightly rotated away from the zero $TCF^{(1)}$ direction. Then the $TCF^{(2)}$ term will dominate the performance characteristics. The angular resolution in these areas is $1^\circ \times 1^\circ \times 1^\circ$. The cuts potentially have one half to one third the temperature coefficients of ST-Cut quartz.

TABLE 2. PROPAGATION CHARACTERISTICS OF SELECTED ORIENTATIONS

Angles of ZTCF ⁽¹⁾ , Degrees (S & T's Program)			TCF ⁽²⁾ /°C ² ($\times 10^{-8}$) Finite Difference Program	TCF ⁽³⁾ /°C ³ ($\times 10^{-10}$) Finite Difference Program
Phi	Theta	Psi		
6	26	136.31	-1.4	
6	27	135.93	-1.3	0.67
6	28	135.59	-1.3	0.57
7	26	135.99	-1.5	
7	27	135.64	-1.4	
7	28	135.27	-1.3	0.65
8	26	135.74	-1.4	0.65
8	27	135.36	-1.4	
8	28	134.97	-1.3	
1	26	137.78	-1.2	0.68
1	27	137.48	-1.2	0.65
1	28	137.17	-1.1	0.67
0	26	138.07	-1.2	0.67
0	27	137.78	-1.1	0.68
0	28	137.49	-1.1	0.62
-1	26	138.37	-1.2	0.60
-1	27	138.09	-1.2	0.62
-1	28	137.80	-1.1	0.73
14	39	40.195	-1.0	0.64
14	40	40.415	-1.0	0.66
14	41	40.64	-1.0	0.75
15	39	39.79	-1.0	0.63
15	40	40	-1.0	0.74
15	41	40.23	-1.0	0.73
16	39	39.4	-1.0	0.68
16	40	39.605	-1.0	0.66
16	41	39.825	-1.1	0.60

d. Piezoelectric Coupling Factor

The piezoelectric coupling factor, denoted by k^2 , is a measure of the coupling efficiency for an interdigitated electrode.

We can express k^2 in terms of the interdigital transducer's input conductance¹ as

$$G_{in}(\omega_n) = -\pi^2 \omega_n M^2 W \epsilon_s^{(\infty)2} G_s P_{n-1}^2 (\cos \eta \pi) / K^2 (\cos \eta \pi / 2) \quad (18)$$

where $\omega_n = 2\pi(2n-1)/\lambda s_0$, M is the number of electrode pairs, w is the length of the electrodes, λ is the spatial periodicity of the array, the width of each electrode is $\eta\lambda/2$, $\epsilon_s^{(\infty)}$ is the value of the effective permittivity at zero velocity, K is the complete elliptic integral of the first kind, and P_n are the Legendre polynomials. G_s is the residue of $1/(s|\epsilon_s)$.

k_s^2 is defined by

$$k_s^2 = -2\epsilon_s^{(\infty)} G_s \quad (19)$$

Thus (18) becomes

$$G_{in}(\omega_n) = (1/2) \pi^2 \omega_n M^2 W \epsilon_s^{(\infty)} k_s^2 P_{n-1}^2 (\cos \eta \pi) / K^2 (\cos \eta \pi / 2) \quad (20)$$

and we see that k_s^2 is related to the input conductance and hence to the coupling efficiency. A good approximation to k_s^2 is given by

$$k_s^2 \cong 2(V_0 - V_s)/V_s = 2\Delta V/V \quad (21)$$

where V_s is the shorted Rayleigh wave velocity and V_0 is the free Rayleigh wave velocity.

It is seen that the quantity $\Delta V/V$ is an important parameter as it is a direct measure of the coupling efficiency and conductance of an interdigitated electrode pair on a piezoelectric substrate. Furthermore, $\Delta V/V$ is easily determined once the shorted and free surface problems have been solved. Programs are available for calculating the Rayleigh wave velocity with either shorted or free boundary conditions.

The shorted velocity calculations assumes a massless, perfectly conducting layer on the surface of the crystal. The boundary condition which must be satisfied is that $\phi=0$ at $x_3=0$. The free surface boundary conditions are such that the potential ϕ and the normal component of the displacement, D_3 , are continuous at the surface. Furthermore, ϕ must satisfy Laplace's equation above the surface, resulting in

$$\phi = \phi_0 \exp(-kx_3) \exp(-ik(x_1 - Vt)), \quad (x_3 \geq 0) \quad (22)$$

¹"Surface Wave Filters," Matthews, Herbert, John Wiley & Sons, New York (1977).

In both calculations the mechanical boundary conditions are the same, that there be no force component in the x_3 direction, or

$$T_{31} = T_{32} = T_{33} = 0 \text{ at } x_3 = 0 \quad (23)$$

$\Delta V/V$ for different crystal types with various orientations were calculated. Results have been found to be in good agreement with experiments.

For example, on ST-quartz,

$$V_o = 3.1586 \times 10^3 \text{ m/s}$$

$$V_s = 3.1569 \times 10^3 \text{ m/s} \quad (24)$$

$$\Delta V/V = 5.4 \times 10^{-4}$$

To insure the suitability of the cuts described in paragraph (8) above for SAW applications, the coupling coefficients have been calculated for these cuts and are summarized in Table 3.

TABLE 3. PROPAGATION CHARACTERISTICS OF SELECTED ORIENTATIONS

Angles of ZTCF ⁽¹⁾ , degrees (S & T's program)			Velocity (msec)	K^2 ($\times 10^{-3}$)	Power Flow Angle (Degrees)
Phi	Theta	Psi			
6	26	136.31	3296.84	1.12	-0.3
6	27	135.93	3293.60	1.12	-0.2
6	28	135.59	3290.63	1.12	-0.1
7	26	135.99	3303.33	1.12	-0.5
7	27	135.64	3299.70	1.12	-0.4
7	28	135.27	3296.33	1.12	-0.3
8	26	135.74	3310.15	1.12	-0.7
8	27	135.36	3306.11	1.12	-0.6
8	28	134.97	3302.32	1.10	-0.5
1	26	137.78	3268.80	1.10	+0.7
1	27	137.48	3267.44	1.10	+0.9
1	28	137.17	3266.36	1.10	+1.0
0	26	138.07	3264.09	1.12	+0.9
0	27	137.78	3263.09	1.10	+1.1
0	28	137.49	3262.35	1.10	+1.2
-1	26	138.37	3259.65	1.10	+1.1
-1	27	138.09	3259.01	1.10	-1.3
-1	28	137.80	3258.64	1.08	+1.5

TABLE 3. PROPAGATION CHARACTERISTICS OF SELECTED ORIENTATIONS (CONT)

Angles of ZTCF ⁽¹⁾ , degrees (S & T's program)			Velocity (msec)	K _s ² (x10 ⁻³)	Power Flow Angle (Degrees)
Phi	Theta	Psi			
14	39	40.195	3298.60	0.96	-7.7
14	40	40.415	3306.67	0.96	-8.1
14	41	40.64	3315.19	0.94	-8.6
15	39	39.79	3301.82	0.96	-7.8
15	40	40.00	3310.14	0.94	-8.3
15	41	40.23	3319.09	0.98	-8.6
16	39	39.4	3305.38	0.96	-8.0
16	40	39.605	3314.03	0.98	-8.4
16	41	39.825	3323.15	0.92	-9.0

e. Power Flow Angle

The power flow angle for a particular direction of propagation is an important design parameter. While the phase fronts always remain parallel to the source transducer, the wave, as a whole, does not propagate perpendicular to the wave fronts (see Figure 7). This is a characteristic of anisotropic substrates where the phase velocity is asymmetric about the propagation direction; i.e., $V(\psi + \Delta\psi) \neq V(\psi - \Delta\psi)$. The major problem which arises is that the acoustic beam may steer off of the desired propagation track, missing the output transducer unless it is properly designed.

The power per unit width carried in a surface wave is found by integrating the mechanical and electrical Poynting vectors to obtain

$$P_i = -\frac{1}{2} \operatorname{Re} \left\{ \int_{-\infty}^0 T_{ij} \mu_j^* dx_3 - i\omega \int_{-\infty}^{\infty} \phi D_i dx_3 \right\}, i = 1, 2 \quad (25)$$

P_1 gives the power flow perpendicular to the wave front and P_2 gives the power flow parallel to the wave front. $P_3 = 0$ for the Rayleigh wave which is confined to the surface. The power flow angle may be defined as

$$\theta = \arctan(P_2/P_1) \cong P_2/P_1 \text{ for } P_2 \ll P_1 \quad (26)$$

The power flow angles are calculated using either the perturbation programs or the finite difference routine. Table 4 gives results of calculations for the ST-Cut quartz. Note that for $\psi = 0$, the power

flow angle is zero, within the single precision accuracy used, as a result of the crystal symmetry. Power flow angles as high as 20 degrees are not uncommon on quartz.

TABLE 4. POWER FLOW ANGLES ST-CUT

ψ	Transverse/Incident Power	Power Flow Angle θ
0°	6.159×10^{-5}	0
10°	6.145×10^{-2}	3.5 degrees
20°	9.502×10^{-2}	5.4 degrees

The beam steering angle was calculated for selected cuts of quartz with TCF=0. The analytical results were compared with experimental measurements. Table 3 contains the results of calculations for the selected orientations described in paragraph (8) above.

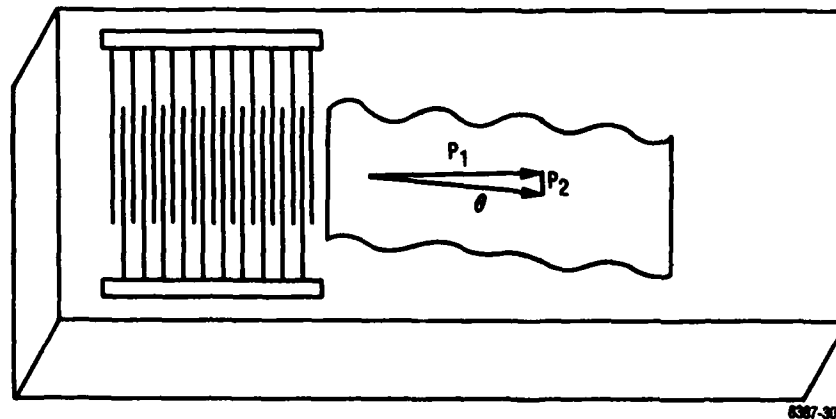


Figure 7. Nonzero Power Flow Angle

f. Proximity and Excitation Strength of Bulk Acoustic Waves (BAW) Spectrum

The purpose of this task is to analytically determine the strength of spurious signals caused by BAW. With this knowledge, one can predict the quality of the SAW device which has been selected for its zero TCD cut.

Interdigital transducers do not couple all of their field energy into surface waves. Bulk waves are also generated at various frequencies in the piezoelectric medium. These bulk waves can bounce off of the bottom surface, undergoing mode conversions in the process, and be received by the output transducer, resulting in unacceptable spurious signals. In most cases, this problem can be virtually eliminated by proper preparation of the bottom surface.

A transducer with periodicity λ excites surface waves at center frequencies

$$f_{\text{SAW}} = (2n + 1)V_{\text{SAW}}/\lambda \quad (27)$$

where V_{SAW} is the surface wave velocity and n is an integer, $n=0, 1, 2, \dots$. The coupling to higher harmonics depends on transducer design. Bulk waves are radiated into the medium at an angle θ at a center fundamental frequency

$$f_n = V_b(\theta) / [\lambda \cos(\theta)] \quad (28)$$

where $V_b(\theta)$ is the velocity of the bulk wave in that particular direction. Equation 28 is a statement of the Bragg condition (see Figure 8). If the medium is isotropic for each mode, V_b is a constant. In the general case, V_b depends on the direction of propagation and hence on θ . To calculate $V_b(\theta)$, the matrix of elastic constants are rotated through the angle θ in the standard way. The quasi-longitudinal velocity and quasi-shear velocities are calculated as¹:

$$\begin{aligned} V_L &= \{[C_{11}(\theta) + e_{11}^2(\theta)/\epsilon_{11}(\theta)]/\rho\}^{1/2} \\ V_{SH} &= \{[C_{66}(\theta) + e_{16}^2(\theta)/\epsilon_{11}(\theta)]/\rho\}^{1/2} \\ V_{SV} &= \{[C_{55}(\theta) + e_{15}^2(\theta)/\epsilon_{11}(\theta)]/\rho\}^{1/2} \end{aligned} \quad (29)$$

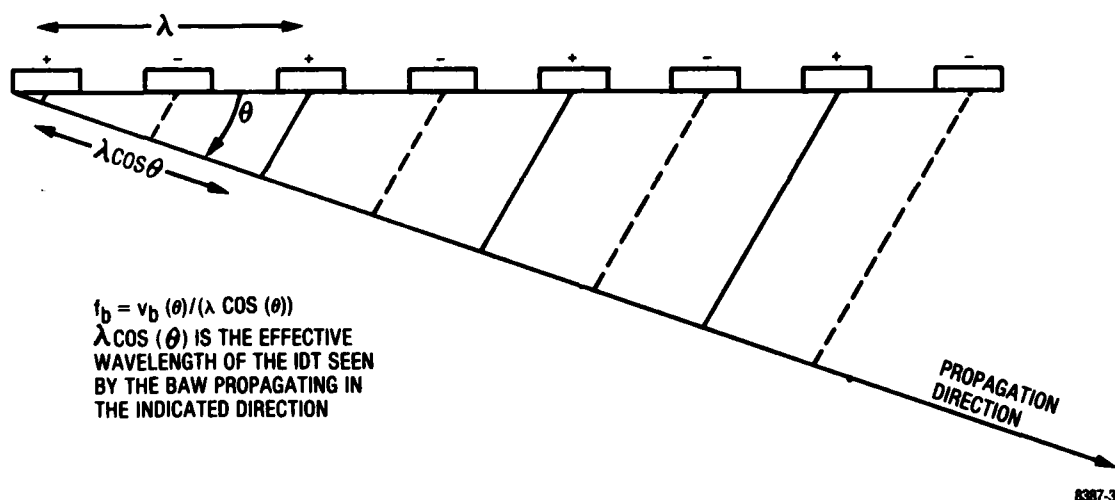


Figure 8. Bragg Condition for Excitation of BAW

The inverse values of these velocities, plotted as a function of θ , form the inverse velocity curves.

Inverse velocity plots as a function of propagation are particularly useful, for as long as $V_b/\cos \theta$, the effective velocity of the bulk wave on the surface, is greater than V_{SAW} , the effects of bulk mode generation may be suppressed by appropriate design and by proper conditioning of the bottom surface. Should $V_b/\cos \theta$ be less than V_{SAW} for any bulk mode, the SAW may couple to the BAW, resulting in a

¹"Physical Acoustics," Mason, Academic Press, NY, Vol. 1, Part A, 1964

leaky surface wave. Inverse velocity plots have been made for orientations with promising SAW temperature characteristics to check for the possibility of leaky surface waves and minimum values of f_s calculated and compared with f_{SAW} .

The polar plots of the inverse velocities for a (YX wlt) 0/27/137.8 and 7/27/135.59 are shown in Figure 9 and Figure 10, respectively. The values of $(1/v_{bulk})$ for the two shear modes and one longitudinal mode for different propagation directions (θ) into the crystal are also shown in Figures 9 and 10. The inverse surface wave velocity for 0/27/137.8 is 3.06×10^{-4} , that for 7/27/137.8 is 3.03×10^{-4} . These values are larger than the maximum $(1/v_{bulk}) \cos \theta (< 2.9 \times 10^{-4})$, therefore, the analysis indicates that a leaky mode does not exist (see Table 3 for the SAW velocities).

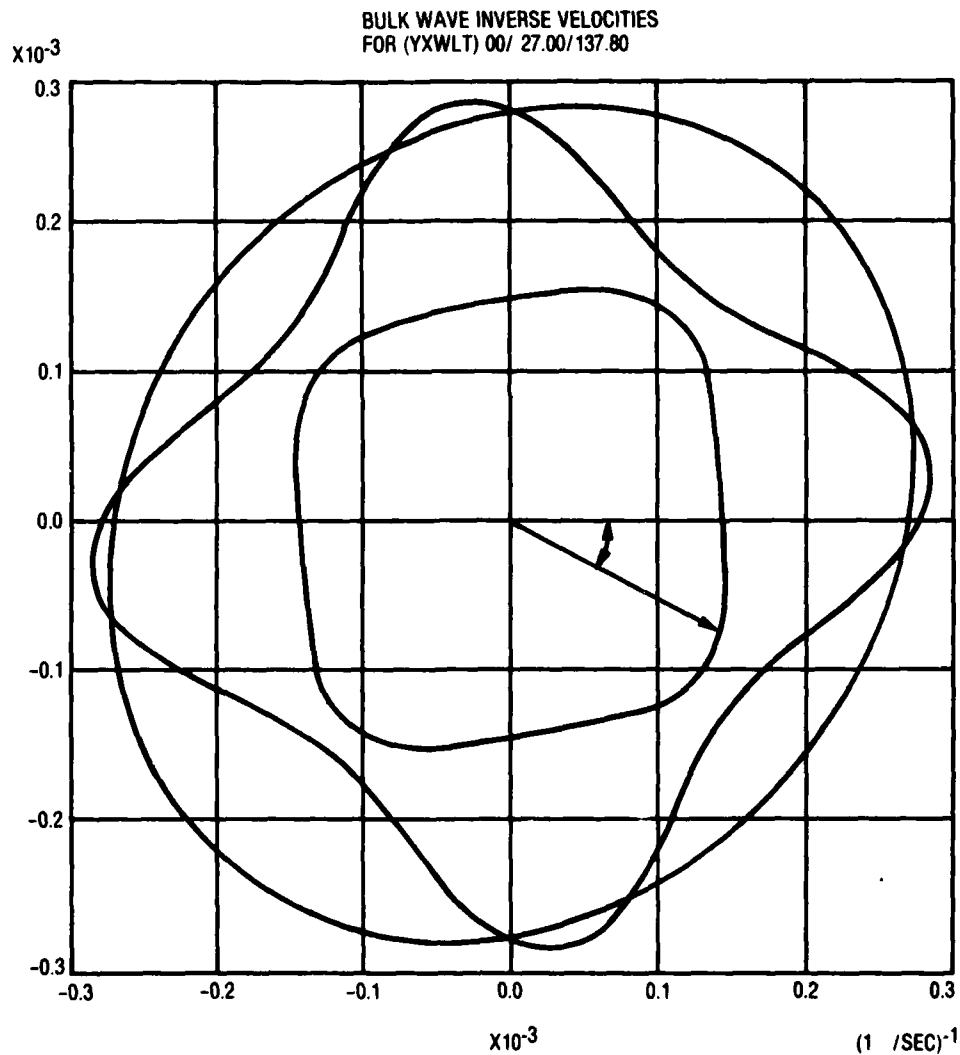


Figure 9. Polar Plots of Inverse Velocities for a (YXwlt) 0/27/137.8

2510-2

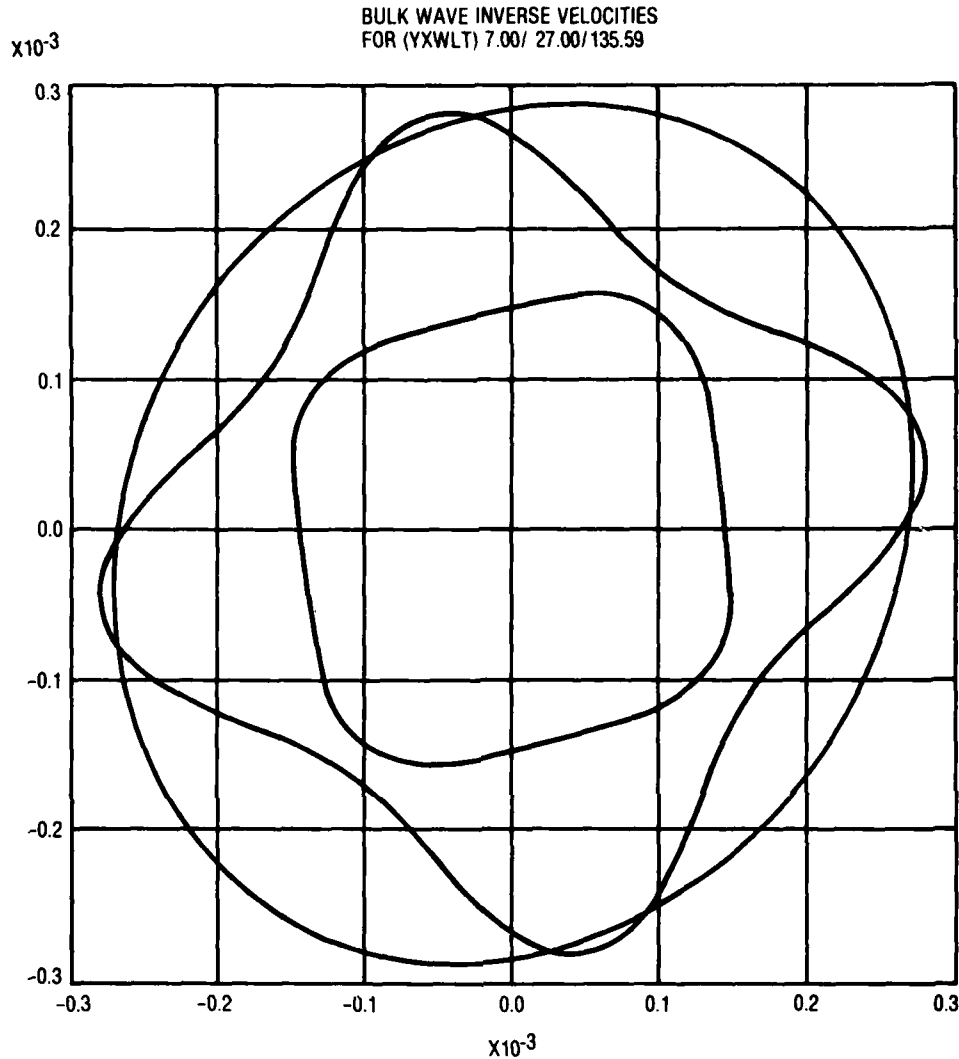


Figure 10. Polar Plots of Inverse Velocities for a (YXwlt) 7/27/135.59

2510-3

g. Degeneracies

Degenerate waves occur when the physical constants are such that equations (30) and (32) decouple.

$$\begin{bmatrix} \Gamma_{11} - \rho V_i^2 & \Gamma_{12} & \Gamma_{13} & \Gamma_{14} \\ \Gamma_{12} & \Gamma_{22} - \rho V_i^2 & \Gamma_{23} & \Gamma_{24} \\ \Gamma_{13} & \Gamma_{23} & \Gamma_{33} - \rho V_i^2 & \Gamma_{34} \\ \Gamma_{14} & \Gamma_{24} & \Gamma_{34} & \Gamma_{44} \end{bmatrix} \begin{bmatrix} \alpha_1 \\ \alpha_2 \\ \alpha_3 \\ \alpha_4 \end{bmatrix} = 0 \quad (30)$$

where

$$\begin{aligned}
 \Gamma_{11} &= c_{55} b^2 + 2c_{15} b + c_{11} \\
 \Gamma_{22} &= c_{44} b^2 + 2c_{46} b + c_{66} \\
 \Gamma_{33} &= c_{33} b^2 + 2c_{35} b + c_{55} \\
 \Gamma_{12} &= c_{45} b^2 + (c_{14} + c_{56}) b + c_{16} \\
 \Gamma_{13} &= c_{35} b^2 + (c_{13} + c_{55}) b + c_{15} \\
 \Gamma_{23} &= c_{34} b^2 + (c_{36} + c_{45}) b + c_{56} \\
 \Gamma_{44} &= -(e_{33} b^2 + 2e_{13} b + e_{11}) \\
 \Gamma_{14} &= e_{35} b^2 + (e_{15} + e_{31}) b + e_{11} \\
 \Gamma_{24} &= e_{34} b^2 + (e_{14} + e_{36}) b + e_{16} \\
 \Gamma_{34} &= e_{33} b^2 + (e_{13} + e_{35}) b + e_{15}
 \end{aligned} \tag{31}$$

The boundary conditions become, in matrix form,

$$\begin{bmatrix}
 \dots (c_{3311} + c_{3313} b^{(m)} \alpha_1^{(m)} + (e_{133} + e_{333} b^{(m)}) \alpha_4^{(m)} \dots \\
 \dots (c_{3111} + c_{3113} b^{(m)} \alpha_1^{(m)} + (e_{131} + e_{331} b^{(m)}) \alpha_4^{(m)} \dots \\
 \dots (c_{3211} + c_{2313} b^{(m)} \alpha_1^{(m)} + (e_{132} + e_{332} b^{(m)}) \alpha_4^{(m)} \dots \\
 \dots (e_{311} + e_{313} b^{(m)}) \alpha_1^{(m)} - (e_{31} + e_{33} b^{(m)} - i\epsilon_0) \alpha_4^{(m)} \dots
 \end{bmatrix}^T \begin{bmatrix} C_1 \\ C_2 \\ C_3 \\ C_4 \end{bmatrix} = 0 \tag{32}$$

The definition of the constants and derivation of the equations are given in Appendix C. The condition for decoupling requires that the matrix in equation 30 has zero elements such that independent, non-Rayleigh wave solutions may exist. Equation 30 may decouple in many ways. If, for example, $\Gamma_{12} = \Gamma_{14} = \Gamma_{34} = 0$, u_1 and u_3 are found to be coupled and u_2 and ϕ are found to be coupled, however u_1 and u_3 are decoupled from u_2 and ϕ . If the physical constants are such that these two solutions are not coupled through the boundary conditions (equation 32) then we find the Rayleigh like wave (u_1 and u_3) is not coupled to ϕ , the potential term, and cannot be excited by electrodes in this cut.

The displacement u_2 which is coupled to ϕ is called the Bleustein — Gulyaev wave and is excited by interdigital transducers. These two waves (u_3 , u_1 and u_2 , ϕ) are degenerate as they propagate with the same velocity. The simplest method to determine whether equation 30 has decoupled for a particular orientation is to calculate the matrix of equation 30. This is presently accomplished using the Rayleigh wave velocity calculation program, which calculates and prints the matrix in equation 30. Because of the variety of special cases¹ which may arise, some of which may ultimately prove useful, each case in which we find the wave equation decouples will be considered on an individual basis.

¹"Propagation of Piezoelectric Surface Waves on Cubic and Hexagonal Crystals," Cambell & Jones, J.A.P., Vol. 41:2796-2801 (1970).

The analytical results of this section allow us to determine which modes can be generated on the selected zero TCD cut of quartz. At the three areas tabulated in Table 2, only Rayleigh wave modes were found.

h. Sensitivities Due to Crystal Misorientation

In cutting quartz and aligning masks on it, there is always some maximum achievable accuracy. Thus it is useful to know how all of the acoustic quantities considered vary with angle. Quantities such as TCD, phase velocity, power flow angle, $\Delta V/V$, bulk wave spectrums, and bulk wave velocity surfaces, are of interest to this program. These quantities can be accurately determined by directly calculating the quantities at $\phi = (\phi_0 + \Delta\phi)$, $\theta = (\theta_0 + \Delta\theta)$, and $\psi = (\psi_0 + \Delta\psi)$ with the same computer program discussed in paragraph 1, where ϕ_0 , θ_0 and ψ_0 are the desired angles, $\Delta\phi$, $\Delta\theta$ and $\Delta\psi$ are the actual directional deviation from the desired direction due to the fabrication tolerance. It is important to calculate the sensitivity of the parameters to the crystal misorientation; i.e., amount of change of a function as a result of small angular misorientation.

For case of the power flow angle (PFA)

$$\begin{aligned} d[\text{PFA}(\phi = 0, \theta = 42.75, \psi = 10^\circ)]/d\psi \\ \cong (\text{PFA}(\psi = 20^\circ) - \text{PFA}(\psi = 0^\circ))/20^\circ \\ \cong 0.27^\circ/\text{degree}. \end{aligned} \quad (33)$$

The quantities $d[\text{PFA}(\phi = 0^\circ, \theta = 42.75, \psi = 10^\circ)]/d\phi$ and $d[\text{PFA}(\phi = 0^\circ, \theta = 42.75^\circ, \psi = 10^\circ)]/d\theta$ are computed in an equivalent manner.

In the case of TCD:

$$d(\text{TCD}) = \frac{\partial(\text{TCD})}{\partial\theta} d\theta + \frac{\partial(\text{TCD})}{\partial\phi} d\phi + \frac{\partial(\text{TCD})}{\partial\psi} d\psi \quad (34)$$

$$\frac{\partial(\text{TCD})}{\partial\theta} = [\text{TCD}(\phi_0, \theta_0, \psi_0) - \text{TCD}(\phi_0, \theta_0 + \Delta\theta, \psi_0)]/\Delta\theta \quad (35)$$

$$\frac{\partial(\text{TCD})}{\partial\phi} = [\text{TCD}(\phi_0, \theta_0, \psi_0) - \text{TCD}(\phi_0 + \Delta\phi, \theta_0, \psi_0)]/\Delta\phi$$

$$\frac{\partial(\text{TCD})}{\partial\psi} = [\text{TCD}(\phi_0, \theta_0, \psi_0) - \text{TCD}(\phi_0, \theta_0, \psi_0 + \Delta\psi)]/\Delta\psi$$

All the TCD (ϕ, θ, ψ) and TCD ($\phi, \theta, \psi + \Delta\psi$) etc., are calculated with the computer programs discussed in paragraph 1. Therefore, all the $\partial(\text{TCD})/\partial\theta$, $\partial(\text{TCD})/\partial\psi$, $\partial(\text{TCD})/\partial\phi$ can be accurately calculated. Hence the sensitivities due to crystal misorientation are determined.

Calculation of the angular dependence on the first, second, and third order TCDs is, of course, our primary task. Of these three quantities, the first order TCF is most sensitive to angular variation. The

angular dependence on these parameters were calculated in the same way as all of the other quantities but on a much smaller angular grid ($\Delta\theta$, $\Delta\phi$ and $\Delta\psi$) about the zero TCD locus. The size of this grid varies, depending on the magnitude and smoothness of the variation about each point on the locus of zero first order TCD orientations as verified by experiment and calculation. In case the function is smooth or linearly varying with angles, large Δ angles may be used.

By performing the above mentioned calculations, we have precise information on the sensitivities due to crystal misorientation. This information will allow us to impose a practical tolerance limit on fabrication and still be able to achieve the required superior performance specification.

Quantities such as velocity (Table 3), power flow angles (Table 3), BAW spectrum (Figures 50 and 51), coupling coefficients (Table 3), and second and third order TCFs (Table 2) do not vary quickly with angle. This is not the case for $TCF^{(1)}$. Table 5 contains a summary of $\partial TCF^{(1)}/\partial\psi$. The large values of $\partial TCF^{(1)}/\partial\psi$ impose strict fabrication tolerances on the SAW cuts and mask alignment. Fabrication accuracy to within 6 minutes is required to keep the total temperature variation due to $TCF^{(1)}$ within 45 ppm for $\partial TCF^{(1)}/\partial\psi = 3(\text{PPM}/^\circ\text{C})/\text{degree}$ over the temperature range -50°C to 100°C . Table 6 contains summaries of $\partial TCF^{(1)}/\partial\phi$ and $\partial TCF^{(1)}/\partial\theta$. These values impose fabrication tolerances on the rotated quartz plate angles ϕ and θ of 12 minutes to keep the total temperature variation due to $\partial TCF^{(1)}(15/40/40)/\partial\phi$ within 45 ppm over the temperature range -50°C to 100°C . This linear temperature variation may be compensated for by varying ψ on any particular cut if all other cut parameters vary slowly with angle.

TABLE 5. $\partial TCF^{(1)}/\partial\psi$ FOR SELECTED CUTS

Angles of ZTCF ⁽¹⁾ , degrees (S & T's program)			$\partial TCF^{(1)}/\partial\psi$
Phi	Theta	Psi	
6	26	136.31	+2.7 (ppm/C°)/degree
6	27	135.93	+2.7
6	28	135.59	+2.7
7	26	135.99	+2.7
7	27	135.64	+2.7
7	28	135.27	+2.7
8	26	135.74	+2.7
8	27	135.36	+2.7
8	28	134.97	+2.7
1	26	137.78	+2.8

TABLE 5. $\partial TCF^{(1)}/\partial \psi$ FOR SELECTED CUTS (CONT)

Angles of ZTCF ⁽¹⁾ , degrees (S & T's program)			$\partial TCF^{(1)}/\partial \psi$
Phi	Theta	Psi	
1	27	137.48	+2.8
1	28	137.17	+2.8
0	26	138.07	+3.0
0	27	137.78	+3.0
0	28	137.49	+3.0
-1	26	138.37	+3.0
-1	27	138.09	+3.0
-1	28	137.80	+3.0
14	39	40.195	-3.5
14	40	40.415	-3.5
14	41	40.64	-3.5
15	39	39.79	-3.5
15	40	40	-3.5
15	41	40.23	-3.5
16	39	39.4	-3.7
16	40	39.605	-3.7
16	41	39.825	-3.7

TABLE 6. $\partial TCF^{(1)}/\partial \phi$ AND $\partial TCF^{(1)}/\partial \theta$ FOR SELECTED CUTS

Angles of ZTCF ⁽¹⁾ (S&T's Program), Degrees			$\partial TCF^{(1)}/\partial \phi$	$\partial TCF^{(1)}/\partial \theta$
Phi	Theta	Psi		
7	27	135.64	-0.7(ppm/C°)/degree	-0.5(ppm/C°)/degree
0	27	137.78	-0.8	-0.8
15	40	40.00	+1.5	-0.7

2. WAFER FABRICATION

During the developmental phase of the doubly rotated cut SAW Devices program, a large number of wafers with 30 different crystal orientations were fabricated and evaluated. To perform this task with good quality control, minimum cost and in a short time, Motorola developed the techniques and processes to fabricate the doubly rotated cut of quartz wafers internally. The crystal boules are supplied by Motorola.

Carlisle, Pennsylvania; the X-ray wafer cutting is performed at Motorola's Semiconductor Group; polishing, fabrication and testing are performed at the Motorola Government Electronics Division. The methods used to fabricate the quartz wafers are described in the following sections.

A computer program was developed to calculate the incident angles and reflected angles for any given cut of crystal. The basic mathematical relations were derived in R.A. Heising's "Quartz Crystals for Electrical Circuits." The relations were formulated to computer programs. The flow diagram is shown in Figure 11. The results are shown in the printout (see Appendix F). The incident angle G , exit angle $(G + G')$, are defined for each plate position. The plate positions are determined by the direction of the rotated axis, $(\pm 1, \pm 2, \pm 3)$, relative to the measuring stage. Once the angles of $(YX \text{ wlt}) \phi/\theta/\psi$ are defined, all of the reflection angles will be calculated for the different reflection planes, defined by Miller indicies. The useful reflection planes that provide intense reflection with low skewed angles (< 5 degrees) are selected for printout. These results, after modification due to change in standards, are used to check the accuracy of the cuts.

a. Face Definitions

The following is an outline of the procedure to be used in this program to make a doubly rotated cut $(YX \text{ wlt}) \phi/\theta/0$. The quartz bars have four lumbered faces with the minus X axis marked. The opposite face is marked by coloring it with a magic marker (blue). One other face not opposite the $-X$ face is colored also with a magic marker (red). The red face is now defined to be the $+Z$ axis as in Figure 12. The direction of the $+Y$ axis may be found by using the right-hand rule ($+X$ crossed into $+Y$ gives $+Z$). The $+Y$ axis will lie along the length of the crystal. Note that there are two ways to set up the axes on the crystal corresponding to choice of the red face (see Figure 12).

b. Running the X-Ray Program

The X-ray orientation program XRAY is run with the angles $\phi/\theta/0$. The sequence of instructions on the Honeywell 560 under the CP-V operating system is as follows:

!SET F:103 DC/MILDAT .538; IN

(This instruction assigns to unit 103 the file containing all of the Miller indicies to be searched.)

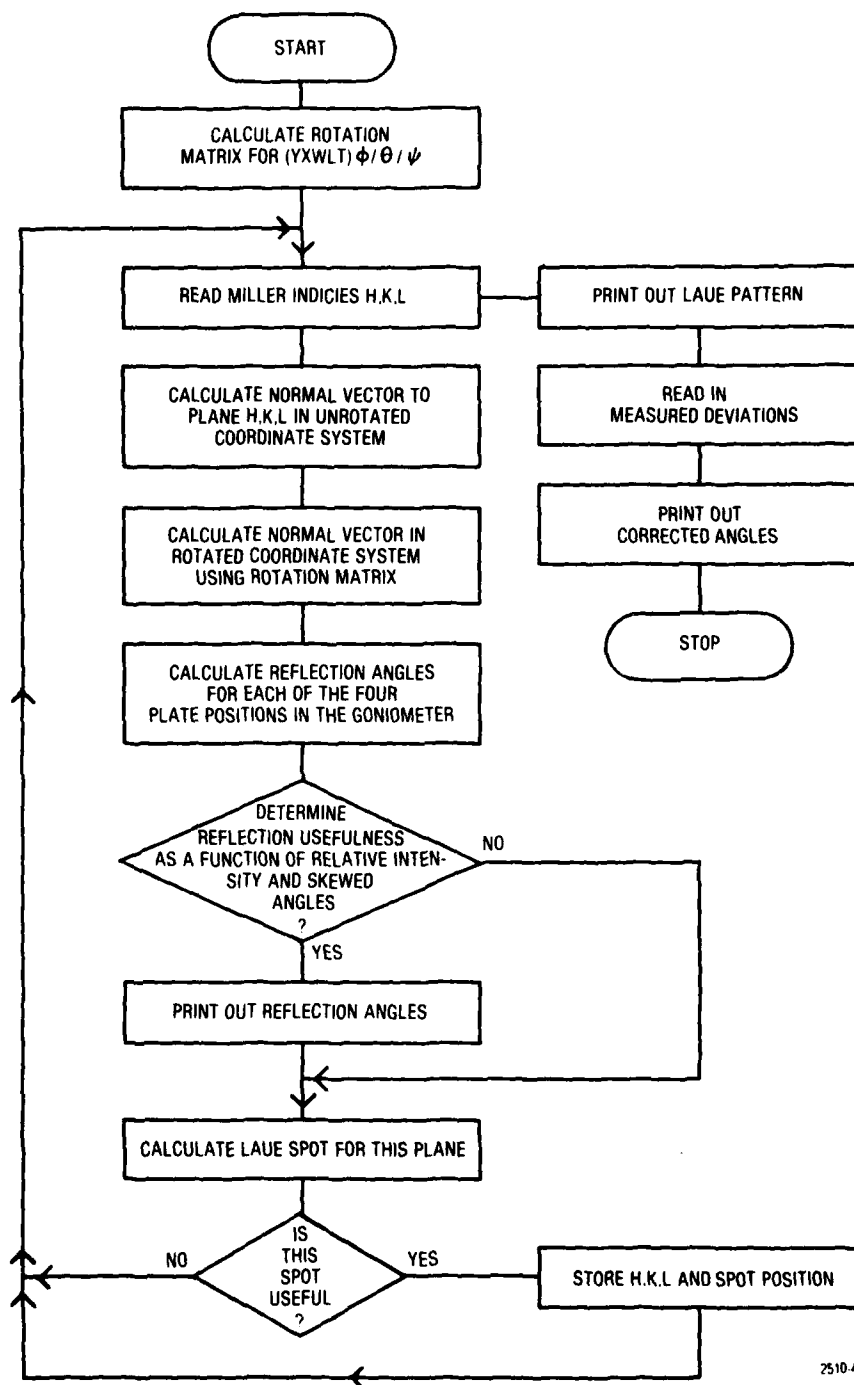
!SET F:104 DC/ERRDAT .538; IN

(This instruction assigns to unit 104 the file containing all of the angle perturbations defined in Heising for use with the Laue photographs.)

!XRAYL M.538

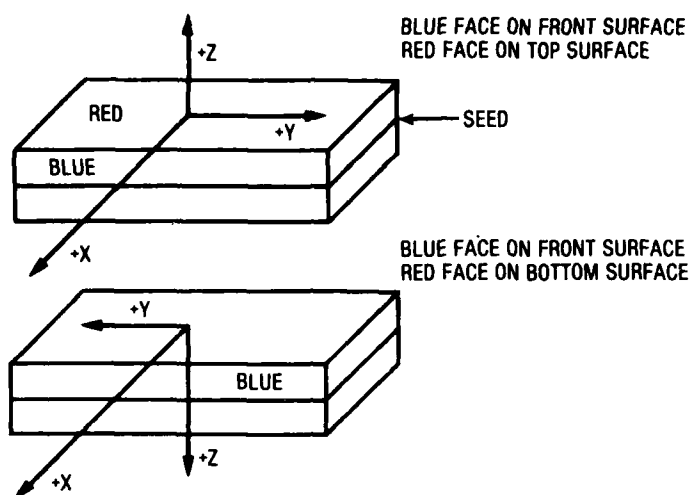
(This instruction loads and begins execution of the program.)

The program will ask for the angles $\phi/\theta/0$. These angles are entered in 3G format [i.e., 10.0, 3.0, 0.0 (carriage return)] and the results of the X-ray analysis printed.



2510-4

Figure 11. Flow Diagram of Calculation for Reflected Angles in Doubly Rotated Cut of Quartz



2510-5

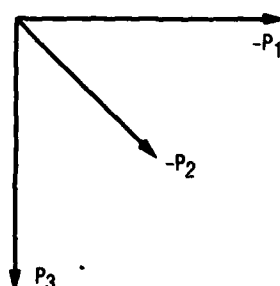
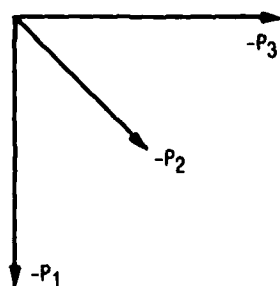
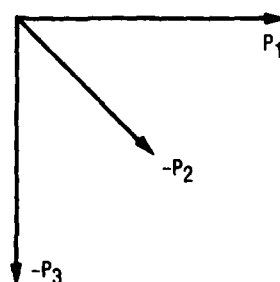
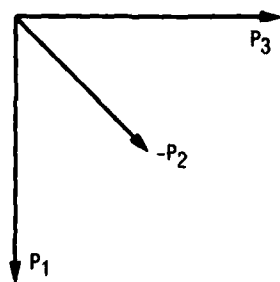
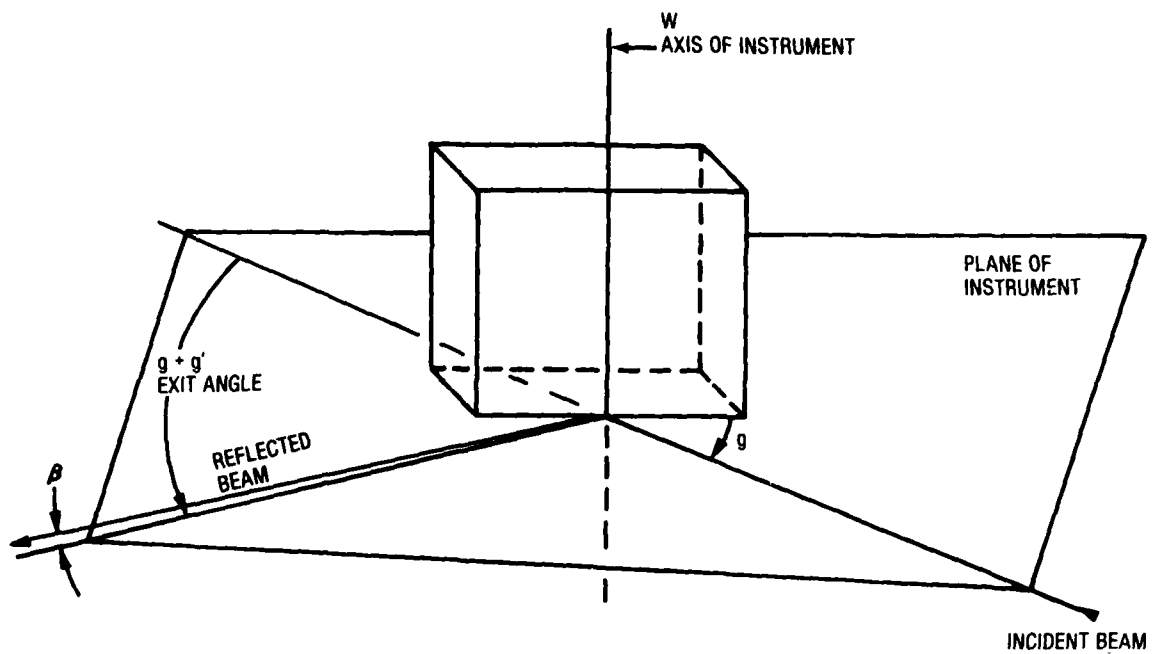
Figure 12. Two Possible Ways of Defining the Crystal Axes on a Lumbered Bar

c. Analysis of X-Ray Program

The X-ray program used follows the development of Heising's which uses a book written before the 1949 IRE Standard we use now. His X, Y, and Z axes will be denoted as \bar{X} , \bar{Y} , and \bar{Z} . The relation to our standard is as follows:

Heising	1949 IRE Standard
$+\bar{X}$	$-X$
$+\bar{Y}$	$-Y$
$+\bar{Z}$	$+Z$

Furthermore, Heising's incident beam comes from the left, while our incident beam comes from the right. When these differences are accounted for, the "position chart" shown in Figure 13 must be used instead of the charts Heising uses in order that our X-ray machine and the 1949 standard may be used. P_1 , P_2 , and P_3 in the "position chart" are the $+X$, $+Y$, and $+Z$ axes of the rotated plate. An important note of caution: the ϕ crystal face off of which we reflect the X-ray beam has \bar{Y} or $-Y$ as its normal. Since we may not assume that the crystal faces are parallel, we must propagate the surface wave on this face. This is important, because to achieve the same crystal properties, we must rotate by ψ about the $+Y$ axis, resulting in a change of the sign of the third rotation (see Figure 14).



POSITION 1

POSITION 2

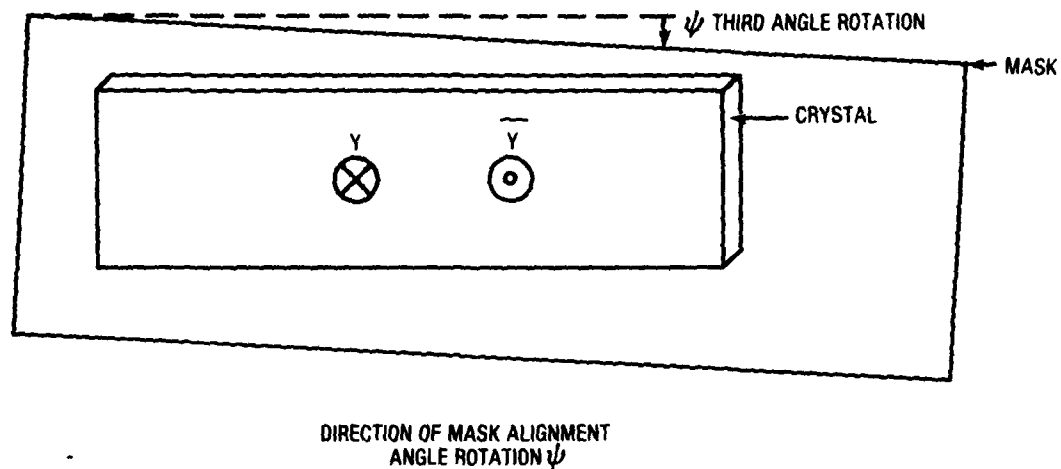
POSITION 3

POSITION 4

2510-7

P_1 , P_2 , and P_3 are the rotated plate axes X, Y, and Z.

Figure 13. X-ray Position Chart



2510-6

Figure 14. Direction of Mask Alignment Angle Rotation ψ

d. Determination of the Actual ψ Angle

The third angle of rotation must be measured from a reference. The reference used is the face opposite the red face of the crystal ($-Z$ face). To determine the actual orientation of the finished crystal edge, we must know the orientation of this plane exactly (see Figure 15).

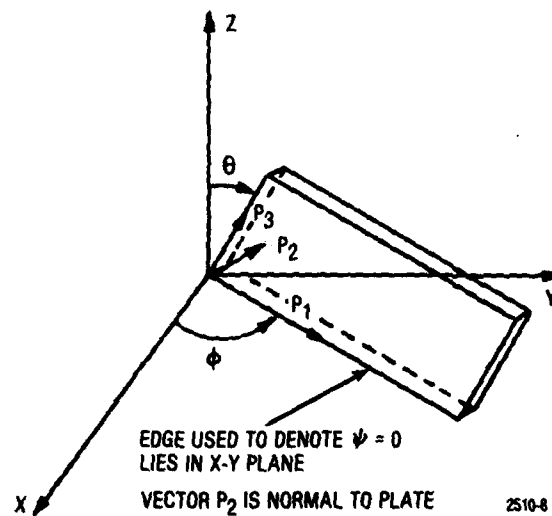


Figure 15. Crystal Rotation (YX w/lt) $\phi/\theta/0$

If the angles α and β in Figure 16 are measured using the (003) plane, which is parallel to the X and Y axes, $\Delta\psi$ is given by:

$$\Delta\psi = -\tan^{-1} [(-\cos \phi \sin \alpha - \sin \phi \sin \beta) / (\sin \theta \sin \phi \sin \alpha - \sin \theta \cos \phi \sin \beta + \cos \theta \sqrt{1 - \sin^2 \alpha - \sin^2 \beta})] \quad (36)$$

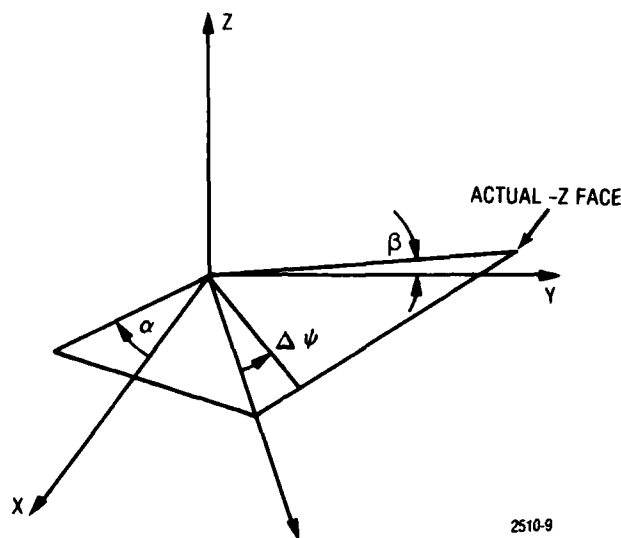


Figure 16. Actual -Z Face, Crystalline Axes, α , β , and $\Delta\psi$

Thus, given a ψ desired which we wish to obtain, we must actually rotate the mask by $\psi_{\text{actual}} = \psi_{\text{des}} - \Delta\psi$ as shown in Figure 17.

e. Determination of α and β

The most appropriate crystal plane to use for determining α and β is the 003 plane. This plane has all of its atoms lying in planes perpendicular to the Z axis, and for a perfect Z face the X-ray deflection angles will be:

G = Angle of incidence = 25 degrees 19 minutes

$G + G'$ = Exit angle = 50 degrees 38 minutes

For all positions on the X-ray machine with the +Z or -Z face being X-rayed. To determine α and β for the -Z face, we use the following relationships.

$$\alpha = 1/2 (G_{-X \text{ TOWARD INCIDENT}} - G_{+X \text{ TOWARD INCIDENT}}) \quad (37)$$

$$\beta = 1/2 (G_{-Y \text{ TOWARD INCIDENT}} - G_{+Y \text{ TOWARD INCIDENT}}) \quad (38)$$

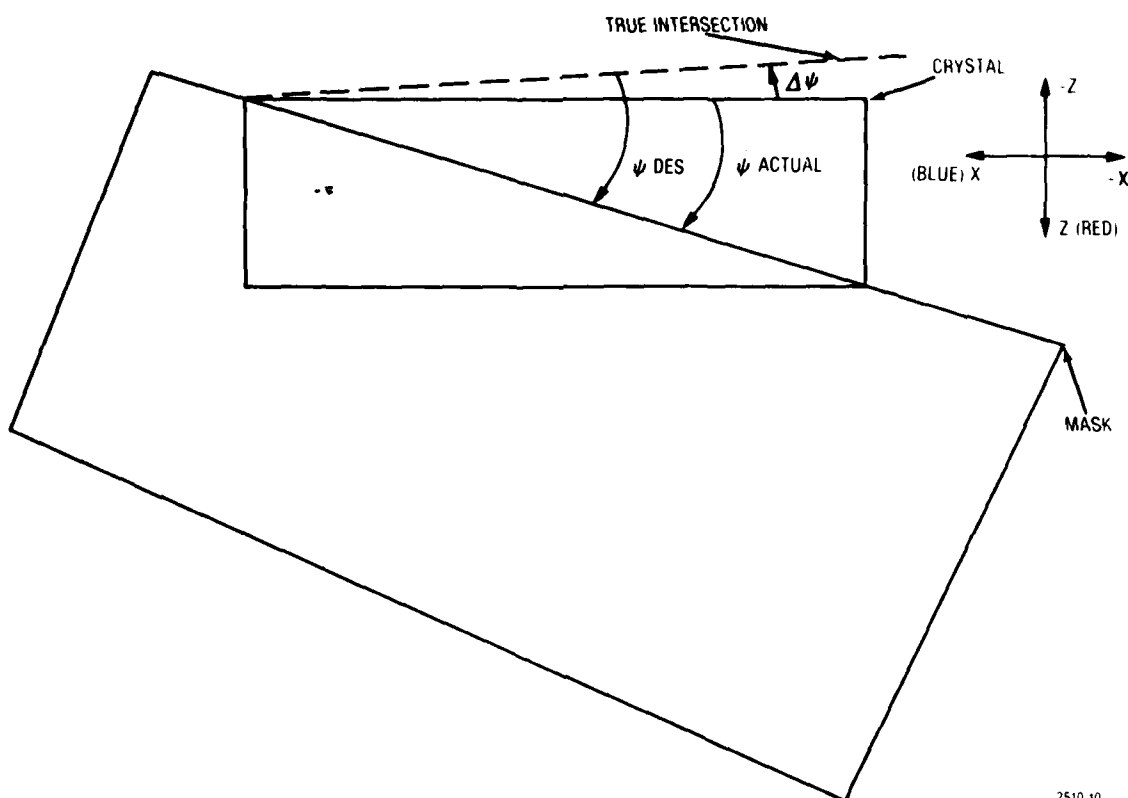


Figure 17. Mask Rotation to Obtain Desired ψ

To determine α and β for the +Z face we use

$$\alpha' = 1/2 (G_{+X} \text{ TO INCIDENT} - G_{-X} \text{ TO INCIDENT}) \quad (39)$$

$$\beta' = 1/2 (G_{-Y} \text{ TO INCIDENT} - G_{+Y} \text{ TO INCIDENT}) \quad (40)$$

α' and β' are the α and β we would have measured for a -Z face that is parallel to the +Z face measured, which means that equation (36) is still valid for α' and β' .

The quartz crystal will now have the orientation (YX wlt) $\phi/\theta/ - \Delta\psi(\alpha, \beta)$ if we use the -Z edge as a reference and (YX wlt) $\phi/\theta/ - \Delta\psi(\alpha', \beta')$ if we use the +Z edge as a reference. The computer X-ray program for these angular orientations must be used if we are to get an accurate measurement. The integrity of these measurements of α and β is checked by comparing $1/2 (G_{-X} + G_{+X})$ and $1/2 (G_{-Y} + G_{+Y})$ with the theoretical result, $G_{AVC} = 25 \text{ degrees } 19 \text{ minutes}$.

f. Procedure Used to Zero X-Ray Machine:

- (1) Use reference quartz plate marked 10.1

- (2) Set X-ray exit angle to 26.5 degrees (marked AT cut on machine)
- (3) Set plate in X-ray machine with marking toward you (X-ray bounces off unmarked surface) and blue line up (width direction vertical). (See Figure 18).
- (4) Adjust with clutch till X-ray reading occurs at incident angle 13 degrees 18 minutes
- (5) Set plate in X-ray machine with marking toward you (X-ray bounces off unmarked surface) and blue line down (width direction vertical). (See Figure 19).
- (6) Angle of incidence should be at 13 degrees 18 minutes + Δ angle.
- (7) Adjust clutch until angle of incidence is at 13 degrees 18 minutes + $1/2 \Delta$ angle.
- (8) Check alignment by measuring in positions of steps 3 and 5. The average of the two readings should be 13 degrees 18 minutes. Any discrepancy represents error in zeroing the machine and may be made less than 1 minute.
- (9) If the 10.1 cut is not available, the same procedure may be used if, for the cut to be used, the theoretical angles of incidence are equal for the particular crystal plane used in both positions.

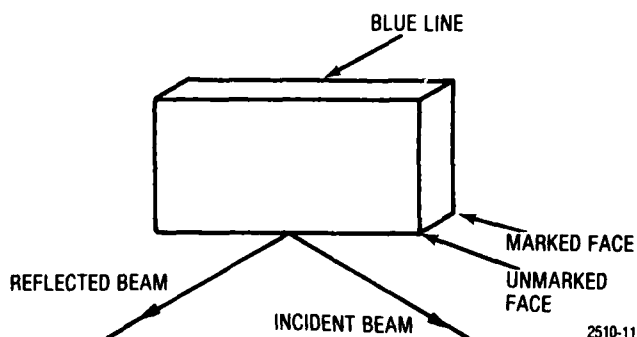


Figure 18. Position of Step 3, 10.1 Alignment Wafer

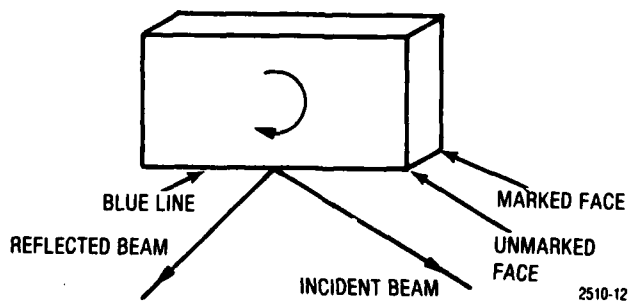


Figure 19. Position of Step 5, 10.1 Alignment Wafer Rotated by 180 Degrees About -Y Axis

g. Cutting Techniques for Doubly Rotated Orientations

A slicing machine built by Meyer and Burger Company, model TS3, was used to slice the quartz boule. The 6 inch diamond impregnated blade is supplied by Maurice Dessau, New York. The drift accuracy of the 2 inch cut is approximately 3 mils (~5 minutes).

The stage of the saw has the capability to rotate in two dimensions; it is designed to make the doubly rotated cut. The adjustment accuracies are graded to 0.5 minute. The X-ray beam resolution is about 2 minutes.

The combined accuracy of the wafers obtained experimentally has been better than 15 minutes. Iterative adjustment of the cutting stage can bring the cutting accuracy to within 10 minutes. The cutting procedures are the following:

- (1) Heat brass plate, glass plate and quartz boule.
- (2) Melt wax on brass plate and mount glass plate.
- (3) Melt wax on glass and mount quartz boule on glass.
- (4) Let cool to room temperature.
- (5) Screw mount brass plate to slice machine.
- (6) Initial cut of boule along the XZ plane (or directly to the desired angle if the boule was lumbered).
- (7) Determine true atomic plane using diffractometer and X-ray computer program.
- (8) Adjust stage to correct for true atomic planes, and obtain the desired rotation.
- (9) Perform doubly rotated cut of quartz.
- (10) Measure the reflection angle and check against the calculated result of the X-ray program. Iterative adjustment of stage can be done if cut accuracy is critical.

These procedures are presently used to cut the wafers with low TCF orientation required for this program.

h. Wafer Polishing

The polishing process for the quartz wafers was established during this period. The procedure includes the following:

- (1) The crystal axis orientation is marked on the back surface of the wafers with marking ink and baked dry. The markings have been demonstrated to stay on the crystal throughout the photolithographic process for easy identification.

(2) The corners of the wafers are ground prior to lapping and polishing to prevent corner breakage.

(3) The polishing is a two step process. The first step is a 15 μm lapping to obtain surface flatness with Microgrit, type WCA, Size 15, on a LAPMASTER, Model 24. The second step is to polish the surface with Cerium oxide on a LogiTech, Ltd. Model PM2 polisher. The polish wheel is made of pitch wax supplied by Hacker Instruments, Inc. The polished wafers have a surface finish with no observable grains or pits under a 50X microscope. The wafers are suitable for surface wave application. X-ray orientation was performed before and after the lapping and polishing processes. The change is normally less than 6 minutes.

SECTION III

TECHNICAL DISCUSSION OF TASK II

1. INTRODUCTION

The search for a temperature stable cut of quartz for application to SAW devices has led to the investigation of the doubly rotated cuts. Theoretical studies have indicated that doubly rotated cuts of quartz promise much better temperature stability than the commonly used ST cut. Task I of this program, which encompassed the first iteration calculations of the doubly rotated cuts of quartz was successfully completed. Task II, with major emphasis on experimental work, is discussed in this section.

In Task I theoretical analyses have been performed and angular rotations promising very low $TCF^{(1)}$ and $TCF^{(2)}$ have been plotted. Important SAW device design parameters, such as coupling coefficient, velocity and power flow angle, have also been computed to characterize each area. As part of Task II, experimental results establishing the degree of correlation with theory have been obtained.

Theoretical propagation characteristics, as discussed in paragraph 2 below, impose strict fabrication tolerances on the SAW cuts and mask alignment due to large values of $\partial TCF1/\partial \psi$. Thus a mask had to be designed to compensate for fabrication errors. This design work is presented in paragraph 3. Since experimental technique is an important criteria in the determination of correlation between theory and experiment, all procedures followed as well as equipment used are discussed in paragraph 4. Paragraph 5 presents experimental determination of propagation characteristics which illustrate an excellent agreement between theoretical calculation and experimental results. Paragraph 6 contains the results of the doubly rotated cut TCF measurements made to date.

Theoretical calculations have been in good agreement with experimental results. Doubly rotated cuts of quartz with an improvement of $TCF^{(2)}$ by at least a factor of two over the ST cut have been obtained. A further improvement was expected after a second iteration and these results are discussed in Section IV.

2. THEORETICAL PROPAGATION CHARACTERISTICS

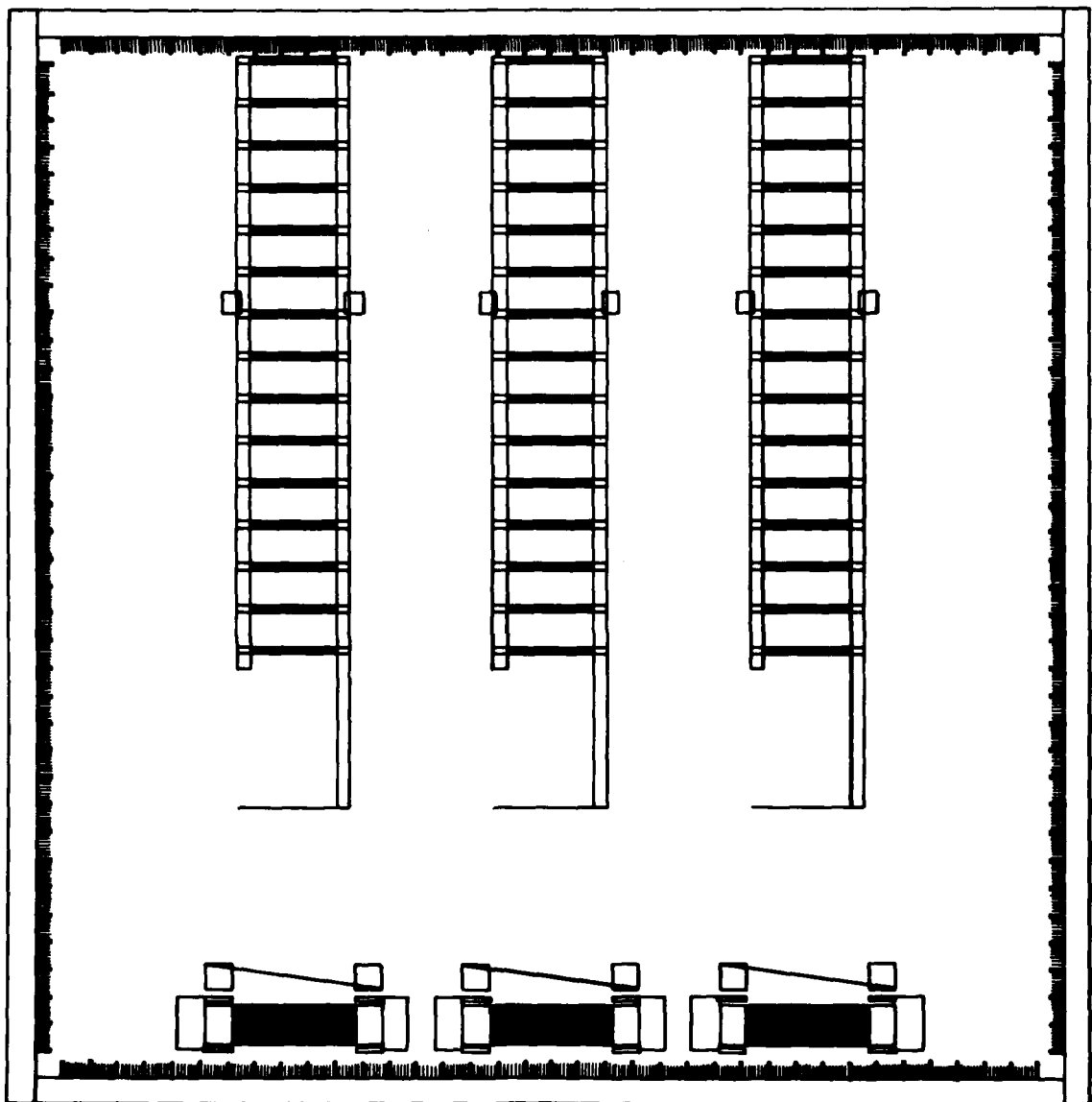
In cutting quartz and aligning masks on it, there is always some maximum achievable accuracy. It is also useful to know how all of the acoustic quantities considered vary with angle. Quantities such as TCF, phase velocity, power flow angle, $\Delta V/V$, and bulk wave velocity surfaces are of interest to this program. These quantities can be accurately determined by directly calculating the quantities at $\phi = (\phi_0 + \Delta\phi)$, $\theta = (\theta_0 + \Delta\theta)$, and $\psi = (\psi_0 + \Delta\psi)$. Calculation of the angular dependence on the first, second, and third order TCF's is, of course, our primary task. Of these three quantities, the first order TCF is most sensitive to angular variation (refer to Tables 2, 3 and 5). Quantities such as velocity (Table 3), power flow angles (Table 3), coupling coefficients (Table 5), and second and third order TCF's (Table 2) do not vary quickly with angle.

This is not the case for $TCF^{(1)}$. Table 5 contains a summary of $\partial TCF^{(1)}/\partial \psi$. The large values of $\partial TCF^{(1)}/\partial \psi$ impose strict fabrication tolerances on the SAW cuts and mask alignment. Therefore it is essential to design a mask with reference registration marks to accurately determine the transducer orientation relative to the crystal edges. These reference markers are fabricated on all of the measured devices, so that propagation direction is accurately determined to within ± 25 minutes. Fabrication accuracy to within 6 minutes is required to keep the total temperature variation due to $TCF^{(1)}$ within 45 ppm for $\partial TCF^{(1)}/\partial \psi = 0.3$ (PPM/°C)/degree over the temperature range of -50°C to 100°C . Table 10 contains summaries of $\partial TCF^{(1)}/\partial \phi$ and $\partial TCF^{(1)}/\partial \theta$. These values impose fabrication tolerances on the rotated quartz plate angles ϕ and θ of $\Delta \phi$ and $\Delta \theta$ less than 12 minutes to keep the total temperature variation due to $\partial TCF^{(1)} (15/40/40)/\partial \phi$ within 45 ppm over the temperature range of -50°C to 100°C for example. This linear temperature variation may be compensated for by varying ψ on any particular cut if all other cut parameters vary slowly with angle. To date all other cut parameters have been found to vary slowly with Phi, Theta and Psi.

3. MASK DESIGN

A mask was designed to take into account the sensitivity of $TCF^{(1)}$ due to small variations in the cut angles. The design incorporates rotated structures. Each device is offset with respect to its neighbor by 0.2° . Three individual devices are illustrated in Figure 20. The device specifications are as follows:

- a. Transducer periodicity: $12.192 \mu\text{m}$ (center frequency ~ 260 MHz; varies with crystal orientation)
- b. Delay time: 360λ ($\sim 1.4 \mu\text{s}$) (varies with crystal orientation)
- c. Number of sets in output transducer: 15
- d. Electrode pairs per set: 2.25
- e. Electrode pairs in input transducer: 24
- f. Aperture width: Input: 70 wavelengths
Output: 50 wavelengths



4147-2

Figure 20. SAW Oscillator Device

Figure 21 is a photograph of a wafer fabricated using the above-mentioned design. Twelve oscillators propagating in different ψ directions are fabricated on a single wafer. The principal advantage of this design is the ability to compensate for fabrication errors. From the experimental results plotted in Figure 22, we are able to observe significant frequency shifts due to small variations in PSI angle. These results confirm our theoretical calculations.

4. EXPERIMENTAL MEASUREMENT OF TCF

Wafers with orientations that provide low temperature coefficients of frequency were used to fabricate SAW oscillator devices. Considerable care has been taken to minimize fabrication tolerances. For angles ϕ and θ , the estimated accuracy is within ± 4 minutes; for angle ψ , the accuracy is within ± 25 minutes.

The delay line oscillators described previously were used to measure the frequency stability at different temperatures. The experimental apparatus is shown in Figure 23. No coils were used to match the devices in order to eliminate inductance changes in the matching circuit over the temperature range tested.

The switches are designed to test ten oscillators in the same temperature chamber. The phase stability of the switches is essential to the measurements. The circuits are shown in Figure 24. The phase stability of the switches was found to be adequate for measuring the temperature stability of the device.

A digital thermocouple (Fluke 2160A-T) was taped to the bottom of the fixture to measure device temperature. The Fluke 2160A-T is accurate to within $\pm 2^\circ\text{C}$ over the temperature range of -75°C to $+150^\circ\text{C}$. A thermometer was also used to measure the oven air temperature. Semi-rigid cable constituted all interconnections. This reduces loss, shields against feedthrough, and makes the apparatus less sensitive to the testing environment. ANZAC DS109 power splitters and AVETEK AWL500M amplifiers were used in the feedback loop. A Systron Donner (PLS 50-1) provided the DC power supply voltage. The mean supply voltage was maintained at 15.000 ± 0.001 volts during the measurements.

Frequency measurements were taken every 10°C , spanning the range from -55°C to $+135^\circ\text{C}$. Stabilization of temperature and frequency was attained for each measurement before data was taken. This ensures that the device is in thermal equilibrium with its environment. The total experimental error is estimated to be less than ± 10 PPM.

5. EXPERIMENTAL PROPAGATION CHARACTERISTICS

The propagation characteristics of selected devices were measured to verify the calculations. The experimental measured velocity is

$$v = f\lambda \quad \lambda = 12.192 \mu\text{m}$$

Table 7 lists the experimental velocities for the various cuts. The deviation (up to 0.2%) is in part caused by the slight deviation of crystal orientation due to the fabrication process, and in part caused by the uncertainty of center frequency due to the unknown phase shift in the feedback loop (± 0.25 MHz).

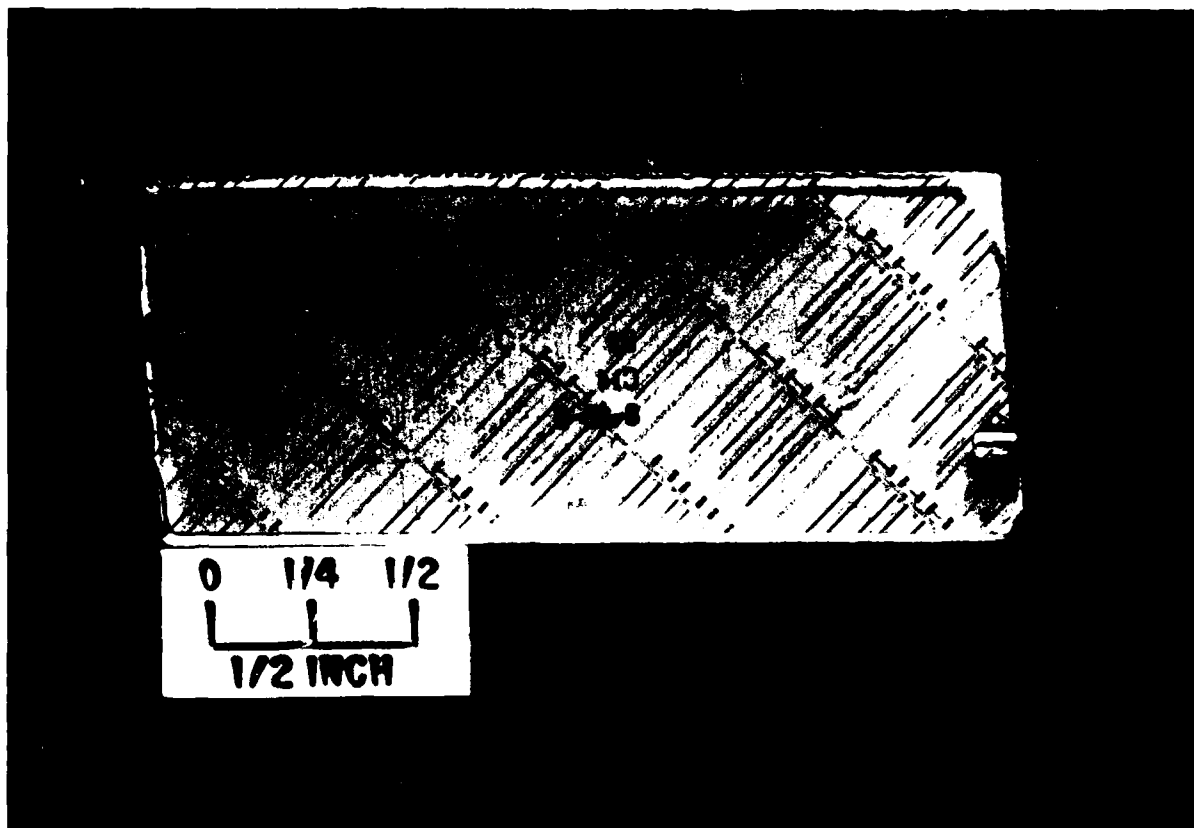


Figure 21. Photograph of a Fabricated Wafer With Propagation Directions of $8^{\circ}27'/27^{\circ}54'/133^{\circ}54' \pm n(0.2^{\circ})$

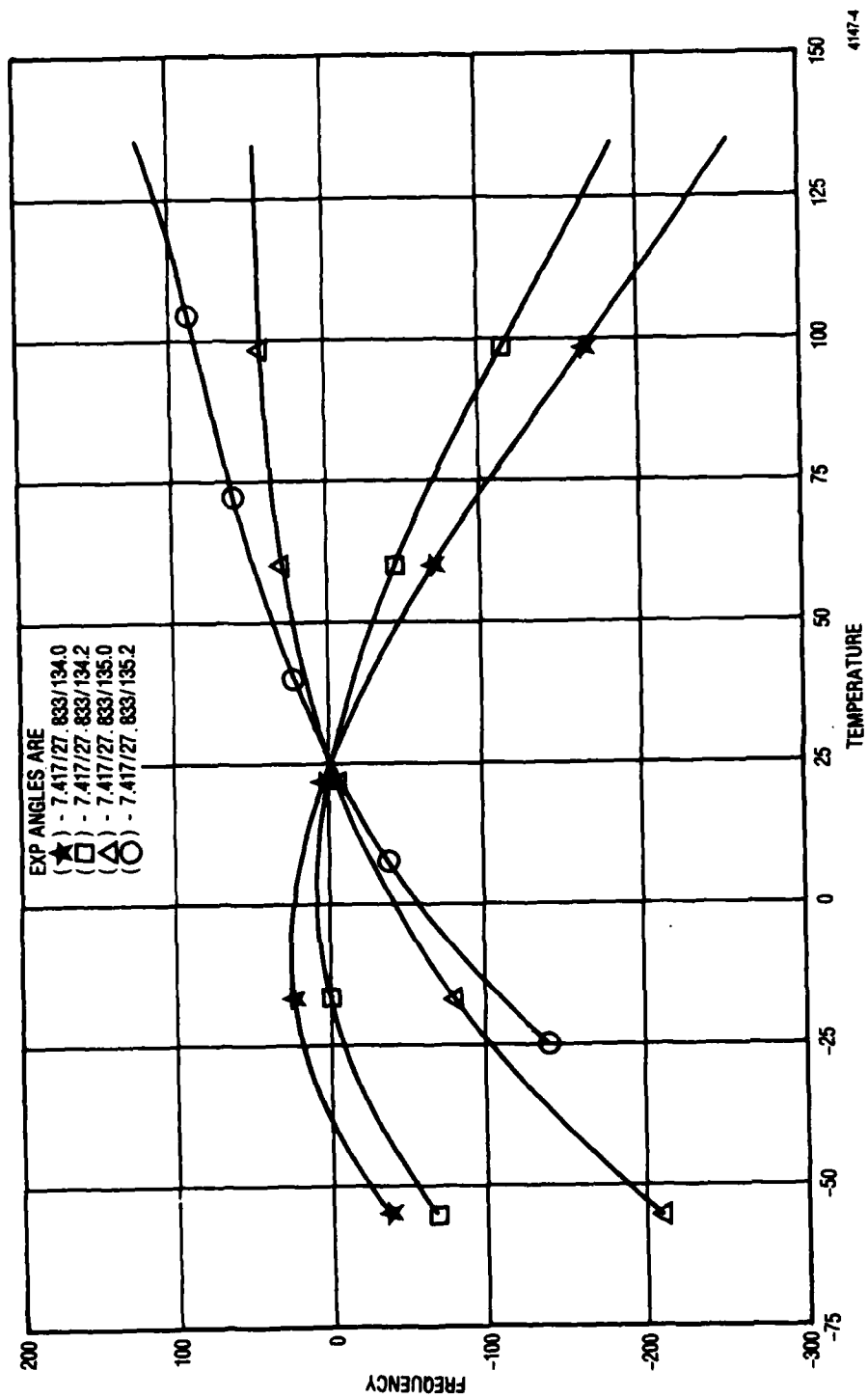
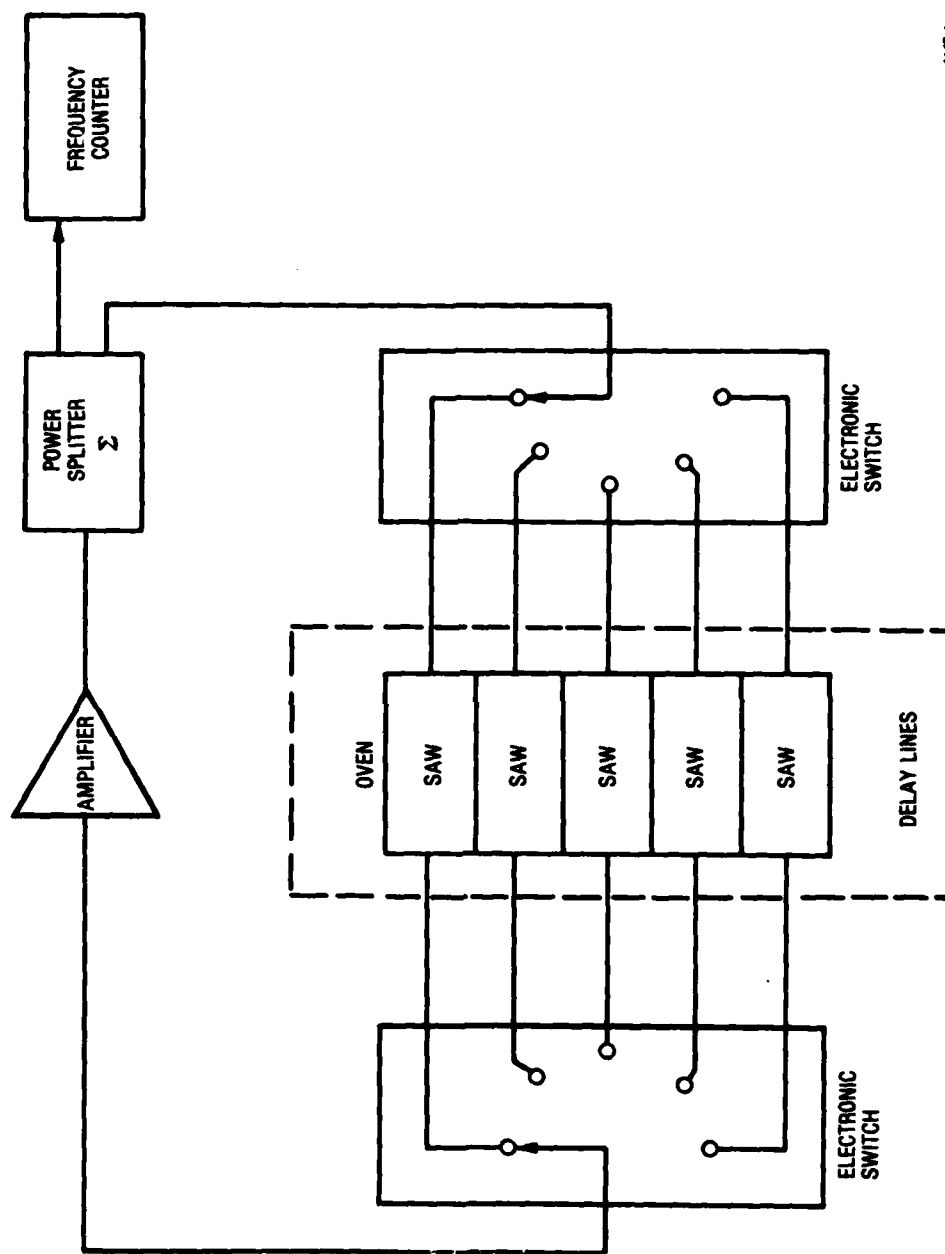
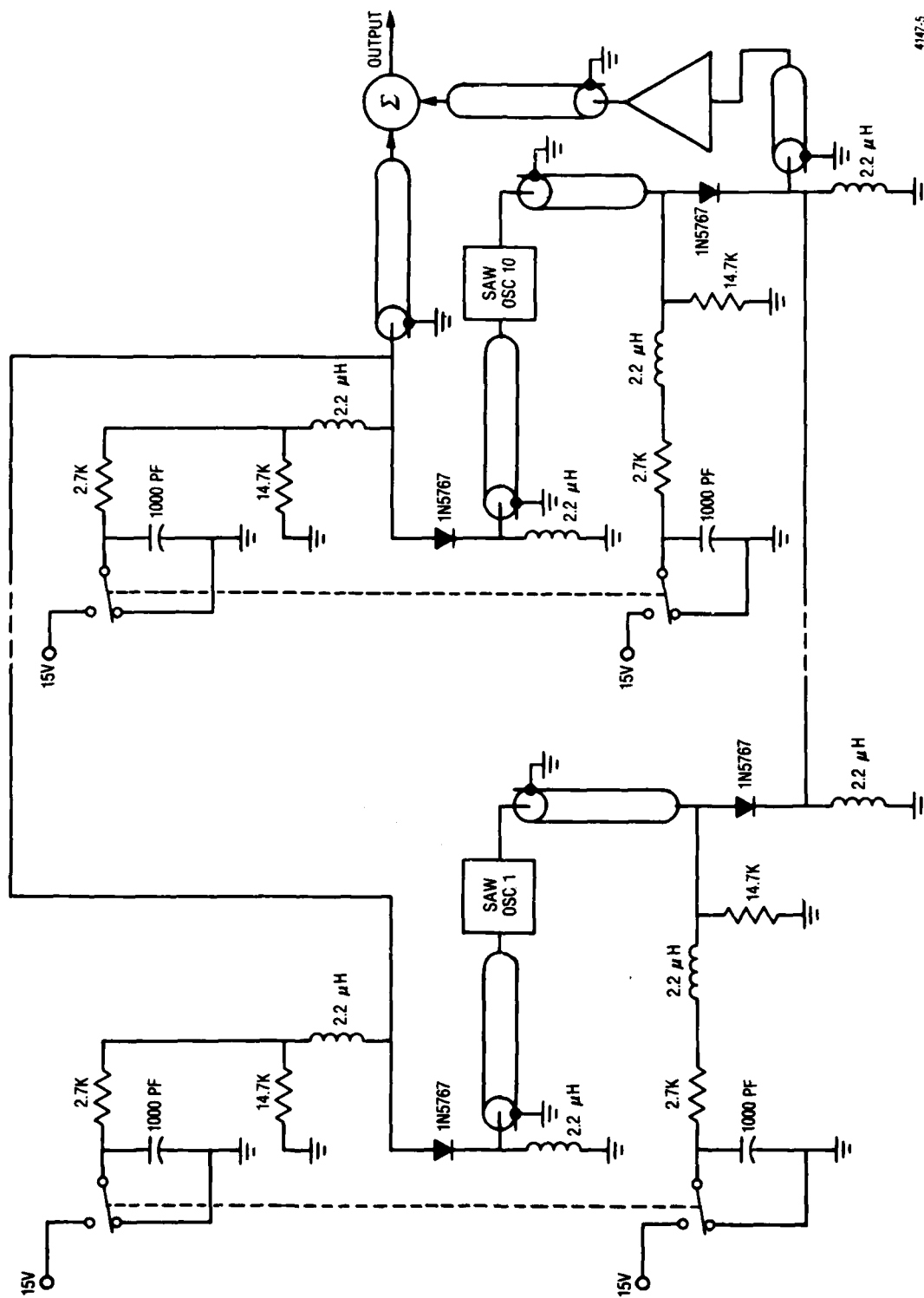


Figure 22. Frequency Temperature Curve With Different ψ Angles



4147-1

Figure 23. Measurement System



4147.5

Figure 24. Test Circuits

The power flow angle of the doubly rotated cut quartz wafer has been measured by the laser probe technique. The measured result is in good agreement with calculations.

TABLE 7. EXPERIMENTAL VELOCITIES OF CUTS

Phi	Theta	Psi	Measured Velocity	Calculated Velocity
-1.05	28.0667	136.534	3257.4	3260.9
-0.9667	26.233	138.449	3256.8	3259.4
-0.133	28.1	137.692	3259.0	3261.5
-0.033	26.7	138.859	3262.1	3262.5
0.633	26.15	137.016	3267.6	3267.7
5.583	27.833	135.194	3289.7	3288.9
5.583	27.833	135.994	3290.7	3288.9
6.0	26.9667	135.812	3288.9	3293.7
6.067	25.933	133.099	3298.8	3299.4
7.41	27.83	134.2	3296.8	3299.1
8.033	26.9667	134.618	3304.1	3306.1
14.2833	39.1167	40.227	3294.8	3301.4
14.2833	39.1167	40.627	3296.8	3304.6
15.25	39.2	39.6187	3300.7	3303.4
15.3	40.6833	40.0308	3314.0	3317.3

The block diagram of the experimental set-up is shown in Figure 25.

In this procedure, the first order deflecting light due to the presence of the acoustic wave is measured by the photomultiplier. The light intensity is proportional to the acoustic power, while the angle of deflection is given by:

$$\sin \theta_n = \sin \theta_0 + \frac{n\lambda}{\Lambda}$$

Where θ_n = angle of deflection of nth order

θ_0 = angle of specular reflection

λ = optical wavelength

Λ = acoustic wavelength

The angular relation is demonstrated in Figure 26. The optical beam is provided by a He-Ne laser with spot size of $\approx 100\mu$. The acoustic waves are generated by a 260 MHz transducer with Λ equal to 12.192μ . During the measurement, the SAW device is translated up and down so that the optical beam is scanned across the acoustic path to detect the acoustic beam intensity distribution. The test equipment is shown in Figure 27.

Figures 28 and 29 show examples of plots of the relative acoustic beam intensities indicated by the deflected laser beam. These plots were taken in the near- and far-field regions, respectively. The exact distance between the near-field scan and the far-field scan is 8.131 mm. The center of the beams is estimated to be 0.05 mm in separation.

The measured power flow angle for this cut is

$$\theta_p = \tan^{-1} \frac{-0.05}{8.131} = -0.352^\circ$$

The calculated power flow angle for this cut is

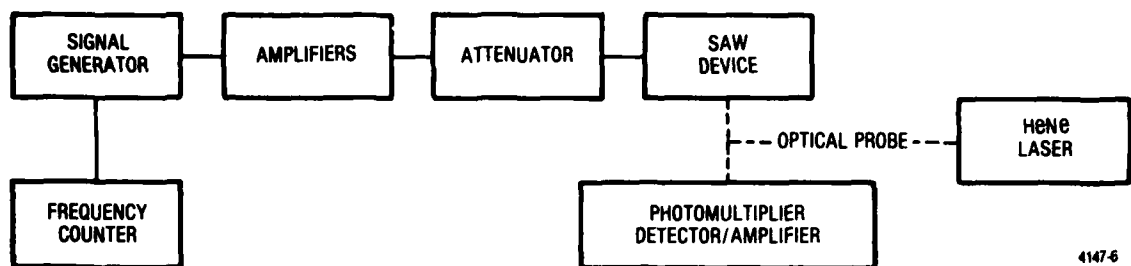
$$\theta'_p = -0.3^\circ$$

The good agreement between the measurement and the calculated results indicates that the calculation is accurate. Acoustic dispersion and loss can also be calculated from this data.

6. EXPERIMENTAL MEASUREMENT OF FREQUENCY VERSUS TEMPERATURE

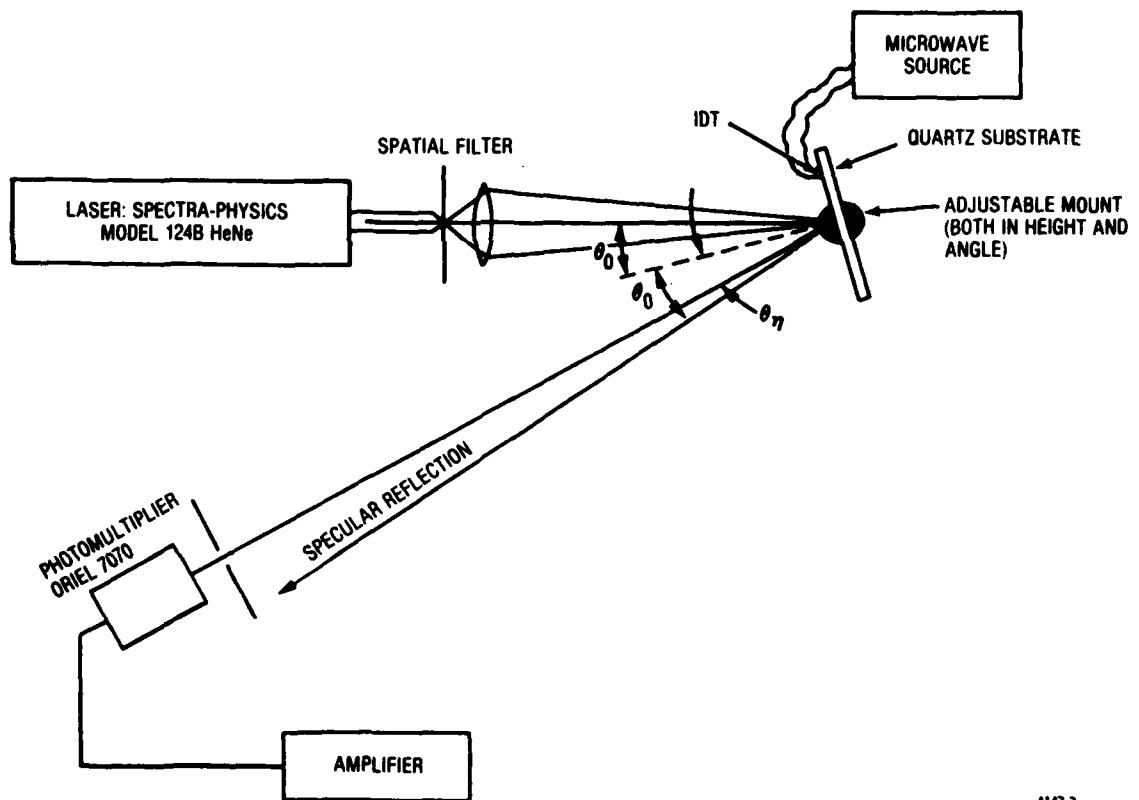
A few representative frequency-temperature measurements are presented in Figures 30 through 34. The stars represent experimental data points. The solid lines are linearly regressed curves used to define the measured first, second, and third order TCF's for these cuts, given in Table 8. Figures 30 through 34 are representative of cuts in region (YX wlt) 7/27/135. Cut (YX/wlt) 6.57/26.88/134.9 of Figure 30 has a small linear frequency term at room temperature and is well suited for use at both high and low temperatures. Its second order TCF is in good agreement with the computer calculations and is considerably smaller than that of ST-cut quartz (see Table 8). Cut (YX wlt) 5.58/27.83/135.1 of Figure 31 displays a larger total frequency variation over the range shown but is much more stable at higher temperatures. This illustrates how a simple change of crystal orientation can be used to temperature-compensate doubly rotated cut SAW devices for different mean operating temperatures. A slight rotation of ψ , as shown in Figure 22, could be used to set the first order TCF to zero while slightly altering the second order TCF of the device. This cut also represents a substantial improvement over the ST-cut (see Table 8). Figures 30 through 34 summarize some of our typical measurements to date. Results in this area are in excellent agreement with the theory. One of these cuts (8.033/26.967/134.6) has temperature stability of approximately 40 ppm from 0°C to 130°C ; it is suitable for systems or weapons operating in elevated temperatures (see Figure 33).

On all cuts tested, the agreement between the experimental and calculated results has been excellent. These results establish a firm basis for performing the second iteration search for the optimum TCF orientations.



4147-6

Figure 25. Experimental Set-Up For Laser Probe



4147-7

Figure 26. Angular Relation of Incidence and Reflected Beam

TABLE 8. COMPARISON OF EXPERIMENTAL AND CALCULATED RESULTS

Angles		Calculated					Measured		
Phi	Theta	Psi	TCF ^{(1)**}	TCF ^{(1)***}	TCF ^{(2)***}	TCF ^{(3)***}	TCF ⁽¹⁾	TCF ⁽²⁾	TCF ⁽³⁾
0	42.75	0*	-0.07 x 10 ⁻⁵	0.06 x 10 ⁻⁵	-0.40 x 10 ⁻⁷	0.11 x 10 ⁻¹⁰	-0.1 x 10 ⁻⁵	-0.37 x 10 ⁻⁷	-0.17 x 10 ⁻¹⁰
8.05	25.9	135.7	-0.01	0.74	-0.15	0.42	0.16	-0.16	0.58
6.57	26.88	134.9	-0.24	0.55	-0.15	0.43	0.025	-0.16	0.47
8.03	26.97	134.6	-0.18	0.60	-0.15	0.46	0.007	-0.13	0.46
7.41	27.83	134.2	-0.26	0.54	-0.15	0.49	-0.08	-0.15	0.63
6.00	26.97	135.8	-0.04	0.75	-0.14	0.46	0.15	-0.13	0.30
5.58	27.83	135.2	-0.15	0.65	-0.14	0.49	0.13	-0.13	0.28

*Wafer obtained commercially, angular tolerance is unknown.

**Calculated using Sinha and Tiersten's program.

***Calculated using the finite difference approach.

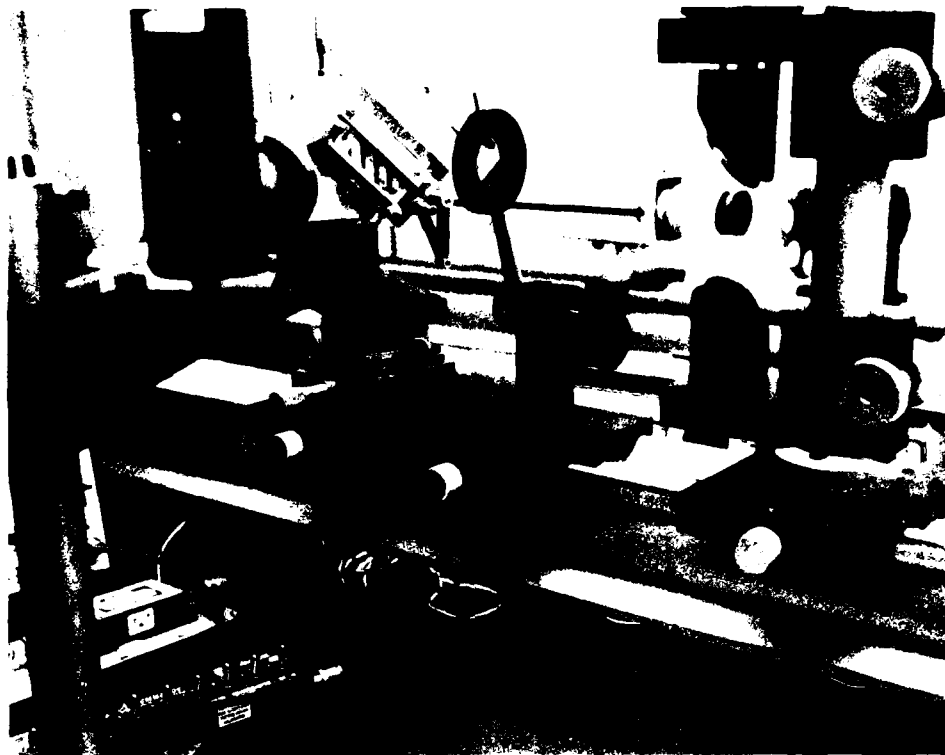


Figure 27. Test Set-up for Laser Probing of Acoustic Wave Beam-Steering Characteristics

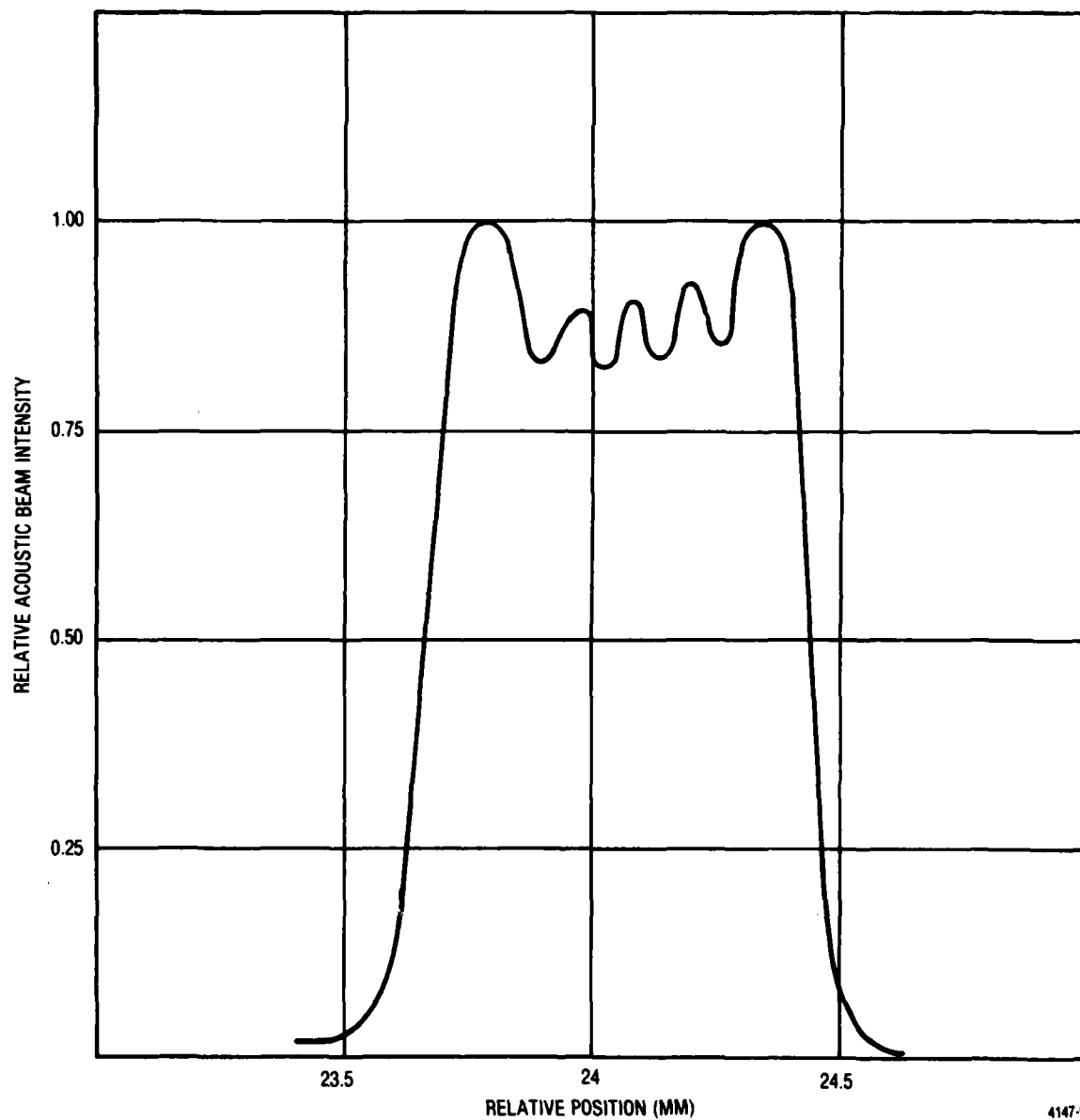
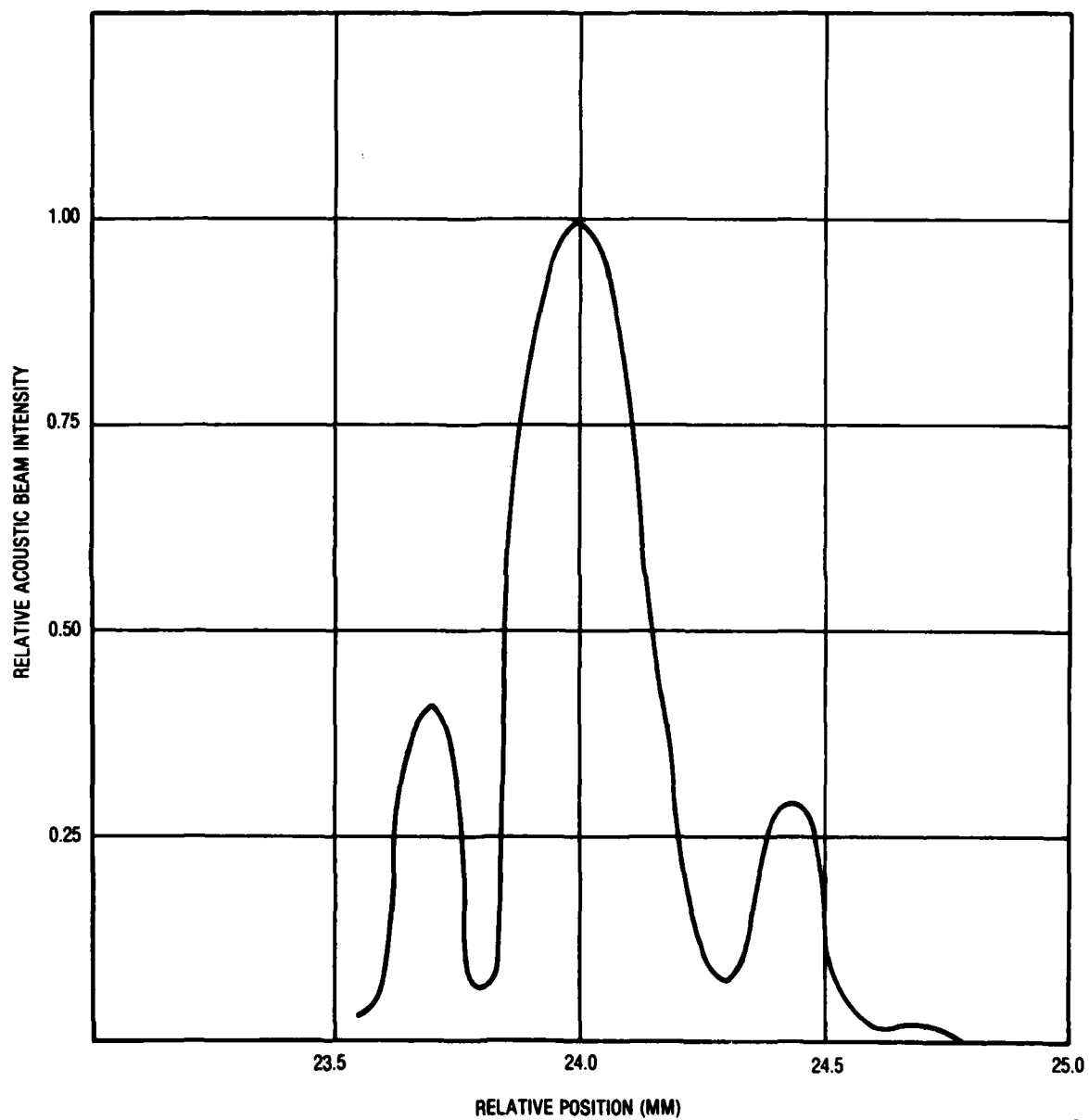


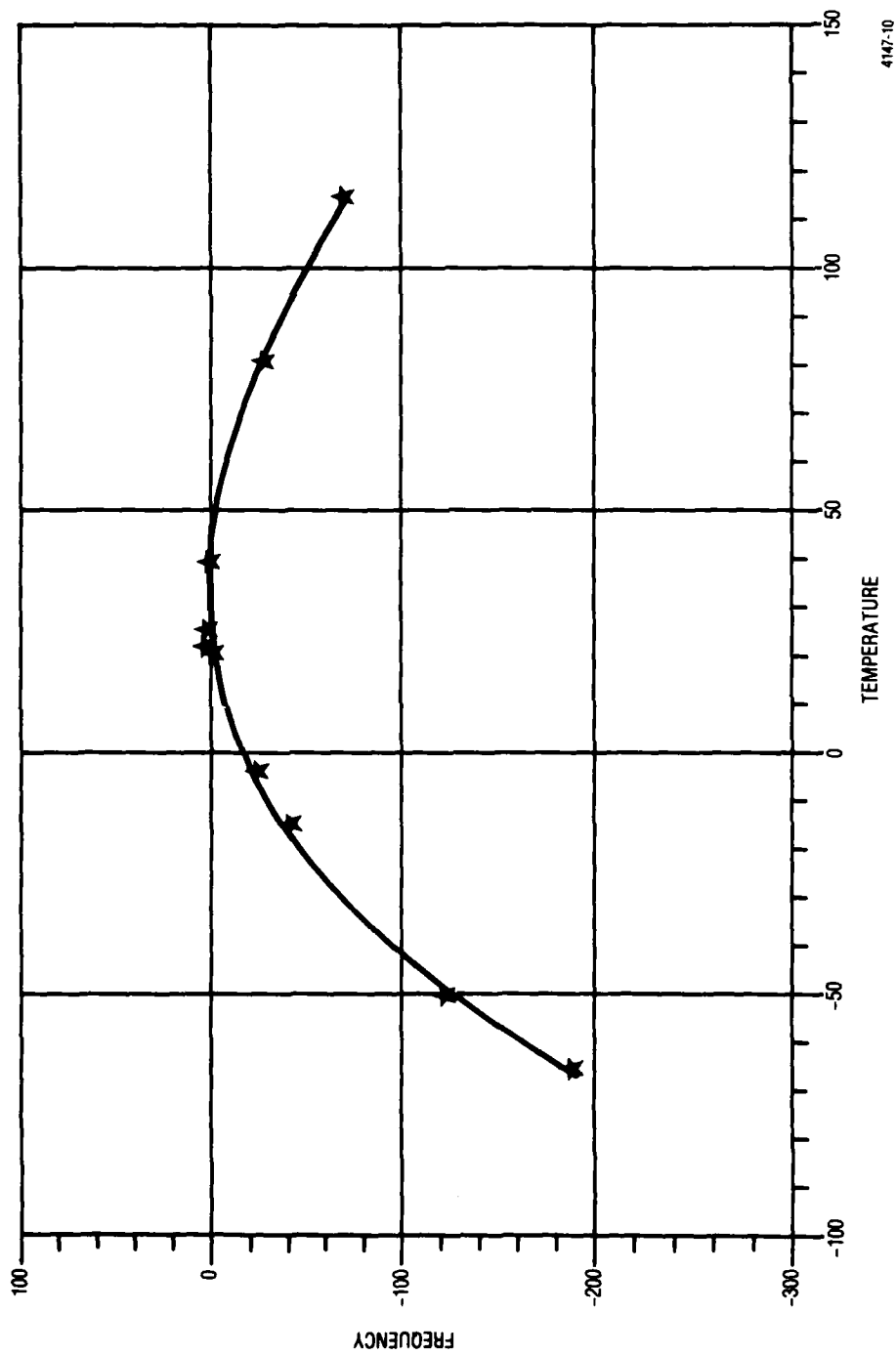
Figure 28. Intensity Distribution at Near Field



4147-15

Figure 29. Intensity Distribution at Far Field

EXP ANGLES ARE 6.567, 26.983, 134.9



4147-10

Figure 30. Experimental Frequency Response (Test No. 1)

EXP ANGLES ARE 5.583, 27.833, 135.1

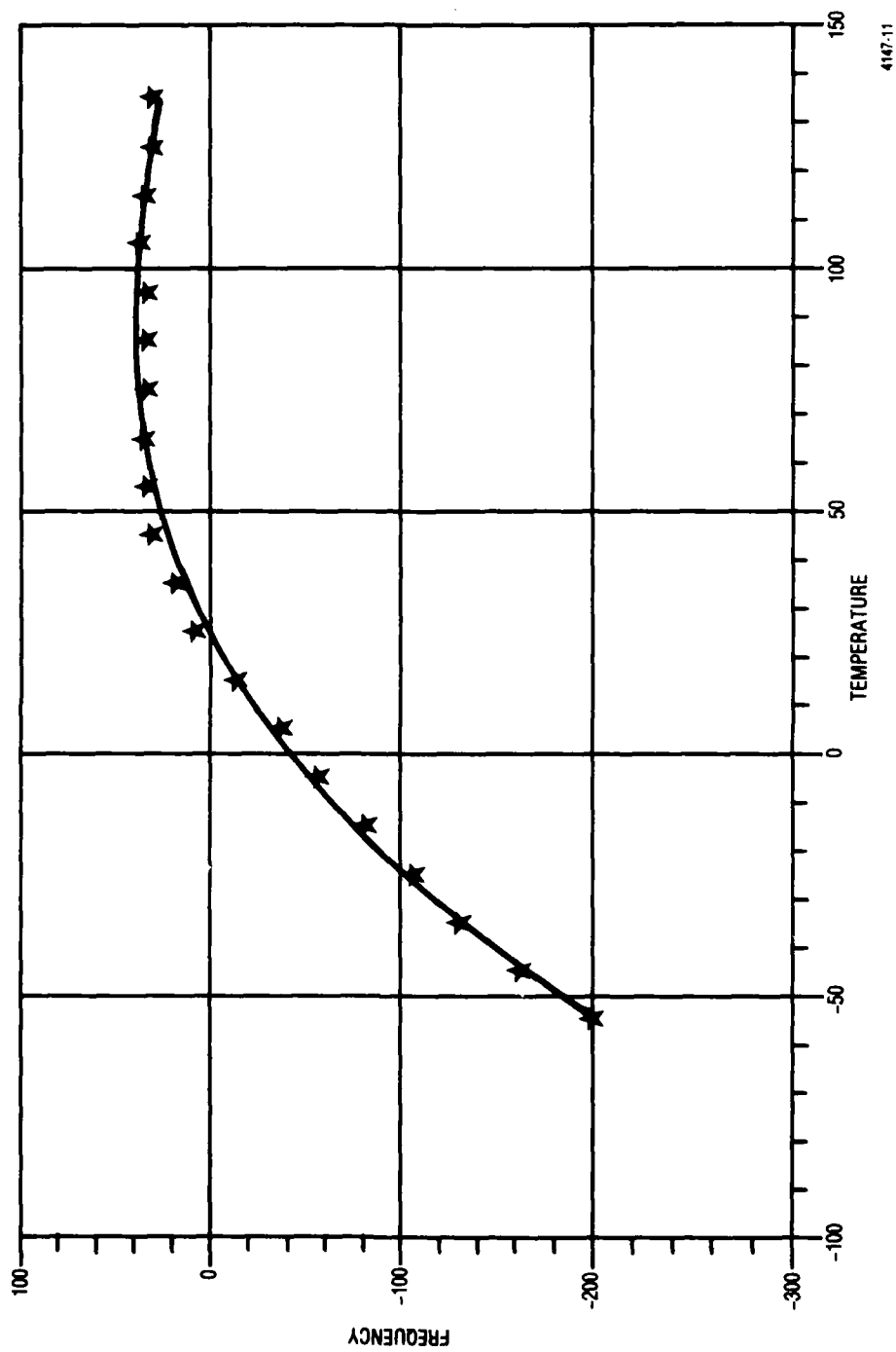
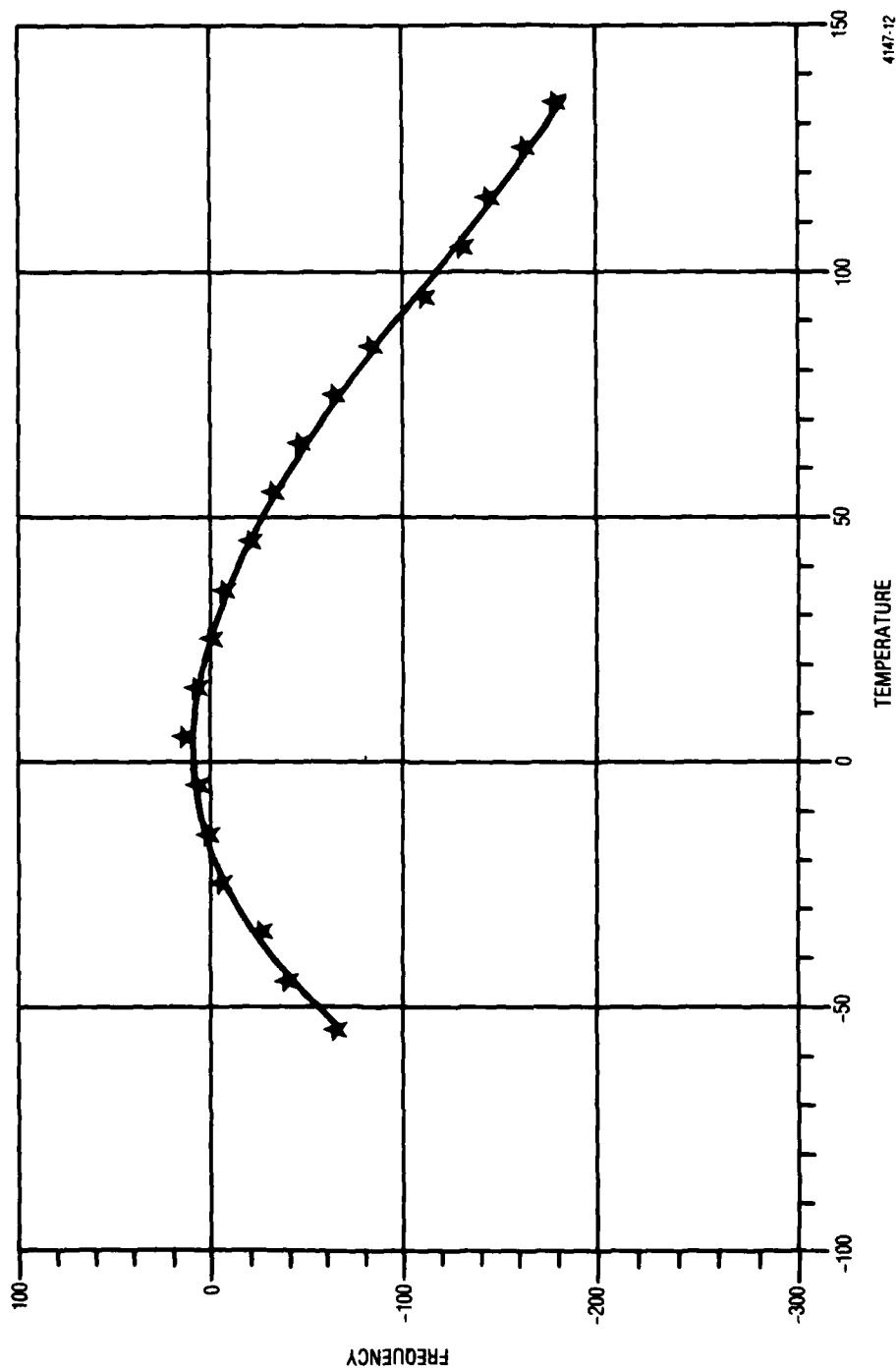


Figure 31. Experimental Frequency Response (Test No. 2)

EXP ANGLES ARE 7.410, 27.830, 134.2



4147-12

Figure 32. Experimental Frequency Response (Test No. 3)

EXP ANGLES ARE 8.033, 26.967, 134.6

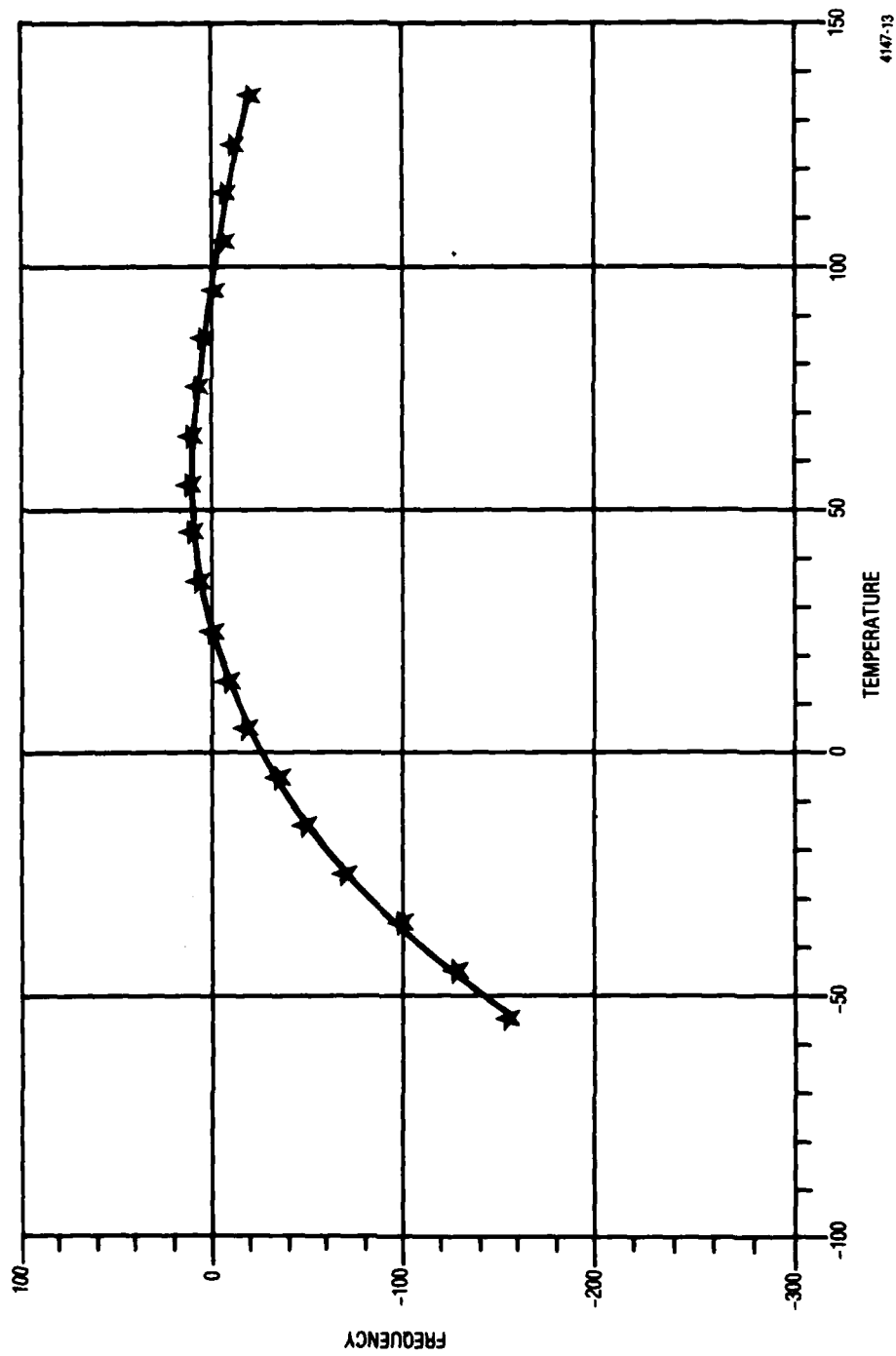
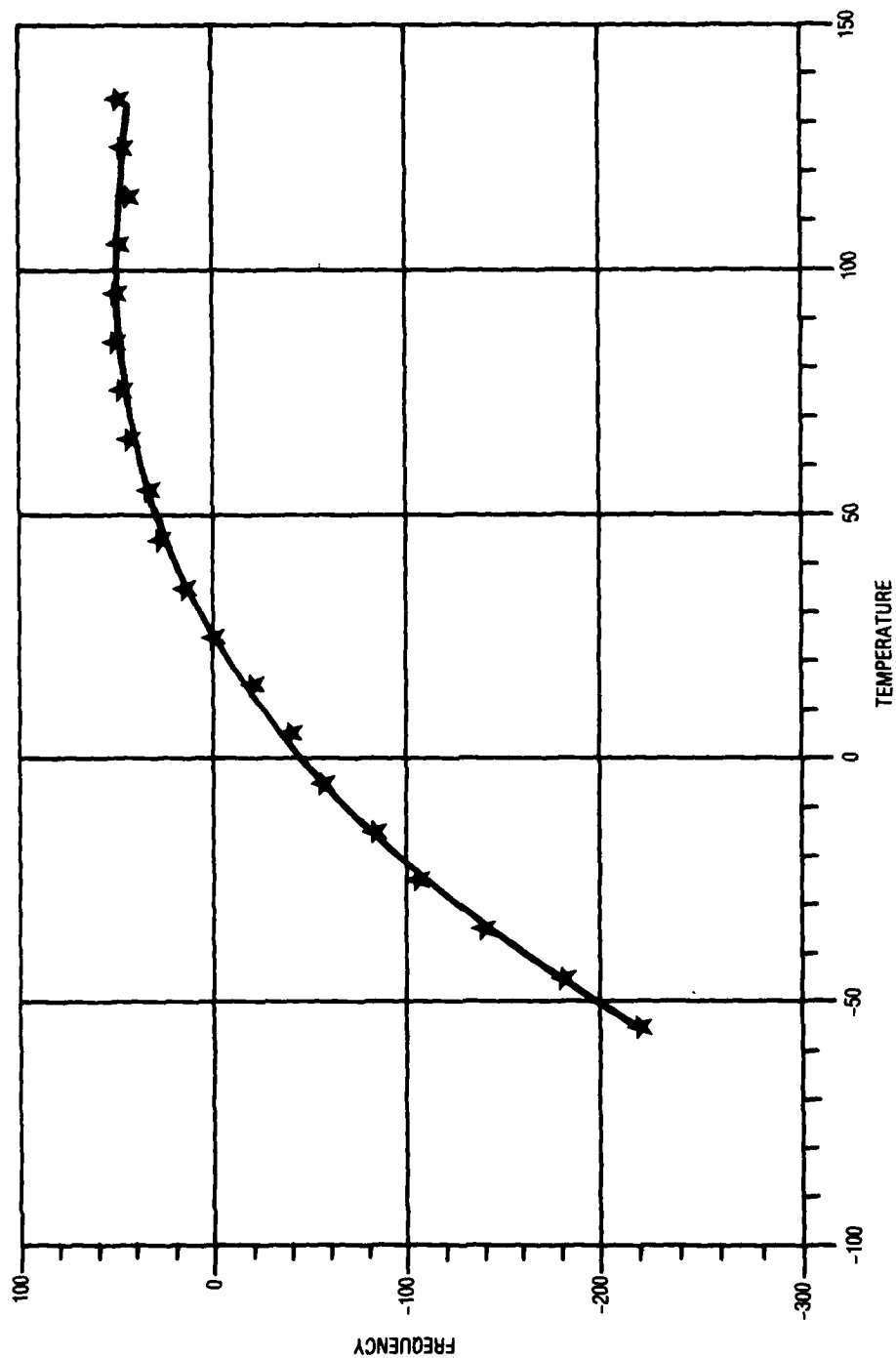


Figure 33. Experimental Frequency Response (Test No. 4)

EXP ANGLES ARE 6.000, 26.967, 135.8



4147-14

Figure 34. Experimental Frequency Response (Test No. 5)

SECTION IV

TECHNICAL DISCUSSION OF 2ND ITERATION

1. INTRODUCTION

The search for a temperature stable cut of quartz for application to SAW devices has led to the investigation of the doubly rotated cuts. Theoretical studies have indicated that doubly rotated cuts of quartz promise much better temperature stability than the commonly used ST cut. The first iteration of this program, which encompassed the Task I calculations of the doubly rotated cuts of quartz, and the Task II experimental work, were discussed in Sections II and III. The second iteration calculations and analysis and experimental results are shown in this section.

In Task I, theoretical analyses were performed and angular rotations promising very low $TCF^{(1)}$ and $TCF^{(2)}$ were plotted. Important SAW device design parameters, such as coupling coefficient, velocity and power flow angle, were computed to characterize each area. As part of Task II, experimental results establishing the degree of correlation with theory were obtained.

Theoretical calculations have been in good agreement with experimental results. Doubly rotated cuts of quartz with an improvement of $TCF^{(2)}$ by at least a factor of two over the ST cut have been obtained. A further improvement was obtained after a second iteration.

Paragraph 2 presents experimental determination of propagation characteristics which illustrate an excellent agreement between theoretical calculation and experimental results. It also contains the results of the doubly rotated cut TCF measurements made to date. In Paragraph 3 the second iteration theoretical results are presented. Doubly rotated cuts with superior temperature characteristics to those discovered in the first iteration are presented. In Paragraph 4 the temperature variation of the power flow angle and a new mask design insensitive to this variation are discussed.

2. EXPERIMENTAL RESULTS

In Section III, experimental results were presented demonstrating the good agreement with the theory. The results of the experimental work performed are summarized in Table 9. The orientations of Table 9 are expressed in the notation of the IRE 1949 standards³ and were obtained by selecting measurements with zero first-order temperature coefficients of frequency. This was done to ease the comparison between the experimental and theoretical results because these angles can be accurately

³"Standards on Piezoelectric Crystals 1949", Pro. IRE 14, Dec. 1949, pp. 1378-1395.

calculated theoretically, and because it is a necessary condition for low TCF orientation. A more accurate measurement of the second-order temperature coefficient of frequency usually results when the first-order coefficient is small. The experimental and calculated results, as can be seen from Table 9, have maintained their high degree of accuracy.

Figure 35 shows a typical frequency-temperature curve used to generate the data in Table 9. The stars represent experimental data points. The solid lines are linearly regressed curves used to define the measured first-, second-, and third-order TCF's for these cuts found in the table. The first order temperature coefficient is small enough so that only a light mask rotation is required to arrive at an orientation with a zero TCF⁽¹⁾. This small rotation is not enough to significantly change the second-order TCF. Experimental devices with a near zero first-order TCF and a second-order TCF of approximately $-1.0 \times 10^{-8}/\text{C}^2$ have been measured. These measured second-order TCF's are significantly lower than the lowest previous measurements of approximately -1.5×10^{-8} with a zero TCF⁽¹⁾. Figures 36 through 41 are graphs of experimental frequency temperature characteristics of devices fabricated at optimum orientations. Changes in the frequency behavior as a function of mask alignment can be seen clearly.

TABLE 9. COMPARISON OF EXPERIMENTAL AND CALCULATED RESULTS

ANGLES			CALCULATED				MEASURED		
PHI	THET	PSI	TCF ¹ ††	TCF ¹ †††	TCF ² †††	TCF ³ †††	TCF ¹	TCF ²	TCF ³
0	42.75	0†	-0.07×10^{-5}	0.06×10^{-5}	-0.40×10^{-7}	0.11×10^{-10}	-0.1×10^{-5}	-0.37×10^{-7}	-0.17×10^{-10}
8.05	25.9	135.7	-0.01	0.74	-0.15	0.42	0.16	-0.16	0.56
8.57	26.88	134.9	-0.24	0.55	-0.15	0.43	0.025	-0.16	0.47
8.03	26.97	134.6	-0.18	0.60	-0.15	0.46	0.067	-0.13	0.46
7.41	27.83	134.2	-0.26	0.54	-0.15	0.49	-0.06	-0.15	0.63
6.00	26.97	135.8	-0.04	0.75	-0.14	0.46	0.15	-0.13	0.30
5.58	27.83	135.2	-0.15	0.65	-0.14	0.49	0.13	-0.13	0.28
-0.03	26.70	138.9	0.28	1.10	-0.11	0.48	0.43	-0.11	0.49
-0.13	26.1	137.7	0.06	0.89	-0.11	0.53	0.24	-0.097	0.25
0.633	26.15	137.0	-0.24	0.57	-0.13	0.47	-0.11	-0.15	0.66
-0.967	26.23	138.4	0.01	0.82	-0.12	0.51	0.34	-0.13	0.79

†WAFER OBTAINED COMMERCIALY. ANGULAR TOLERANCE IS UNKNOWN.

††CALCULATED USING SINHA AND TIERSTEN'S PROGRAM.

†††CALCULATED USING FINITE DIFFERENCE APPROACH.

3. THEORETICAL RESULTS

The first iteration results were utilized to refine the theoretical results obtained earlier. The close agreement between theory and experiment demonstrated earlier prompted a more thorough theoretical search for promising temperature-stable doubly rotated orientations. An attempt to determine optimum orientations was felt justified in light of the accuracy of the calculated results. Second-order TCF's are predicted by the finite difference method to within $0.005 \text{ ppm}/\text{C}^2$. First-order TCF's are predicted to within $3 \text{ ppm}/\text{C}^\circ$ by the Sinha and Tiersten perturbation method.

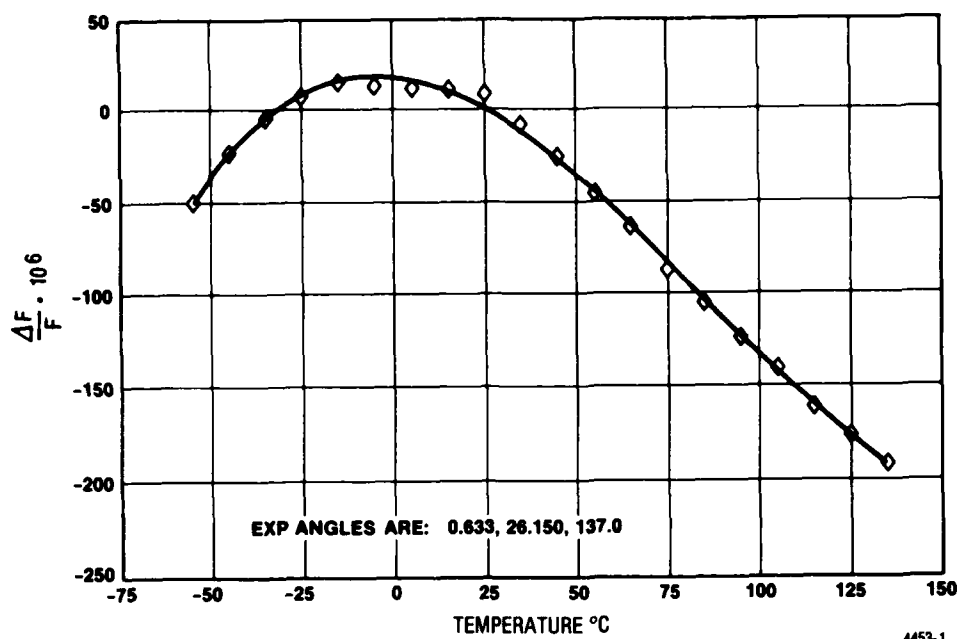


Figure 35. Frequency-Temperature Dependence for (YX wlt) 0.633/26.15/137.0

A more thorough search in and near previously discovered near-optimum orientations did not yield any new results. Other areas previously considered as not quite optimum, on closer examination, were found to have a greater predicted temperature stability than any other orientations yet measured. A second-order TCF of $-0.93 \times 10^{-8}/\text{C}^2$ with a zero first-order TCF is predicted for a new family of cuts. The significance of this family of temperature-stable cuts will become evident only after devices are built and experimental results are compared, as the difference in $\text{TCF}^{(2)}$'s is about 10 percent. The addition of this family of cuts to our investigation is also significant as it opens up the possibility of selecting cuts not only for improved temperature stability but for improved stress compensation.

Table 10 contains a list of crystal orientations with zero first-order TCF's and low second-order TCF's. Two new families of cuts, centered about (YX wlt) $15^\circ/30^\circ/38^\circ$ and (YX wlt) $12.5^\circ/35^\circ/130^\circ$ are included in Table 10. Second-order $\text{TCF}^{(2)}$'s of -1.0×10^{-8} and -0.93×10^{-8} are predicted for the two families. Each of the families extends over a surface with a PHI variation of 20° and 15° respectively, and a THETA variation of about 5° and 10° respectively, the PSI angle for obtaining a zero $\text{TCF}^{(2)}$ being fixed for each PHI and THETA. Figures 42 through 45 show these areas in detail. Both the zero $\text{TCF}^{(1)}$ curves calculated by Sinha and Tiersten's perturbation approach and the finite difference method are shown. Overlapping second-order TCF contours are also plotted.

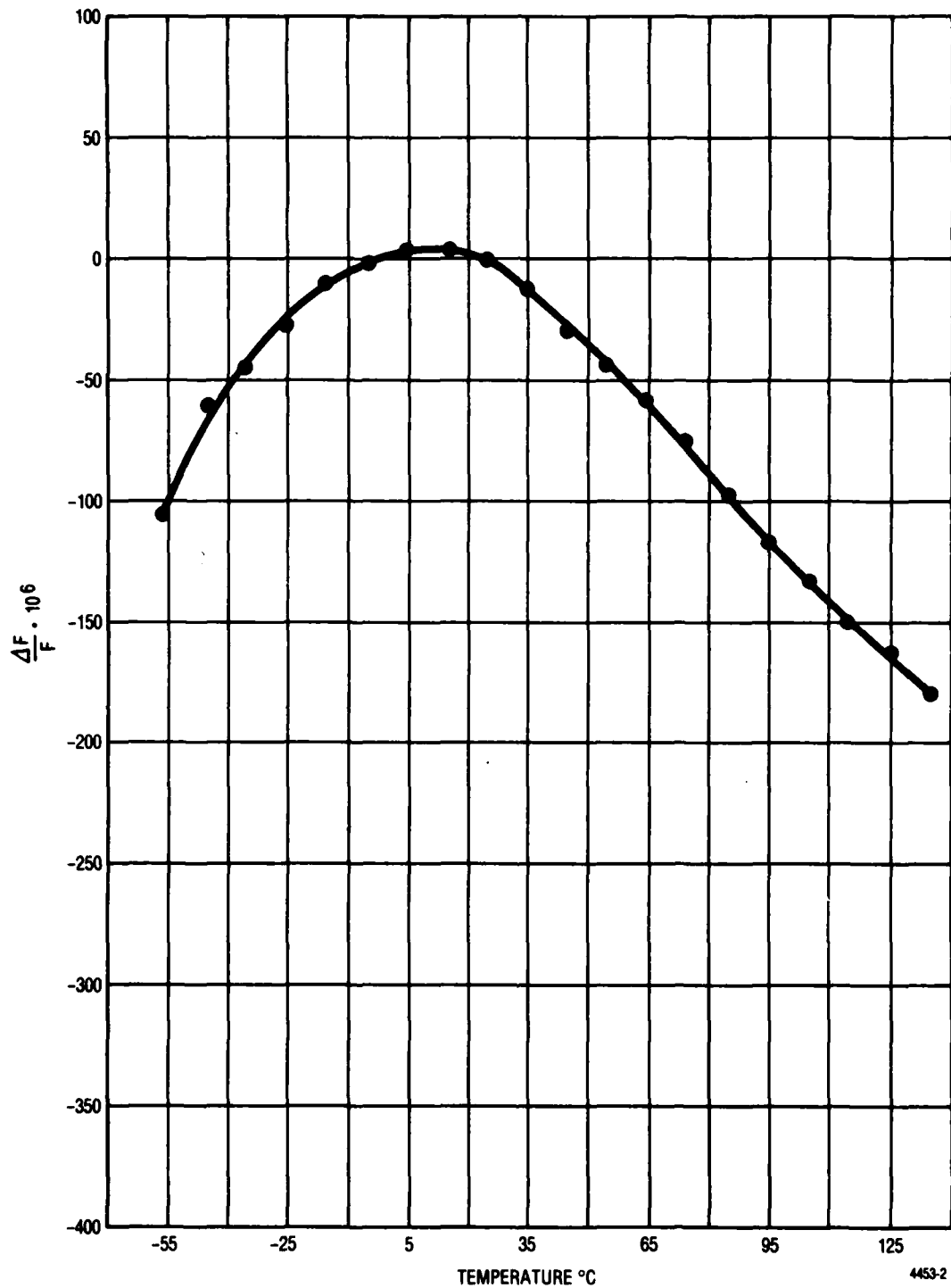


Figure 36. Frequency-Temperature Dependence for (YX wlt)-1.05/28.0667/136.534

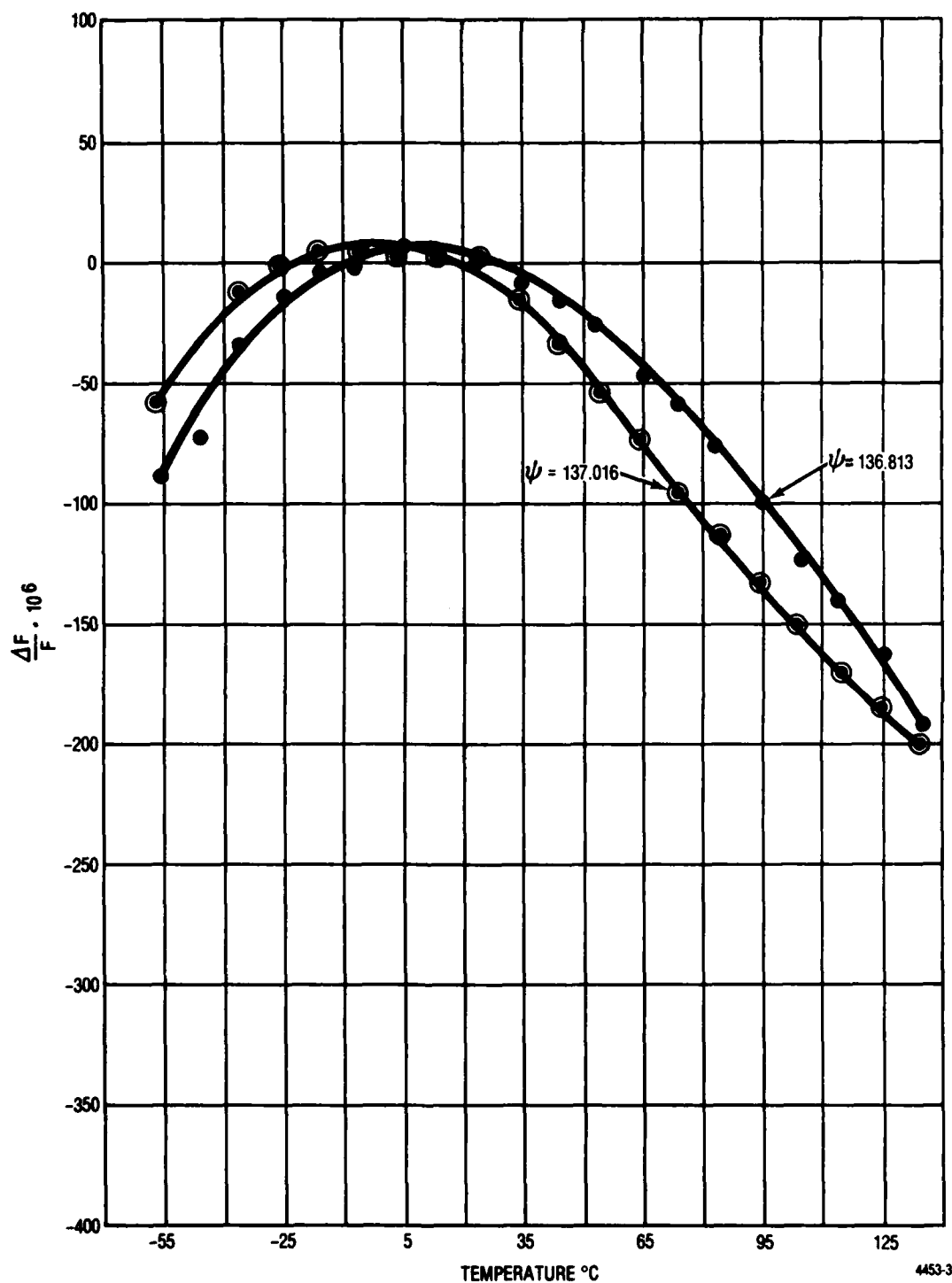


Figure 37. Frequency-Temperature Dependence for
(YX wlt) 0.633/26.15/136.813 to (YX wlt) 0.633/26.15/137.016

4453-3

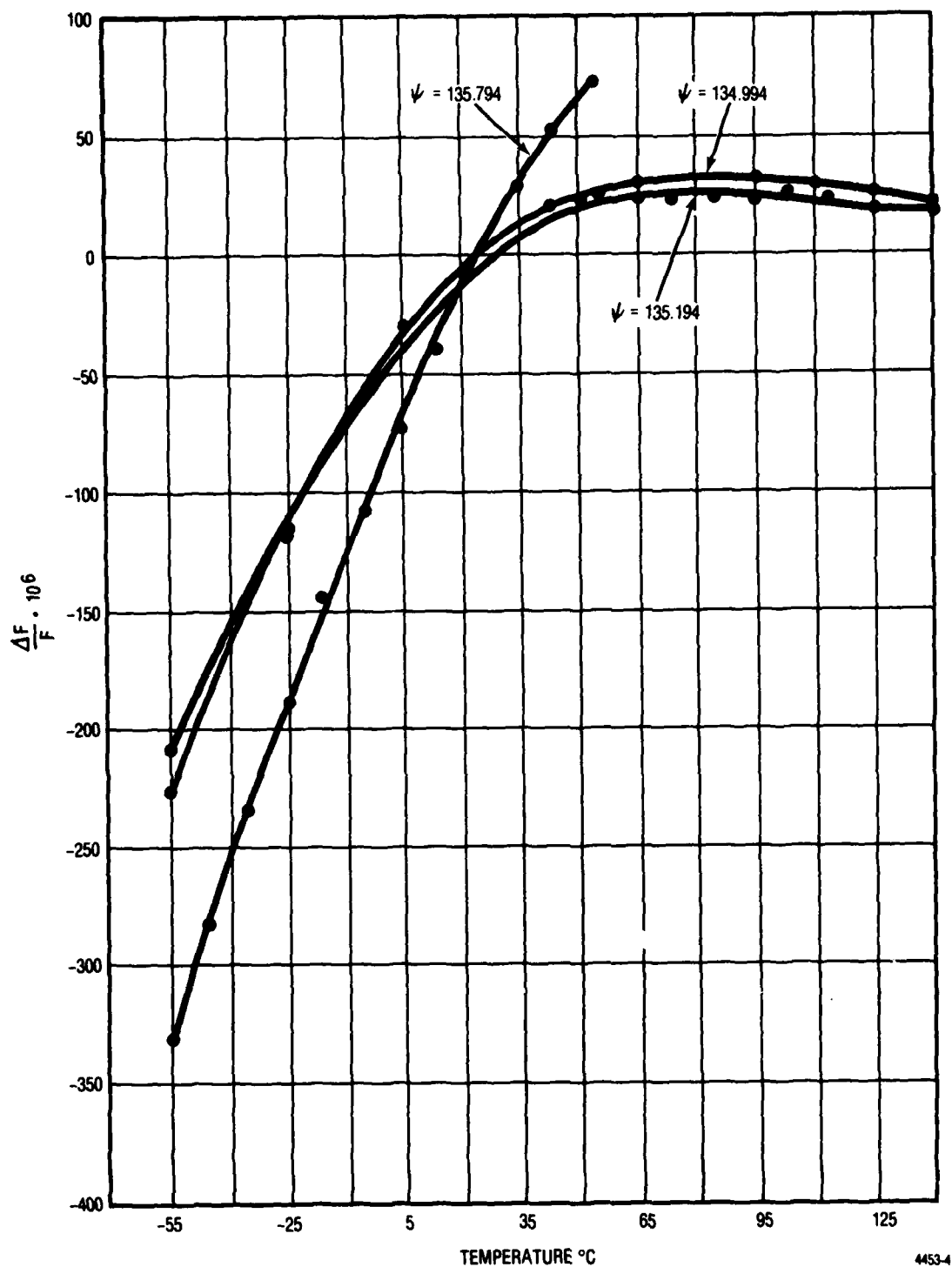


Figure 38. Frequency-Temperature Dependence for
(YX wlt) 5.583/27.833/134.994 to (YX wlt) 5.583/27.833/135.794

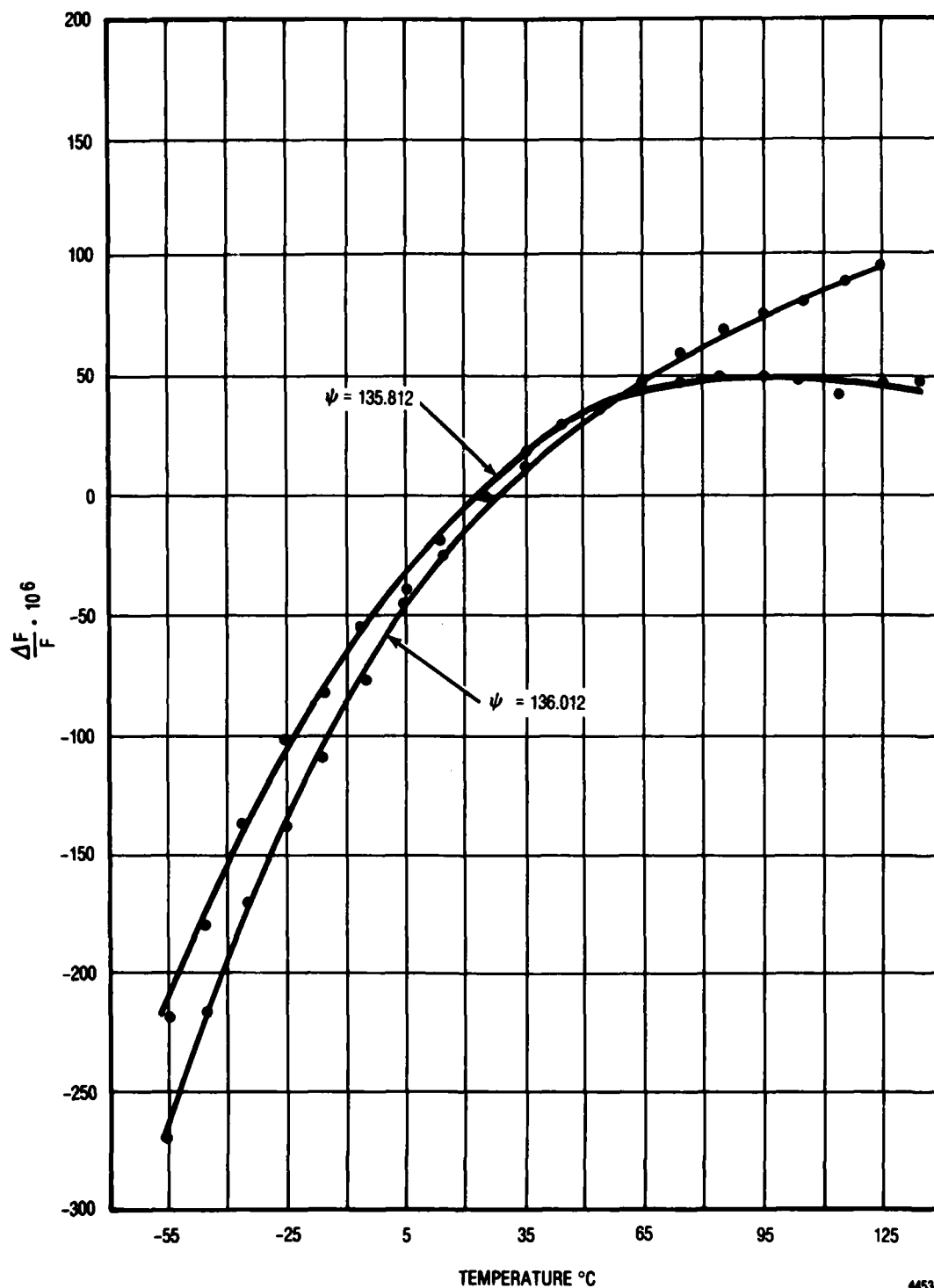


Figure 39. Frequency-Temperature Dependence for
(YX wlt) 6/26.967/135.812 to (YX wlt) 6/26.967/136.012

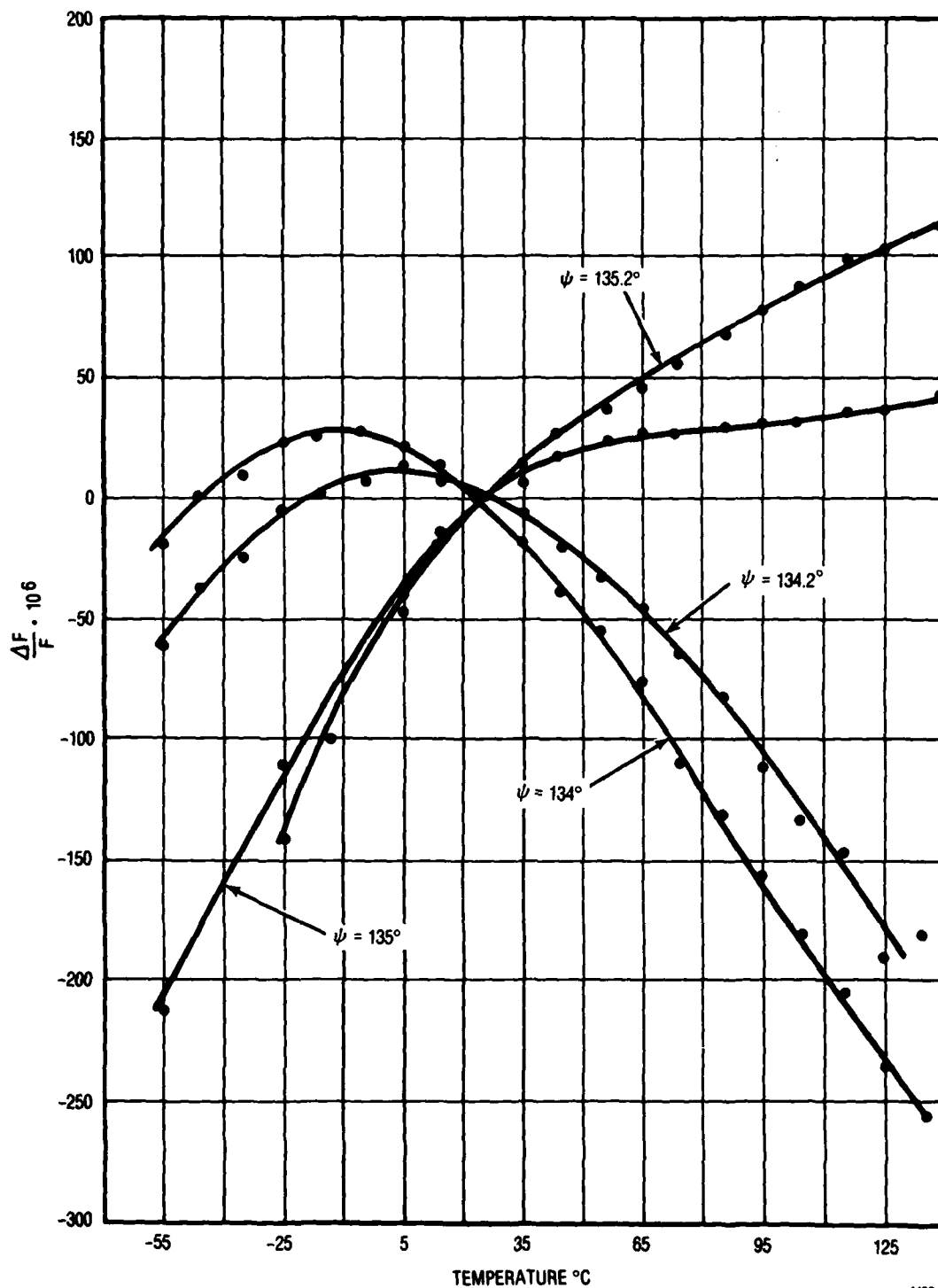


Figure 40. Frequency-Temperature Dependence for
(YX wlt) 7.417/27.833/134 to (YX wlt) 7.417/27.833/135.2



Figure 41. Frequency-Temperature Dependence for
(YX wlt) 8.033/26.9667/134.618 to (YX wlt) 8.033/26.9667/136.818

TABLE 10. PROPAGATION CHARACTERISTICS OF CRYSTAL ORIENTATIONS

ANGLES OF ZTCF(1) DEGREES (S AND T'S PROGRAM)			TCF(2)/°C ² (X10 ⁻⁸) FINITE DIFFERENCE PROGRAM	TCF(3)/°C ³ (X10 ⁻¹⁰) FINITE DIFFERENCE PROGRAM
PHI	THETA	PSI		
6	26	136.31	-1.4	
6	27	135.93	-1.3	0.67
6	28	135.59	-1.3	0.57
7	26	135.99	-1.5	
7	27	135.64	-1.4	
7	28	135.27	-1.3	0.65
8	26	135.74	-1.4	0.65
8	27	135.36	-1.4	
8	28	134.97	-1.3	
1	26	137.78	-1.2	0.68
1	27	137.48	-1.2	0.65
1	28	137.17	-1.1	0.67
0	26	138.07	-1.2	0.67
0	27	137.78	-1.1	0.68
0	28	137.49	-1.1	0.62
-1	26	138.37	-1.2	0.60
-1	27	138.09	-1.2	0.62
-1	28	137.80	-1.1	0.73
14	39	40.195	-1.0	0.64
14	40	40.415	-1.0	0.66
14	41	40.64	-1.0	0.75
15	39	39.79	-1.0	0.63
15	40	40	-1.0	0.74
15	41	40.23	-1.0	0.73
16	39	39.4	-1.0	0.68
16	40	39.605	-1.0	0.66
16	41	39.825	-1.1	0.60
7.5	35.0	41.77	-0.95	0.58
10	35	40.82	-0.94	0.58
12.5	30	38.88	-0.93	0.57
12.5	32.5	39.4	-0.93	0.57
15.0	30.0	38.12	-0.93	0.57
15.0	32.5	38.55	-0.93	0.57
17.5	30.0	37.35	-0.94	0.56
20.0	30.0	36.6	-0.97	0.55
22.5	30.0	35.85	-1.0	0.54
25.0	30.0	35.07	-1.0	0.52
27.5	30.0	34.28	-1.1	0.50
7.5	35.0	132.68	-1.1	0.54
10.0	40.0	129.4	-1.1	0.57
12.5	35.0	130.82	-1.0	0.41
12.5	42.5	127.15	-1.1	0.58
15.0	45.0	124.43	-1.1	0.58
17.5	40.0	126.14	-1.1	0.54
20.0	40.0	124.92	-1.0	0.44

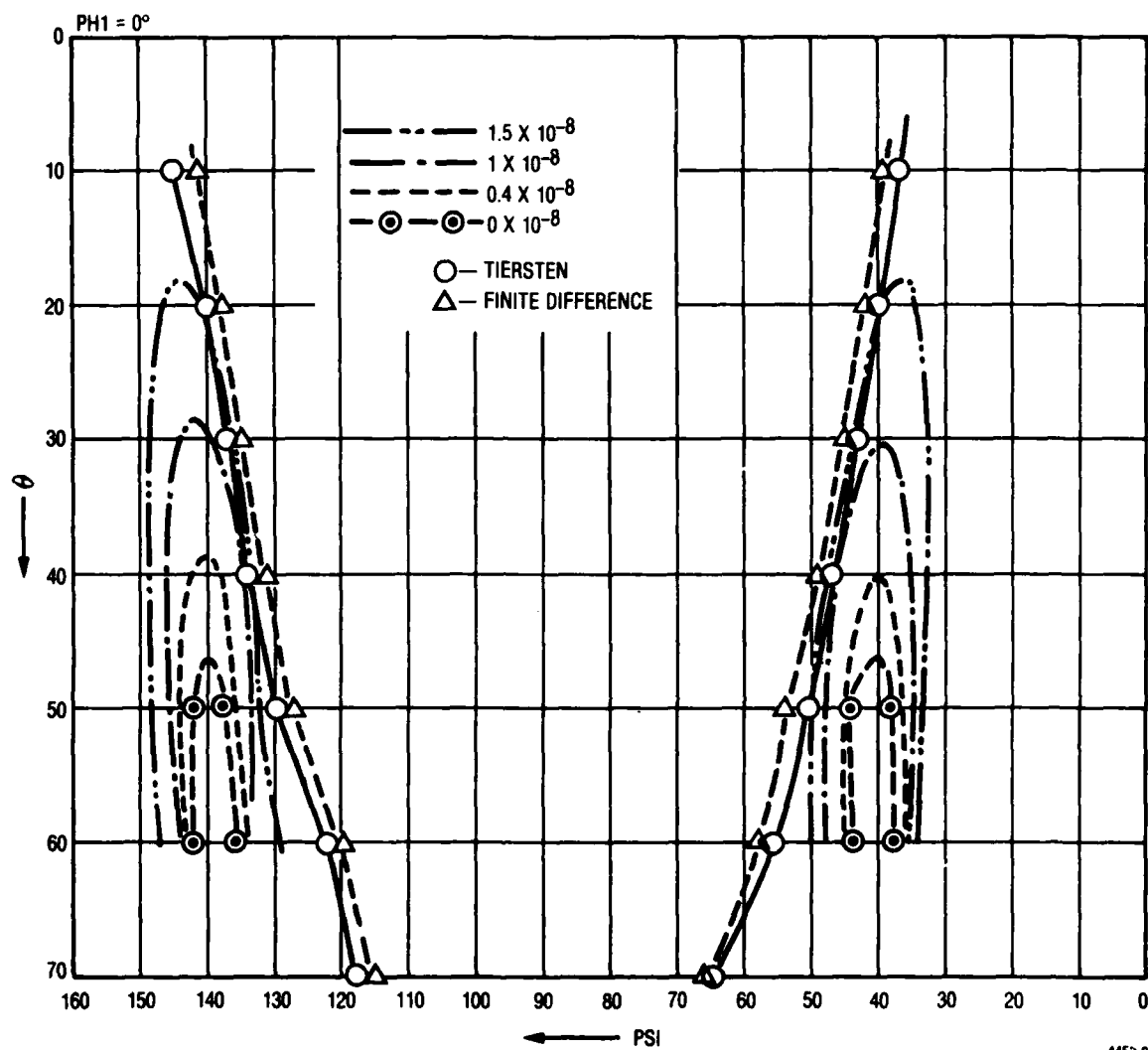


Figure 42. TCF Contour Map (PHI = 0°)

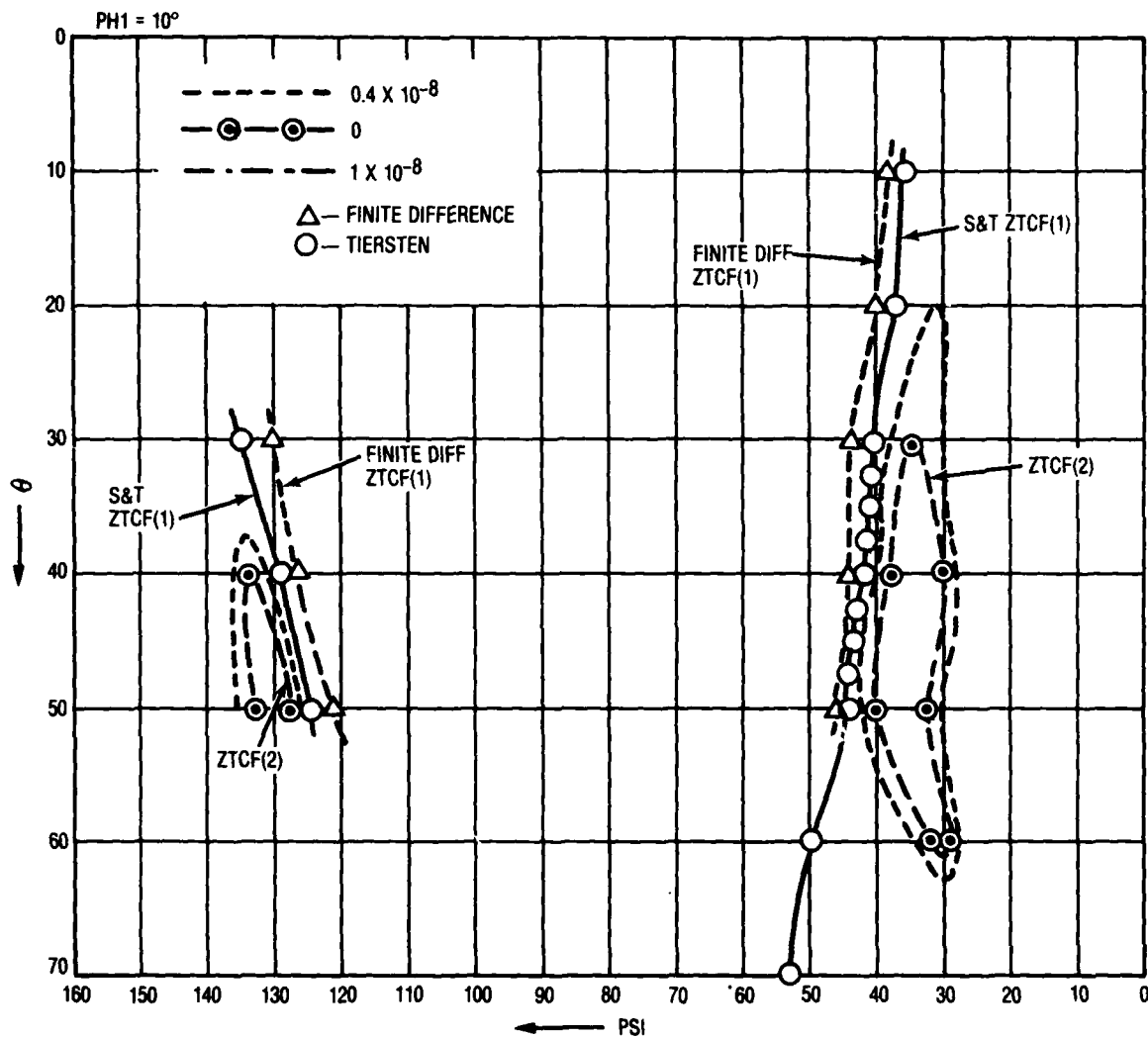


Figure 43. TCF Contour Map ($\phi = 10^\circ$)

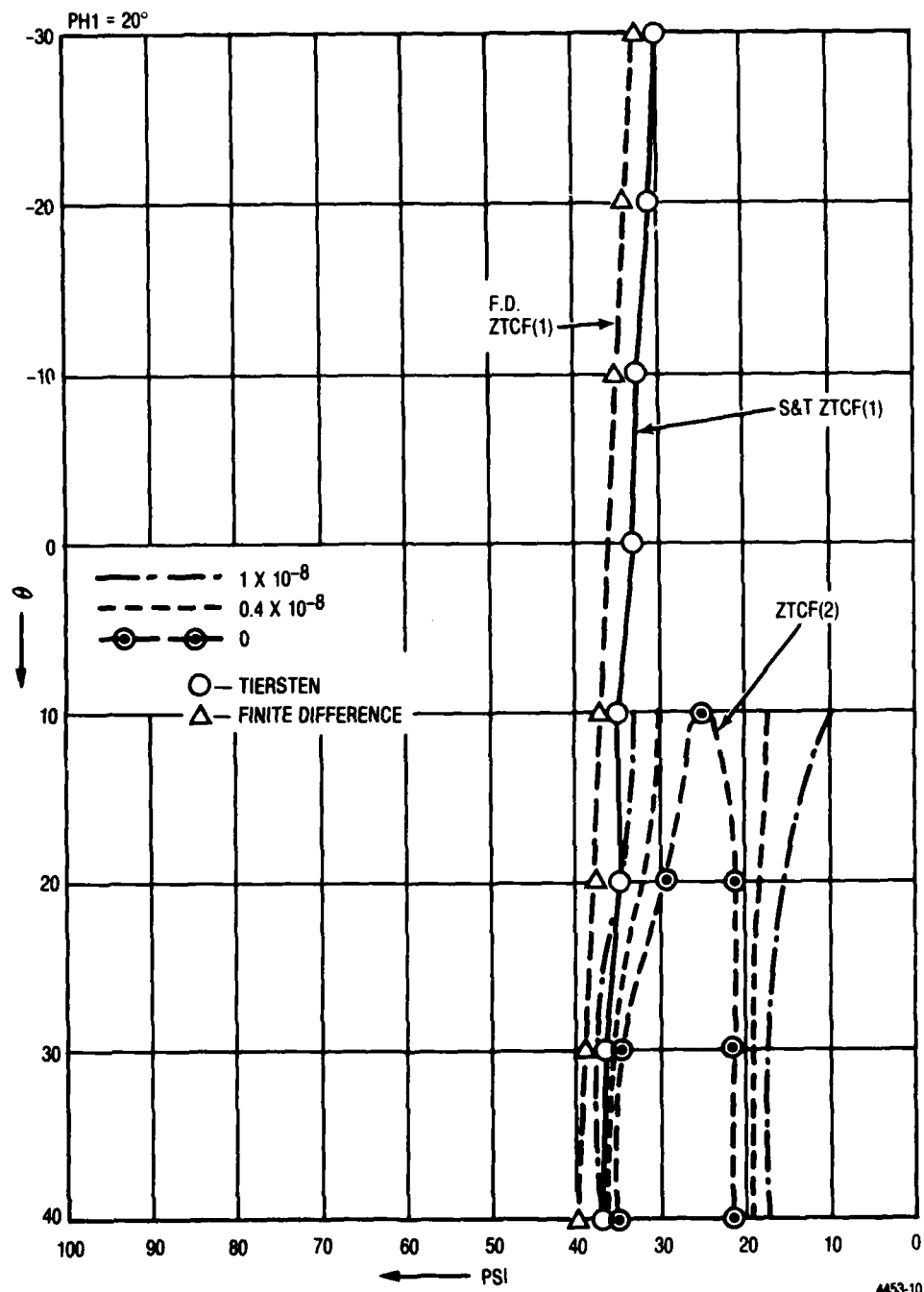
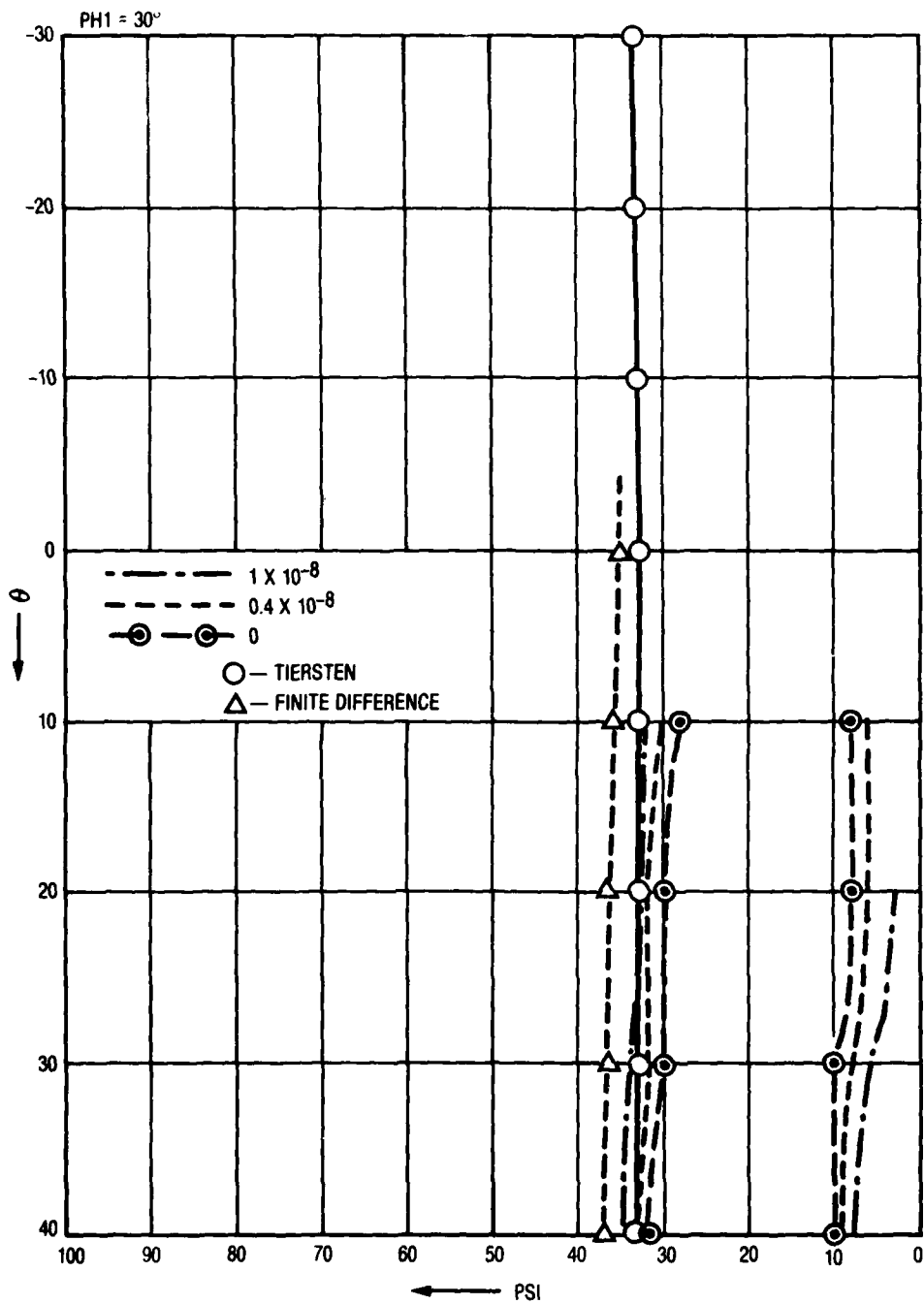


Figure 44. TCF Contour Map (PHI = 20°)



4453-11

Figure 45. TCF Contour Map ($\text{PHI} = 30^\circ$)

Table 11 contains some of the propagation characteristics of these selected orientations. The velocities, coupling coefficients, and power flow angles are seen to be quite reasonable. Tables 12 and 13 contain the derivatives of the first-order temperature coefficients of frequency with respect to angular changes in orientation. These derivatives determine the accuracy with which one must fabricate to ensure a negligible $TCF^{(1)}$. The nonzero value of $\partial TCF^{(1)}/\partial\phi$ allows a compensation for misalignment of the wafer orientation by a compensation in mask orientation as the values of $\partial TCF^{(2)}/\partial\phi$, $\partial TCF^{(2)}/\partial\theta$, and $\partial TCF^{(2)}/\partial\psi$ are small. In the first iteration of Task II, it was demonstrated that devices with these $TCF^{(1)}$ angular derivatives are easily fabricated with low $TCF^{(1)}$. These two families of cuts are believed to be entirely suitable to temperature-stable SAW device fabrication.

TABLE 11. PROPAGATION CHARACTERISTICS OF SELECTED ORIENTATIONS

ANGLES OF ZTCF ⁽¹⁾ , DEGREES (S AND T'S PROGRAM)			VELOCITY (MSEC)	K ² (X10 ⁻³)	POWER FLOW ANGLE (DEGREES)
PH	THETA	PHI			
6	26	136.31	3296.84	1.12	-0.3
6	27	136.93	3293.80	1.12	-0.2
6	28	136.59	3290.63	1.12	-0.1
7	26	136.99	3303.33	1.12	-0.5
7	27	136.64	3299.70	1.12	-0.4
7	28	136.27	3296.33	1.12	-0.3
8	26	135.74	3310.15	1.12	-0.7
8	27	135.36	3306.11	1.12	-0.6
8	28	134.97	3302.32	1.10	-0.5
1	26	137.79	3268.80	1.10	+0.7
1	27	137.48	3267.44	1.10	+0.8
1	28	137.17	3266.36	1.10	+1.0
0	26	136.07	3284.08	1.12	+0.9
0	27	137.78	3283.08	1.10	+1.1
0	28	137.49	3282.36	1.10	+1.2
-1	26	136.37	3259.65	1.10	+1.1
-1	27	136.09	3259.01	1.10	-1.3
-1	28	137.80	3258.84	1.08	+1.5
14	39	40.196	3298.80	0.96	-7.7
14	40	40.415	3306.87	0.96	-8.1
14	41	40.64	3315.19	0.94	-8.6
15	39	39.79	3301.82	0.96	-7.8
15	40	40.00	3310.14	0.94	-8.3
15	41	40.23	3319.09	0.96	-8.8
16	39	39.4	3306.38	0.96	-8.0
16	40	39.605	3314.03	0.96	-8.4
7.5	36.0	41.77	3282.43	1.00	-4.6
10	36.0	40.82	3284.23	1.01	-5.3
12.5	30.0	38.88	3243.27	1.01	-4.1
12.5	32.5	39.4	3254.48	1.00	-4.9
15.0	30.0	38.12	3244.99	0.98	-4.6
15.0	32.5	38.55	3257.82	0.98	-5.3

TABLE 12. $\partial TCF^{(1)}/\partial \psi$ FOR SELECTED CUTS

Angles of ZTCF ⁽¹⁾ , Degrees (S and T'S Program)			$\partial TCF^{(1)}/\partial \psi$
PHI	THETA	PSI	
6	26	136.31	+2.7 (PPM/C°)/DEGREE
6	27	135.93	+2.7
6	28	135.59	+2.7
7	26	135.99	+2.7
7	27	135.64	+2.7
7	28	135.27	+2.7
8	26	135.74	+2.7
8	27	135.36	+2.7
8	28	134.97	+2.7
1	26	137.78	+2.8
1	27	137.48	+2.8
1	28	137.17	+2.8
0	26	138.07	+3.0
0	27	137.78	+3.0
0	28	137.49	+3.0
-1	26	138.37	+3.0
-1	27	138.09	+3.0
-1	28	137.08	+3.0
14	39	40.195	-3.5
14	40	40.415	-3.5
14	41	40.64	-3.5
15	39	39.79	-3.5
15	40	40	-3.5
15	41	40.23	-3.5
16	39	39.4	-3.7
16	40	39.605	-3.7
16	41	39.825	-3.7
7.5	35.0	41.77	-3.3
10.0	35.0	40.82	-3.4
12.5	30.0	38.88	-3.3
12.5	32.5	39.4	-3.2
15.0	30.0	38.12	-3.4

TABLE 12. $\partial \text{TCF}^{(1)} / \partial \psi$ FOR SELECTED CUTS (Cont)

Angles of ZTCF ⁽¹⁾ , Degrees (S and T'S Program)			$\partial \text{TCF}^{(1)} / \partial \psi$
PHI	THETA	PSI	
15.0	32.5	38.55	-3.6
17.5	30.0	37.35	-3.4
20.0	30.0	36.6	-3.5
22.5	30.0	35.85	-3.5
25.0	30.0	35.07	-3.3
27.5	30.0	34.28	-3.4
7.5	35.0	132.68	+2.7
10.0	40.0	129.40	+2.8
12.5	35.0	130.62	+2.0
12.5	42.5	127.15	+2.5
15.0	45.0	124.43	+2.6
17.5	40.0	126.14	+2.1
20.0	40.0	124.92	+2.6

TABLE 13. $\partial \text{TCF}^{(1)} / \partial \phi$ AND $\partial \text{TCF}^{(1)} / \partial \theta$ FOR SELECTED CUTS

Angles of ZTCF ⁽¹⁾ , Degrees (S and T's Program)			$\partial \text{TCF}^{(1)} / \partial \phi$	$\partial \text{TCF}^{(1)} / \partial \theta$
PHI	THETA	PSI		
7	27	135.64	-0.7 (PPM/C°)/DEGREE	-0.5 (PPM/C°)/DEGREE
0	27	137.78	-0.8	-0.8
15	40	40.00	+1.5	-0.7
15.0	32.5	38.55	-1.2	0.6
12.5	35.0	130.62	0.95	1.1

4. TEMPERATURE VARIATION OF THE SAW POWER FLOW ANGLE

An unexpected rapid fluctuation of the surface acoustic wave power flow angle on doubly rotated cut quartz saw devices was discovered during the testing of temperature-stable SAW devices. In this paragraph the phenomenon of a temperature variation in the SAW power flow angle will be discussed.

The power flow angle for a particular direction of propagation is an important parameter. While the phase fronts always remain parallel to the source transducer, the wave as a whole does not propagate

perpendicular to the wavefronts. This is a characteristic of anisotropic substrates where the phase velocity is asymmetric about the propagation direction; i.e. $v(\psi + \Delta\psi) \neq v(\psi - \Delta\psi)$. The major problem which arises is that the acoustic beam may steer off the desired propagation track missing the output transducer unless it is properly designed.

The power per unit width carried in a surface wave is found by integrating the mechanical and electrical Poynting vectors, to obtain

$$P_i = -\frac{1}{2} \operatorname{Re} \left[\int_{-\infty}^0 T_{ij} \mu_j^* dx_3 - i\omega \int_{-\infty}^0 \phi D_i dx_3 \right] \quad (i = 1, 2)$$

where μ_j is the particle displacement, T_{ij} the stress tensor, ϕ the electric potential and D_i the electric displacement. P_1 and P_2 give the power flow perpendicular and parallel to the wavefront, respectively. $P_3 = 0$ for the Rayleigh wave which is confined to the surface. The power flow angle may be defined as $\theta = \arctan (P_2/P_1)$. Power flow angles as high as 20° are not uncommon on quartz.

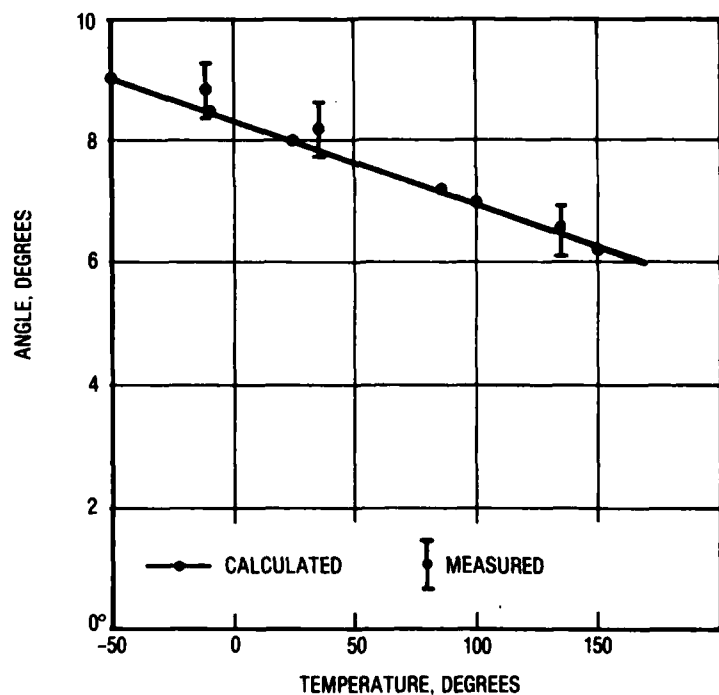


Figure 46. Power Flow Angle Against Temperature for (YX wlt) 14-283/39-117/40-6

Calculations^{3,4} of the power flow angle at different temperatures for doubly rotated cuts of quartz have been performed. The cuts are designated by the 1949 IRE³ standard. Figure 46 illustrates the temperature variation of the power flow angle for the doubly rotated cut of quartz (YX wlt) 14-283/39-117/40-6. The important feature of this dependence is the large variation of the power flow angle over the temperature range shown.

Figure 47 contains a pictorial representation of a device fabricated at (YX wlt) 14-3/39-1/40-6. The input transducer on the left generates an acoustic wave which only partially illuminates the output transducer on the right. Figure 48 (a and b) are photographs of the device response with a short gated RF pulse as the input, showing the response at 131°C and 34°C, respectively. The first notch is a result of missing finger pairs. The anisotropy parameter⁵ was calculated to be 0.625 at -50°C, 0.614 at 25°C and 0.586 at 150°C. The transducer apertures are 34 mils and 24 mils, the length of the device is 260 mils and the acoustic wavelength is 0.48 mils. The temperature dependent effects of diffraction on the envelope were found to be negligible. The shortening of the device response is clearly evident from the photographs and is due to the rapidly decreasing power flow angle successively illuminating more of the output transducer as the temperature increases. The power flow angles estimated from these photographs are displayed in Figure 42, alongside the theoretical results. Table 14 contains a summary of the power flow angles temperature dependence for several temperature-stable doubly rotated cuts.

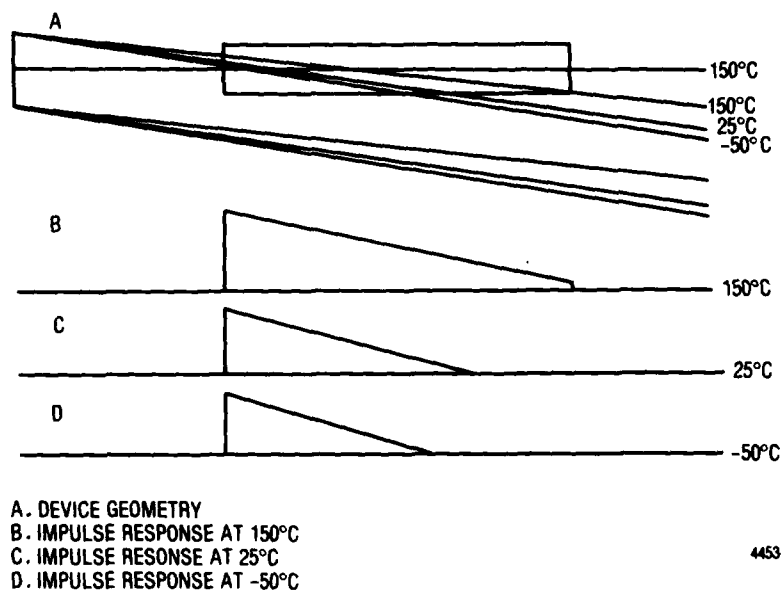
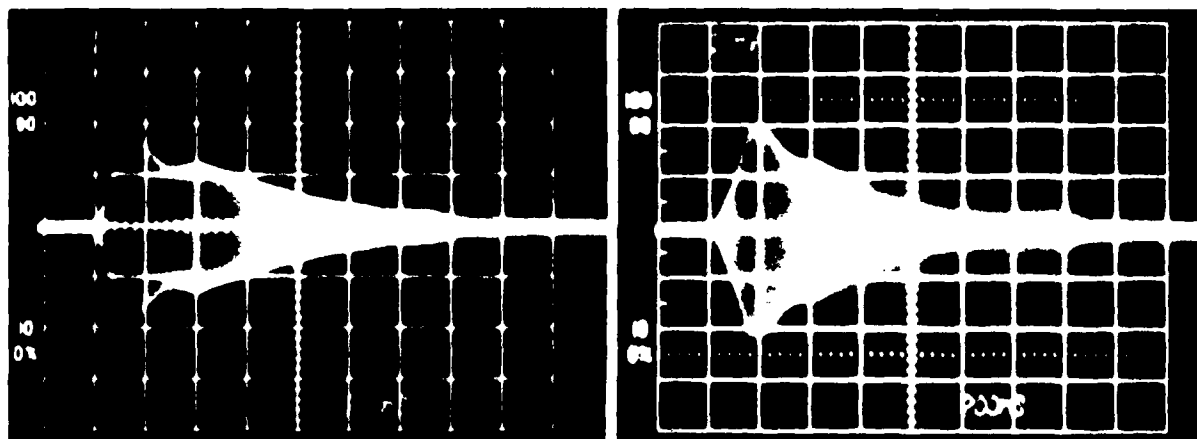


Figure 47. Pictorial Representation of Device Response

⁴"Higher Order Temperature Coefficients of the Elastic Stiffness and Compliances of Alpha-Quartz", Bechmann, R., Ballato, A., and Lukaszek, T., IRE Trans., 1962, pp. 1812-1822.

⁵"Compensation for Diffraction in SAW Filters", Savage, E. B., and Matthaiei, G. L., 1979 IEEE Ultrasonics Symposium, CH1482-9/79/, pp. 527-532.



a. AT 131°C

b. AT 34°C

Figure 48. Device Response to Short Gated 270.4 MHz Input Pulse

TABLE 14. TEMPERATURE DEPENDENCE OF THE POWER FLOW ANGLE ON DOUBLY ROTATED CUTS AT ORIENTATIONS (YX WLT) PHI/THETA/PSI

Orientation			Power Flow Angle		
PHI	THETA	PSI	T = 25°C	T = 150°C	T = -50°C
-1.330	28.100	137.692	+1.2	-0.1	+1.8
-1.050	28.067	136.534	+2.5	+1.0	+3.2
-0.967	26.233	138.449	+1.1	-0.2	+1.8
-0.33	26.700	138.859	+0.5	-0.7	+1.1
0.633	26.150	137.016	+1.4	+0.1	+2.1
5.583	27.833	135.194	+0.3	-0.9	+1.0
5.583	27.833	134.940	+0.5	+0.1	+1.1
5.583	27.833	134.994	+0.4	-0.8	+1.1
6.000	26.967	135.812	-0.1	-1.2	+0.5
6.067	25.933	133.099	+1.7	+0.3	+2.4
6.567	26.883	134.925	+0.1	-1.0	+0.7
7.410	27.380	134.2	+0.1	-1.0	+0.8
8.033	26.967	134.618	-0.3	-1.4	-0.3
8.05	25.900	135.71	-0.7	-1.6	-0.1
14.283	39.117	40.627	-8.1	-6.2	-9.0
15.300	40.683	40.031	-8.6	-6.8	-9.6
16.117	41.267	37.309	-7.2	-5.5	-8.1

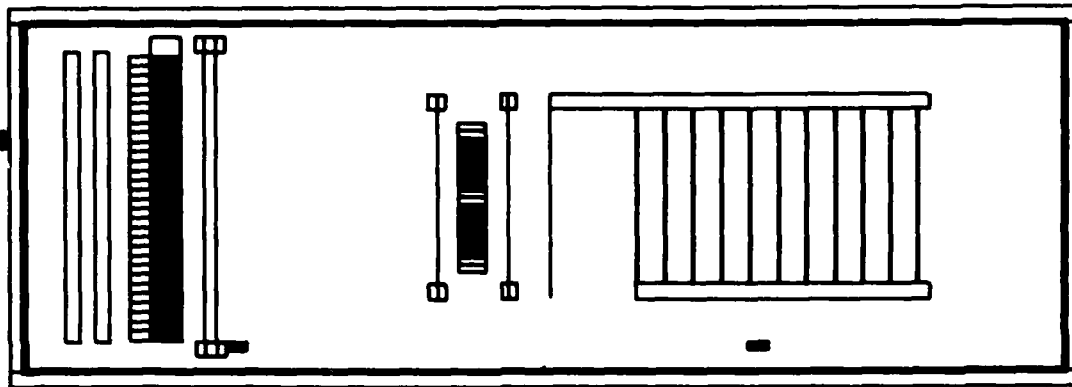
When the oscillator frequency is not exactly at the synchronous frequency of the SAW delay line, the phase response of the delay line becomes temperature dependent. The use of doubly rotated cut SAW devices clearly requires designs which can accommodate a large variation in the SAW power flow angle. Consequently, a special mask used for testing was designed.

Figure 49 contains an illustration of the pattern to be used for doubly rotated cuts with a large power flow angle temperature variation. The large aperture of the output transducer is required to accommodate rapid variation of the power flow angle.

The center frequency of the device is approximately 260 MHz. The electrode and line spacing are 0.06 mil (double electrodes), so the acoustic wavelength is 0.48 mil. The input transducer has 40 pairs of electrodes and the output transducer has 11 sections of electrodes with 4.5 pairs in each section. The spacing of each section is 19.2 mils. The width of the input transducer is 36 mils, and that for the output transducer is 120 mils. The design allows a maximum of 12 degrees beam steering, which is adequate for most of the desired cuts in this study. The final mask is a stepped and reduced design having a family of patterns with relative rotation of a fraction of a degree, so that a family of TCF's with small increments of the propagation angle 0.4° can be measured.

The input transducer is divided into two sections. Selecting the upper or lower section ensures that the complete wavefront of the acoustic waves will propagate over the output transducer aperture throughout the temperature range of interest.

In designing filters and reflective array devices on rotated cuts of quartz, additional care must be taken to ensure that the temperature dependent power flow angle does not degrade device response. If improperly designed, device time delay, bandwidth and phase all become temperature dependent when fabricated on a rotated cut. These observations are especially important for reflective array devices in which rotated cuts of quartz are often used to achieve temperature compensation in two different propagation directions. Suitable device design can overcome these problems and result in temperature compensated delay lines useful for oscillator applications. The moving acoustic beam may be made to illuminate different parts of the output transducer at different temperatures in such a way as to maintain a steady phase over the entire temperature range. A design using the temperature dependent PFA is currently being fabricated in which a compensation signal maintains a relatively constant output phase despite the temperature dependent delay time. Input beam aperture compression may be used to achieve increasingly accurate adjustments of the output phase. Materials such as lithium niobate with higher coupling coefficients may be useful in this respect.



4453-17

Figure 49. Transducer Design

By proper selection of the output transducer location, one may obtain temperature stable SAW oscillator due to the power flow angle sweeping as a function of temperature. Figure 50 shows compensated SAW oscillator using the combination of two 90° out of phase transducers shown in Figure 49. Where the combined output phase of the transducers is compensated to a minimum change as the temperature varies; hence improved temperature characteristics are obtained.

5. REPRESENTATIVE EXPERIMENTAL DATA IN THE SELECTED AREAS

Several selected areas have zero first order TCF and low $TCF^{(2)}$ and $TCF^{(3)}$ have been fabricated and evaluated. These areas provide some of the best results in the study. The cut YX wlt $\phi/\theta/\psi$ of 12.01/31.21/39.8 has less than 80 PPM shift of frequency in the temperature -40°C to $+140^{\circ}\text{C}$. The experimental result is shown in Figure 51. This cut has measured $TCF^{(1)}$ of 0.55×10^{-7} $TCF^{(2)}$ of -1.19×10^{-8} and $TCF^{(3)}$ of 0.45×10^{-10} Figure 52 shows the experimental results of a device in the 15.13/31.13/37.33 orientation. The device has $TCF^{(1)}$ of 1.1×10^{-7} , $TCF^{(2)}$ of -1.18×10^{-8} and $TCF^{(3)}$ of 0.253×10^{-10} . This device has less than 50 PPM shift from -30°C to $+100^{\circ}\text{C}$ temperature range. Other selected cuts are shown in Figures 53 and 54. These cuts all have relatively good temperature characteristics.

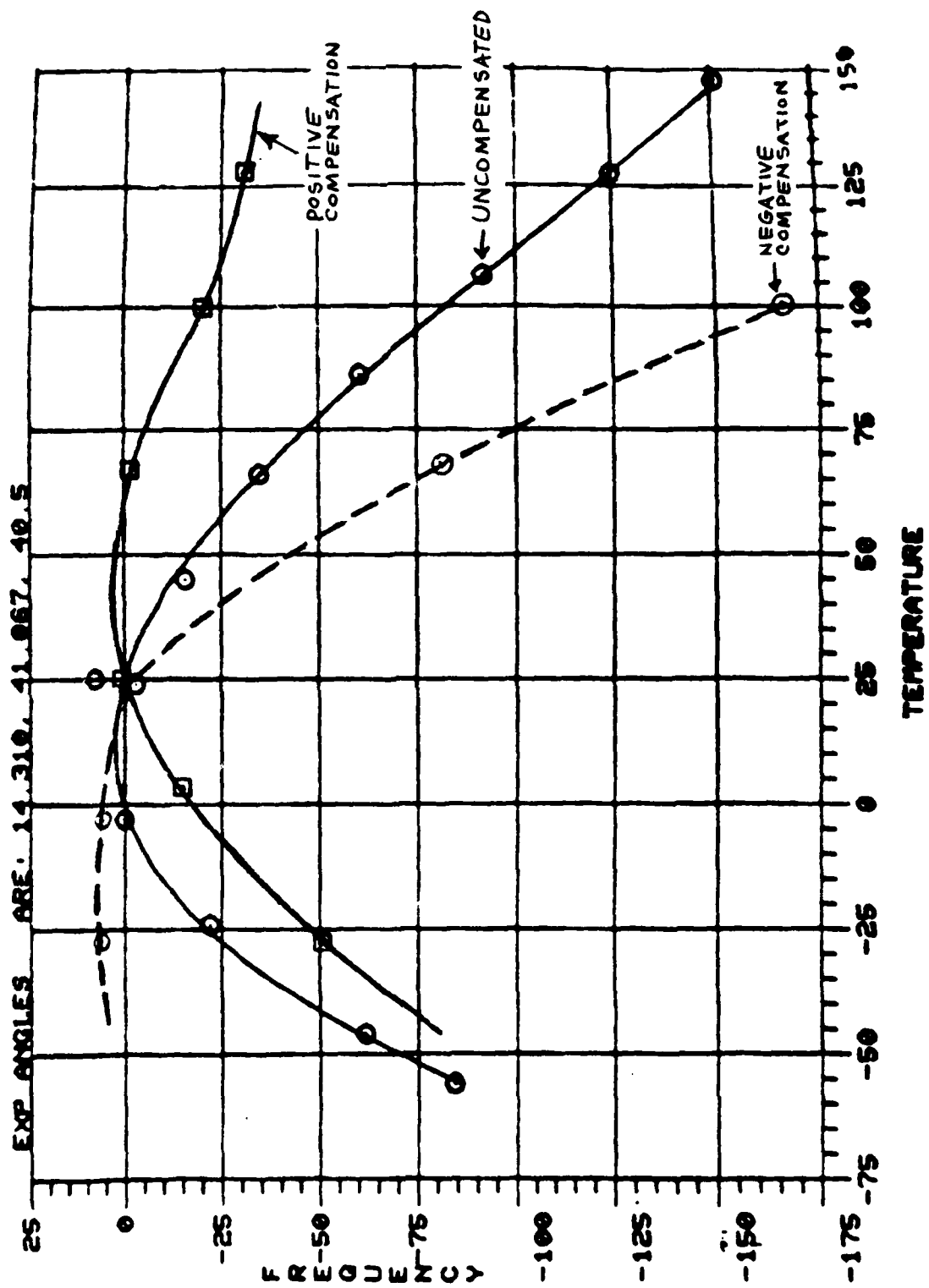


Figure 50. Power Flow Angle Compensated SAW Device

EXP angles (recorded AUG 25, '81) are:
 12.010 31.210 39.800

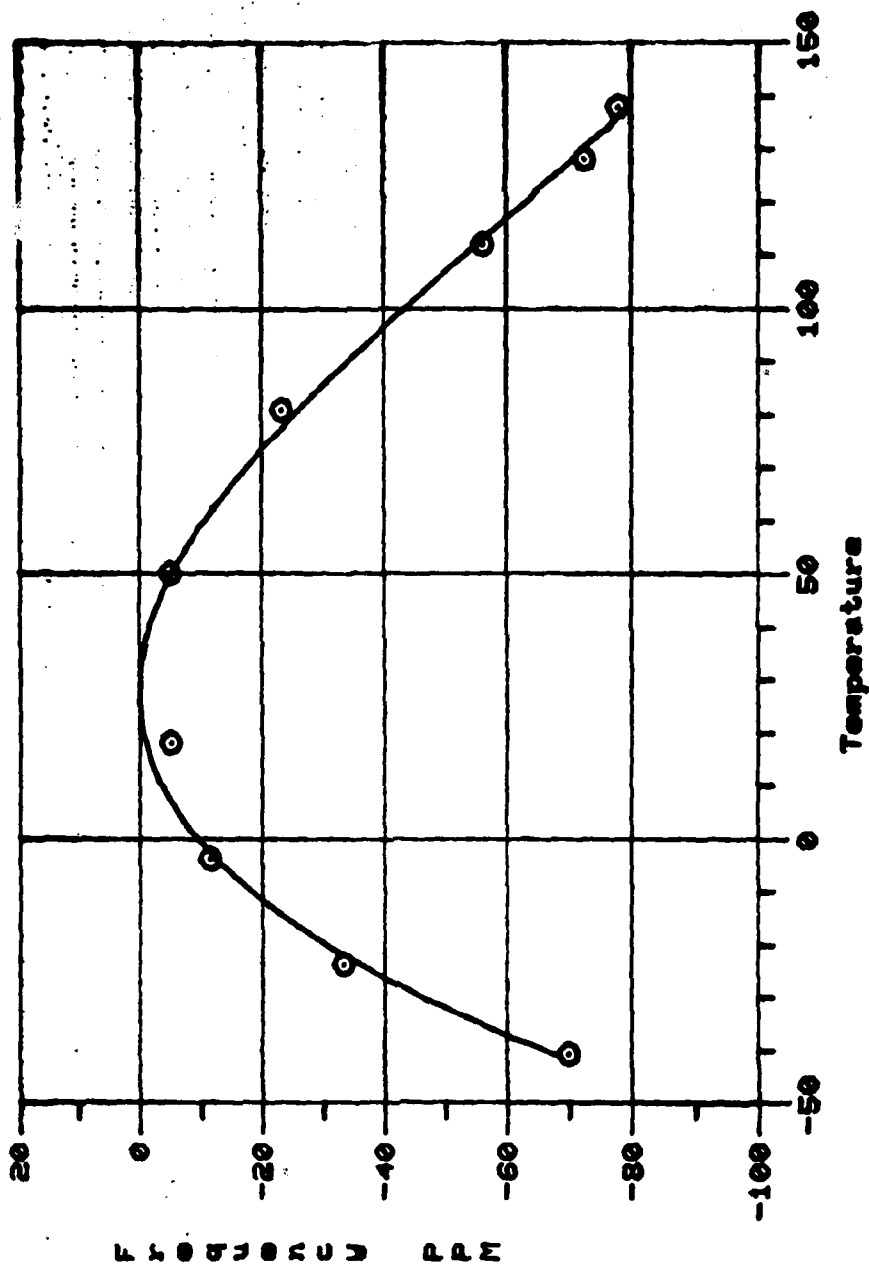


Figure 51. Temperature Stable Cut of Quartz for SAW

EXP angles (recorded AUG 28, '81) are:
 15.130 31.130 37.330

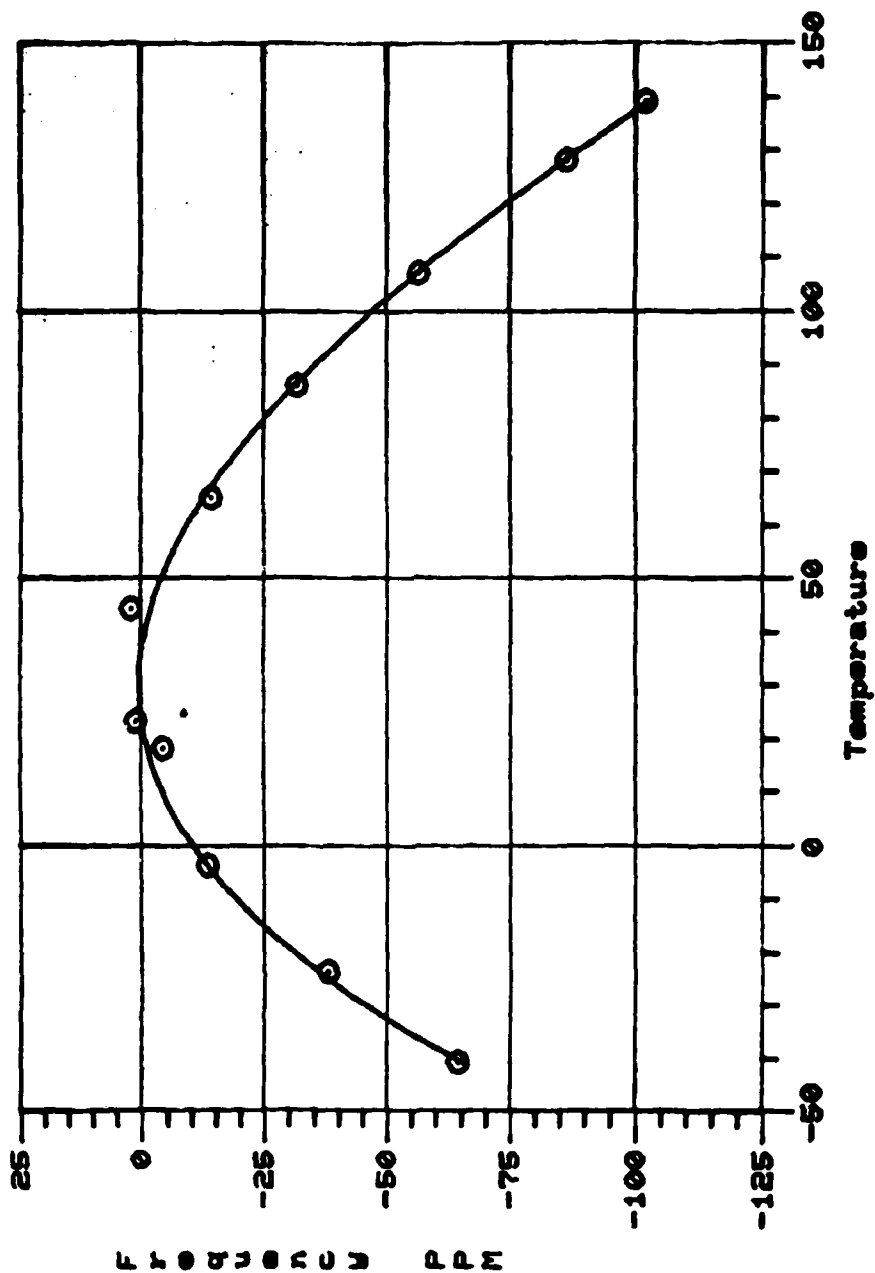


Figure 52. Temperature Stable Cut of Quartz for SAW

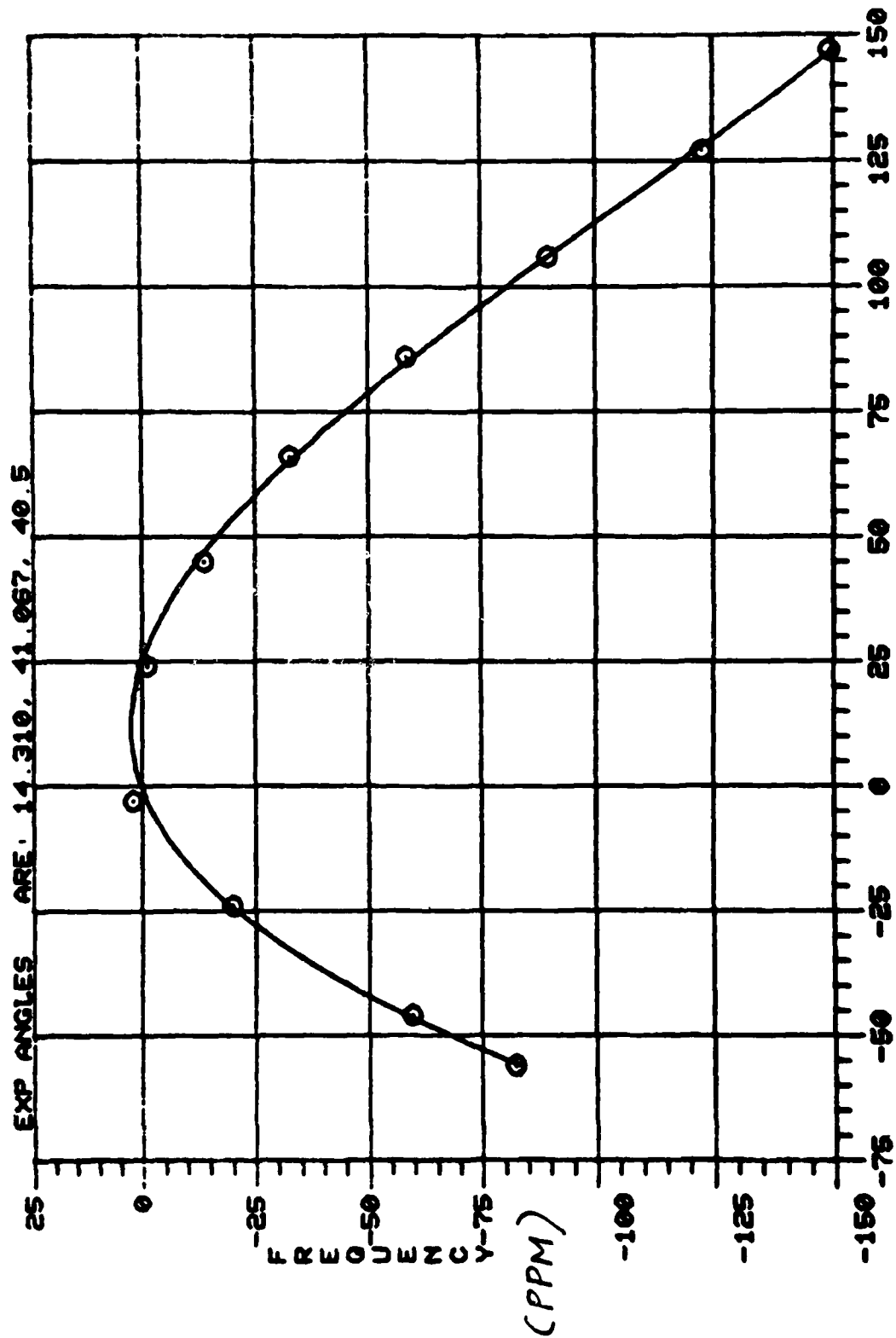


Figure 53. Temperature Stable Cut of Quartz for SAW

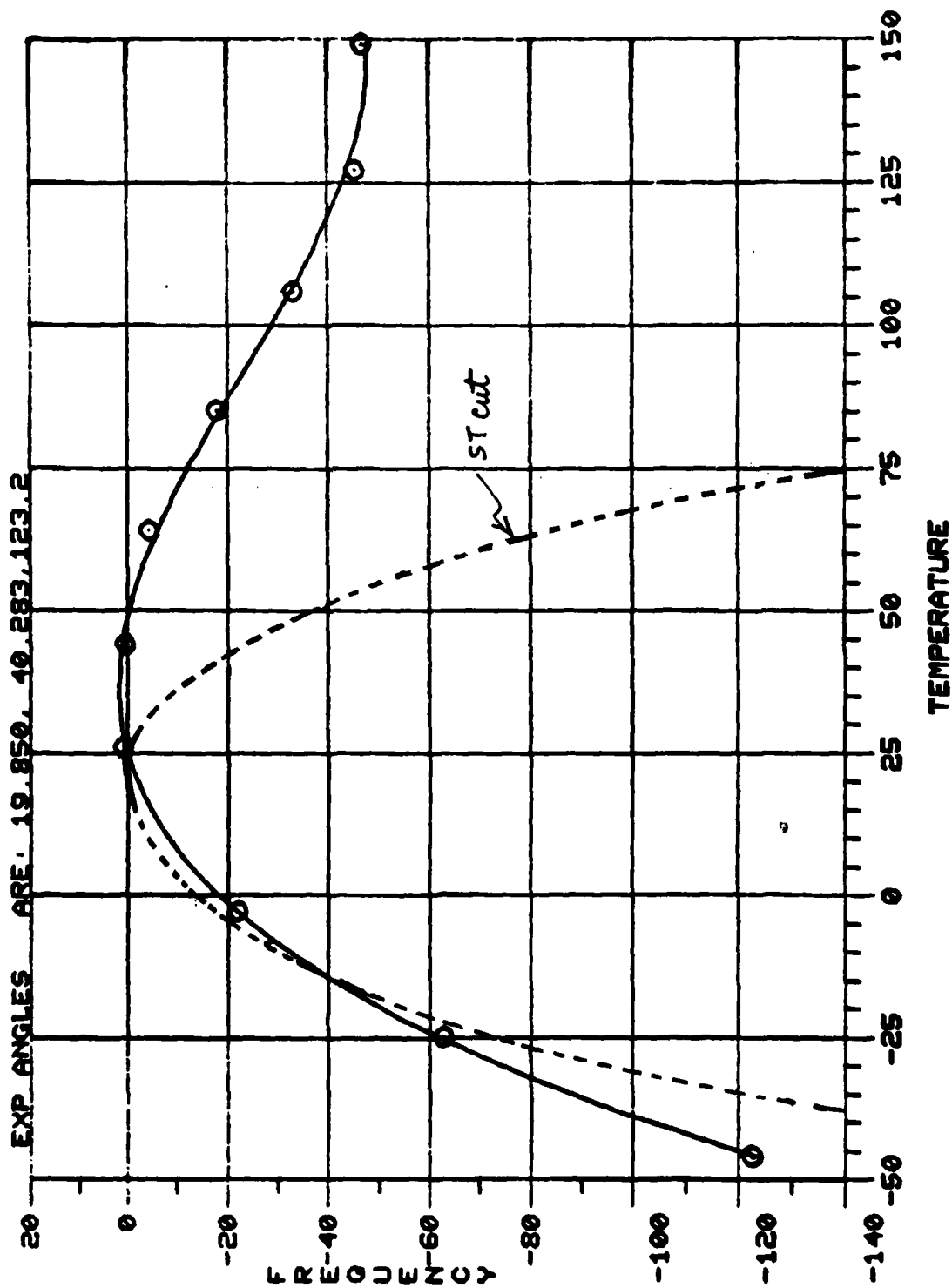


Figure 54. Temperature Stable Cut of Quartz for SAW

SECTION V

CONCLUSION

The temperature coefficients of frequency (TCF) have been analyzed for doubly rotated cuts of quartz for surface acoustic wave devices. The analysis procedure is shown below:

- (1) Using Finite Difference program, identify angular areas with zero $TCF^{(1)}$ and low $TCF^{(2)}$ on $10^\circ \times 10^\circ \times 10^\circ$ grid.
- (2) Calculate in these areas with $2.5^\circ \times 2.5^\circ \times 2.5^\circ$ grid to locate the rotation with minimum $TCF^{(2)}$ which has $TCF^{(1)} = 0$.
- (3) Identify the accurate zero $TCF^{(1)}$ with Sinha and Tiersten's program in areas obtained in (2).
- (4) Calculate $TCF^{(1)}$, $TCF^{(2)}$ and $TCF^{(3)}$ in selected areas obtained in (3) with $1^\circ \times 1^\circ \times 1^\circ$ span.
- (5) Calculate the coupling coefficients, propagation velocities, power flow angles and inverse bulk wave velocities for these angles.

The conclusions of the study are:

- (a) The zero $TCF^{(1)}$ surface and zero $TCF^{(2)}$ surface data does not show an intersection in the $10^\circ \times 10^\circ \times 10^\circ$ grid. However, orientations with frequency variation ≈ 100 ppm from -50°C to 100°C , better than ST Cut by a factor of two, have been found in several areas where $TCF^{(1)} = 0$ and $TCF^{(2)}$ is less than $-1.5 \times 10^{-8}/^\circ\text{C}^2$.
- (b) The $\Delta TCF/\Delta$ angle is normally very large in the areas with zero $TCF^{(1)}$ and low $TCF^{(2)}$, therefore accurate crystal orientation is critical. It is estimated that the orientation accuracy of 6 minutes is required to obtain a $TCF^{(1)}$ of ≈ 50 ppm in the -50°C to 100°C temperature range in the three areas investigated. These are $\phi/\theta/\psi$ of 6/27/135.93 (4.45×10^{-2} ppm/ $^\circ\text{C} \cdot \text{minute}$), 14/40/40.415 (5.83×10^{-2} ppm/ $^\circ\text{C} \cdot \text{minute}$) and 0/27/137.78 (5.00×10^{-2} ppm/ $^\circ\text{C} \cdot \text{minute}$). Orientations with less sensitivity to orientation accuracy have been evaluated. These are the cuts that have $\partial[TCF^{(1)}]/\partial\psi = 0$ when $TCF^{(1)} = 0$. The cuts evaluated were $\phi/\theta/\psi = 20/30/155$, 20/20/150, 10/40/168. The $TCF^{(2)}$ of these cuts are approximately $4 \times 10^{-8}/^\circ\text{C}^2$, comparable or higher than ST cut.
- (c) Coupling coefficients, velocities and beam steering angles were defined for the selected areas, no leaky modes were found in these areas. Determinations of experimental propagation characteristics using the laser probe technique demonstrated good agreement between measured and calculated values.

(d) Methods to X-ray orient the quartz crystals, cut the doubly rotated wafers and polish such crystal wafers were developed.

(e) It has been determined that $TCF^{(1)}$ is the most sensitive to angular variations; thus the large values of $\partial TCF / \partial \psi$ imposes strict fabrication tolerances on processing. It was necessary to incorporate a mask design using rotated structures to compensate for processing errors within the allowed fabrication tolerances.

(f) Theoretical calculations of power flow angle, coupling coefficients, and second and third order TCF's indicate that they do not vary quickly with angle. Thus, by varying ψ on any particular cut, linear temperature variations can be compensated for while all other cut parameters vary only slightly.

(g) Experimental design and procedures followed during the measurements of the TCF's indicate that the experimental error is within 10 PPM. Tables 8 and 9 which display the comparison of theoretical and experimental results, illustrate the excellent agreement.

(h) Experimental results of the 1st iteration indicate that an improvement in $TCF^{(2)}$ by at least a factor of two over ST quartz can be obtained. A second iteration approach using a higher resolution and better selected areas has improved the $TCF^{(2)}$ of the doubly rotated quartz over the ST cut by a factor of three or better.

The best experimental data was obtained with the devices in the 12.01/31.21/39.8 orientation. The total shift of frequency of less than 80 PPM in the -45°C to $+140^{\circ}\text{C}$ was obtained. Several other areas that will provide comparable temperature characteristics are described.

(i) The temperature variation of the power flow angle on doubly rotated cuts of quartz and its effect on device design was discussed. An oscillator design accommodating large temperature-varying power flow angles was discussed. The utilization of the temperature variation of the power flow angle to achieve temperature compensation of the oscillator was demonstrated.

APPENDIX A

VOLUME PERTURBATION OF AULD

Perturbation techniques, as used here, allow calculations of small changes in the solutions to a problem caused by small changes in the physical parameters of the problem, once the solution to the unperturbed problem is known.

Our general approach to the problem of determining the temperature dependence of V , will be as follows. First, the Rayleigh wave propagation problem will be solved in the standard way in its entirety at room temperature, T_0 . Given the solution of problem at T_0 and the dependence of the physical constants (such as c_{ij}) on temperature at T_0 , we will apply the volume perturbation formula, calculating the temperature dependence of V . The dependence of V on T is then used to calculate the frequency characteristics of the actual device given the thermal expansion coefficients as a function of temperature. At this point, the frequency temperature dependence of the substrate as a function of crystal cut and direction can be thoroughly explored.

The Volume Perturbed Formula.

Denoting $u_i(T_0)$ by u_i , etc., the volume perturbation formula is given by¹:

$$\begin{aligned} \beta_R = \omega \int_0^\infty [A] dy / \int_0^\infty & (-u^* \cdot T' - u' \cdot T^* \\ & + \phi^* (i\omega D') + \phi' (i\omega D)^*) \cdot z dy \\ [A] = [\Delta \rho u^* \cdot u' + T^* : (\Delta s^E : T' + \Delta d \cdot E') \\ & + E^* \cdot (\Delta \epsilon^T \cdot E' + \Delta d : T')] \end{aligned} \quad (A-1)$$

This equation is exact, but involves knowing the solution u' . However, we can set $u = u'$ if the temperature dependence of the solution is small and use $P = (1/2) \text{Re} \int (-u^* \cdot T + E \cdot H^*) dy$ to obtain the approximate solution

$$\begin{aligned} \Delta \beta_R = (\omega/4P) \int_0^\infty [\Delta \rho |u|^2 + S : \Delta c : S \\ + E^* \cdot \Delta \epsilon^T \cdot E + E^* \cdot \Delta d : S + S : \Delta d \cdot E] dy \end{aligned} \quad (A-2)$$

The u 's and E 's, and ρ come directly from the computer solution at T_0 .

¹Auld, B.A., "Acoustic Fields and Waves in Solids," Vol. II.

The Δ terms can be written as expansions of the form:

$$\Delta\beta_R = \beta_R(T_0)(\alpha_\beta^{(1)} dT + \alpha_\beta^{(2)} dT^2 + \alpha_\beta^{(3)} dT^3) \quad (A-3)$$

$$\Delta\rho = \rho(T_0)(\alpha_\rho^{(1)} dT + \alpha_\rho^{(2)} dT^2 + \alpha_\rho^{(3)} dT^3) \quad (A-4)$$

$$= \rho^{(1)} dT + \rho^{(2)} dT^2 + \rho^{(3)} dT^3 \quad (A-5)$$

$$\Delta c_{ijkl} = c_{ijkl}^{(1)} dT + c_{ijkl}^{(2)} dT^2 + c_{ijkl}^{(3)} dT^3, \text{ etc.} \quad (A-6)$$

to obtain

$$\begin{aligned} \Delta\beta_R &= \beta_R(T_0) (\alpha_\beta^{(1)} dT + \beta_R(T_0) \alpha_\beta^{(2)} dT^2 + \beta_R(T_0) \alpha_\beta^{(3)} dT^3) \\ &= (\omega dT/4P) \int_0^\infty (\rho(T_0) \alpha_\rho^{(1)} |u|^2 + S:c^{(1)}:S + E^* \cdot \epsilon^{(1)} \cdot E \\ &\quad + E^* \cdot \epsilon^{(1)} \cdot S + S:e^{(1)} \cdot E) dy \\ &\quad + (\omega dT^2/4P) \int_0^\infty (\rho(T_0) \alpha_\rho^{(2)} |u|^2 + S:c^{(2)}:S + \dots) dy \\ &\quad + (\omega dT^3/4P) \int_0^\infty (\rho(T_0) \alpha_\rho^{(3)} |u|^2 + S:c^{(3)}:S + \dots) dy \end{aligned} \quad (A-7)$$

or

$$\alpha_\beta^{(j)} = (\omega/4P\beta_R(T_0)) \int_0^\infty (\rho(T_0) \alpha_\rho^{(j)} |u|^2 + S:c^{(j)}:S + \dots) dy \quad (A-8)$$

For the problem of quartz, the electrostatic coupling is small and the electric terms can be ignored. Thus Δd and $\Delta\epsilon$ in (A-8) may be set to zero resulting in the simplified equation.

$$\alpha_\beta^{(j)} = (\omega/4P\beta_R) \int_0^\infty (\rho(T_0) \alpha_\rho^{(j)} |u|^2 + S:c^{(j)}:S) dy \quad (A-9)$$

The integrals are calculable, for instance, from (14),

$$\begin{aligned} &\int_0^\infty \rho(T_0) \alpha_\rho^{(1)} |u|^2 dy \\ &= \rho(T_0) \alpha_\rho^{(1)} \sum \int_0^\infty \left[\sum_m C_m \alpha_i^{(m)} \exp(-i\beta_R b^{(m)} y) \right] \\ &\quad \left[\sum_n C_n^* \alpha_i^{(n)*} \exp(i\beta_R b^{(n)} y) \right] dy \end{aligned} \quad (A-10)$$

The problem can easily be extended to multi-layered media by simply performing the integral over each layer separately. For the double layer (A-9) becomes:

$$\int_0^{\alpha} \rho_1(T_0) \alpha_{\rho_1}^{(1)} |u|^2 dy + \int_{\alpha}^{\infty} \rho_2(T_0) \alpha_{\rho_2}^{(2)} |u|^2 dy + \dots \quad (\text{A-11})$$

Because the dependence of u_i is given explicitly by (13), it is not necessary to use numerical integration procedures, as demonstrated in (A-10).

Once the $\alpha_{\beta}^{(i)}$ have been calculated from (A-9) the $\alpha_v^{(i)}$ are simply determined. Using $\beta = \omega/V_*$, and (A-9) we determine $\alpha_F^{(i)}$.

APPENDIX B

VOLUME PERTURBATION FORMULA OF SINHA AND TIERSTEN

The approach used by Sinha and Tiersten includes the effects of distortion caused by heating a substrate of quartz and is based in the coordinate system to which the fundamental elastic constants refer. In this reference system, the density is constant and the $\alpha_F^{(i)}$ are equivalent to the $\alpha_V^{(i)}$.

In this new reference system, the perturbation formula becomes¹

$$(\Delta v_i/v_i) = (1/2\beta_R^2 v^2) (H/N^2), \quad (B-1)$$

$$N^2 = (\rho^0 \pi i / \beta_R^2) \sum_{m=1}^4 \sum_{n=1}^4 (c^{(m)} \alpha^{(m)} c^{(n)*} \alpha^{(n)*}) / (\beta_m - \beta_n^*) \quad (B-2)$$

$$H = - \int_0^\infty dy \int_{-\pi/\beta_R}^{\pi/\beta_R} dz (K_{zz} u_{z,z} + K_{zy} u_{y,z} + K_{zx} u_{x,z} + K_{yz} u_{z,y} + K_{yy} u_{y,y} + K_{yx} u_{x,y}) \quad (B-3)$$

$$K_{L\gamma} = (c_{L\gamma M\alpha} + \Delta c_{L\gamma M\alpha}) u_{\alpha, M} \quad (B-4)$$

For the first order perturbation in T we have:

$$c_{L\gamma M\alpha} = (c_{L\gamma M\nu AB} \alpha_{AB} + c_{L\gamma KM} \alpha_{\nu K} + c_{LKM\nu} \alpha_{\gamma K}) dT \quad (B-5)$$

$$\Delta c_{L\gamma M\alpha} = (d c_{L\gamma M\alpha} / dT) dT \quad (B-6)$$

Where $c_{L\gamma M\alpha}$ are the second order elastic constants previously denoted simply as $c_{L\gamma M\alpha}$ and $c_{L\gamma M\nu AB}$ are the third order elastic constants. The terms $\Delta c_{L\gamma M\alpha}$ as calculated by Tiersten² is available only to first order in T, and the higher order elastic constants $c_{L\gamma M\nu ABCD}$ have never been determined.

¹"On The Temperature Dependence Of The Velocity Of Surface Waves On Quartz," B.K. Sinha and H.F. Tiersten, 1978 Ultrasoncs Symposium Proceeding, IEEE, pp. 662-665.

²"Temperature dependence of the Fundamental Elastic Constants of Quartz," B.K. Sinha and H.F. Tiersten, Proceedings of the 32nd Annual Symposium on Frequency Control, 1978, pp. 150-153.

APPENDIX C

THE DIFFERENTIATION METHOD

A method for determining the theoretical temperature dependence of Rayleigh Surface Waves consists of formally differentiating the wave equation and boundary conditions. The boundary conditions and wave equation must be true at all temperatures, placing restraints on how the parameters of the wave equation may vary. In this technique, the derivatives of these equations with respect to temperature are set to zero and solved for the velocity temperature dependence. This method follows the methods used by Bechmann, Ballato, and Lukaszek¹ to compute the temperature dependence of the fundamental elastic constants from frequency data, except that the simplifying assumptions of assuming bulk wave solutions cannot be made. This method was later used by Hauden² to search for temperature stable cuts of quartz.

Christoffel's wave equation can be written in matrix form as

$$\begin{bmatrix} \Gamma_{11} - \rho V_s^2 & \Gamma_{12} & \Gamma_{13} & \Gamma_{14} \\ \Gamma_{12} & \Gamma_{22} - \rho V_s^2 & \Gamma_{23} & \Gamma_{24} \\ \Gamma_{13} & \Gamma_{23} & \Gamma_{33} - \rho V_s^2 & \Gamma_{34} \\ \Gamma_{14} & \Gamma_{24} & \Gamma_{34} & \Gamma_{44} \end{bmatrix} \begin{bmatrix} \alpha_1 \\ \alpha_2 \\ \alpha_3 \\ \alpha_4 \end{bmatrix} = 0 \quad (C-1)$$

where

$$\begin{array}{ll} \Gamma_{11} = c_{55} b^2 + 2c_{15} b + c_{11} & \Gamma_{23} = c_{34} b^2 + (c_{36} + c_{45}) b + c_{56} \\ \Gamma_{22} = c_{44} b^2 + 2c_{46} b + c_{66} & \Gamma_{44} = -(\epsilon_{33} b^2 + 2\epsilon_{13} b + \epsilon_{11}) \\ \Gamma_{33} = c_{33} b^2 + 2c_{35} b + c_{55} & \Gamma_{14} = e_{35} b^2 + (e_{15} + e_{31}) b + e_{11} \\ \Gamma_{12} = c_{45} b^2 + (c_{14} + c_{56}) b + c_{16} & \Gamma_{24} = e_{34} b^2 + (e_{14} + e_{36}) b + e_{16} \\ \Gamma_{13} = c_{35} b^2 + (c_{13} + c_{55}) b + c_{15} & \Gamma_{34} = e_{33} b^2 + (e_{13} + e_{35}) b + e_{15} \end{array} \quad (C-2)$$

¹"Higher Order Temperature Coefficients of the Elastic Stiffnesses and Compliances of Alpha Quartz," Bechmann, Ballato, and Lukaszek, Proc. IRE, Aug 1962, pp. 1812-1822.

²"Higher Order Temperature Coefficients of Quartz SAW Oscillators," D. Handen, M. Michael, J.J. Gagnepain, Proc. Frequency Control Symposium (1978), pp. 77-86.

following the notation used in the previous section and in Matthews¹. This equation holds for each of the four modes, hereafter designated by a superscript m.

The boundary conditions become, in matrix form,

$$\begin{bmatrix} \dots(C_{3311} + C_{3313} b^{(m)}) \alpha_1^{(m)} + (e_{133} + e_{333} b^{(m)}) \alpha_4^{(m)} \dots \\ \dots(C_{3111} + C_{3113} b^{(m)}) \alpha_1^{(m)} + (e_{131} + e_{331} b^{(m)}) \alpha_4^{(m)} \dots \\ \dots(C_{3211} + C_{2313} b^{(m)}) \alpha_1^{(m)} + (e_{132} + e_{332} b^{(m)}) \alpha_4^{(m)} \dots \\ \dots(e_{311} + e_{313} b^{(m)}) \alpha_1^{(m)} - (e_{31} + e_{33} b^{(m)} - i\epsilon_0) \alpha_4^{(m)} \dots \end{bmatrix} \begin{bmatrix} C_1 \\ C_2 \\ C_3 \\ C_4 \end{bmatrix} = 0 \quad (C-3)$$

where only the m'th column is shown and the C_m 's are the amplitudes of each mode. This formulation assumes a normalization of the α 's

$$(\alpha_1^{(m)})^2 + (\alpha_2^{(m)})^2 + (\alpha_3^{(m)})^2 + (\alpha_4^{(m)})^2 = 1. \quad (C-4)$$

The first condition we can place on the wave equation is that the determinant of Christoffel's equation vanishes for all temperature, or

$$d/dT \begin{vmatrix} \Gamma_{11} - \rho V_s^2 & \Gamma_{12} & \Gamma_{13} & \Gamma_{14} \\ \Gamma_{12} & \Gamma_{22} - \rho V_s^2 & \Gamma_{23} & \Gamma_{24} \\ \Gamma_{13} & \Gamma_{23} & \Gamma_{33} - \rho V_s^2 & \Gamma_{34} \\ \Gamma_{14} & \Gamma_{24} & \Gamma_{34} & \Gamma_{44} \end{vmatrix} = 0 \quad (C-5)$$

For each of the four modes, this equation is valid, resulting in four equations in five unknowns, dV_s/dT , and $db^{(m)}/dT$ of the form $F_1^{(m)}(dV_s/dT, db^{(m)}/dT) = 0$, $m = 1, 2, 3, 4$.

For each mode, Christoffel's matrix equation (C-1) must vanish, yielding the set of equations

$$\begin{aligned} (d/dT) (\alpha_1^{(m)} (\Gamma_{11}^{(m)} - \rho V_s^2) + \alpha_2^{(m)} \Gamma_{12}^{(m)} + \alpha_3^{(m)} \Gamma_{13}^{(m)} + \alpha_4^{(m)} \Gamma_{14}^{(m)}) &= 0 \\ (d/dT) (\alpha_1^{(m)} \Gamma_{12}^{(m)} + \alpha_2^{(m)} (\Gamma_{22}^{(m)} - \rho V_s^2) + \alpha_3^{(m)} \Gamma_{23}^{(m)} + \alpha_4^{(m)} \Gamma_{24}^{(m)}) &= 0 \\ (d/dT) (\alpha_1^{(m)} \Gamma_{13}^{(m)} + \alpha_2^{(m)} \Gamma_{23}^{(m)} + \alpha_3^{(m)} (\Gamma_{33}^{(m)} - \rho V_s^2) + \alpha_4^{(m)} \Gamma_{34}^{(m)}) &= 0 \\ (d/dT) (\alpha_1^{(m)} \Gamma_{14}^{(m)} + \alpha_2^{(m)} \Gamma_{24}^{(m)} + \alpha_3^{(m)} \Gamma_{34}^{(m)} + \alpha_4^{(m)} \Gamma_{44}^{(m)}) &= 0. \end{aligned} \quad (C-6)$$

This results in 16 equations (four per mode) and an additional 16 unknowns (the $\alpha_i^{(m)}$'s) of the form

$$F_{2i}^{(m)}(dV_s/dT, db^{(m)}/dT, d\alpha_1^{(m)}/dT, d\alpha_2^{(m)}/dT, d\alpha_3^{(m)}/dT, d\alpha_4^{(m)}/dT) = 0$$

¹"Surface Wave Filters," H. Matthews, John Wiley and Sons, New York (1977).

Using (C-3) we obtain the single equation

$$(d/dt) \begin{vmatrix} \dots\dots (C_{3311} + C_{3313}b^{(m)}) \alpha_1^{(m)} + (e_{133} + e_{333}b^{(m)}) \alpha_4^{(m)} \dots\dots \\ \dots\dots (C_{3111} + C_{3113}b^{(m)}) \alpha_1^{(m)} + (e_{131} + e_{331}b^{(m)}) \alpha_4^{(m)} \dots\dots \\ \vdots \\ \vdots \end{vmatrix} = 0 \quad (C-7)$$

of the form $F_3^{(m)} (db^{(1)}/dT, db^{(2)}/dT, \dots, d\alpha_1^{(m)}/dT) = 0$

and four equations of the form

$$\begin{aligned} (d/dT) \sum_m C_m [(C_{3311} + C_{3313}b^{(m)}) \alpha_1^{(m)} + (e_{133} + e_{333}b^{(m)}) \alpha_4^{(m)}] &= 0 \\ (d/dT) \sum_m C_m [(C_{3111} + C_{3113}b^{(m)}) \alpha_1^{(m)} + (e_{131} + e_{331}b^{(m)}) \alpha_4^{(m)}] &= 0 \\ \vdots \end{aligned} \quad (C-8)$$

of the form $F_4^{(m)} (db^{(m)}/dT, d\alpha_1^{(m)}/dT, dC_m/dT) = 0$ (C-9)

From (5) $\alpha_1^{(m)} (d\alpha_1^{(m)}/dT) + \alpha_2^{(m)} (d\alpha_2^{(m)}/dT) + \alpha_3^{(m)} (d\alpha_3^{(m)}/dT) + \alpha_4^{(m)} (d\alpha_4^{(m)}/dT) = 0$ (C-10)

or

$$F_5^{(m)} (d\alpha_1^{(m)}/dT) = 0 \quad (C-11)$$

Combining the above results gives 25 equations in the 25 unknowns.

$$dV_s/dT, db^{(m)}/dT, d\alpha_1^{(m)}/dT, dC_m/dT$$

which are solved simultaneously. Once the temperature dependence of the Rayleigh wave velocity is found, the frequency dependence is found in the usual way.

To obtain the second order dependence of V_s , the 25 equations are differentiated again. The values of dV_s/dT , $db^{(m)}/dT$, $d\alpha_1^{(m)}/dT$ and dC_m/dT previously obtained are used to obtain d^2V_s/dT^2 , etc.

APPENDIX D

SOLUTION METHOD

Calculating the velocity of a Rayleigh wave requires a complete solution of the problem to be performed. All of the constants in equation (13) must be evaluated. The standard used at Motorola as developed by Campbell and Jones is outlined below.

First the fundamental constants are rotated into the coordinate system of interest. Next a value of V , is picked. The coefficients τ_{ij} of equation (C-2) are evaluated and the determinant of the matrix in equation (C-1) is set to zero, as it must be if a solution of (C-1) is to be found. This results in an eighth order equation in b . This equation is solved for the eight complex roots. The four roots $b^{(m)}$ in the lower complex plane are retained, the four discarded roots not satisfying the boundary conditions at infinity. Equation (C-1) is then solved for the four eigenvectors $\alpha_i^{(m)}$. The $b_i^{(m)}$ and the corresponding eigenvector $\alpha_i^{(m)}$ are substituted into equation (C-3) and the determinant of the matrix in equation (C-3) is evaluated. This determinant must be zero for a solution to (C-3) exist. If it is not zero, V , is varied, and the whole procedure repeated, until it is. Once a value of V , is found such that the determinant in equation (C-3) vanishes, the solution to (C-3) is found, giving the values for C_m . These constants completely describe the solution of equation (13), as well as providing the exact velocity.

APPENDIX E

EQUIVALENCE OF TEMPERATURE COEFFICIENTS OF FREQUENCY AND DELAY

In the following section, the relations relating the first, second, and third order temperature coefficients of delay and frequency will be derived. These relations show implicitly the equivalence of each representation of the device temperature characteristics, and justify their interchangeable usage.

In the text, we have used the following notation:

$$\tau = \text{delay time of delay line oscillator} \quad (\text{E-1})$$

$$i\text{th order temperature coefficient of delay} = \text{TCD}^{(i)} = \alpha_{\tau}^{(i)} \quad (\text{E-2})$$

$$F = \text{frequency of delay line oscillator} \quad (\text{E-3})$$

$$i\text{th order temperature coefficient of frequency} = \alpha_F^{(i)} \quad (\text{E-4})$$

$$\tau = \tau_0 (1 + \alpha_{\tau}^{(1)} (T - T_0) + \alpha_{\tau}^{(2)} (T - T_0)^2 + \alpha_{\tau}^{(3)} (T - T_0)^3 + \dots) \quad (\text{E-5})$$

$$F = F_0 (1 + \alpha_F^{(1)} (T - T_0) + \alpha_F^{(2)} (T - T_0)^2 + \alpha_F^{(3)} (T - T_0)^3 + \dots) \quad (\text{E-6})$$

where T is temperature and T_0 is a reference temperature, 25°C in our case. For a SAW oscillator, $F\tau = \text{constant}$ or

$$\begin{aligned} \tau/\tau_0 &= F_0/F \\ &= 1/(1 + \alpha_F^{(1)} (T - T_0) + \alpha_F^{(2)} (T - T_0)^2 + \alpha_F^{(3)} (T - T_0)^3 + \dots) \end{aligned} \quad (\text{E-7})$$

Using the relation

$$1/(1 + X) \cong 1 - X + X^2 - X^3 \text{ for } X \ll 1 \quad (\text{E-8})$$

we can write

$$\begin{aligned} \tau/\tau_0 &= 1 - [\alpha_F^{(1)} (T - T_0) + \alpha_F^{(2)} (T - T_0)^2 + \alpha_F^{(3)} (T - T_0)^3] \\ &\quad + [(\alpha_F^{(1)})^2 (T - T_0)^2 + 2\alpha_F^{(1)} (T - T_0) \alpha_F^{(2)} (T - T_0)^2] \\ &\quad - [\alpha_F^{(1)} (T - T_0)]^3 + \text{higher order terms} \end{aligned} \quad (\text{E-9})$$

$$= 1 - \alpha_F^{(1)} (T - T_0) + (-\alpha_F^{(2)} + (\alpha_F^{(1)})^2) (T - T_0)^2 + (-\alpha_F^{(3)} + 2\alpha_F^{(1)} \alpha_F^{(2)} - (\alpha_F^{(1)})^3) (T - T_0)^3 \quad (\text{E-10})$$

Equating powers of $T - T_0$ in (E-5) and (E-10), we obtain

$$\alpha_T^{(1)} = -\alpha_F^{(1)} \quad (E-11)$$

$$\alpha_T^{(2)} = -\alpha_F^{(2)} + (\alpha_F^{(1)})^2 \quad (E-12)$$

$$\alpha_T^{(3)} = -\alpha_F^{(3)} + 2\alpha_F^{(1)} \alpha_F^{(2)} - (\alpha_F^{(1)})^3 \quad (E-13)$$

As the only assumption on F and τ used is that of equation (E-7) which is symmetric in F and τ , we immediately obtain

$$\alpha_F^{(1)} = -\alpha_T^{(1)} \quad (E-14)$$

$$\alpha_F^{(2)} = -\alpha_T^{(2)} + (\alpha_T^{(1)})^2 \quad (E-15)$$

$$\alpha_F^{(3)} = -\alpha_T^{(3)} + 2\alpha_T^{(1)} \alpha_T^{(2)} - (\alpha_T^{(1)})^3 \quad (E-16)$$

Using (E-11) through (E-16), we can always relate one set of temperature coefficients to the other.

APPENDIX F

X-RAY RUN

The following is an example of the computer results from the FORTRAN X-ray orientation computer program for the doubly rotated cut 7/27/0. File MILDAT contains only the two Miller indices shown on the printout on this run.

16105 APR 19, '80 1000047
 JOB 538, MILLIAM(352200), 7, FILE=XRAYJOB, ID=63, LINE=22
 LIMIT (TIME,2),(CO,30),(UO,30)
 ASSIGN P1103,(FILE,MILDAT),(IN)
 ASSIGN P1104,(FILE,ERRDAT),(IN)
 RUN (LMN,XRAYLM)
 INPUT THE THREE ANGLES PHI,THETA,PSI

***** ANGLES ARE (YXWLT)7,00000 (0 MIN,)/27,0000 (0 MIN,)/,000000 (0 MIN,)

MILLER INDICIES: 0 -1 1

NORMAL VECTOR =.957534E=01 =.975690 .197133
 THETA= 13.3213

PLATE IN POSITION 1 (-1 AXIS VERTICAL, 2 AXIS NORMAL)

G = ANGLE OF INCIDENCE:24.8064 (48 MIN.)

BETA:2.52901 (32 MIN.)

G PLUS G PRIME:EXIT ANGLE:26.5310 (32 MIN.)

INTENSITY FACTOR:1.709521E=01 INTENSITY:1.000000

PLATE IN POSITION 3 (1 AXIS VERTICAL, 2 AXIS NORMAL)

G = ANGLE OF INCIDENCE:11.96138 (58 MIN.)

BETA:2.52901 (32 MIN.)

G PLUS G PRIME:EXIT ANGLE:26.5310 (32 MIN.)

INTENSITY FACTOR:1.924245 INTENSITY:1.000000

MILLER INDICIES: 0 -2 1

NORMAL VECTOR =.113399 =.989196 =.929136E=01
 THETA= 22.6995

PLATE IN POSITION 2 (-3 AXIS VERTICAL, 2 AXIS NORMAL)

G = ANGLE OF INCIDENCE:29.5043 (33 MIN.)

BETA:4.14657 (9 MIN.)

G PLUS G PRIME:EXIT ANGLE:45.0526 (39 MIN.)

INTENSITY FACTOR:1.362103 INTENSITY:1.000000

PLATE IN POSITION 4 (3 AXIS VERTICAL, 2 AXIS NORMAL)

G = ANGLE OF INCIDENCE:16.4650 (28 MIN.)

BETA:4.14657 (9 MIN.)

G PLUS G PRIME:EXIT ANGLE:45.0526 (39 MIN.)

INTENSITY FACTOR:1.633495 INTENSITY:1.000000


```

*****
LAUE ANGLES DEFINED SUCH THAT ALPHA = ANGLE FROM BEAM,
BETA = ROTATION CLOCKWISE FROM P1, DIST TO CRYSTAL = 10.0000
MILLER INDICES: 0 -1 1 LAUE SPOT ANGLES: ALPHA=25.3188 BETA=64.0927 X=2.06704 Y=-4.25554
MILLER INDICES: 0 -2 1 LAUE SPOT ANGLES: ALPHA=16.8600 BETA=39.3295 X=2.34422 Y=1.92073
*****
LAUE ANGLES DEFINED SUCH THAT ALPHA = ANGLE FROM BEAM,
BETA = ROTATION CLOCKWISE FROM P1.
FOR ROTATIONS E(1) = .000000 E(2) = .000000 E(3) = .000000 ACTUAL ANGLES ARE
(YXWLT) 6.99998 (60 MIN.)/27.0000 (60 MIN.)/.000000 ( 0 MIN.)
FOR ROTATIONS E(1) = .500000 E(2) = -.116660 E(3) = .000000 ACTUAL ANGLES ARE
(YXWLT) 6.99998 (60 MIN.)/27.5011 (30 MIN.)/.117251 ( 7 MIN.)
*STOP* NORMAL
DATA INFORMATION=IGNORED

```

APPENDIX G

X-RAY PROGRAM

The following is the FORTRAN computer program used to calculate X-ray diffraction angles for a doubly rotated cut of quartz.

15154 APR 1A, '60 DC/XRAY.536

1 -	0.500	COMMON /INTEN/REF
2 -	1.000	INTEGER M
3 -	2.000	COMMON /MILLER/H,K,L
4 -	3.000	COMMON /ERR/EA
5 -	4.000	DIMENSION EA(3)
6 -	5.000	CALL CLEAR
7 -	6.000	CALL ROTATE
8 -	7.000	CONTINUE
9 -	8.000	READ(103,10,END=99)H,K,L,REF
10 -	9.000	CALL NORMAL(IERR)
11 -	10.000	CALL SPOTS
12 -	11.000	IF(IERR.EQ.0)CALL GONIM
13 -	12.000	GOTO 20
14 -	13.000	CONTINUE
15 -	14.000	CALL LAST
16 -	15.000	CONTINUE
17 -	16.000	READ(104,30,END=99)EA(1),EA(2),EA(3)
18 -	17.000	CALL ERROR
19 -	18.000	GOTO 9A
20 -	19.000	FORMAT(30)
21 -	20.000	FORMAT(312,0)
22 -	21.000	STOP 'NORMAL'
23 -	22.000	END
24 -	23.000	SUBROUTINE ROTATE
25 -	24.000	REAL R(3,3)
26 -	25.000	COMMON /ROT/R
27 -	26.000	COMMON /ANGLE/A1,A2,A3
28 -	27.000	CALL SCFUN(A1,S1,C1)
29 -	28.000	CALL SCFUN(A2,S2,C2)
30 -	29.000	CALL SCFUN(A3,S3,C3)
31 -	30.000	R(1,1)=C1*C3-S1*S2*S3
32 -	31.000	R(1,2)=S1*C3+C1*S2*S3
33 -	32.000	R(1,3)=C2*S3
34 -	33.000	R(2,1)=S1*C2
35 -	34.000	R(2,2)=C1*C2
36 -	35.000	R(2,3)=S2
37 -	36.000	R(3,1)=C1*S3-S1*S2*C3
38 -	37.000	R(3,2)=S1*S3+C1*S2*C3
39 -	38.000	R(3,3)=C2*C3
40 -	39.000	RETURN
41 -	40.000	END

```

42 - 41.000 SUBROUTINE CLEAR
43 - 42.000 COMMON/CLEAN/
44 - 43.000 COMMON /ANGLE/A1,A2,A3
45 - 44.000
46 - 45.000 WRITE(100,10)
47 - 46.000 10 FORMAT(' INPUT THE THREE ANGLES PHI,THETA,PSI')
48 - 47.000 READ(105,30)A1,A2,A3
49 - 48.000 30 FORMAT(30)
50 - 49.000 WRITE(100,20)A1,MI(A1),A2,MI(A2),A3,MI(A3)
51 - 50.000 20 FORMAT('1 ***** ANGLES ARE',
52 - 51.000 ' (YMLT)',G,' (°12.° MIN.)',G,' (°12.° MIN.)',G,' (°12.°
53 - 52.000 ' MIN.)',/)
54 - 53.000 RETURN
55 - 54.000 END
56 - 55.000 SUBROUTINE NORMAL(IERR)
57 - 56.000 INTEGER M
58 - 57.000 COMMON /ROT/R
59 - 58.000 COMMON /NORM/RN,THETA
60 - 59.000 COMMON /MILLER/M,K,L
61 - 60.000 REAL RM(3),RNI(3),R(3,3)
62 - 61.000 IERR=0
63 - 62.000 RNI(1)=M
64 - 63.000 RNI(2)=FLOAT(M+2+K)/SQRT(3.0)
65 - 64.000 RNI(3)=FLOAT(L)/1.0997
66 - 65.000 DO 10 I=1,3
67 - 66.000 10 S=S+RNI(I)*RNI(I)
68 - 67.000 S=SQRT(S)
69 - 68.000 DO 20 I=1,3
70 - 69.000 20 RNI(I)=RNI(I)/S
71 - 70.000 DO 30 I=1,3
72 - 71.000 30 RNI(I)=0.
73 - 72.000 DO 30 J=1,3
74 - 73.000 30 RNI(I)=RNI(I)+R(I,J)*RNI(J)
75 - 74.000 A=90.903
76 - 75.000 CDIVA=1.0997
77 - 76.000 D=AO/(SQRT((A./3.)*FLOAT(M+M+K+K+K)+FLOAT(L*L)/(CDIVA*CDIVA)))
78 - 77.000 RLAMDA=1.5374
79 - 78.000 IF (RLAMDA.GE.2.0+ABS(D)) GO TO 40
80 - 79.000 THETA=ASIN(PLAMDA/(2.*D))
81 - 80.000 THETA=THETA+180./3.141592654
82 - 81.000 RETURN
83 - 82.000 CONTINUE
84 - 83.000 40

```

```

85 - 83,000
86 - 84,000
87 - 85,000
88 - 86,000
89 - 87,000
90 - 88,000
91 - 89,000
92 - 90,000
93 - 91,000
94 - 92,000
95 - 92,500 C
96 - 92,600 C
97 - 93,000
98 - 94,000
99 - 95,000
100 - 96,000
101 - 97,000
102 - 98,000
103 - 99,000
104 - 100,000
105 - 101,000
106 - 102,000
107 - 103,000
108 - 104,000
109 - 105,000
110 - 106,000
111 - 107,000
112 - 108,000
113 - 108,500
114 - 109,000
115 - 110,000
116 - 111,000
117 - 112,000
118 - 113,000
119 - 113,500
120 - 113,600
121 - 113,700
122 - 113,800
123 - 113,900
124 - 114,000
125 - 115,000
126 - 116,000
127 - 117,000

IFRM1
RETURN
END
SUBROUTINE SPOTS
COMMON /CLEAN/N
DIMENSION IREM(3,250),REM(2,250)
INTEGER M
COMMON /NORM/RN,THETA
COMMON /MILLER/H,K,L
REAL RN(3)
HERE WE USE TWICE THE VALUE PUT IN BY HEISING, WHICH HE TAKES
INTO ACCOUNT BY USE OF HIS SPECIAL SCALE ON THE FILM ITSELF.
ALPHA2.0=ACOS(-RN(2))/180./3.141592654
IF(ABS(ALPHA).GT.60.)RETURN
BETA=90.
IF(RN(3).LT.0)BETA=90.
IF(RN(1).EQ.0.)GOTO 10
BETATAN(RN(3)/RN(1))*180./3.141592654
CONTINUE
NEN+1
IF(N.GT.250)STOP'ARRAY SIZE TOO SMALL'
IREM(1,N)=H
IREM(2,N)=K
IREM(3,N)=L
REM(1,N)=ALPHA
REM(2,N)=BETA
RETURN
ENTRY LAST
DIST=10.0
WRITE(106,40)DIST
FORMAT('1 *****')
+ LAUE ANGLES DEFINED SUCH THAT ALPHA = ANGLE FROM BEAM,°,C)
+ BETA = ROTATION CLOCKWISE FROM P1, DIST TO CRYSTAL =°,C)
DO 30 I=1,N
CALL SCFUN(REM(1,I),ALB,ALC)
CALL SCFUN(REM(2,I),BES,BEC)
ALTBAL/ALC
X=DIST*ALTBES
Y=DIST*ALTBES
WRITE(106,20)(IREM(J,I),J=1,3),REM(1,I),REM(2,I),X,Y
CONTINUE
30
WRITE(106,41)
FORMAT(' *****')

```

```

128 - 119.000
129 - 119.000
130 - 120.000
131 - 121.000
132 - 122.000
133 - 123.000
134 - 124.000
135 - 125.000
136 - 125.500
137 - 126.000
138 - 127.000
139 - 128.000
140 - 129.000
141 - 130.000
142 - 131.000
143 - 131.100
144 - 131.150
145 - 131.200
146 - 131.300
147 - 131.400
148 - 131.500
149 - 132.000
150 - 133.000
151 - 134.000
152 - 135.000
153 - 136.000
154 - 137.000
155 - 138.000
156 - 139.000
157 - 140.000
158 - 141.000
159 - 142.000
160 - 143.000
161 - 144.000
162 - 145.000
163 - 146.000
164 - 147.000
165 - 148.000
166 - 149.000
167 - 150.000
168 - 151.000
169 - 152.000
170 - 153.000

** LAUE ANGLES DEFINED SUCH THAT ALPHA = ANGLE FROM BEAM, **/,
** BETA = ROTATION CLOCKWISE FROM P1.**)
FORMAT(' MILLER INDICES:',3(I2,1X), ' LAUE SPOT ANGLES: ALPHA',
+G, ' BETA', G, ' XE', G, ' YE', G)
RETURN
END
SUBROUTINE GONIOH
INTEGER M
COMMON /INTEN/IFF
COMMON /MILLER/M,K,L
COMMON /NORMARN,THETA
LOGICAL NO1,NO2,NO3,NO4
DIMENSION RN(3)
DATA PHI/5.18159054/,BETAMAX/5.0/
IF(ABS(RN(2)).LT. 0.9)RETURN
IF(L.GT.0)GOTO 12
IF(L.LT.0)RETURN
IF(K.GT.0)GOTO 12
IF(K.EQ.0 .AND. H.GT.0)GOTO 12
RETURN
CONTINUE
NO1=TRUE.
NO2=TRUE.
CALL SCFUN(THETA,TTS,TTG)
T1=2.*TTS*RN(1)
T2=2.*TTS*RN(3)
IF(ABS(T1).GT.1.0)NO1=FALSE.
IF(ABS(T2).GT.1.0)NO2=FALSE.
IF(NO1)MET1=180.*ASIN(T1)/PHI
IF(NO2)MET2=180.*ASIN(T2)/PHI
IF(ABS(MET1).GT.BETAMAX)NO1=FALSE.
IF(ABS(MET2).GT.BETAMAX)NO2=FALSE.
IF(.NOT.NO1 .AND. .NOT.NO2)RETURN
DELTP1=180.*ATAN(RN(3)/RN(2))/PHI
DELTP2=180.*ATAN(RN(1)/RN(2))/PHI
T1=180.*ASIN(RN(1))/PHI
CALL SCFUN(THETA,TTS,TTG)
T=TTG/TC
IF(ABS(T).GT.1.0)NO1=FALSE.
IF(NO1)T=180.*ASIN(T)/PHI
T=180.*ASIN(RN(3))/PHI
CALL SCFUN(T,T8,TC)

```

```

171 - 154,000
172 - 155,000
173 - 156,000
174 - 157,000
175 - 158,000
176 - 159,000
177 - 160,000
178 - 161,000
179 - 162,000
180 - 163,000
181 - 164,000
182 - 165,000
183 - 166,000
184 - 167,000
185 - 168,000
186 - 169,000
187 - 170,000
188 - 171,000
189 - 172,000
190 - 173,000
191 - 174,000
192 - 175,000
193 - 176,000
194 - 177,000
195 - 178,000
196 - 179,000
197 - 180,000
198 - 181,000
199 - 182,000
200 - 183,000
201 - 184,000
202 - 185,000
203 - 186,000
204 - 187,000
205 - 188,000
206 - 189,000
207 - 190,000
208 - 191,000
209 - 192,000
210 - 193,000
211 - 194,000
212 - 195,000
213 - 196,000

TBTB/TC
IF(ABS(T).GT.1.0)NO2=FALSE.
IF(NO2)THETP=180.*ASIN(T)/PHI
G1=THETP-DELT1
G2=THETP+DELT2
G3=THETP+DELT1
G4=THETP-DELT2
CALL SCFUN(2.*THETA,TS,TC)
CALL SCFUN(BET1,TS,TC)
IF(ABS(TC/TT).GT.1.0)NO1=FALSE.
IF(NO1)GPP1=180.*ACOS(TC/TT)/PHI
CALL SCFUN(BET2,TS,TC)
IF(ABS(TC/TT).GT.1.0)NO2=FALSE.
IF(NO2)GPP2=180.*ACOS(TC/TT)/PHI
IF(.NOT.NO1 .AND. .NOT.NO2)RETURN
NO3=NO1
NO4=NO2
IF(G1.LT.0. .OR. GPP1.LT.0)NO1=FALSE.
IF(G2.LT.0. .OR. GPP2.LT.0)NO2=FALSE.
IF(G3.LT.0. .OR. GPP1.LT.0)NO3=FALSE.
IF(G4.LT.0. .OR. GPP2.LT.0)NO4=FALSE.
CALL SCFUN(2.*THETA-G1,TS,TC)
CALL SCFUN(G1,G8,GC)
FACT1=TS/(TS+GS)
CALL SCFUN(2.*THETA-G2,TS,TC)
CALL SCFUN(G2,GS,GC)
FACT2=TS/(TS+GS)
CALL SCFUN(2.*THETA-G3,TS,TC)
CALL SCFUN(G3,GS,GC)
FACT3=TS/(TS+GS)
CALL SCFUN(2.*THETA-G4,TS,TC)
CALL SCFUN(G4,GS,GC)
FACT4=TS/(TS+GS)
IF(FACT1.LT.0. .OR. FACT1.GT.1.0)NO1=FALSE.
IF(FACT2.LT.0. .OR. FACT2.GT.1.0)NO2=FALSE.
IF(FACT3.LT.0. .OR. FACT3.GT.1.0)NO3=FALSE.
IF(FACT4.LT.0. .OR. FACT4.GT.1.0)NO4=FALSE.
IF(.NOT.NO1 .AND. .NOT.NO2 .AND. .NOT.NO3 .AND. .NOT.NO4)RETURN
WRITE(108,10)M,K,L
FORMAT(' ',33) MILLER INDICES',313,/)
WRITE(108,20)(RN(I),I=1,3),THETA
FORMAT(' NORMAL VECTOR ',35,/, THETA',6)
FORMAT(' PLATE IN POSITION ',11, ( ,
10
20
100

```

```

214 - 196,000
215 - 197,000
216 - 198,000
217 - 199,000
218 - 200,000
219 - 201,000
220 - 202,000
221 - 203,000
222 - 204,000
223 - 205,000
224 - 206,000
225 - 207,000
226 - 208,000
227 - 209,000
228 - 210,000
229 - 211,000
230 - 212,000
231 - 213,000
232 - 214,000
233 - 215,000
234 - 216,000
235 - 217,000
236 - 218,000
237 - 219,000
238 - 220,000
239 - 221,000
240 - 222,000
241 - 223,000
242 - 224,000
243 - 225,000
244 - 226,000
245 - 227,000
246 - 228,000
247 - 229,000
248 - 230,000
249 - 231,000
250 - 232,000
251 - 233,000
252 - 234,000
253 - 235,000
254 - 236,000
255 - 237,000
256 - 238,000

+I2,° AXIS VERTICAL, 2 AXIS NORMAL)°)
FORMAT(' G ° ANGLE OF INCIDENCE',G,° ('I2,° MIN.),°)
+° BETAI,G,° ('I2,° MIN.),°)
+° G PLUS G PRIMEEXIT ANGLEI',G,° ('I2,° MIN.),°)
+° INTENSITY FACTORI',G,° INTENSITYI',G)
IF(N01)WRITE(108,100)1,-1
IF(N01)WRITE(108,110)G1,MI(G1),BETI,MI(BETI),GPP1,MI(GPP1),FACT1
+REF+FACT1
IF(N02)WRITE(108,100)2,-3
IF(N02)WRITE(108,110)G2,MI(G2),BET2,MI(BET2),GPP2,MI(GPP2),FACT2
+REF+FACT2
IF(N03)WRITE(108,100)3,1
IF(N03)WRITE(108,110)G3,MI(G3),-REY1,MI(-BET1),GPP1,MI(GPP1),
+FACT3,REF+FACT3
IF(N04)WRITE(108,100)4,3
IF(N04)WRITE(108,110)G4,MI(G4),-BET2,MI(-BET2),GPP2,MI(GPP2),
+FACT4,REF+FACT4
RETURN
END
INTEGER FUNCTION MIX(X)
REAL X,X1
X1=ABS(X)
MIX=INT(0.0+(X1-INT(X1))*0.5)
RETURN
END
SUBROUTINE ERROR
COMMON /ERR/EA
COMMON /RNT/R
DIMENSION EA(3),R(3,3),ES(3)
DATA PHI/3.141592654/
DO 10 I=1,3
CALL SCFUN(EA(I),ES(I),Y)
TMR(2,2)=ES(1)+R(3,2)+ES(3)+R(2,1)
TMR(1,2,1)=ES(1)+R(3,1)+ES(3)+R(1,1)
A1=90.
IF(T,NE.0.)A1=180.-ATAN(T1/T)/PHI
TMR(2,3)=ES(1)+R(3,3)+ES(3)+R(1,3)
A2=180.-ASIN(T)/PHI
TMR(3,3)=ES(2)+R(1,3)+ES(1)+R(2,3)
T1=-(R(1,3)-ES(3)+R(2,3)+ES(2)+R(3,3))
A3=90.
IF(T,NE.0.)A3=180.-ATAN(T1/T)/PHI
WRITE(108,20)(I,EA(I),1=1,3),A1,MI(A1),A2,MI(A2),A3,MI(A3)

```


ELECTRONICS TECHNOLOGY AND DEVICES LABORATORY
MANDATORY CONTRACT DISTRIBUTION LIST

101	Defense Technical Information Center ATTN: DTIC-TCA Cameron Station (Bldg 5) Alexandria, VA 22314	001	Arlington, VA 22212
012		602	Cdr, Night Vision & Electro-Optics ERADCOM ATTN: DELNV-D
203	GIDEP Engineering & Support Dept TE Section PO Box 398 NORCO, CA 91760	001	Fort Belvoir, VA 22060
001		603	Cdr, Atmospheric Sciences Lab ERADCOM ATTN: DELAS-SY-S
205	Director Naval Research Laboratory ATTN: CODE 2627 Washington, DC 20375	001	White Sands Missile Range, NM 88002
001		607	Cdr, Harry Diamond Laboratories ATTN: DELHD-CO, TD (In Turn) 2800 Powder Mill Road Adelphi, MD 20783
301	Rome Air Development Center ATTN: Documents Library (TILD) Griffiss AFB, NY 13441	001	
001		609	Cdr, ERADCOM ATTN: DRDEL-CG, CD, CS (In Turn) 2800 Powder Mill Road Adelphi, MD 20783
437	Deputy for Science & Technology Office, Asst Sec Army (R&D) Washington, DC 20310	001	
001		612	Cdr, ERADCOM ATTN: DRDEL-CT 2800 Powder Mill Road Adelphi, MD 20783
438	HQDA (DAMA-ARZ-D/Dr. F.D. Verderame) Washington, DC 20310	001	
001		680	Commander US Army Electronics R&D Command Fort Monmouth, NJ 07703
482	Director US Army Materiel Systems Analysis Actv ATTN: DRXSY-MP	000	1 DELET-MQ 1 DELEW-D 1 DELET-DD 1 DELSD-L (Tech Library) 2 DELSD-L-S (STINFO) 34 Originating Office 1 DELET-MF
001	Aberdeen Proving Ground, MD 21005	681	Commander US Army Communications R&D Command ATTN: USMC-LNO Fort Monmouth, NJ 07703
563	Commander, DARCOM ATTN: DRCDE 5001 Eisenhower Avenue Alexandria, VA 22333		
001			
564	Cdr, US Army Signals Warfare Lab ATTN: DELSW-OS Vint Hill Farms Station Warrenton, VA 22186		
001			
705	Advisory Group on Electron Devices 201 Varick Street, 9th Floor New York, NY 10014		
002			
579	Cdr, PM Concept Analysis Centers ATTN: DRCPM-CAC Arlington Hall Station		

**ELECTRONICS TECHNOLOGY AND DEVICES LABORATORY
SUPPLEMENTAL CONTRACT DISTRIBUTION LIST**

(ELECTIVE)

103	Code R123, Tech Library DCA Defense Comm Engrg Ctr 1800 Wiehle Ave Reston, VA 22090	475	Cdr, Harry Diamond Laboratories ATTN: Library 2800 Powder Mill Road Adelphi, MD 20783
104	Defense Communications Agency Technical Library Center Code 205 (P. A. Tolovi) Washington, DC 20305	477	Director US Army Ballistic Research Labs ATTN: DRXBR-LB Aberdeen Proving Ground, MD 21005
206	Commander Naval Electronics Laboratory Center ATTN: Library San Diego, CA 92152	*481	Harry Diamond Laboratories ATTN: DELHD-RCB (Dr. J. Nemerich) 2800 Powder Mill road Adelphi, MD 20783
207	Cdr, Naval Surface Weapons Center White Oak Laboratory ATTN: Library Code WX-21 Silver Spring, MD 20910	482	Director US Army Materiel Systems Analysis Actv ATTN: DRXSY-T, MP (In Turn) Aberdeen Proving Ground, MD 21005
314	Hq, Air Force Systems Command ATTN: DLCA Andrews Air Force Base Washington, DC 20331	507	Cdr, AVRADCOM ATTN: DRSAV-E PO Box 209 St. Louis, MO 63166
403	Cdr, MICOM Redstone Scientific Info Center ATTN: Chief, Document Section Redstone Arsenal, AL 35809	511	Commander, Picatinny Arsenal ATTN: SARPA-FR-5, -ND-A-4, -TS-S (In Turn) Dover, NJ 07801
406	Commandant US Army Aviation Center ATTN: ATZQ-D-MA Fort Rucker, AL 36362	515	Project Manager, REMBASS ATTN: DRCPM-FFR-TM Fort Monmouth, NJ 07703
407	Director, Ballistic Missile Defense Advanced Technology Center ATTN: ATC-R, PO Box 1500 Huntsville, AL 35807	517	Commander US Army Satellite Communications Agcy ATTN: DRCPM-SC-3 Fort Monmouth, NJ 07703
418	Commander HQ, Fort Huachuca ATTN: Technical Reference Div Fort Huachuca, AZ 85613	518	TRI-TAC Office ATTN: TT-SE Fort Monmouth, NJ 07703

*For Millimeter & Microwave Devices Only

**ELECTRONICS TECHNOLOGY AND DEVICES LABORATORY
SUPPLEMENTAL CONTRACT DISTRIBUTION LIST (CONT)
(ELECTIVE)**

519	Cdr, US Army Avionics Lab AVRADCOM ATTN: DAVAA-D	608	Commander ARRADCOM DRDAR-TSB-S
001	Fort Monmouth, NJ 07703	001	Aberdeen Proving Ground, MD 21005
520	Project Manager, FIREFINDER ATTN: DRCPM-FF	614	Cdr, ERADCOM ATTN: DRDEL-LL, -SB, -AP (In Turn)
001	Fort Monmouth, NJ 07703		2800 Powder Mill Road
521	Commander Project Manager, SOTAS ATTN: DRCPM-STA	001	Adelphi, MD 27083
001	Fort Monmouth, NJ 07703	617	Cdr, ERADCOM ATTN: DRDEL-AQ
531	Cdr, US Army Research Office ATTN: DRXRO-PH (Dr. Lontz) DRXRO-IP (In Turn)		2800 Powder Mill Road
	PO Box 12211	001	Adelphi, MD 20783
001	Research Triangle Park, NC 27709	619	Cdr, ERADCOM ATTN: DRDEL-PA, -ILS, -ED (In Turn)
556	HQ, TCATA Technical Information Center ATTN: Mrs. Ruth Reynolds		2800 Powder Mill Road
001	Fort Hood, TX 76544	001	Adelphi, MD 20783
568	Commander US Army Mobility Eqp Res & Dev Cmd ATTN: DRDME-R	701	MTI — Lincoln Laboratory ATTN: Library (RM A-082)
001	Fort Belvoir, VA 22060		PO Box 73
604	Chief Ofc of Missile Electronic Warfare Electronic Warfare Lab, ERADCOM	002	Lexington, MA 02173
001	White Sands Missile Range, NM 88002	703	NASA Scientific & Tech Info Facility Baltimore/Washington Intl Airport
606	Chief Intel Materiel Dev & Support Ofc Electronic Warfare Lab, ERADCOM	001	PO Box 8757, MD 21240
001	Fort Meade, MD 20755	704	National Bureau of Standards Bldg 225, RM A-331
			ATTN: Mr. Leedy
		001	Washington, DC 20231
		707	TACTEC Batelle Memorial Institute
			505 King Avenue
		001	Columbus, OH 43201

AD-A110 663

MOTOROLA INC SCOTTSDALE AZ GOVERNMENT ELECTRONICS DIV

F/8 9/1

DOUBLY ROTATED CUT SAW DEVICES. (U)

JAN 82 D F WILLIAMS, F Y CHO

DAAK20-79-C-0275

UNCLASSIFIED

DELET-TR-79-0275-F

ML

3-3

3-3



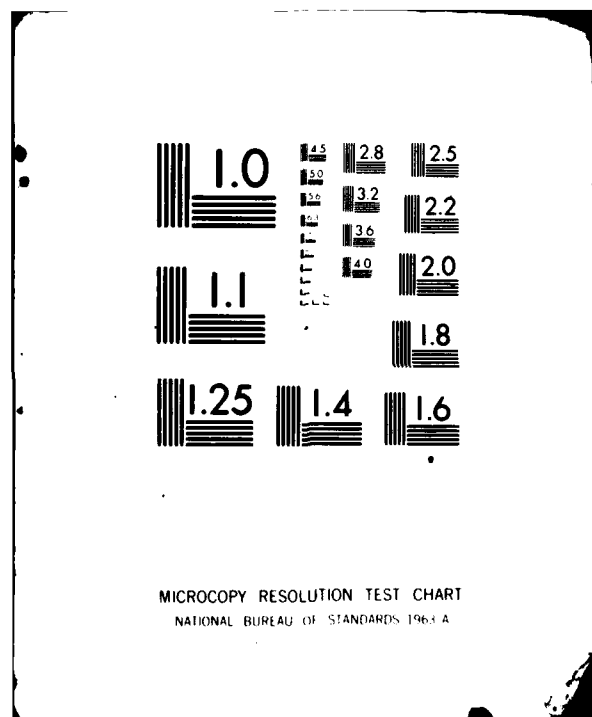
END

DATE

FILED

13-82

DTIC



**ELECTRONICS TECHNOLOGY AND DEVICES LABORATORY
SUPPLEMENTAL CONTRACT DISTRIBUTION LIST (CONT)**

(ELECTIVE)

Coordinated Science Laboratory University of Illinois Urbana, Illinois 61801 ATTN: Dr. Bill J. Hunsinger	(1)	Anderson Laboratories, Inc. 1280 Blue Hills Ave ATTN: Dr. A.A. Comparini Bloomfield, Conn. 06002	(1)
Dr. J.S. Bryant OCD ATTN: DARD-ARP Washington, DC 20310	(1)	Mr. Henry Friedman RADC/OCTE Griffiss AFB, NY 13440	(1)
Dr. R. LaRosa Hazeltine Corporation Greenlawn, New York 11740	(1)	Autonetics, Division of North American Rockwell P.O. Box 4173 3370 Miraloma Avenue Anaheim, CA 92802 ATTN: Dr. G.R. Pulliam	(1)
General Electric Co. Electronics Lab Electronics Park Syracuse, NY 13201 ATTN: Mr. S. Wanuga	(1)	General Dynamics, Electronics Division P.O. Box 81127 San Diego, CA 92138 ATTN: Mr. R. Badewitz	(1)
Air Force Cambridge Labs ATTN: CRDR (Dr. P. Carr & Dr. A.J. Slobodnik) Bedford, MA 01730	(2)	Texas Instruments, Inc. P.O. Box 5936 13500 N. Central Expressway Dallas, Texas 75222 ATTN: Dr. L.T. Clairborne	(2)
Mr. R. Weglein Hughes Research Laboratories 3011 Malibu Canyon Road Malibu, California 90265	(1)	Raytheon Company Research Division 28 Seyon Street Waltham, Massachusetts 02154 ATTN: Dr. M.B. Schulz	(1)
Mr. H. Bush CORC RADC Griffiss Air Force Base New York 13440	(1)	Sperry Rand Research Center 100 North Road Sudbury, Massachusetts 01776 ATTN: Dr. H. Van De Vaart	(1)
Dr. Tom Bristol Hughes Aircraft Company Ground Systems Group Bldg 600/MS D235 1901 W. Malvern Fullerton, CA 92634	(2)	Microwave Laboratory W.W. Hansen Laboratories of Physics Stanford University Stanford, CA 94305 ATTN: Dr. H.J. Shaw	(2)
Commander, AFAL ATTN: Mr. W.J. Edwards, TEA Wright-Patterson AFB, Ohio 45433	(1)		

**ELECTRONICS TECHNOLOGY AND DEVICES LABORATORY
SUPPLEMENTAL CONTRACT DISTRIBUTION LIST (CONT)**

(ELECTIVE)

Polytechnic Institute of Brooklyn Route No. 110 Farmingdale, NY 11735 ATTN: Dr. A.A. Oliner	(1)	Advanced Technology Center, Inc. Subsidiary of LTV Aerospace Corp. P.O. Box 6144 Dallas, Texas 75222 ATTN: Mr. A.E. Sobey	(1)
Westinghouse Electric Corp. Research & Development Center Beulah Road Pittsburgh, PA 15235 ATTN: Dr. J. DeKlerk	(1)	United Aircraft Research Labs ATTN: Dr. Thomas W. Grudkowski East Hartford, Conn. 06108	(1)
Stanford Research Institute Menlo Park, CA 94025 ATTN: Dr. A. Bahr	(1)	Science Center Rockwell International Thousand Oaks, CA 91360 ATTN: Dr. T.C. Lim	(1)
International Business Machines Corp. Research Division P.O. Box 218 Yorktown Heights, NY 10598 ATTN: Dr. F. Bill	(1)	University of Southern CA Electronic Science Lab School of Engineering University Park, Los Angeles California 900 ATTN: Dr. K. Lakin, SSC 303	(1)
TRW Defense and Space Sys Group One Space Park Redondo Beach, CA 90278 ATTN: Dr. R.S. Kagiwada	(1)	SAWTEK, Inc. P.O. Box 7756 2451 Shader Road Orlando, Florida 32854 ATTN: Mr. S. Miller	(1)
Tektronix Inc. P.O. Box 500 Beaverton, OR 97077 ATTN: Dr. R. Li	(1)	Prof. P.C.Y. Lee School of Engineering Princeton University Princeton, NJ 08540	(1)
Dr. Fred S. Hickernell Integrated Circuit Facility Motorola Government Electronics Division 8201 East McDowell Road Scottsdale, AZ 85257	(1)	Mr. John A. Kusters Hewlett-Packard 5301 Stevens Creek Boulevard Santa Clara, CA 95050	(1)
Prof. H.F. Tiersten Jonsson Engineering Center Rensselaer Polytechnic Institute Troy, NY 12181	(1)	Dr. Tom Young Sandia Laboratories P.O. Box 5800 Albuquerque, NM 87185	(1)
McGill University ATTN: G.W. Farnell Montreal 110, Canada	(1)	Dr. William J. Tanski Sperry Research Center 100 North Road Sudbury, MA 01776	(1)

**ELECTRONICS TECHNOLOGY AND DEVICES LABORATORY
SUPPLEMENTAL CONTRACT DISTRIBUTION LIST (CONT)**

(ELECTIVE)

Dr. B.A. Auld
E.L. Ginzton Laboratory
Stanford University
Stanford, CA 94305

(1)

Mr. Marvin E. Frerking
MS 137-138
Collins Radio Company
855 35th Street, NE
Cedar Rapids, IA 52406

(1)

Dr. William R. Shreve
HP Laboratories
1501 Page Mill Road
Palo Alto, CA 94304

(1)

Dr. Thomas M. Reeder
MS 50-362
Tektronix, Inc.
P.O. Box 500
Beaverton, OR 97077

(1)

Dr. Robert L. Rosenberg
Bell Laboratories
Crawfords Corner Road
Holmdel, NJ 07733

(1)

Dr. B.K. Sinha
Schlumberger-Doll Research Center
P.O. Box 307
Ridgefield, CT 06877

(1)

Dr. Robert S. Wagers
Texas Instruments, Inc.
13500 N. Central Expwy.
P.O. Box 225936, MS 134
Dallas, TX 75265

(1)

Dr. Richard C. Williamson
Lincoln Laboratory
P.O. Box 73
Lexington, MA 02173

(1)

SUPPLEMENT TO DISTRIBUTION LIST

D. Chrissotimos, Code 763
National Aeronautics and Space
Administration
Goddard Space Flight Center
Greenbelt, MD 20771

(1)

Naval Research Laboratories
Code 5237
Washington, DC 20375
ATTN: Dr. D. Webb

(1)

HQ ESD (DRI)
L.G. Hanscom AFB
Bedford, MA 01731

(1)

Commander
US Army Missile Command
ATTN: DRSMI-RE (Mr. Pittman)
Redstone Arsenal, AL 35809

(1)

Army Materials and Mechanics Research
Center (AMMRC)
Watertown, MA 02172
ATTN: DMXMR-EO

(1)

Commander, Picatinny Arsenal
ATTN: SARPA-FR-S
Bldg. 350
Dover, NJ 07801

(2)

A. Kahan
RADC/ESE
Hanscom AFB
Bedford, MA 01731

(1)

Dr. Robert O'Connell
Department of EE
Univ. of Missouri - Columbia
Columbia, MO 65201

(1)

Prof. John F. Vetelino
Dept of EE
Univ. of Maine - Orono
Orono, ME 04469

(1)

SUPPLEMENT TO DISTRIBUTION LIST

Dr. Robert O'Connell
Department of EE
University of Missouri - Columbia
Columbia, MO 65201 (1)

Prof. John F. Vetelino
Dept of EE
University of Maine - Orono
Orono, ME 04469 (1)

Dr. Franz Sauerland
Transat Corp.
3713 Lee Road
Shaker Heights, OH 44120 (1)

Mr. Leon Marchand
Damon Corp.
80 Wilson Way
Westwood, MA 02090 (1)

DATE
FILMED
8